Imaging and Spectroscopy of Solid-State Quantum Emitters

Pragati Kumar

Thesis submitted for the degree of Doctor of Philosophy

Heriot-Watt University

School of Engineering and Physical Sciences

Institute of Photonics and Quantum Sciences

January 2018

Abstract

Efficient generation of single photons can revolutionize the field of quantum communication and linear optical quantum computing. Solid-state semiconductor quantum dots present a promising platform to realize this long term vision. In particular, self-assembled InAs quantum dots exhibit near unity radiative efficiency. Enhancement of collection efficiency of photon from self-assembled InAs quantum dots is a key necessity to realize quantum technologies. In this respect, GaAs nanowire single photon source and planar membrane devices have shown considerable promise. Photoluminescence spectroscopy has been undertaken to study the photon collection from these devices and the behaviour such as lifetime of quantum dots when embedded in these nanophotonic structures. The ease of implementing electrical contacts onto the planar membrane devices is another significant feature which allows complete control over the number of electrons in the quantum dot.

The key concept behind the enhancement of photon emission from planar membrane devices is the radiation from an electric dipole emitter whose angular radiation pattern is modified by choice of materials and design of sample. Using Fourier microscopy also known as back focal plane imaging, a match between the design of the angular radiation profile and the obtained experimental data is made. This is an excellent way to figure out if the light being emitted by the quantum emitter is being collected into the optical system. In addition, the transfer-matrix model used for design of angular radiation profile also yields different efficiency depending upon the orientation of the emission dipole in the quantum emitter. Thus, in order to design samples for higher photon collection efficiency, the knowledge of the orientation of the emission dipole is important. In order to extract the full three-dimensional orientation of the quantum emitter, defocused imaging of the dipole radiation is performed.

A relatively new material system for quantum photonics is based on novel two-dimensional semiconductors such as WSe_2. To understand the nature of emission from these solid-state emitters, Fourier microscopy and defocused imaging have been used to obtain the angular distribution of radiation and orientation of emission dipoles in these emitters, respectively.

Dedicated to

my grandma Late Mrs. Sushila Sahay

Acknowledgement

I would like to thank Prof. Brian Gerardot for giving me the opportunity to work in a truly world-class lab and for introducing me to the ever growing field of quantum photonics. I would like to extend my gratitude to all members of the research group for working with me during experiments, simulations and while setting up the experiments. I would like to extend special thanks to Dr. Raphael Proux, Guillem-Ballesteros Garcia, Dr. Santosh Kumar and Dr. Yong Ma from whom I learned a great deal during my stay. Last but not the least, I would like to thank my parents and loved ones for their support and guidance all through.

HERIOT
WATT
UNIVERSITY

ACADEMIC REGISTRY
Research Thesis Submission

Name:	Pragati Kumar		
School:	School of Engineering and Physical Sciences		
Version: *(i.e. First, Resubmission, Final)*	Final	Degree Sought:	PhD

Declaration

In accordance with the appropriate regulations I hereby submit my thesis and I declare that:

1) the thesis embodies the results of my own work and has been composed by myself
2) where appropriate, I have made acknowledgement of the work of others and have made reference to work carried out in collaboration with other persons
3) the thesis is the correct version of the thesis for submission and is the same version as any electronic versions submitted*.
4) my thesis for the award referred to, deposited in the Heriot-Watt University Library, should be made available for loan or photocopying and be available via the Institutional Repository, subject to such conditions as the Librarian may require
5) I understand that as a student of the University I am required to abide by the Regulations of the University and to conform to its discipline.
6) I confirm that the thesis has been verified against plagiarism via an approved plagiarism detection application e.g. Turnitin.

* *Please note that it is the responsibility of the candidate to ensure that the correct version of the thesis is submitted.*

Signature of Candidate:	Pragati Kumar	Date:	11-01-2018

Submission

Submitted By *(name in capitals)*:	
Signature of Individual Submitting:	
Date Submitted:	

For Completion in the Student Service Centre (SSC)

Received in the SSC by *(name in capitals)*:			
Method of Submission *(Handed in to SSC; posted through internal/external mail)*:			
E-thesis Submitted ***(mandatory for final theses)***			
Signature:		Date:	

Please note this form should be bound into the submitted thesis.
Academic Registry/Version (1) August 2016

Contents

List of Tables

List of Figures

Chapter 1

Introduction

1.1 Motivation

The amount of parallel processing in quantum systems has an exponential dependence on the physical size of the system by virtue of the principle of superposition yielding a significant edge over state-of-the-art supercomputers where the processing speed is linearly tied up with device footprint. Quantum parallelism is useful for prime factoring of large numbers which lies at the heart of information security on the internet [1], for fast database searching [2], and for fast solutions of complex problems [3]. With this motivation, there are several material platforms that have been investigated to realize the hardware for such a quantum processor such as ion traps [4], quantum dots [5] [6], Josephson junctions [7], nuclear spins in molecules [8] and nuclear spins in silicon [9]. In addition to the promise of computing capabilities, the field of quantum information also entails applications in quantum communication [10] for secure communication between two parties, and in quantum metrology to achieve higher resolution by making use of entanglement [11].

Optics provides integration with classical optical communication channels [12] and the immunity to decoherence of photons is another favourable factor in realization of large distance quantum communication links using optics. With optics/photonics as the platform, scalable linear optical quantum computing (LOQC) [13] and quantum encrypted communication (e.g. BB84 protocol [14]) require source and detector hardware for their realization.

Polarized single photons have been envisaged to be used for BB84 quantum communication protocol since the information carried by a single photon cannot be copied [14] without altering it. No cloning theorem further prevents the generation of more photons from the photon carrying the information [16]. Thus, secure transmission of information is ensured as the information cannot be stolen without being detected. Single photons can be generated by attenuating a laser pulse, by parametric down-conversion or by using a single quantum emitter. For Quantum Key Distribution (QKD), faint laser pulses are sufficient for completely secure communication using a Decoy-state protocol, in which an intensity-modulated signal is transmitted [17] [18] [19] [20]. The eavesdropper cannot reconstruct information from the signal due to no prior knowledge of the modulation pattern, and the receiver can ascertain any change in output pattern due to an eavesdropping event. Even in this scenario, a malfunction during the manufacturing process of the equipment or a deliberate tamper with the device can allow information to be extracted by an eavesdropper. Sources based on parametric downconversion are again limited by the poissonian statistics of photon emission. The efficiency of the photon source is greatly reduced in an attempt to reduce multiphoton events. A source with sub-poissonian photon statistics can overcome efficiency and security drawbacks. Single quantum emitter based single photons are useful for QKD when the security of the key has to be device-independent i.e. completely secure communication even with manufacturer negligence [21]. The protocol in this scenario is based on entanglement and requires a source of indistinguishable single photons.

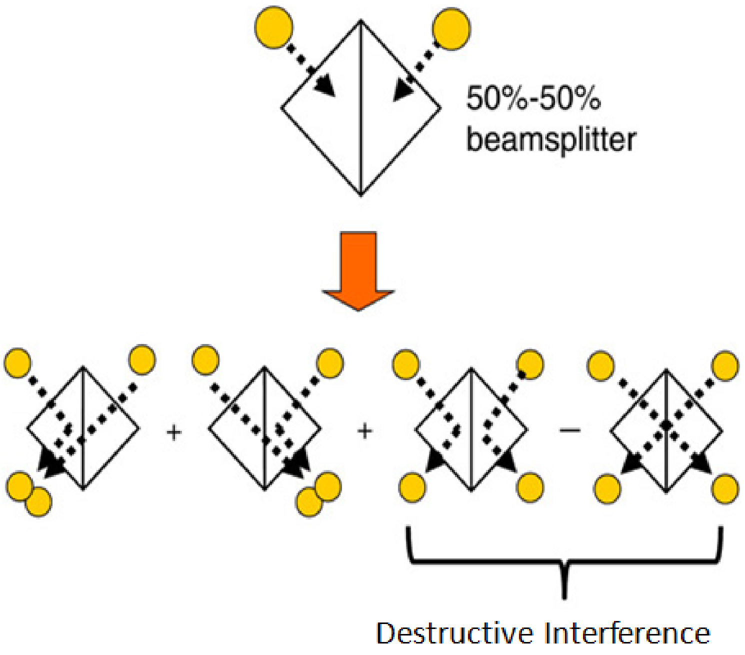

Figure 1.1: Two-photon interference can have four possible outcomes out of which when the two photons arrive at the same detector are the only possible options when the two photons are indistinguishable [picture courtesy: Ralph Malein]

Indistinguishability of photons can be verified by two-photon interference experiment shown in Figure 1.1. When two photons are incident on a beamsplitter from two sides, there can be four possible outcomes i.e. i) the first photon gets reflected and second photon gets transmitted, ii) the first is transmitted and second reflected, iii) both photons reflected and iv) both are reflected. When the two photons are completely indistinguishable i.e. identical emission wavelength, polarization, and are overlapping temporally and spatially, then the last two outcomes destructively interfere. In this case, the two possible outcomes have both photons travelling together to the same detector.

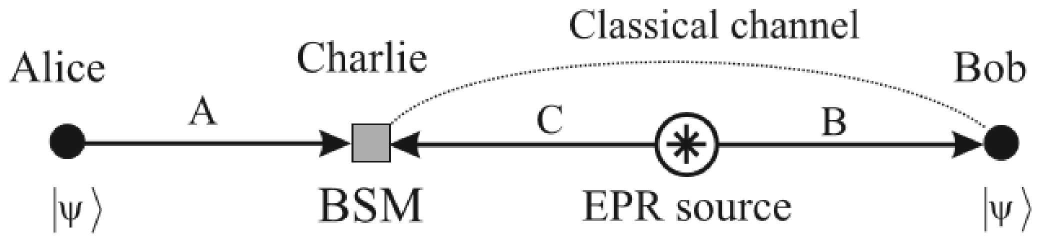

Figure 1.2: Quantum teleportation acting as a quantum relay for long haul communication network [23]

For future long distance quantum communication links, it is necessary to have quantum repeaters (like there are repeaters for classical optical networks) at the nodes of the transmission network. This is possible through quantum teleportation of the quantum state in the scenario where the sender (Charlie) and receiver (Bob) share an entangled state created by an Einstein-Podolsky-Rosen (EPR) pair source and are able to communicate via a classical channel [22]. Quantum teleportation is referred to as the transmission of the quantum state of a particle rather than the particle itself. The sender is unaware of the basis of the quantum state $|\psi_0>$ that needs to be transmitted. Thus in order to teleport the quantum state to the next network node, a joint measurement also known as Bell-State Measurement is carried out between Alice's photon and one half of the EPR pair at the sender (Charlie's) end. This interaction transfers the information from the quantum state $|\psi_0>$ to the interacting half of the EPR pair and projects the Bob's photon to Alice's photon. For a quantum communication network with several nodes, entanglement swapping is carried out between different segments of the network (which share entanglement) to transmit the quantum state to the final destination node [23]. The Bell-State Measurement requires indistinguishability of photons.

In LOQC, the purity of the single photon state is a necessity for realization of the quantum computation scheme based on linear optics. The method relies on interaction of photons on beam-splitters [13] [25] [26] for realization of quantum gates, which can demand long measurement times as the process relies on statistics of photon arrival times. An efficient source of single photons from a quantum emitter can cut down the measurement time for applications in LOQC [27] [28].

1.2 Coherence Function and Photon Antibunching

A two-level emitter cannot emit more than one photon at once because after each photon emission event, the carrier decays to the ground state with a finite recovery time. The occupation probability of the excited-state reaches the steady-state population only after a finite time. This behaviour in photon emission is termed as photon antibunching [29] as no photons can be emitted simultaneously. In order to understand it mathematically, a modicum of mathematical vocabulary needs to be adopted. The mathematical approach to explain the coherence function and antibunching is taken from reference [30] and [31].

A quantum light source can be distinguished from classical light by study of second order correlation of photon arrival times on two photon detectors. With the intensities obtained from two photodetectors, the correlation is proportional to the transition rate for a joint absorption of photons at the two points. The transition probability of the detector (sensitive to field E$^{(+)}$) for absorbing a photon at position ’r’ and time ’t’ is given by,

$$T_{if} = | < f|E^{(+)}(r,t)|i > |^2 \tag{1.1}$$

where $|i >$ and $|f >$ are the initial and final states of the field. The average field intensity is then described by a summation of a complete set of final states as shown below.

$$I(r,t) = \sum_f T_{fi} = \sum_f < i|E^{(-)}(r,t)|f >< f|E^{(+)}(r,t)|i > = < i|E^{(-)}E^{(+)}|i > \tag{1.2}$$

The above expression for the intensity however is under the assumption that field is in a pure state $|i >$. In case of a statistical mixture, the result can be generalized by averaging over the initial states with the probability P$_i$,

$$I(r,t) = \sum_i P_i < i|E^{(-)}(r,t)E^{(+)}(r,t)|i >= Tr\{\rho E^{(-)}(r,t)E^{(+)}(r,t)\} \tag{1.3}$$

where ρ is the density operator defined as $\rho = \sum_i P_i|i >< i|$.

The correlation between the field at the space-time point x = (r,t) and the field at x' = (r,t') can be written as the correlation function,

$$G^{(1)}(x,x') = Tr\{\rho E^{(-)}(x)E^{(+)}(x')\} \tag{1.4}$$

The first order correlation function can account for classical interference experiments. For Hanbury-Brown-Twiss experiment, second order correlation function is necessary. The joint counting rate at two photodetectors at positions r_1 and r_2 is given by,

$$T_{fi} = | < f|E^{(+)}(r_2,t_2)E^{(+)}(r_1,t_1)|i > |^2 \tag{1.5}$$

On taking a summation over all the final states as calculated for first order correlation,

$$I(r_1,t_1,r_2,t_2) = \sum_f T_{fi} = Tr\{\rho E^{(-)}(r_1,t_1)E^{(-)}(r_2,t_2)E^{(+)}(r_2,t_2)E^{(+)}(r_1,t_1)\} \tag{1.6}$$

As can be observed from the above equation, the correlation function of the field operators are in normal order i.e. annihilation operators stay on the right. The quantum mechanical first and second degree of coherence thus come to be defined as,

$$g^{(1)}(r,\tau) = \frac{< E^{(-)}(r,t)E^{(+)}(r,t+\tau) >}{\sqrt{E^{(-)}(r,t)E^{(+)}(r,t)E^{(-)}(r,t+\tau)E^{(+)}(r,t+\tau)}} \tag{1.7}$$

$$g^{(2)}(r,\tau) = \frac{< E^{(-)}(r,t)E^{(-)}(r,t+\tau)E^{(+)}(r,t+\tau)E^{(+)}(r,t) >}{E^{(-)}(r,t)E^{(+)}(r,t)E^{(-)}(r,t+\tau)E^{(+)}(r,t+\tau)} \tag{1.8}$$

In the above expression, the quantized electric field is defined as,

$$E(r,t) = \int E_k(r,t)dk \tag{1.9}$$

$$E_k(r,t) = E_k^+(r,t) + E_k^-(r,t) = i\sqrt{\frac{\hbar\omega_k}{2\epsilon_0 V}}\varepsilon_k[a_k e^{-i\omega_k t + ik\cdot r} - a_k^\dagger e^{i\omega_k t - ik\cdot r}] \tag{1.10}$$

where ε_k denotes the field polarization vector. Assuming no dependence on position, the second order coherence function can be written as,

$$g^{(2)}(\tau) = \frac{< E^{-}(t)E^{-}(t+\tau)E^{+}(t+\tau)E^{+}(t) >}{< E^{-}(t)E^{+}(t) >^{2}} = \frac{<: I(t+\tau)I(t) :>}{< I(t) >^{2}} \tag{1.11}$$

:: denotes normal ordering of field amplitudes. For single mode field, Equation 1.11 can be simplified to,

$$g^{(2)}(\tau) = \frac{< a_k^{\dagger}(t)a_k^{\dagger}(t+\tau)a_k(t+\tau)a_k(t) >}{< a_k^{\dagger}(t)a_k(t) >^{2}} \tag{1.12}$$

For a classical light source, the second order coherence function at time t = 0 lies in the range $1 \leq g^{(2)}_{classical}(0) < \infty$. For a coherent-state i.e. laser, $g^{(2)}(0) = 1$. For an n-photon Fock state,

$$g^{(2)}(\tau) = \frac{< n_k \mid a_k^{\dagger}(t)a_k^{\dagger}(t+\tau)a_k(t+\tau)a_k(t) \mid n_k >}{< n_k \mid a_k^{\dagger}(t)a_k(t) \mid n_k >^{2}} = \frac{n-1}{n} \tag{1.13}$$

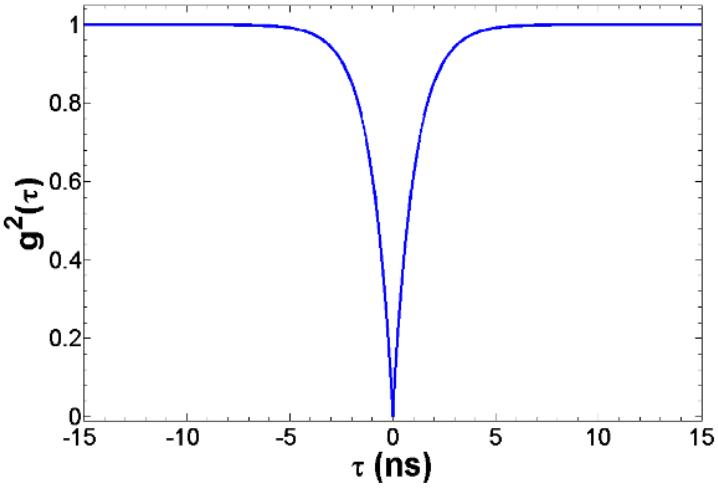

Figure 1.3: Single photon purity of a source shows a dip at zero time delay in second-order correlation measurement

As can be seen above, $g^{(2)}(0) < 1$ for all Fock states and is a signature of non-classical light emission. Thus, for emission from a single quantum emitter $g^{(2)}(0) \leq 0.5$ under experimental conditions. Under ideal conditions the dip at zero delay goes to zero as shown in Figure 1.3.

1.3 Emitter Systems

In the late 1970s, sodium atoms were excited by continuous wave lasers to generate single photons [32]. Solid state platforms started with the use of dye molecules by demonstration of antibunching [33]. Nitrogen vacancy centres in diamond [34] and CdSe quantum dots [35] have been investigated for single photon sources as well. Epitaxial self-assembled quantum dots [36] as single photon source were demonstrated the same year as CdSe quantum dots. These epitaxial self-assembled quantum dots have the advantage of ease of description of microcavities around them.

Atoms and ions present a clean two-level system for reproducible generation of single photons. However, they have long lifetimes ($\sim$ 30ns) which correspond to linewidths of few MHz, which puts a limit on the rate of generation of photons. Stringent requirement of trapping of atoms is another complexity for practical systems [37]. Molecules have also been traditionally researched for single photons. However, the photostability, blinking and environmental fluctuations limit the prospect of molecules to be used for quantum information processing. Colour centers or defects in crystals also generate fluorescence and of particular promise is a nitrogen vacancy (NV) center in diamond. The lifetime of NV center is 12 ns and the lifetime gets affected by proximity to etched surface, thus it can be a problem using microcavities together with NV centre based single photon source. Nanocrystals are limited by long lifetime of 20ns and spectral diffusion affecting the linewidth of the emission. Blinking is another concern with nanocrystals. Self-assembled semiconductor quantum dots are bright sources with lifetime-limited linewidths at cryogenic temperatures. Being on a semiconductor chip makes it easy to integrate structures around them. Electrical contacts and piezoelectric element can be integrated easier in these structures. They are particularly promising for quantum information processing at high data rates. A relatively new material platform for general of single photons is a monolayer of two-dimensional semiconductor such as MoS_2 and WSe_2. The ease of fabrication and positioning of quantum emitters in monolayer of WSe_2 makes this material platform particularly promising for quantum photonics.

1.3.1. Self-Assembled InAs Quantum Dots

Quantum dots are artificial solid structures which comprise 10^3 to 10^9 atoms, typically with a size ranging from a few nanometres to a few microns. The confinement of electrons in all three spatial dimensions causes discrete energy states in dots like in atoms, as shown in Figure 1.4. Of particular interest are self-assembled quantum dots in a solid state material as they allow realization of electrically injected devices which can be put to use in quantum

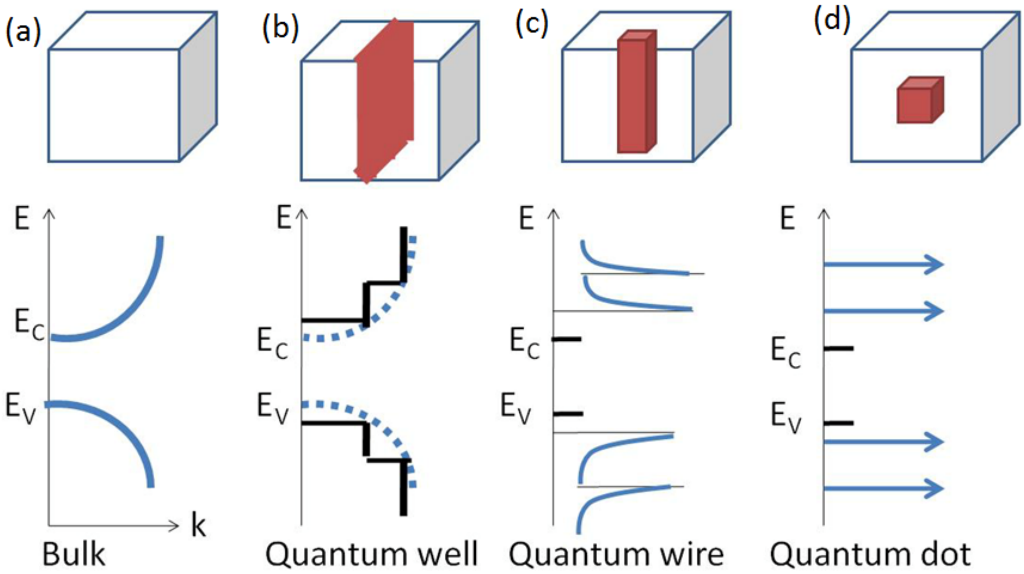

Figure 1.4: Density of states of (a) bulk semiconductor, (b) quantum well, (c) quantum wire and (d) quantum dot with three-dimensional confinement

technologies. The density of states for quantum dots is a δ-function. These artificial atoms exhibit a shell structure and they follow Pauli's exclusion principle for occupation of states.

Self-assembled InAs quantum dots are grown by molecular beam epitaxy (MBE) on a rotating wafer of GaAs. Due to lattice mismatch ($\sim 7\%$) between InAs and GaAs, after the deposition of a wetting layer, strain accumulates in the system and tiny islands are formed to minimise surface energy as can be seen in Figure 1.5. This is the Stranski-Krastanov mode of growth of quantum dots. The transition from two-dimensional wetting layer to three-dimensional islands occurs at a threshold of 1.5 monolayers of InAs as can be seen in Figure 1.6(c).

Typically, InAs quantum dots in GaAs emit at a wavelength > 1100 nm but the emission wavelength can be reduced to 900 nm - 980 nm by partial capping and annealing. Following an overgrowth of GaAs, the uncapped quantum dot tips are desorbed during a growth interruption using a background pressure of As [39]. This results in intermixing of quantum dot and GaAs as well which reduces the emission wavelength. In Figure 1.6, dome-like three-dimensional islands of InAs can be seen on GaAs wafer. The lateral dimension of these quantum dots are around 13 nm - 18nm and the height of the quantum dot is ~ 4 nm - 7 nm. The dot density is observed to be around 10^{10}cm^{-2} [40] [43].

Self-assembled quantum dots are dominated by quantum confinement due to their small size. Electrons and holes are confined in the InAs layer due to the energy band offsets of

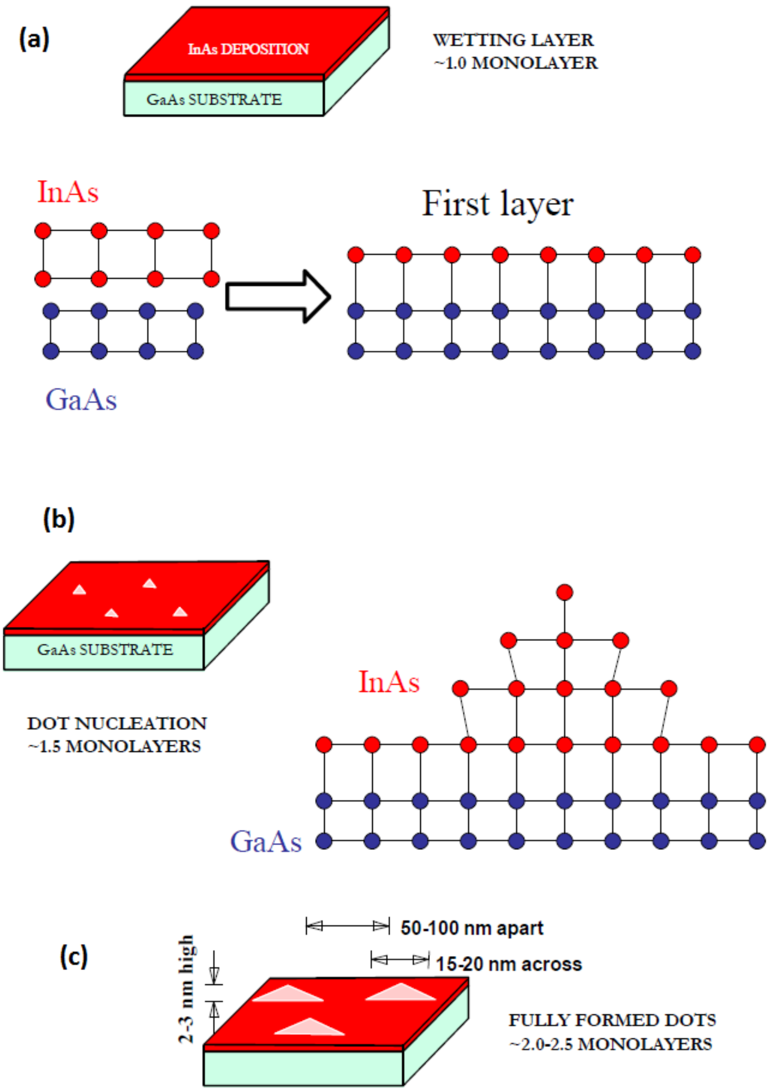

Figure 1.5: Self-assembled InAs quantum dots on GaAs in Stranski-Krastanov mode are grown by Molecular Beam Epitaxy as shown in the schematic diagram here: (a) In and As ions are deposited on GaAs wafer at a rate of 0.01 monolayer/sec at a temperature of 500^{o}C. A wetting layer/quantum well of InAs is formed for a thickness of one monolayer deposited on GaAs. (b) At a thickness of $\sim$1.6 monolayers of InAs, nucleation of quantum dots begin and (c) between 2-2.5 monolayers, self-assembled InAs quantum dot arrays are obtained [38].

the conduction band and the valence band of GaAs and InAs. Due to Coulomb force of attraction between electron and hole, excitons are observed in InAs/GaAs material system. The neutral exciton X^0 consists of one electron in conduction band and one heavy hole in valence band. Due to a higher effective mass of the heavy hole, the heavy hole forms the lowest energy state in the valence band and thus is involved in formation of excitons con-

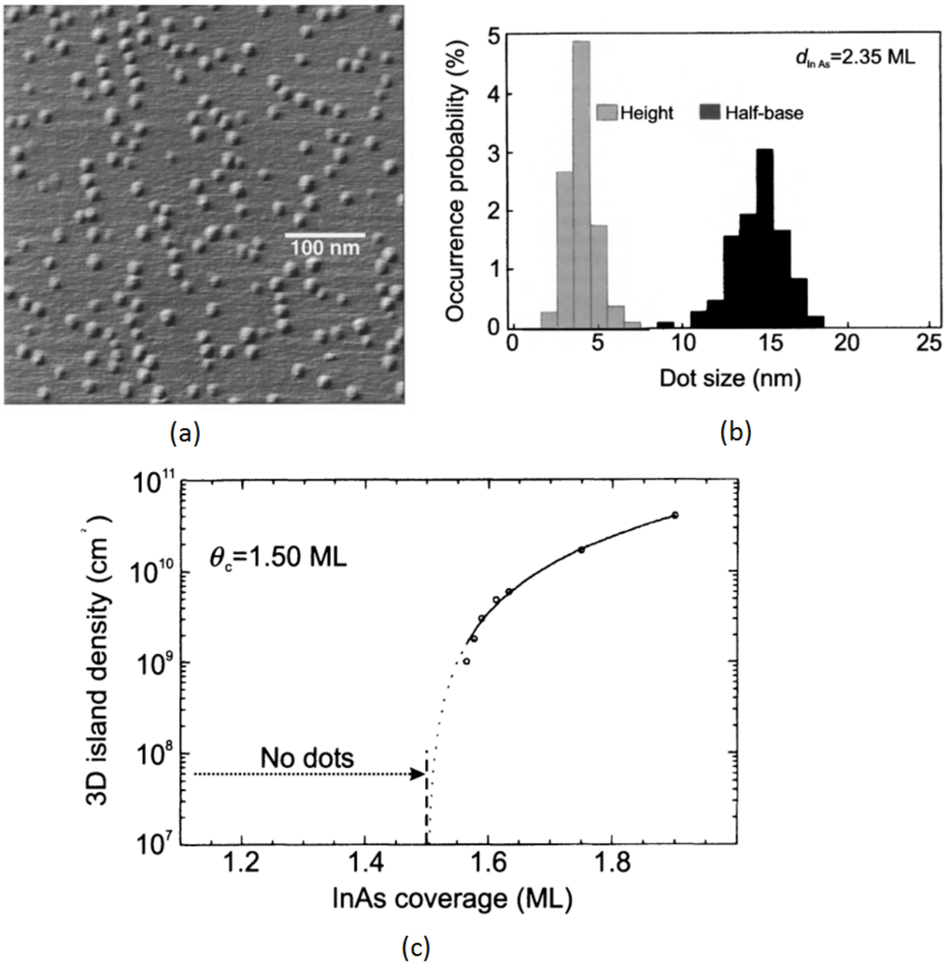

Figure 1.6: (a) AFM micrograph of uncapped InAs/GaAs dots when the deposited InAs corresponds to 1.46 monolayer. The image has been taken with a 20 nm radius tip ([40]), (b) size distribution of self-assembled InAs quantum dots in GaAs shows the height to be between 4nm-7nm and the lateral dimension is between 13nm-18nm [41], (c) clear threshold for two-dimensional to three-dimensional growth is observed for an InAs concentration of 1.5 monolayers [41].

fined in the heterostructure. Dark exciton is another feature of the neutral exciton when the spin of the electron and hole in the quantum dot are same. This leads to a non-radiative transition. Under non-resonant excitation i.e. optical excitation of the quantum dot at a lower wavelength than the emission wavelength, the spin of the generated electron is random and thus dark excitons and bright excitons are generated with equal probability. A secondary lifetime in the decay of a neutral exciton marks the signature of a dark exciton [49].

In a symmetric quantum dot, the two radiative X^0 states are degenerate and lead to left or right circularly polarized emission for the transitions (denoted by $\sigma_{+,-}$). When there is an asymmetry in the shape of the quantum dot, it causes an energy split between the

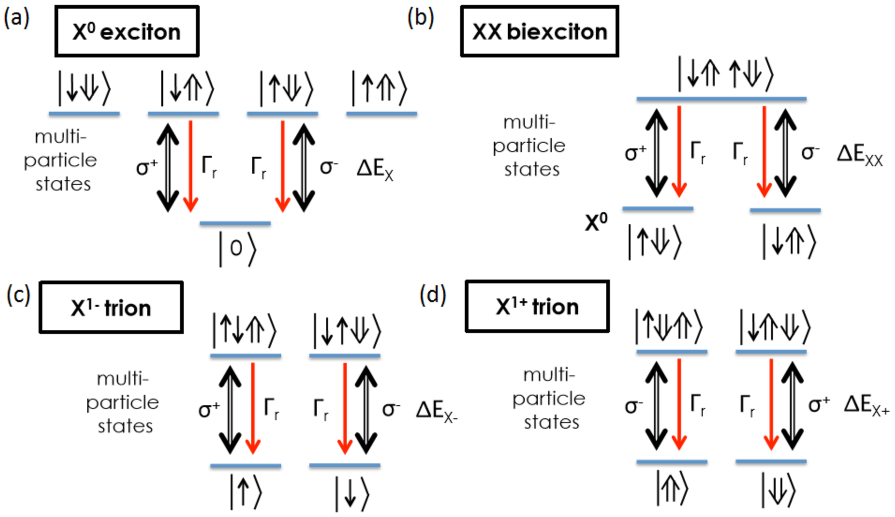

Figure 1.7: Schematic energy level structure of excitons confined in the quantum dot is shown: (a) neutral exciton, X^0, has two radiative transitions viz spin-up electron + spin-down hole and spin-down electron+spin-up hole. The other two configurations where the spins of the electron and the hole are the same, do not radiate. (b) Biexciton has two electron-hole pairs bound together. After emission of a photon, the quantum dot is in one of the radiative neutral exciton configurations. In (c) a single negatively charged exciton also known as trion is shown. After radiative transition, trions are left with single electron state. (d) A single positively charged exciton has a surplus hole left behind after a radiative transition [42].

two configurations for the X^0 state, and lifts the degeneracy. This causes linearly polarized photons as shown in Figure 1.8 [46] [47]. The lens-shaped self-assembled InAs quantum dots exhibit this asymmetry.

Amid the other exciton states observed in quantum dots, negatively-charged exciton or trion X^{1-} are quite prominent. This consists of two electrons and one hole as can be seen in Figure 1.7(c). Recombination of this exciton results in a single electron ground state which can be potentially useful for applications in LOQC.

Due to spatially separated electron and hole wavefunctions in a quantum dot, there is a permanent dipole moment in the dots. In presence of an external electric field F, the exciton emission energy can be tuned due to quantum confined Stark effect. By putting the quantum dot layer between a heavily-doped Ohmic Contact and a Schottky contact, vertical electric field can be applied to the dot [48]. The layer structure of such a sample is shown in figure 1.9. A change in applied gate voltage shifts the energy band diagram such that at high positive voltage V_g^a, the quantum dot energy level lies above the Fermi energy and the

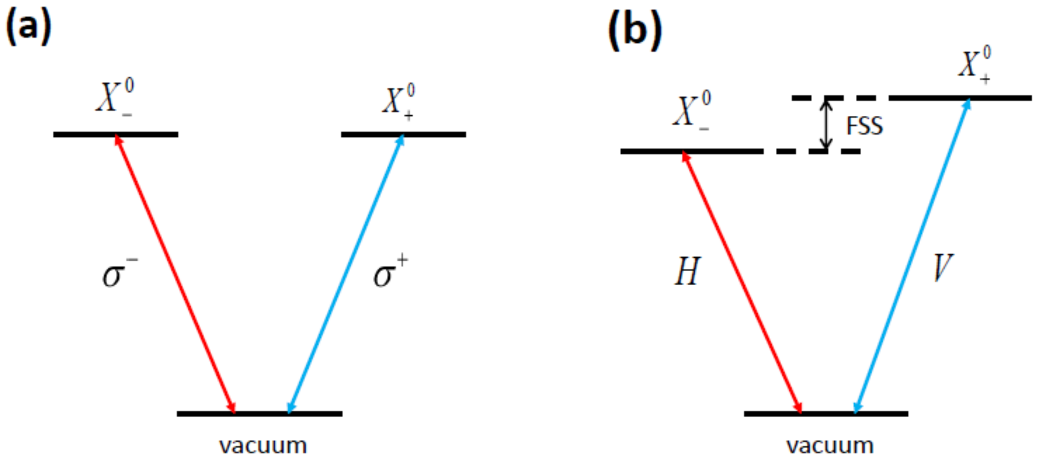

Figure 1.8: (a) In case of a symmetric dot, the energy levels are degenerate for the two X^0 transitions and left or right circularly polarized emission (σ^- or σ^+) is observed, (b) in absence of symmetry, fine structure splitting arises between the two X^0 configurations and linearly polarized photons (horizontal, H or vertical, V) are obtained in emission [47].

quantum dot stays unoccupied. At V$_g^b$, the Fermi level becomes resonant with the energy level in the dot and an electron can tunnel into the quantum dot.

$$\Delta E = -pF + \beta F^2 \tag{1.14}$$

The application of gate voltage tunes the emission energy/wavelength of the emission to the quantum confined Stark effect. As shown in the above equation, ΔE refers to the tuning of the emission energy, p is the permanent dipole moment, β is the polarizability of the exciton in quantum dot and F is the applied electric field.

1.3.2. Two-Dimensional Semiconductors

The discovery of Graphene has spurred interest in two-dimensional materials with remarkable physical properties [50]. The ease of fabrication, i.e. mechanical exfoliation using a scotch tape, has allowed groups all over the world to delve into research on graphene. Graphene has a hexagonal lattice of carbon atoms and an absence of energy bandgap. While several groups tried to create a bandgap in graphene by doping it with other materials, however, the dopant takes away the most important feature of using graphene i.e. the high electron mobility [51]. In contrast, Transition Metal Dichalcogenides (TMD) form a layered

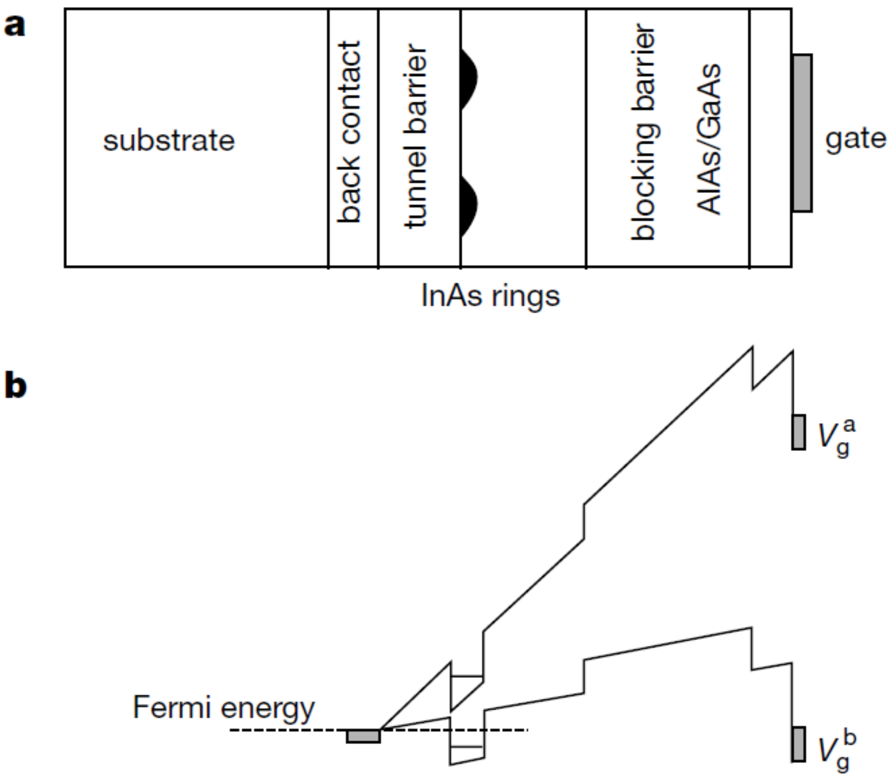

Figure 1.9: A GaAs/InAs semiconductor heterostructure device for charging InAs quantum dots with electrons. (a) The layer structure of such a sample is shown where there is a tunnel barrier 25 nm thick and an electron blocking layer of AlAs/GaAs superlattice. (b) A change in applied gate voltage shifts the energy band diagram [48].

structure with a plane of hexagonal metal atoms (Molybdenum or Tungsten) surrounded by two planes of chalcogen atoms (Sulphur, Selenium etc.) in a trigonal prismatic coordination as shown in Figure 1.10. So unlike single atomic layer in Graphene, a monolayer of TMD has three atomic layers in it.

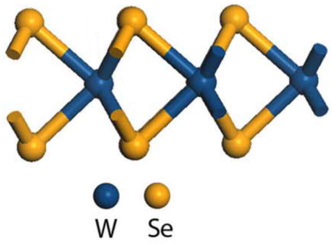

Figure 1.10: A monolayer of Transition Metal Dichalcogenide (TMD) has a layer of transition metal (Molybdenum or tungsten) surrounded by two layers of chalcogens (sulphur or selenium). The height of the monolayer is 0.7 nm.

In TMDs, the direct and indirect bandgaps co-exist at all layer thicknesses. While the direct gap exists between spin-orbit split valence band and the doubly degenerate conduction band at K-point [100] in reciprocal space, an indirect gap forms between a local conduction band minimum which is located at the midpoint between Γ and K-point and the valence band maximum at the Γ point in reciprocal space as shown in Figure 1.11 [52] [53] [56].

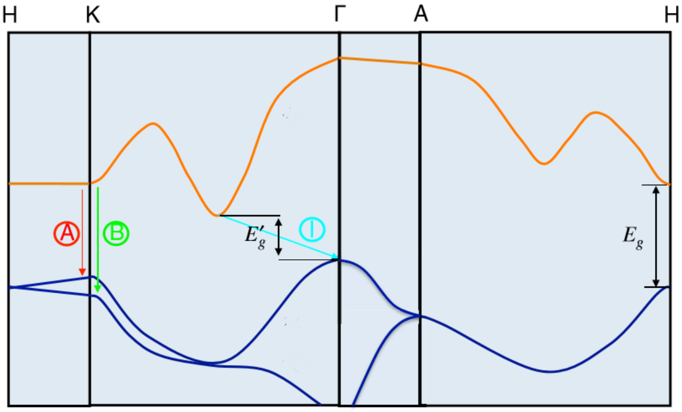

Figure 1.11: The band structure of bulk MoS_2, shows the lowest conduction band and the highest split valence bands at Γ point in reciprocal space. A and B correspond to the direct-gap transitions at K-point, and I is the indirect-gap transition. The indirect energy bandgap for the bulk is denoted by E'$_g$, and E$_g$ is the direct gap for the monolayer [56].

TMD crystal are non-centrosymmetric i.e. the inversion symmetry is broken since the two sublattices are occupied, respectively, by one transition metal and two chalcogen atoms. The breaking of inversion symmetry creates two non-equivalent valleys at the boundary of the brillouin zone, K and K- [54]. The K or K- valley can be selectively accessed by use of left- or right-circularly polarized light as shown in Figure 1.12. This is particularly useful for realization of valleytronic devices.

Following the footsteps of research on graphene, TMD monolayers are mechanically exfoliated using a scotch tape. Mechanical exfoliation, however, produces inhomogeneous flakes i.e. of different sizes and thicknesses at random positions on the substrate. When the mechanically exfoliated TMD flakes are looked at under an optical microscope under white light illumination, they appear to have different colours. The variation in colour among different flakes corresponds to varying number of layers in the flakes as shown in Figure 1.13.

A key feature of the exfoliated layers of TMDs is the increase in photoluminescence when the layers are thinned down to a single monolayer. The monolayer in the flake is identified via optical contrast [58] in reflection or transmission mode. Optical contrast from

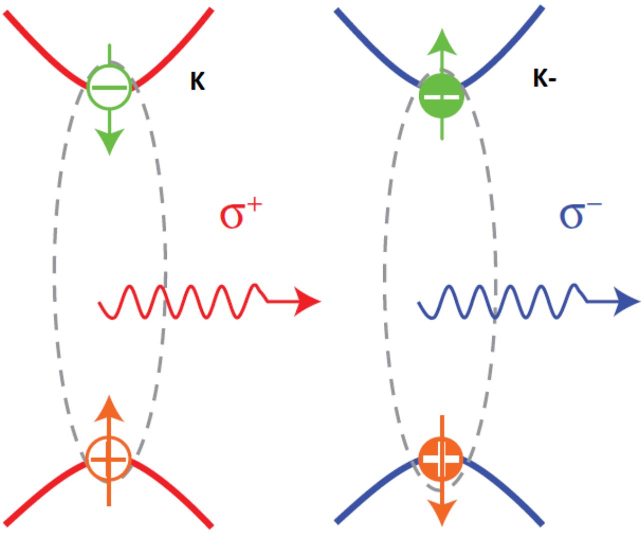

Figure 1.12: K and K- valleys of WSe_2 can be addressed by right and left-circularly polarized light respectively [55]

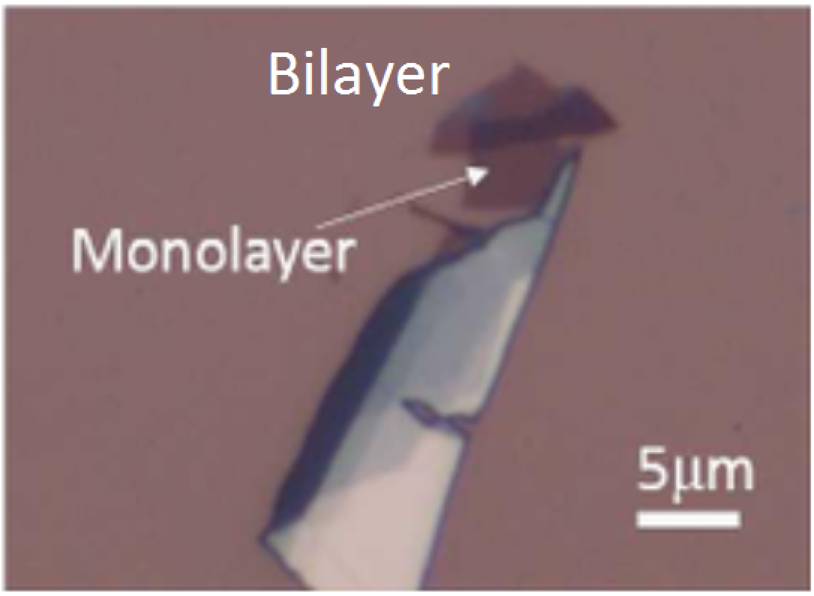

Figure 1.13: Mechanically exfoliated TMD flakes when looked at under an optical microscope under white light illumination appear to have different optical contrasts depending upon the thickness [57].

a monolayer is much lower than that from bilayer as can be seen in the Figure 1.13, where the flake is put on 285 nm of SiO_2/Si. Silica/silicon substrate offers the highest optical contrast between monolayer and bilayer while trying to identify the monolayer.

Due to the monolayer nature of the material, dielectric screening in TMDs like WSe_2 is much lower than semiconductor materials like GaAs. This gives rise to strong Coulombic interaction in these materials. Generation of excitons and high exciton binding energy have been observed in 2D-TMDs. When a typical monolayer of WSe_2 is cooled down to liquid helium temperatures ($\sim$4K), three pronounced photoluminescence peaks are observed under non-resonant excitation. The peaks are assigned to exciton, trion and localized states from excitation power dependence measurements. Neutral exciton emission at 1.75eV and trion emission at 1.72eV have been observed as can be seen in Figure 1.14 [62]. At further lower energy, a defect band continuum is observed. The red curve is for photoluminescence from bi-layer. As expected, the quantum well 2D-exciton emission is absent in photoluminescence from the bilayer. The indirect bandgap which is between the conduction band minimum at the midpoint of Γ and K-point, and valence band maximum at Γ point shows up as a weak photoluminescence peak. The defect band ensemble emission is also present although less pronounced than that in the monolayer of WSe_2.

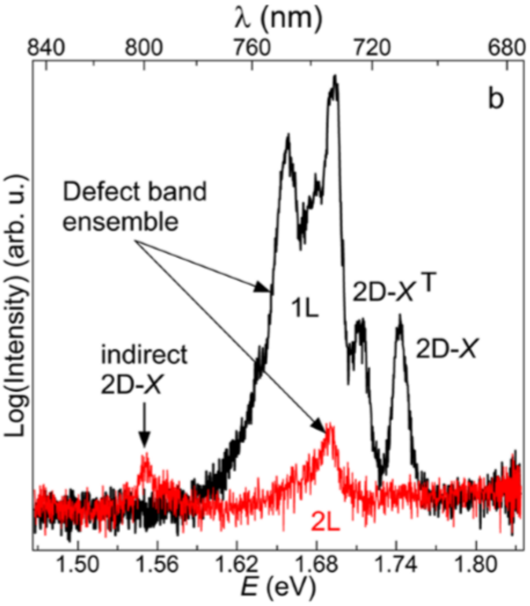

Figure 1.14: Emission spectrum at 4K from WSe_2 monolayer when excited by a non-resonant laser at 532nm: the black curve is for photoluminescence obtained from the monolayer where the neutral exciton and trion are present at 1.74eV and 1.72eV with linewidths of $\sim$10meV. The red curve denotes the photoluminescence obtained from a bilayer sample where the exciton and trion emission are absent [62].

Excitons in WSe_2 have different saturation powers. At low excitation power, the emission intensities from monolayer exciton and monolayer trion are low as can be seen in Figure 1.15. Defect band, however, can be observed at low excitation powers. This suggests a saturation behaviour at very low powers which is analogous to defects and impurities in III-V semiconductor quantum wells. Optically generated excitons relax by phonon emission

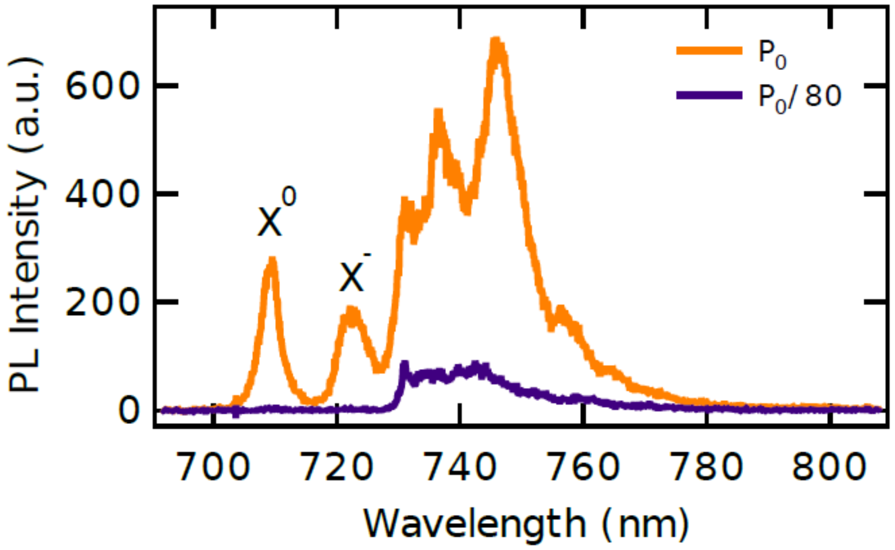

Figure 1.15: Excitation power dependence of photoluminescence spectrum from monolayer WSe_2 at 4K. A 633 nm He-Ne laser was used for excitation [63].

into the localized states, quenching the delocalized exciton emission [63].

Of particular interest are quantum dot-like emission from the monolayers. The origin of these quantum emitters is attributed to a local strain gradient in the monolayer sample [62]. They can be observed at the edges of the monolayer [64], can also arise due to defects in the fabric of monolayer WSe_2 [65], and can be deterministically generated in periodic 2D-arrays by local strain engineering [66]. The linewidth of emission from localized excitons is $\sim 100\mu$eV at a temperature of 4K. Antibunching data yields a lifetime of the order of few nanoseconds. Having a single photon source in a monolayer of a 2D-semiconductor with easy fabrication and site-controlled single photon source engineering by creating strain-pockets has great prospects for applications in solid-state quantum photonics.

1.4 Theory of Electric Dipole Radiation

The emission from quantum dot excitons and excitons in 2D-semiconductors arise due to dipole transitions. A semi-classical treatment is suited to study how the radiation pattern from a dipole emitter gets altered when it is placed in a homogeneous medium or adjacent to a planar interface. While the situation can be mathematically explained using the Green's function approach as in reference [67], reference [68] takes a Maxwell's equations approach and is shown here.

$$\nabla \cdot (\epsilon \mathbf{E}) = 4\pi\rho \tag{1.15}$$

$$\nabla \cdot \mathbf{B} = 0 \tag{1.16}$$

$$\nabla \times \mathbf{E} = -\frac{1}{c}\frac{\partial B}{\partial t} = \frac{i\omega}{c}B \tag{1.17}$$

$$\frac{\nabla \times \mathbf{B}}{\mu} = \frac{1}{c}\frac{\partial(\epsilon E)}{\partial t} + \frac{4\pi}{c}J \tag{1.18}$$

where E and B are the magnetic fields, ρ and J are the electric charge density and current density. Further, for a single dipole located at the origin of the coordinate system and oscillating with frequency ω, $\rho = 0$ and $J = -i\omega$ p $\delta(r)e^{-i\omega t}$. Thus the curl of magnetic field can be expressed by Equation 1.19.

$$\nabla \times \mathbf{B} = \frac{-i\omega\epsilon}{c}E + \frac{4\pi}{c}J = \frac{-i\omega\epsilon}{c}E - \frac{4\pi i\omega}{c}p\delta(r) \tag{1.19}$$

If the curl of the Maxwell's 3^{rd} equation is performed again and result from Equation 1.19 is used,

$$\begin{aligned} \nabla \times (\nabla \times \mathbf{E}) &= \frac{i\omega}{c}(\nabla \times \mathbf{B}) \\ \nabla \times (\nabla \times \mathbf{E}) - \frac{\epsilon\omega^2}{c^2}E &= \frac{4\pi\omega^2}{c^2}p\delta(r) \end{aligned} \tag{1.20}$$

In Fourier space, ∇ is replaced by ik and using $k_0 = \omega/c$,

$$\begin{aligned} -k \times (k \times E) - \epsilon k_0^2 E &= 4\pi k_0^2 p \\ (k^2 - \epsilon k_0^2)E - k(k \cdot E) &= 4\pi k_0^2 p \end{aligned} \tag{1.21}$$

If the dot product of the wave-vector k is taken on both sides of the above equation, the equation for (k.E) is obtained as shown below,

$$(k^2 - \epsilon k_0^2)(k \cdot E) - (k \cdot k)(k \cdot E) = 4\pi k_0^2 (k \cdot p) \tag{1.22}$$

$$(k \cdot E) = -\frac{4\pi}{\epsilon}(k \cdot p) \tag{1.23}$$

When the expression for (k.E) is put back in Equation 1.21, the expression for electric field in the Fourier space can be obtained,

$$E = \frac{4\pi}{\epsilon(k^2 - \epsilon k_0^2)} \left[\epsilon k_0^2 p - k(k \cdot p) \right] \tag{1.24}$$

At this moment, a switch from Fourier space to real space is made. The electric field in the real space can be expressed as,

$$E = \frac{4\pi}{\epsilon} \int_k \frac{d^3k}{(2\pi)^3} \frac{e^{ik \cdot r}}{(k^2 - \epsilon k_0^2)} \left[\epsilon k_0^2 p - k(k \cdot p) \right] \tag{1.25}$$

The above expression can be used as the starting point for prediction of radiation pattern from dipoles in arbitrary structures. In this study, the emphasis is on behaviour of dipoles embedded in planar structures. In order to build up to emission pattern of dipoles in planar structures, an understanding of emission pattern in homogeneous medium is a logical stepping stone.

1.4.1. Dipole in a Homogeneous Medium

In order to understand the radiation pattern of a dipole emitter embedded in a homogeneous medium, a coordinate transformation is made from cartesian system to spherical coordinate system. The x, y and z-components of wavevector $'k'$ can be used to compute the coordinates in the spherical coordinate system as shown below.

$$\begin{aligned} k = \sqrt{k_x^2 + k_y^2 + k_z^2} = k \\ \phi = tan^{-1}\left(\frac{k_y}{k_x}\right) \\ \theta = tan^{-1}\left(\frac{\sqrt{k_x^2 + k_y^2}}{k_z}\right) \end{aligned} \tag{1.26}$$

$$\begin{aligned} dkd\theta d\phi &= \frac{1}{\sqrt{k_x^2 + k_y^2}\sqrt{k_x^2 + k_y^2 + k_z^2}} dk_x dk_y dk_z \\ dkd\theta d\phi &= \frac{1}{k^2 sin\theta} dk_x dk_y dk_z \end{aligned} \tag{1.27}$$

$$E = \frac{4\pi}{\epsilon(2\pi)^3} \int_0^{2\pi} d\phi \int_0^{\infty} dk k^2 \int_0^{\pi} d\theta sin\theta \frac{e^{ikrcos\theta}}{(k^2 - \epsilon k_0^2)} \left[\epsilon k_0^2 p - k(k.p) \right] \tag{1.28}$$

$$E = \frac{1}{\epsilon\pi}\left(\epsilon k_0^2 p + \nabla(\nabla\cdot\mathbf{p})\right)\int_0^\infty dk k^2 \int_0^\pi \frac{d\theta sin\theta e^{ikrcos\theta}}{(k^2-\epsilon k_0^2)} \tag{1.29}$$

Cauchy's reduced theorem is applied to solve the above integral and the expression for electric field is reduced to,

$$E = \frac{1}{\epsilon}\left[\epsilon k_0^2 + \nabla(\nabla\cdot)\right]\left[p\frac{e^{ink_0r}}{r}\right] \tag{1.30}$$

In spherical coordinate system, when $\theta = 0$ is along p,

$$\begin{aligned}\nabla(\nabla\cdot)\left[p\frac{e^{ink_0r}}{r}\right] &= \nabla\left[\left(\frac{ik}{r}-\frac{1}{r^2}\right)(p\cdot\hat{r})e^{ikr}\right]\\ &= \left[\left(-\frac{k^2}{r}-\frac{2ik}{r^2}+\frac{2}{r^3}\right)(p\cdot\hat{r})\hat{r}-\right.\\ &\left.\frac{1}{r}\hat{r}\times(\hat{r}\times p)\left(\frac{ik}{r}-\frac{1}{r^2}\right)\right]e^{ikr}\end{aligned} \tag{1.31}$$

$$\begin{aligned}E(r) = k_0^2 k&\left[\left(-1-\frac{3i}{kr}+\frac{3}{(kr)^2}\right)\hat{r}(\hat{r}\cdot p)+\right.\\ &\left.\left(1+\frac{i}{kr}-\frac{1}{(kr)^2}\right)p\right]\frac{e^{ikr}}{kr}\end{aligned} \tag{1.32}$$

For farfield, terms which fall faster than r^{-1} do not contribute, so the effective expression for E-field is then,

$$E(r) =\sim k_0^2 k\left[-\hat{r}(\hat{r}\cdot p)+p\right]\frac{e^{ikr}}{kr} \tag{1.33}$$

In order to calculate the Poynting vector, the magnetic field also needs to be calculated which can be obtained by performing the curl on Equation 1.30,

$$\begin{aligned}B(r) &= \frac{1}{ik_0}\nabla\times\mathbf{E}(\mathbf{r}) = \frac{1}{ik_0}\nabla\times\frac{1}{\epsilon}\left[\epsilon k^2+\nabla(\nabla\cdot)\right]\left[p\frac{e^{ikr}}{r}\right]\\ &= -ik_0\nabla\times\left[p\frac{e^{ikr}}{r}\right]\sim\frac{k_0k}{r}(\hat{r}\times p)e^{ikr}\end{aligned} \tag{1.34}$$

Thus the energy density or Poynting vector is expressed by the following equation.

$$S \sim \frac{cnk_0^4}{8\pi r^2}\left[p-\hat{r}(\hat{r}\cdot p)\right]\times(\hat{r}\times p) = \frac{cnk_0^4}{8\pi r^2}\hat{r}\left[p^2-(\hat{r}\cdot p)^2\right] \tag{1.35}$$

$$\frac{d^2S}{sin\theta d\theta d\phi} = \frac{cnk_0^4}{8\pi}sin^2\theta \tag{1.36}$$

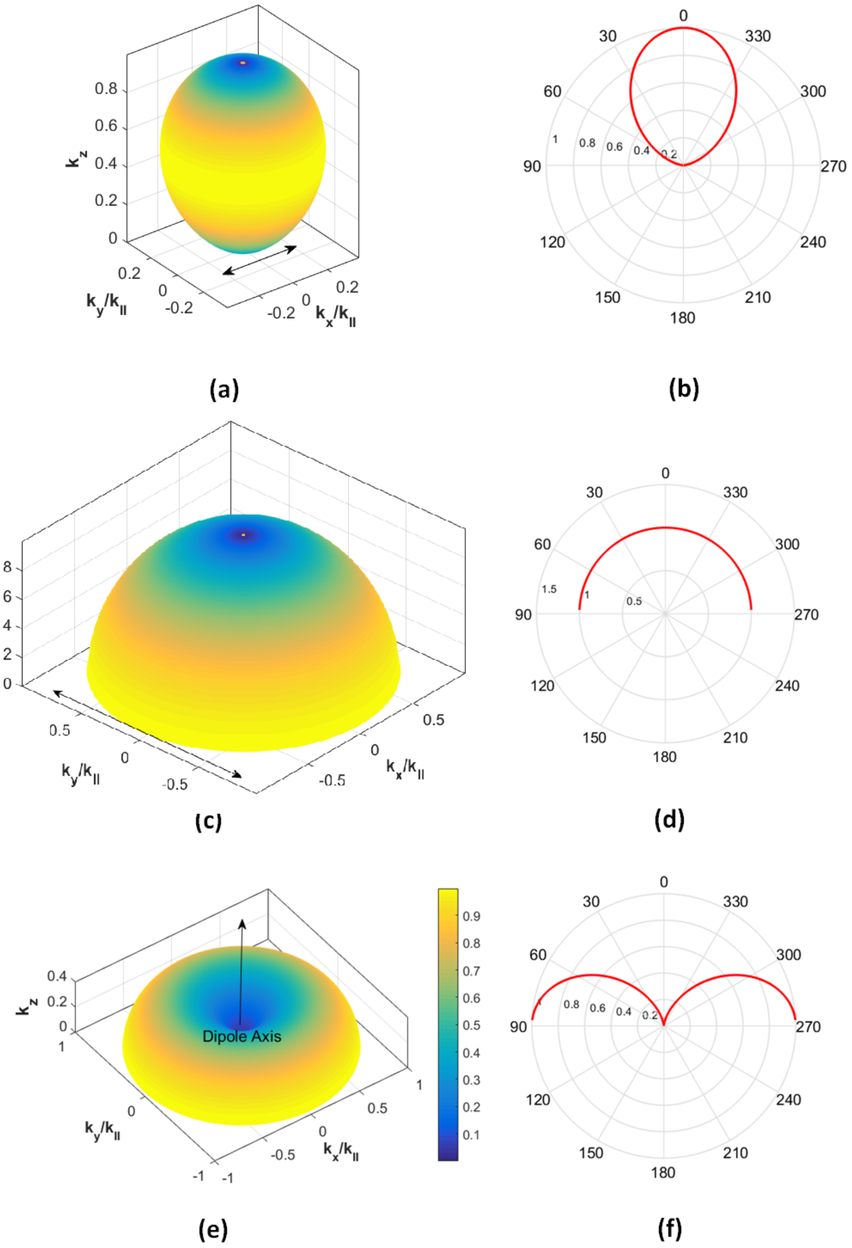

Figure 1.16: The 3D Radiation pattern that arises from an oscillating electric dipole; the emission profile has a $\sin^2\theta$ dependence where θ is the angle between the dipole axis and the point of observation: (a) directivity of the radiation and (b) polar emission density towards the collection side due to an in-plane dipole with s-polarized photon, (c) directivity of dipole radiation and (d) polar radiation density due to an in-plane dipole with p-polarized photon, (e) and (f) show the radiation directivity and angular emission density for a vertical dipole, respectively

As can be seen from the above equation, the radiation points away from the dipole and has a $sin^2\theta$ distribution. This is a classic result for a dipole where the optic axis of the measurement system is aligned parallel to the axis of the dipole. The radiation is distributed in the plane perpendicular to the optic axis for dipoles oriented along the optic axis in this scenario as can be seen in Figure 1.16(f). Since the dipole is in a homogeneous medium here, the radiation travelling towards the collection side and away from it have identical angular emission profiles.

1.4.2. Dipole Emission near Planar Interface

When the dipole is placed close to an interface, due to interference between the directly radiated and the reflected radiation from the interface, the radiation pattern gets altered. This is particularly interesting for increasing the collection efficiency of photons from quantum emitters [69].

In this formulation, the radiation from a dipole is expanded into plane waves and the Fresnel reflection coefficients are applied and refraction is taken into account via Snell's law at a dielectric interface. The planar interface divides two media with index of refraction n$_j$ and n_{j+1} . There can be up to four interconnected plane waves as shown in Figure 1.17 denoted by E$_j^{\pm}$ and E$_{j+1}^{\pm}$, where the subscript refers to the medium, and the $\pm$-sign to whether the wave travels into a positive direction (from medium j towards medium j+1) or into a negative direction (from j+1 towards j). Electric field vectors within the plane of the directions of wave propagation are called transverse electric (TE) or p-wave; if the electric field vectors are parallel to the boundary, the wave is called transverse magnetic (TM) or s-wave. The reflection coefficients at interfaces are polarization-dependent as shown in the fresnel coefficients for interfaces.

The periodicity condition of the plane waves at the interface between media j and j+1 dictates the relationship between the wavevectors. Along the boundary, the periodicity of the electric field on both sides of the boundary has to be the same. The periodicity is given by the projections of the wave vectors onto the boundary. The in-plane components of k-vector can be denoted as q, and is conserved across different media. When the k-vector in vacuum is assumed to be unity, the relationship between angle of incidence and q are related by the following equation.

$$sin\theta_{j,j+1} = \frac{q}{n_{j,j+1}} \tag{1.37}$$

The perpendicular to the interface component is referred to as $w_{j,j+1}$. Thus, n$_{j,j+1}$ $=\sqrt{w^2 + q^2}$.

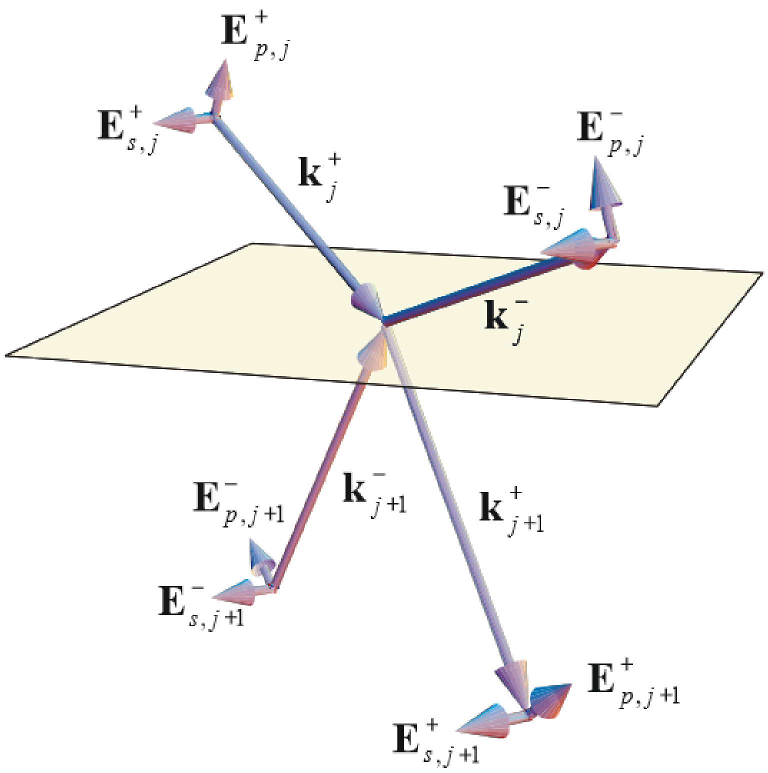

Figure 1.17: The planar interface divides two media with index of refraction n$_j$ and n_{j+1} . The connected plane waves are denoted by E$_j^{\pm}$ and E$_{j+1}^{\pm}$, where the subscript refers to the medium, and the ±-sign to whether the wave travels into a positive direction (from medium j towards medium j+1) or into a negative direction (from j+1 towards j) ([68]).

In addition to the periodicity of the plane wave, the continuity condition at the interface requires the tangential component of the electric field to be the same in both media, and the normal component of the electric displacement vector $\vec{D}$ or the product of the dielectric permittivity and electric field (given that it is an isotropic medium) perpendicular to the interface to be the same across the interface as well. All these conditions when put in place leads to the following relationship between the electric fields.

$$\begin{pmatrix} E^{+}_{p,j} \\ E^{-}_{p,j} \end{pmatrix} = \frac{1}{2} \begin{pmatrix} n_j/w_j & 1/n_j \\ -n_j/w_j & 1/n_j \end{pmatrix} \begin{pmatrix} w_{j+1}/n_{j+1} & -w_{j+1}/n_{j+1} \\ n_{j+1} & n_{j+1} \end{pmatrix} \begin{pmatrix} E^{+}_{p,j+1} \\ E^{-}_{p,j+1} \end{pmatrix}$$

When light is incident from the medium j such that $n_j > n_{j+1}$, then the critical angle for the interface is defined as,

$$\theta_{critical} = sin^{-1}(\frac{n_{j+1}}{n_j}) \tag{1.38}$$

Beyond the critical angle of incidence while incident from medium j, the light undergoes total internal reflection into medium j and an evanescent wave travels into medium j+1. Similar to the matrix relationship that has been represented above for p-polarization, the relationship between electric field components can be obtained for s-polarized light as shown below.

$$\begin{pmatrix} E^{+}_{s,j} \\ E^{-}_{s,j} \end{pmatrix} = \frac{1}{2}\begin{pmatrix} 1 & 1/w_j \\ 1 & -1/w_j \end{pmatrix}\begin{pmatrix} 1 & 1 \\ w_{j+1} & -w_{j+1} \end{pmatrix}\begin{pmatrix} E^{+}_{s,j+1} \\ E^{-}_{s,j+1} \end{pmatrix}$$

The reflection and transmission coefficients for p-polarization are described as $r_p = E^{-}_{p,j}/E^{+}_{p,j}$ and $t_p = E^{+}_{p,j+1}/E^{+}_{p,j}$, and similarly for r_s and t_s. When the media are represented as 1 and 2, instead of j and j+1, the coefficients for reflection and transmission are defined as shown below.

$$r_s = \frac{n_1 cos\theta_i - n_2 cos\theta_t}{n_1 cos\theta_i + n_2 cos\theta_t} \tag{1.39}$$

$$t_s = \frac{2 n_1 cos\theta_i}{n_1 cos\theta_i + n_2 cos\theta_t} \tag{1.40}$$

$$r_p = \frac{n_2 cos\theta_i - n_1 cos\theta_t}{n_1 cos\theta_t + n_2 cos\theta_i} \tag{1.41}$$

$$t_p = \frac{2 n_1 cos\theta_t}{n_1 cos\theta_t + n_2 cos\theta_i} \tag{1.42}$$

When the index of the medium 1 is smaller than refractive index of medium 2 i.e $n_2 > n_1$, as can be seen in Figure 1.18, and the separation between the dipole and the substrate is less than a wavelength in the medium, evanescent field components of the dipole radiation interacts with the layer, and thus propagate in the lower half-space as it is optically denser [67]. While for a vertical dipole (dipole axis same as optic axis) in free space, the radiation was in plane, the addition of a second medium reduced the intensity in the first medium and the narrows the cone of angles into which emission was emanated into (black curves in Figure 1.18(a)(b)(c)). For the in-plane dipole (dipole axis perpendicular to optic axis), the two orthogonal orientations register different responses to addition of another layer. While both lose a certain amount of light in the lower half space, the angular response of p-polarized light gets narrower which is useful for coupling light into a microscope objective with modest numerical aperture.

While the radiation into the lower half space is difficult to study in experiment due to reflection-mode microscope setups used for this research (described in Chapter 2), in theory the angular distribution of light in the lower half space can also be calculated. This is important for choice of optimum distances and material refractive index to enhance light

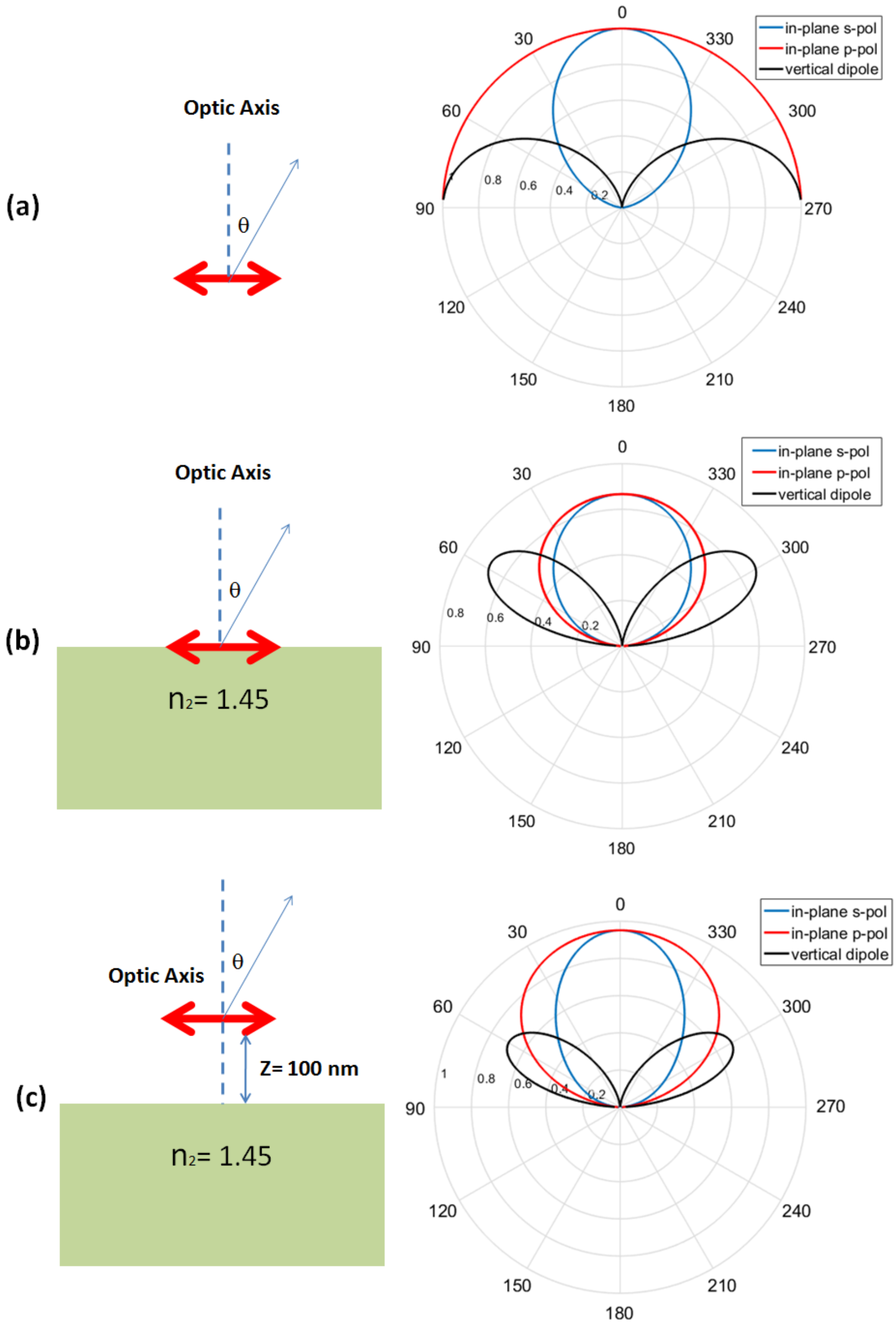

Figure 1.18: Simulated angular radiation profile for dipole with arbitrary orientation (a) in vacuum, (b) when placed at the interface between air and a polymer with refractive index of 1.45 and (c) at a distance of 100 nm from air-polymer interface

emission into one or the other media. This criteria forms one of the design constraints for high photon extraction efficiency samples based on planar dielectric materials.

1.5 Transfer-Matrix Model

When a uniform plane wave is incident at the interface of two media with different refractive indices, a fraction of the incident electric field is reflected towards the medium where the field is incident from and a complementary fraction gets transmitted such that $E_{incident} = E_{transmitted} + E_{reflected}$. The electric fields in the two media are calculated by a transfer-matrix approach. The transfer-matrix for any interface involves a propagation matrix and a matching matrix. An electric field, linearly polarized in the x-direction and propagating along the z-direction is assumed in a lossless (homogeneous and isotropic) dielectric medium i.e. E(z) $= E_{0+}e^{-ikz} + E_{0-}e^{ikz} = [E_+(z) + E_-(z)]$, where $E_+(z)$ and $E_-(z)$ represent the forward and backward scattered electric fields.

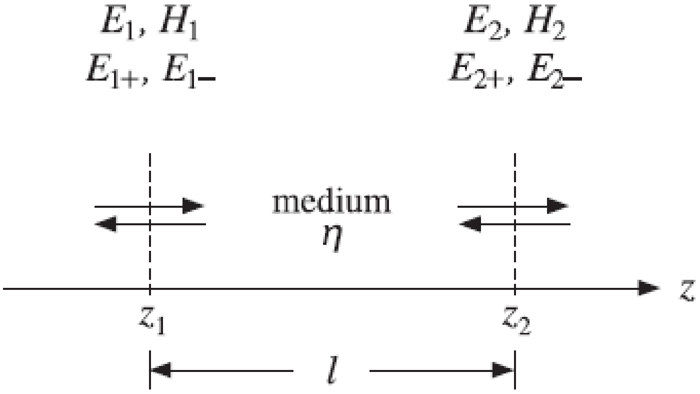

Figure 1.19: Field propagated between two positions in space [71]

In Figure 1.19, the propagation of electric field between two points z_1 and z_2 separated by a distance 'l' in space in a uniform medium is shown. The forward and backward fields at these points can be written as,

$$E_{2+} = E_{0+}e^{-ikz_2}, E_{1+} = E_{0+}e^{-ikz_1} = E_{0+}e^{-ik(z_2-l)} = E_{2+}e^{ikl} \tag{1.43}$$

$$E_{1-} = E_{2-}e^{-ikl} \tag{1.44}$$

and in matrix form as shown below.

$$\begin{bmatrix} E_{1+} \\ E_{1-} \end{bmatrix} = \begin{bmatrix} e^{ikl} & 0 \\ 0 & e^{-ikl} \end{bmatrix} \begin{bmatrix} E_{2+} \\ E_{2-} \end{bmatrix} \tag{1.45}$$

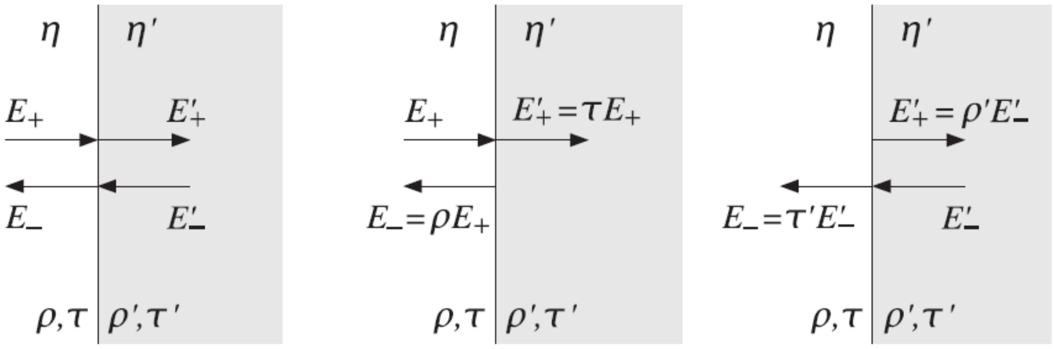

Figure 1.20: Fields at the interface of two media [71]

In addition to the propagation matrix, boundary conditions for the tangential component of electric fields give the matching matrix. The situation is shown in Figure 1.20 where ρ and τ are reflection and transmission coefficients. The continuity condition dictates the following relationships between the electric fields in the two media,

$$\begin{bmatrix} E_+ \\ E_- \end{bmatrix} = \frac{1}{\tau} \begin{bmatrix} 1 & \rho \\ \rho & 1 \end{bmatrix} \begin{bmatrix} E'_+ \\ E'_- \end{bmatrix} \tag{1.46}$$

$$\begin{bmatrix} E'_+ \\ E'_- \end{bmatrix} = \frac{1}{\tau'} \begin{bmatrix} 1 & \rho' \\ \rho' & 1 \end{bmatrix} \begin{bmatrix} E_+ \\ E_- \end{bmatrix} \tag{1.47}$$

The reflection and transmission coefficients in the above shown matching matrix can be expressed by the following equations when their angle of incidence θ_i and angle of refraction into the second medium θ_t are known.

$$\rho_s = \frac{n_1 cos\theta_i - n_2 cos\theta_t}{n_1 cos\theta_i + n_2 cos\theta_t} \tag{1.48}$$

$$\tau_s = \frac{2n_1 cos\theta_i}{n_1 cos\theta_i + n_2 cos\theta_t} \tag{1.49}$$

$$\rho_p = \frac{n_2 cos\theta_i - n_1 cos\theta_t}{n_1 cos\theta_t + n_2 cos\theta_i} \tag{1.50}$$

$$\tau_p = \frac{2n_1 cos\theta_t}{n_1 cos\theta_t + n_2 cos\theta_i} \tag{1.51}$$

The representation of electric fields in different media by using propagation and matching matrices allows the handling of multiple interface problems in a straight-forward way. For the case of a single dielectric slab of width l_1 surrounded by two infinite media on each side, where the field is propagated from the left medium, the overall transmission response

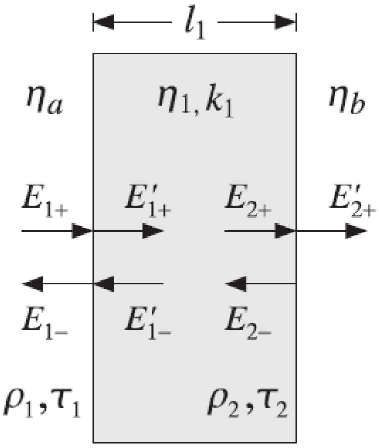

Figure 1.21: Single dielectric slab [71]

into medium η_b can be obtained by successively applying the matching and propagation matrices as shown below.

$$\begin{aligned}\begin{bmatrix} E_{1+} \\ E_{1-} \end{bmatrix} = \frac{1}{\tau_1}\begin{bmatrix} 1 & \rho_1 \\ \rho_1 & 1 \end{bmatrix}\begin{bmatrix} E'_{1+} \\ E'_{1-} \end{bmatrix} &= \frac{1}{\tau_1}\begin{bmatrix} 1 & \rho_1 \\ \rho_1 & 1 \end{bmatrix}\begin{bmatrix} e^{ik_1l_1} & 0 \\ 0 & e^{-ik_1l_1} \end{bmatrix}\begin{bmatrix} E_{2+} \\ E_{2-} \end{bmatrix} \\ &= \frac{1}{\tau_1}\begin{bmatrix} 1 & \rho_1 \\ \rho_1 & 1 \end{bmatrix}\begin{bmatrix} e^{ik_1l_1} & 0 \\ 0 & e^{-ik_1l_1} \end{bmatrix}\frac{1}{\tau_2}\begin{bmatrix} 1 & \rho_2 \\ \rho_2 & 1 \end{bmatrix}\begin{bmatrix} E'_{2+} \\ E'_{2-} \end{bmatrix}\end{aligned} \tag{1.52}$$

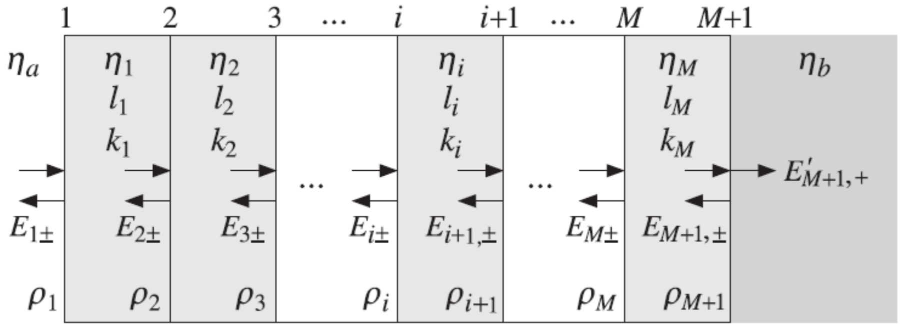

Figure 1.22: Transmission for multilayer dielectric slab [71]

The approach for a single dielectric slab can be extended to a stack of multiple planar layers on top of each other. The situation is shown in Figure 1.22. For this multilayer stack configuration, one can obtain the relationship between the incident field at the first interface and the transmitted field at any of the following interfaces by multiplying the transfer matrices for each interface. The mathematical approach is shown below.

$$\begin{bmatrix} E_{i+} \\ E_{i-} \end{bmatrix} = \frac{1}{\tau_i} \begin{bmatrix} 1 & \rho_i \\ \rho_i & 1 \end{bmatrix} \begin{bmatrix} e^{jk_i l_i} & 0 \\ 0 & e^{-jk_i l_i} \end{bmatrix} \begin{bmatrix} E_{i+1,+} \\ E_{i+1,-} \end{bmatrix}, i = M, M-1, M-2, ..., 1 \quad (1.53)$$

If $A_{i,i+1} = \frac{1}{\tau_i} \begin{bmatrix} 1 & \rho_i \\ \rho_i & 1 \end{bmatrix} \begin{bmatrix} e^{jk_i l_i} & 0 \\ 0 & e^{-jk_i l_i} \end{bmatrix}$, then

$$\begin{bmatrix} E_{i+} \\ E_{i-} \end{bmatrix} = A_{i,i+1} \begin{bmatrix} E_{i+1,+} \\ E_{i+1,-} \end{bmatrix} = A_{i,i+1} \frac{1}{\tau_{i+1}} \begin{bmatrix} 1 & \rho_{i+1} \\ \rho_{i+1} & 1 \end{bmatrix} \begin{bmatrix} e^{jk_{i+1} l_{i+1}} & 0 \\ 0 & e^{-jk_{i+1} l_{i+1}} \end{bmatrix} \begin{bmatrix} E_{i+2,+} \\ E_{i+2,-} \end{bmatrix}$$

$$\begin{bmatrix} E_{1+} \\ E_{1-} \end{bmatrix} = A_{2,3} A_{3,4} ... A_{M+1,M+2} \frac{1}{\tau_1} \begin{bmatrix} 1 & \rho_1 \\ \rho_1 & 1 \end{bmatrix} \begin{bmatrix} E'_{M+1,+} \\ 0 \end{bmatrix}$$

The relationship between the input field at the first interface i.e. E_{1+}, the transmitted field after the multilayer stack i.e. E_{M+1}' and the reflected field at the first interface i.e. E_{1-} are expressed by the Equation (1.54). The approach shown here assumed that there is no back-reflected field from the output end. In order to simulate the radiation pattern of quantum emitters buried in multilayer device, the radiation from the emitter is made incident on the layers underneath the emitter and the total reflected field is calculated. Again, the transmission of the radiation travelling towards the layers on top of the emitter's embedding layer is calculated and the reflected field from the bottom layers is added to it. The obtained expression resembles an infinite geometric progression and can be analytically calculated as shown.

The radiation from the emitter is divided into the upward travelling component E_1 and downward travelling component E_2 where $E_1 = E_2$ in amplitude. The contribution of both these fields is added to calculate the transmitted field $E_{T,up}$.

$$E_{T,up} = E_{T_1} + E_{T_2}$$

$$\begin{aligned} E_{T_1} &= E_0 e^{-jkn_1(d-z)} t_u + E_0 e^{-jkn_1(d-z)} r_u r_d e^{-jkn_1 2d} t_u + ... \\ &= E_0 e^{-jkn_1(d-z)} \frac{t_u}{1 - r_u r_d e^{-jkn_1 2d}} \end{aligned} \quad (1.54)$$

$$\begin{aligned} E_{T_2} &= E_0 e^{-jkn_1 z} r_d . e^{-jkn_1 d} t_u + E_0 e^{-jkn_1 z} r_u r_d^2 * e^{-jkn_1 3d} t_u + ... \\ &= E_0 e^{-jkn_1(d+z)} r_d \frac{t_u}{1 - r_u r_d e^{-jkn_1 2d}} \end{aligned} \quad (1.55)$$

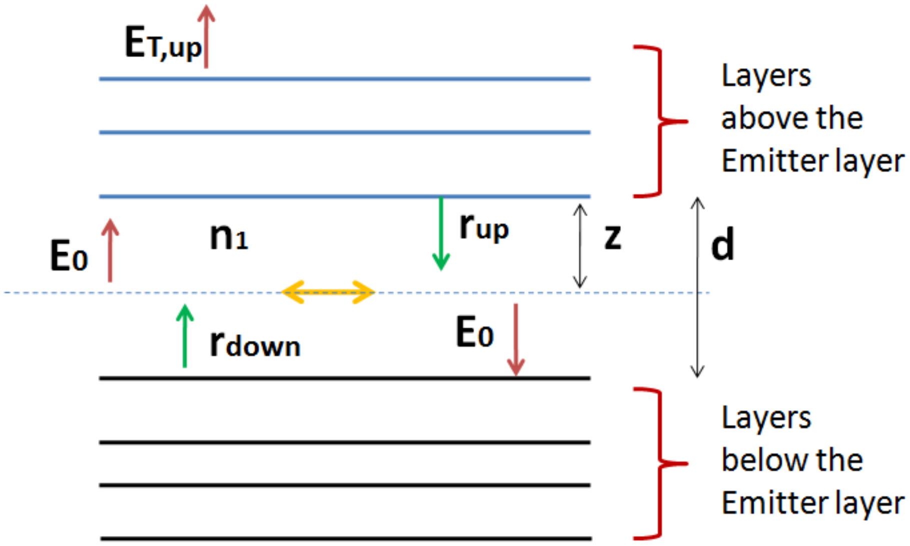

Figure 1.23: Transfer-matrix formulation to calculate transmission of radiation from a source embedded in the multilayer stack

In the expressions above, the field transmission coefficient (t_u) and field reflection coefficient (r_u) of the layer stack above the emitter's layer are calculated using the transfer-matrix model. Similarly, the field reflection coefficient of the bottom stack r_d is calculated and put in the above equations. The wavevector in the equations are the z-components of the wavevector which depend on the angle w.r.t. the normal (θ) as k = $k_0 cos\theta$. The emitter's embedding layer has a refractive index of n_1. With this approach, the field transmission through any layer stack can be calculated.

1.6 Strategies for Efficient Photon Extraction

The coupling between quantum emitters and optical radiation is inherently poor because the atomic wavefunctions and the wavelength of the emitted radiation have a dimensional mismatch. Quantum dots are bigger in size compared to natural atoms, however the wavefunction overlap with the radiation is still poor. In addition, in order to preserve the radiative efficiency of quantum dot excitons from surface states, self-assembled quantum dots are buried in the substrate at least 50 nm from the surface [76]. The collection efficiency of photons is quite low ($\sim$1%) even with high NA microscope objective lenses due to critical angle of 16.7^o at air-GaAs interface (the situation is shown in Figure 1.24). Thus the problem is two-fold, (a) the extraction of photons from the sample has to increase and (b) the collection of photons has to improve by using high NA objective lenses and by making sure that the emitter emits in a narrow cone of angles.

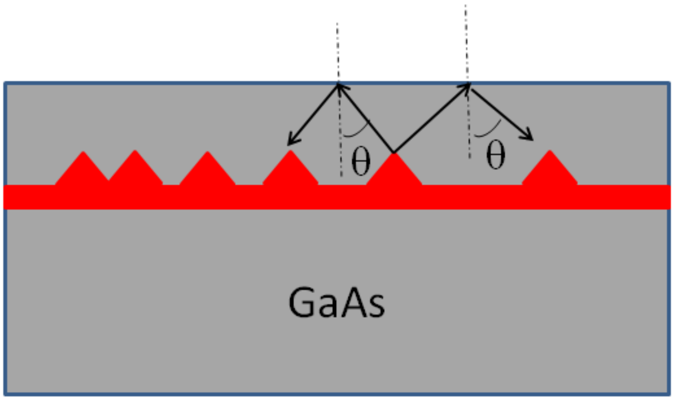

Figure 1.24: Light emitted by quantum dots gets reflected at the air-GaAs interface if $\theta > \theta_c = 16.7^o$ for air-GaAs interface

A promising and efficient source of single photons from InAs quantum dots is a photonic crystal cavity [77]. Owing to the small volume in a photonic crystal cavity (high-Q value where Q = $\lambda/\delta\lambda$), the local density of states in the cavity gets modified. This modification in local density of states implies reduction in lifetime as there are more states available to decay into. This effect is called Purcell effect. Due to this Purcell enhancement in a photonic crystal cavity, high repetition rate in photon emission can be obtained which makes quantum dots in photonic crystals a promising single photon source. In reference [78], a single photon collection efficiency of (44.3 $\pm$ 2.1)% into the first lens (see the confocal microscope details in Chapter 2) is observed.

A micropillar single photon source for InAs quantum dots (shown in Figure 1.25(2)) exhibits high efficiency of 0.79 $\pm$ 0.08 collected photon per pulse. In order to collect photons from the top, the number of superlattice layers on the top is lower [79]. Due to the necessity of self-assembled InAs quantum dots being in resonance with the high-Q resonant micropillar cavity for high collection efficiency, it is difficult to generate entangled photon sources from micropillars. In InAs quantum dots, the generation of polarization-entangled photon pairs depends on the biexciton emission and subsequent exciton emission which implies that the cavity should sustain both wavelengths which are $>$3 nm apart. Thus, GaAs micropillar based single photon source has high efficiency and indistinguishability but not optimal for applications where entangled photon pairs would be necessary. Similar resonant-behaviour is also observed for photon extraction from high-Q microcavity shown in Figure 1.25(4), where 31MHz photons were observed into the first lens and 4MHz into

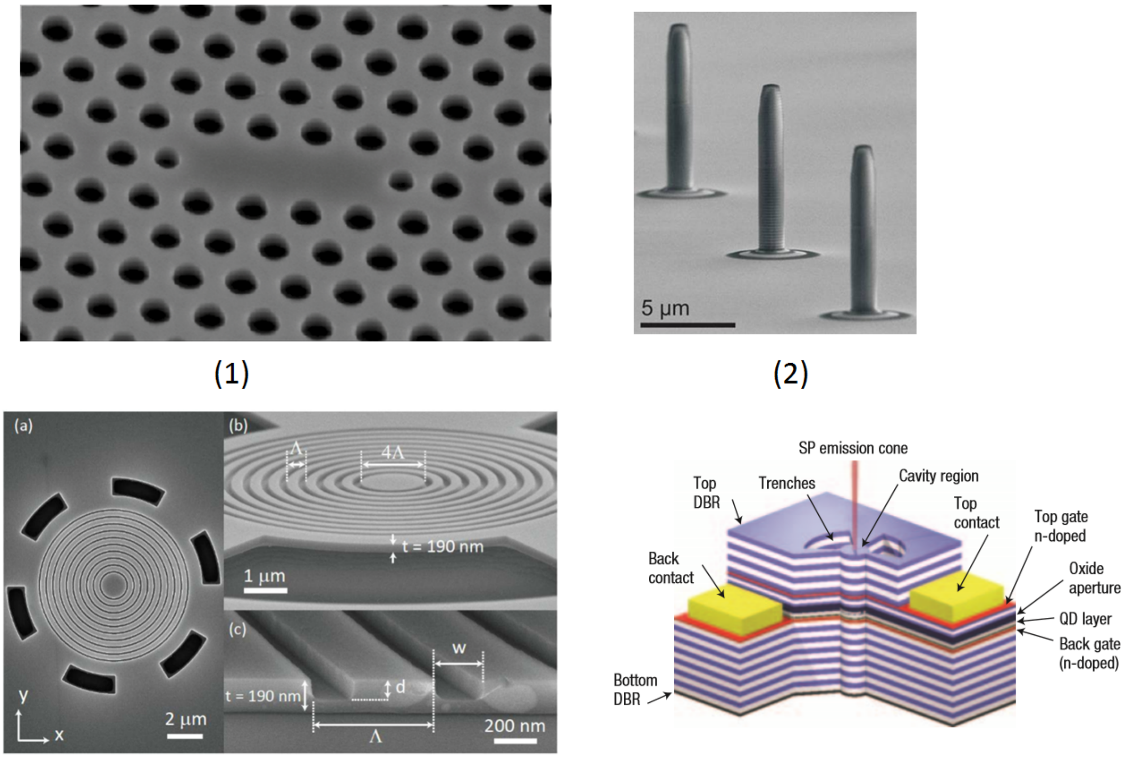

(1) (2) (3) (4)

Figure 1.25: Single photon sources based on cavities or photonic structures: (1) Photonic crystal cavity [78], (2) Micropillar single photon source [79], (3) Circular Bragg grating for enhanced photon extraction efficiency [80] [81] and (4) high-Q microcavity with mirrors [82].

the fibre. In Figure 1.25(3), efficiency of 10% is experimentally obtained into a NA of 0.42. The circular Bragg grating device shows broadband operation with simpler fabrication procedure. The placement of dot at the centre of the circular Bragg cavity gives a purcell enhancement of 12 and high efficiency.

The varying morphology of the self-assembled quantum dots necessitates the pursuit of novel broadband antenna designs. Broadband antennas are useful for multilevel systems for generation of entangled photon pairs [83] [84] and spin initialization and read-out [85]. The use of solid immersion lenses presents a geometric approach to increase the collection NA of the optical system. Nanowire single photon source [98] [99] and planar microcavity [92] [102] [101] approaches have also shown considerable promise in increasing the photon collection efficiency.

1.6.1. Solid Immersion Lens

In farfield microscopy, the resolution of an optical microscope is given by the following equation [87],

$$\Delta x = \Delta y = 0.51\frac{\lambda}{NA} \tag{1.56}$$

where λ is the wavelength of the light in free space and NA (= n sinθ, where n is the refractive index of the medium) is the numerical aperture of the microscope objective lens. As can be seen from equation 1.56, an increase in NA and a decrease in wavelength improve the resolution of a conventional optical microscope. The NA of the optical system can be increased by using an immersion of higher refractive index ($n > 1$). However, due to experiments being conducted at $T<4K$, oil immersion is not an option. Solid immersion lenses (SIL) are a viable option in this scenario and further the refractive index of SIL material is higher than that of immersion oils.

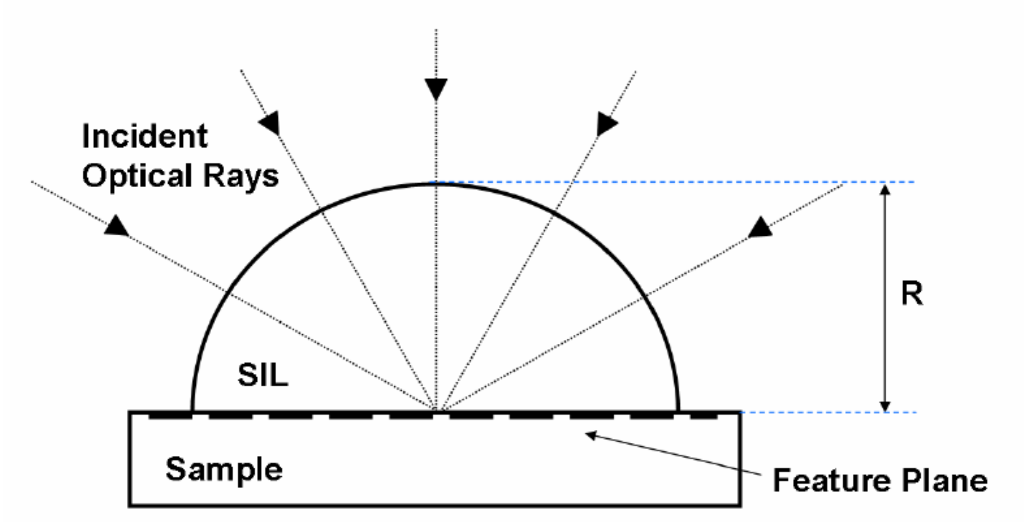

Figure 1.26: Hemispherical solid immersion lens has the focus at the centre of the hemisphere. It increases the effective numerical aperture of the optical system i.e. $NA_{eff} = NA_{objective} \times n_{SIL}$ and reduces the size of the diffraction-limited focus spot on the sample which helps towards isolating single quantum emitters for spectroscopy [87].

The solid immersion lens was invented by Kino and Mansfield [86] in 1990. It improves the resolution in imaging and increases effective numerical aperture due to high refractive index of SIL (n_{SIL}=2). In quantum dot spectroscopy, the density of quantum dots can be quite large within the focus of a microscope. The addition of a SIL assists in isolation of

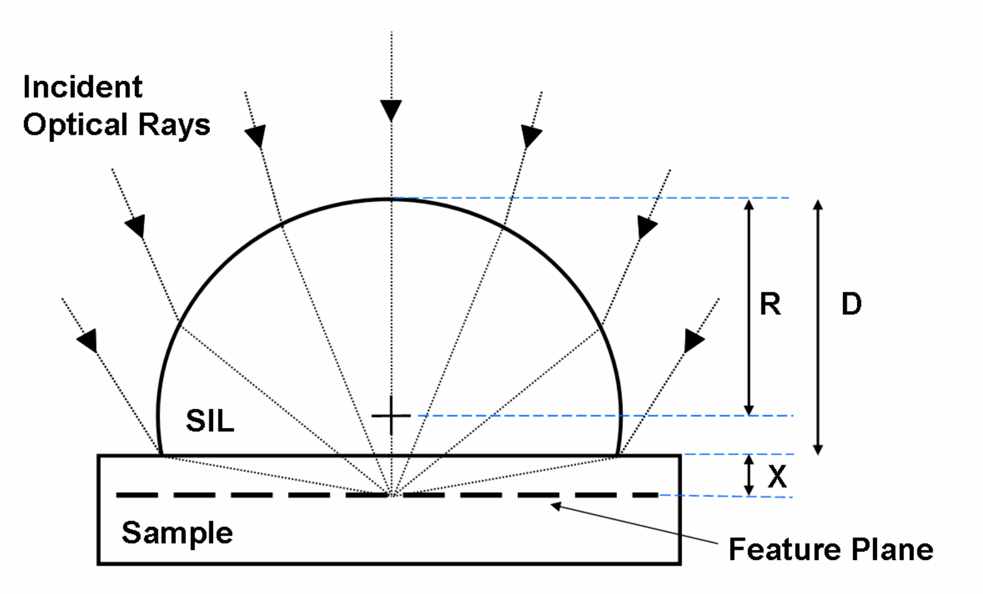

Figure 1.27: Schematic diagram of a super solid immersion lens (SIL) [from reference [87]]

single quantum dots for spectroscopy and microscopy. Further, the critical angle condition gets alleviated as $\theta_{critical}$ for SIL-GaAs is $\sim$35^o for n$_{SIL}$=2.

In the theory described by Born and Wolf [88], light can be focused without any aberrations inside a sphere made of high refractive index material at the centre of the sphere which led to the design of hemispherical SIL (h-SIL), shown in Figure 1.26. There is no refraction at the air-SIL interface due to normal incidence at the SIL surface. The h-SIL has played a significant role in enhancing the collection efficiency and in improvement of spatial resolution of the sample under investigation. An h-SIL also introduces magnification into an imaging system by a factor of n$_{SIL}$. In single quantum dot spectroscopy system with NA$_{objective}$ = 0.65 including a h-SIL of n = 2.0 increases the collection efficiency of a single dot to 3.5% (from 0.87% without h-SIL) whilst the spot size reduces by a factor of 4 [87]. This is a straight-forward way to enhance the collection efficiency of photons from quantum emitters without any wavelength-related variations.

The second aberration-free focus in a spherical high index material is a distance $z = R\frac{n_1}{n_{s-SIL}}$ from the centre of the sphere, where R is the radius of the sphere and n_{s-SIL} and n_1 are the refractive indices of sphere and air respectively. Light undergoes refraction in super-SIL when incident at air-superSIL interface. In a superSIL, the numerical aperture increases by a factor of n$^2_{s-SIL}$, as long as NA$_{eff}$ $\leq$ n$_{s-SIL}$. In figure 1.27, the height of the super-SIL can be calculated as following,

$$D = R(1 + \frac{1}{n_{s-SIL}}) - X \tag{1.57}$$

Due to wavelength dependence of refractive index, the focal position of a super-SIL varies. An h-SIL, in contrast, always has its focus located at the centre of the sphere. The advantages of super-SIL are higher NA, higher magnification and better spatial resolution. In single quantum dot spectroscopy system with $\text{NA}_{objective}$ = 0.65 including a h-SIL of n = 2.0 increases the collection efficiency of a single dot to 3.5$\%$ (from 0.87$\%$ in absence of h-SIL) whilst the spot size reduces by a factor of 4 [87]. This is a straight-forward way to enhance the collection efficiency of photons from quantum emitters without any wavelength-related variations.

1.6.2. Photonic Nanowire

Nanowires overcome the narrow bandwidth limitation of high-Q microcavities and allow control on spontaneous emission in a broad spectrum. Tapers in nanowires further allow adiabatic funneling of photons from the cavity. Taper also reduces reflections at the air-GaAs interface and thus improves the efficiency of the source in addition to a Gaussian mode profile. Nanowires also have directional emission which allows use of off-the-shelf objectives to efficiently couple out light from the system [95] [96].

The design aspect of a GaAs nanowire requires a gold mirror integrated at the bottom to reflect the downward travelling quantum dot radiation towards the collection side. The Gold mirror reflects the downward travelling photons and with the right vertical position of quantum dot w.r.t the gold mirror, constructive interference between the forward travelling emission and reflected emission can be ensured. The diameter of the nanowire and the wavelength of the fundamental mode show a strong correlation. In order for the nanowire single photon source to work at a wavelength of 950 nm, the optimum ratio of diameter of the wire to λ has been demonstrated to be 0.23 [98] [99]. The radial position of the quantum dot on the nanowire axis also has a strong role to play in the coupling of QD emission to the nanowire waveguide mode and also to obtain a gaussian modal profile which matches to the profile of a single mode optical fibre. The design of a nanowire with taper is simulated using Lumerical FDTD software. Mode coupling efficiency, purcell factor and coupling efficiency into a lens with a numerical aperture of 0.82 are the top criteria for extracting all the correct parameters for the devices. The schematic diagram pursued for this simulations

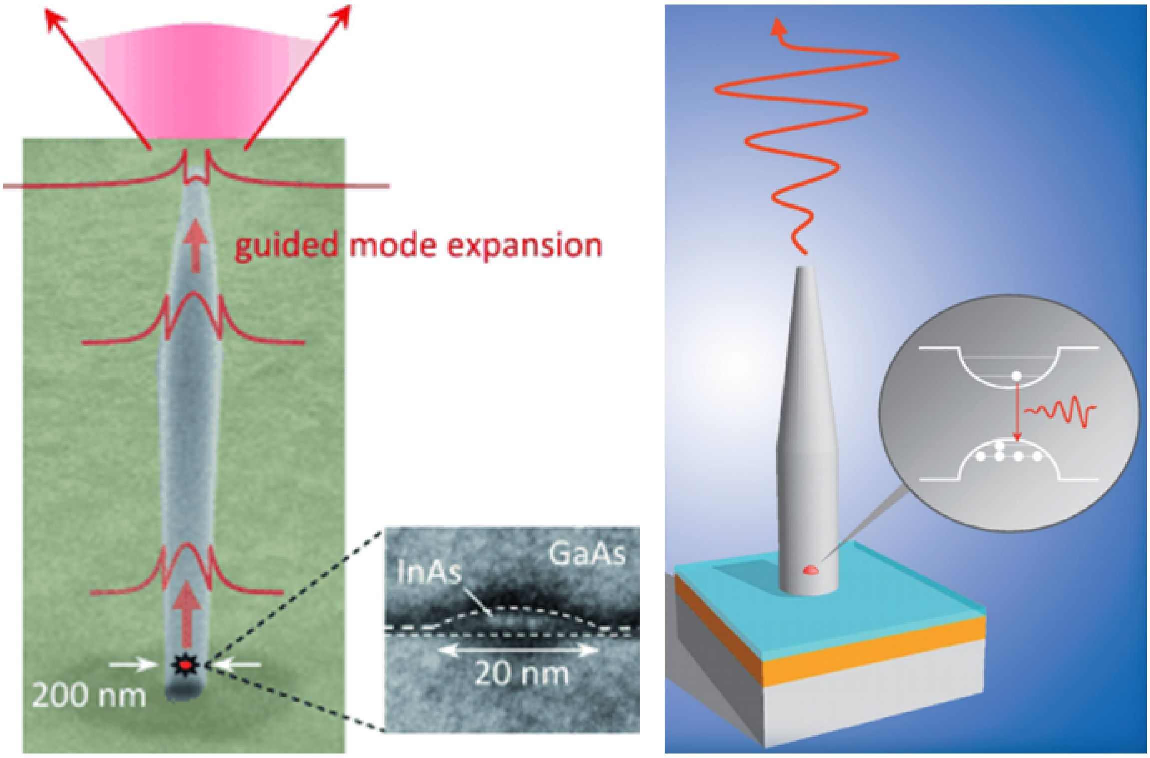

Figure 1.28: Schematic diagram of GaAs Nanowire embedded with InAs quantum dot ([95])

is shown in Figure 1.29. The diameter of the nanowire is chosen as 209 nm for a wavelength of 950 nm. The angle of the taper is kept at 10°.

Amid other design constraints, the position of the self-assembled InAs quantum dot in the nanowire waveguide has to coincide with an anti-node of the fundamental waveguide mode for effective coupling into the waveguide mode [97]. In order to ascertain the optimal position of the quantum dot w.r.t. the gold mirror at the bottom, the position is varied in simulation and the effect is studied on collection efficiency, extraction efficiency, purcell factor (F_p) and mode coupling (β). The result is shown in Figure 1.30.

When the dipole distance is increased from 0 nm to 210 nm, purcell factor (F_p) decreases, and is minimum ($\sim$0.2) when the dipole is separated by 210 nm from the mirror. It increases with increase in the dipole-mirror separation thereafter. The oscillations thereafter in F_p are expected to vanish when dipole position increases. The effect of an interface near a quantum emitter has also been studied in past by Drexhage where the lifetime of the emitter oscillates with varying separation from a metal mirror [91]. The obtained result for purcell factor is a theoretical confirmation of the expected behaviour.

The mode coupling efficiency has a similar trend when dipole position increases. It

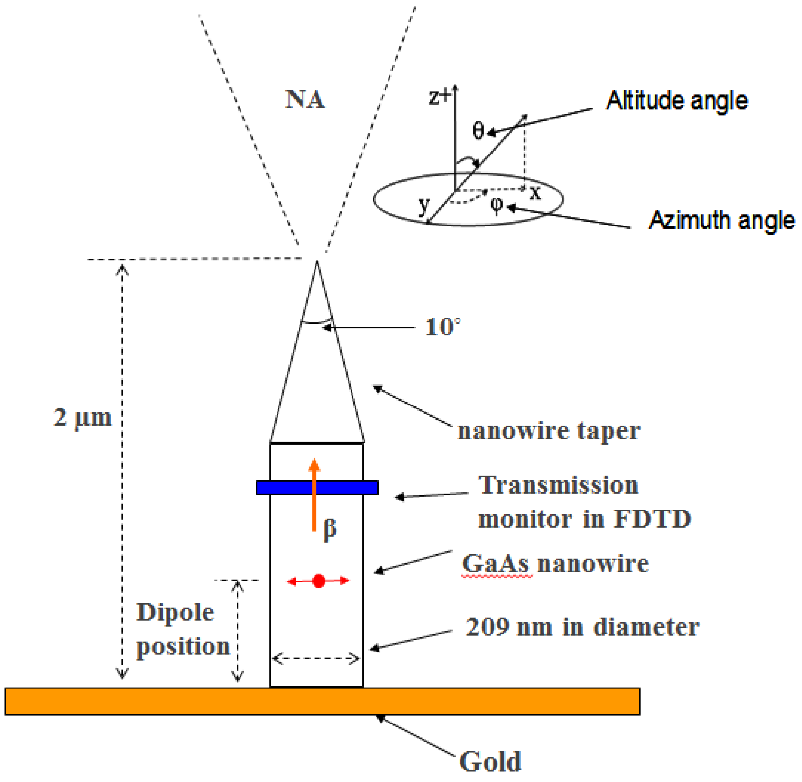

Figure 1.29: Design of the GaAs nanowire embedded with a dipole for FDTD simulation.

seems to approach a value between ∼0.5-0.7 at infinitely large dipole position.

1.6.3. Planar Microcavity for High Efficiency

Planar microcavity approach for enhancement of photon extraction from a sample with high refractive index works in the low-Q regime where the lifetime of the emitter is not modified and the enhancement of rate of spontaneous emission due to Purcell factor $(Q/4\pi^2)(\lambda^3/V)$ is absent. Following the approach taken by Benisty *et al.* for the design of light-emitting-diodes [92], high extraction efficiency (∼25%) of photons can be obtained by tailoring the angular radiation profile of emission. This entails the placement of a mirror at the rear end of the device so that it reflects the emission towards the microscope objective. The emitter is also placed at an antinode of the cavity which is closer to the mirror.

Interference from a Single Rear Mirror for Extraction

When a dipole emitter at a vacuum wavelength λ in a high-index medium (refractive index, n) is located at a distance $z = m\lambda/2n$ from a mirror with reflectivity r, the radiated electric field is given by,

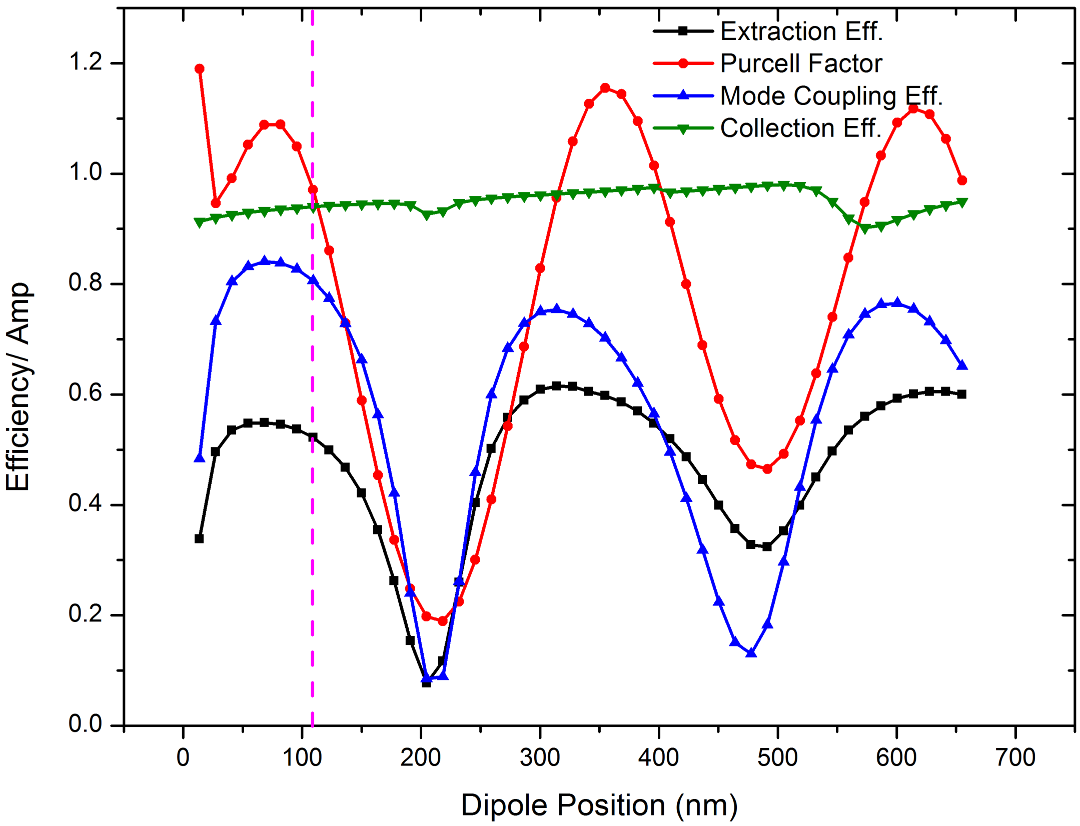

Figure 1.30: Extraction efficiency, Purcell factor, mode coupling efficiency and collection efficiency of the dipole emitter in the numerical aperture of the objective lens as a function of vertical separation of dipole w.r.t the botom gold mirror. This result is obtained from FDTD simulations in Lumerical where the position of the dipole w.r.t. the gold mirror is varied [100].

$$E^2 = E_0^2|1 \pm re^{2i\phi'}|^2 = E_0^2(1 + r^2 \pm 2rcos2\phi') = E_0^2 \times 2\chi \tag{1.58}$$

where $2\phi' = 2kzcos\theta$ and E_0 is the dipole radiation in absence of the mirror. In the above equation, χ is called the antinode factor. If constructive interference occurs for normal incidence i.e. θ=0, 2kz = 2mπ or z = mλ/2n. For n = 3.48 (GaAs), λ = 950nm and m=1, z = 136.5 nm. Similarly for PMMA, n = 1.45, λ = 750nm and m=1, the distance z = 258.6nm. For metallic mirrors, m takes half-integer values and reflectivity is taken as -r. If m=1/2, then z = λ/4n i.e. the emitter is located a quarter of the wavelength away from the metallic mirror for constructive interference. When m $> n^2$, the emitter is located very far from mirror, and both constructive and destructive interferences are observed so at most the output field can be given as $E = E_0^2(1 + r^2)$. The estimated effect on extraction efficiency of photons can be seen in Figure 1.31. This trend of brightness seen for the emitter is for monochromatic emission as it relies on constructive interference of light at particular wavelengths into particular angles. Thus it can be inferred that this behaviour/enhancement is due to modification of intensity of light in different directions or k-vectors (wavevectors).

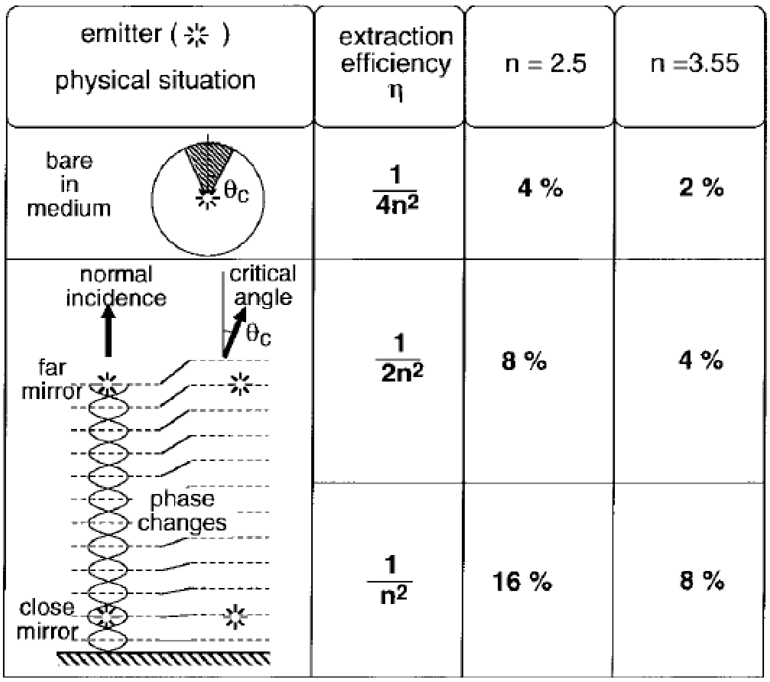

emitter (⁂) physical situation	extraction efficiency η	n = 2.5	n =3.55
bare in medium θ_c	$\frac{1}{4n^2}$	4 %	2 %
normal incidence critical angle θ_c far mirror phase changes close mirror	$\frac{1}{2n^2}$	8 %	4 %
	$\frac{1}{n^2}$	16 %	8 %

Figure 1.31: Extraction efficiencies are estimated for emitter in bare surrounding and when at a near or far antinode from the rear mirror [92]

Order of the Cavity

For an emitter buried between two mirrors, the same approach is taken as for the single mirror case. However, in a given direction or k-vector, two series of multiple beams need to be summed together. The situation is shown in Figure 1.32.

$$|E_{out}|^2 = |E_{in}|^2 \frac{T_1|1 + r_2 e^{2i\phi'}|^2}{|1 - r_1 r_2 e^{2i\phi}|^2} = |E_{in}|^2 \times \chi \times \frac{2T_1}{|1 - r_1 r_2 e^{2i\pi}|^2} \tag{1.59}$$

where $2\phi = 2kLcos\theta$ gives the round-trip phase and for a lossless mirror $T_1 = 1 - R_1 = 1 - r_1^2$. The round-trip phase $2\phi \equiv 2\pi$ yields that k$\propto$ $1/cos\theta$. It can be concluded that the cavity favours different wavelengths at different angles or in other words the angular distribution of light varies in k-space as a function of wavelength. Extraction from the top side requires high reflectivity r$_2$ from bottom mirror. The denominator of Equation (1.59) resembles an Airy function and is 2π periodic with 2ϕ as well as $k_z = kcos\theta$,

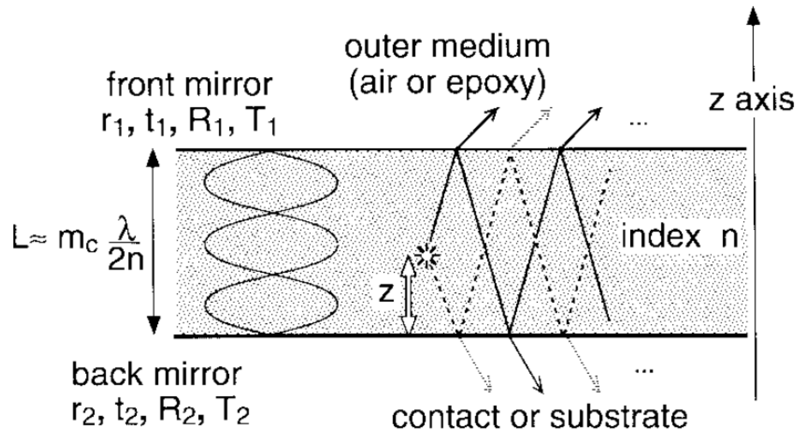

Figure 1.32: Schematic of an emitter in a cavity surrounded by mirrors on each side [92]

which gives finite number of resonances. The number of resonances (calculated for normal incidence) gives the cavity order i.e. m$_c$ = integer[$2\phi(\theta = 0)/2\pi$] = integer[$2nL/\lambda$]. Since $2\phi = 2kLcos\theta$, there are m$_c$ resonant angles θ_i that are obtained. The lowest value of $\theta_i = \theta_0$ which gives the value closest to the normal drawn to the microcavity sample. The values of θ_i that are larger than the critical angle θ_c become guided modes.

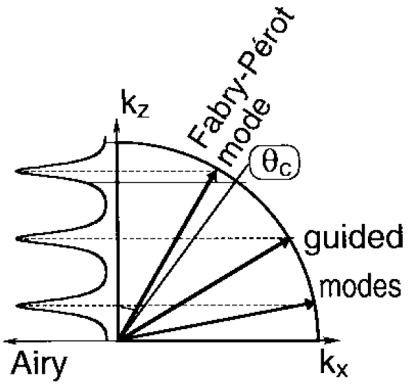

Figure 1.33: K-space plot to depict cavity mode, critical angle, guided modes and the Airy function [92]

For a microcavity sample with a thickness of 642 nm designed for emission at a wavelength of 950 nm, the order of the cavity is obtained to be 5. The corresponding resonance angles w.r.t. the normal are obtained to be 77.7^o, 64.8^o, 50.4^o, 31.7^o and 0^o for m$_c$ = 1, 2, 3, 4 and 5, respectively. If the critical angle θ_c is 35.1^o for an interface of glass solid-immersion lens with n$_{SIL}$ $=$ 2 and GaAs (n$_{GaAs}$ = 3.48), there is a single resonance that escapes from the system with an angle of 31.74^o. The angle increases with decreasing wavelength of emission approaching 35^o for emission at a wavelength of 915 nm. Light escaping the microcavity sample is collected within a solid angle, dΩ = sin$\theta d\theta d\phi$.

In a similar approach undertaken in reference [101], near unity photon extraction efficiency was predicted from planar microcavity single photon source. In order to achieve this, the device design has to minimize guided modes inside the sample. When the refractive index of the embedding layer is larger than the surrounding layer, light can be guided within the embedding layer by total internal reflection at the interfaces. The situation is shown in Figure 1.34(a). By making the embedding layer sufficiently thin, one can make sure that no modes can be sustained in the layer and thus light can be efficiently coupled out. As can be seen in the dipole radiation images for the two cases shown in Figure 1.34, higher index medium at the output half space allows coupling of radiation to the collection end in a more efficient manner.

Thinning down the thickness of the embedding layer can ensure that no modes are guided in the layer. Also a crucial parameter is the difference in the refractive index of the embedding layer and the surrounding layer i.e. n_2-n_1. For AlAs-GaAs heterostructures, this difference is very small and thus the structure is only weakly guiding, which is desirable. The critical angle for these 2 layers is $\sim$70^o that means most of the light is in the surrounding. As can be seen in Figure 1.34(b), the emitter layer (n_2) when sandwiched between two layers of different refractive indices such that $n_1 > n_2 > n_3$, allows light to couple out of the material as a radiation mode. The dipole radiation patterns are simulated for in-plane orientation, black curve for p-polarization and red curve for s-polarization in Figure 1.34. As can be seen for case (a), light is lost away from the collection side as well in addition to being guided in the higher index substrate. In case (b), the angular emission density is much higher for p-polarized dipole with little light leaving the sample from the rear end.

Using the understanding of radiation from dipoles and extraction of photons in microcavities, a brighter source of single photons can be designed and engineered for self-assembled InAs quantum dots in GaAs. There are three device designs that are relevant. In Figure 1.35(b), a bulk sample with a glass SIL is shown (n_{SIL}=2). The collection efficiency from InAs quantum dots in bulk GaAs (case 1) is 0.87% which in presence of SIL increases four-fold, thus $\eta = 3.5\%$ for case 2. A maximum $\eta = 34\%$ is predicted for d'=2.44 for case 3. Non-integer d' values arise due to phase shift at reflection from gold mirror. Increase in d' increases the order of the microcavity and gives rise to guided modes. For d'$>$100, $\eta = 15\%$ is predicted for case 3 as the power gets distributed across a number of modes. For

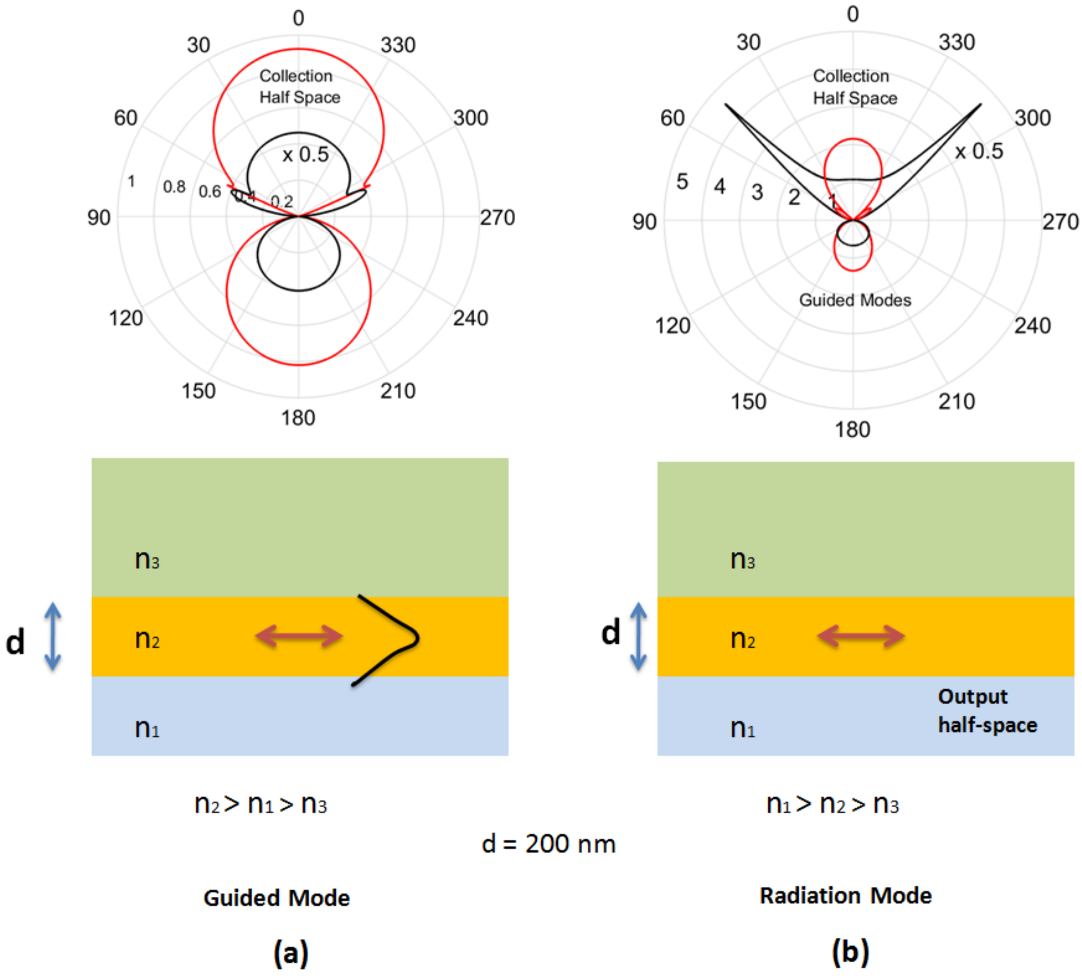

Figure 1.34: The radiation patterns are simulated for in-plane dipoles: (a) When emission propagates through a medium of higher index (n_2=1.8) flanked by lower refractive indices (n_1=1.45, n_3=1.33) on either side, the emission is either guided by total internal reflection inside the substrate and the collected light and light travelling in the opposite direction have equal distribution of dipole radiation. (b) When the refractive index of the output half-space $n_1 = 1.8 > n_2 = 1.45$ most light couples out as radiation mode in the collection half-space in this scenario. The thickness of the embedding layer is 200 nm and the dipole is at the center of the layer.

d’=4.48, $\eta = 27\%$ as can be seen for the 3rd phase resonance of the microcavity (circled in Figure 1.35(f)). The relative ease of fabrication of these samples make them particularly useful for realization of efficient quantum dot single photon sources.

For electrostatic tuning, the bulk sample with SIL has a thin layer of NiCr as the Schottky gate on top between the SIL and the GaAs layer. The transmission of such a device reduces by $\sim 20\%$ for every 1 nm of NiCr. Thus for a 3nm thin NiCr layer, the photon collection efficiency η of case 2 sample is less than 50% of the expected four-fold increase

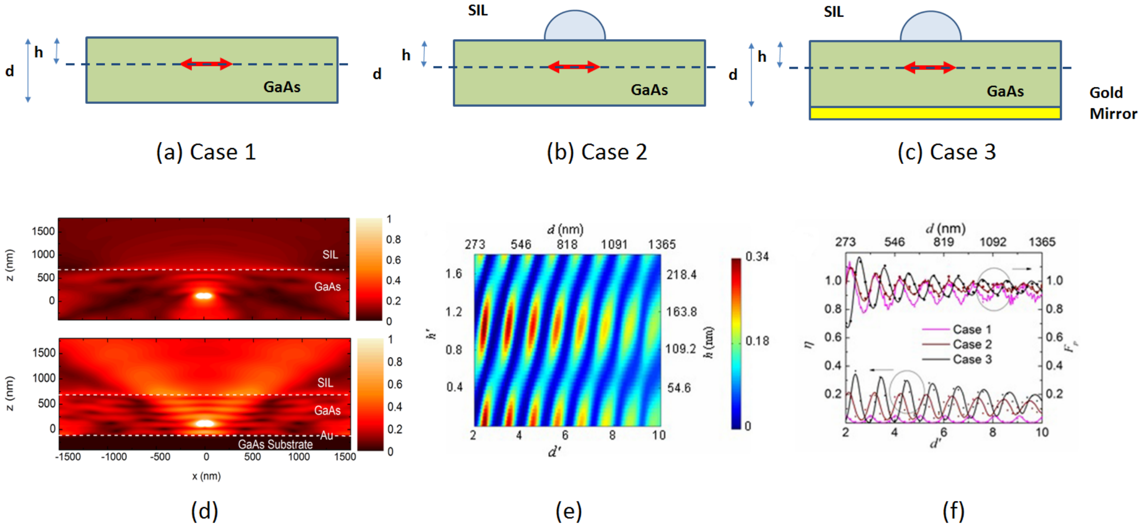

(a) Case 1 (b) Case 2 (c) Case 3

(d) (e) (f)

Figure 1.35: Schematic sketch of the considered structure: (a) InAs quantum dot is embedded in a GaAs layer with h=136.5 nm, and a SIL is attached on the top cavity mirror, (b) FDTD simulation shows that despite the SIL (n_{SIL}=2), a large fraction of light is still confined inside the GaAs membrane. (c) GaAs membrane with a glass SIL on top and a back mirror consisting of gold, (d) FDTD simulation exhibits a significant fraction of light escaping the sample for the microcavity sample while the case 2 design has light confined inside the GaAs layer. (e) Variation in d and h for the microcavity sample (case 3) produces phase resonances as shown. (f)$\eta = 34\%$ is theoretically predicted for the first phase resonance of device shown as case 3. Solid lines are from transfer-matrix model and dots are from FDTD simulations.

i.e. reduced to 1.75%. In the planar microcavity sample, gold layer at the bottom of the sample acts both as a mirror and the Schottky contact. Thus the efficiency η = 27% is maintained for the 5th order microcavity sample. This implies that photon counts from the microcavity sample should be 15 times that of the bulk sample with SIL. However, it was observed in experiment that at saturation 400,000 photons per second (400kHz) were collected on a single photon detector from the bulk sample with SIL (case 2), while the planar microcavity sample yielded 3 million photons per second (3MHz) i.e. a factor of 7.5 against an expected factor of 15. The saturation curve is shown in Figure 1.36. Since the radiation from a quantum dot, in the microcavity sample case, favours light into certain angles w.r.t. the normal in k-space depending on the wavelength, imaging of the emission pattern in k-space can help to identify if the cavity is functioning as it was expected to based on the design. The saturation curves shown in Figure 1.36 were obtained by Ted Santana.

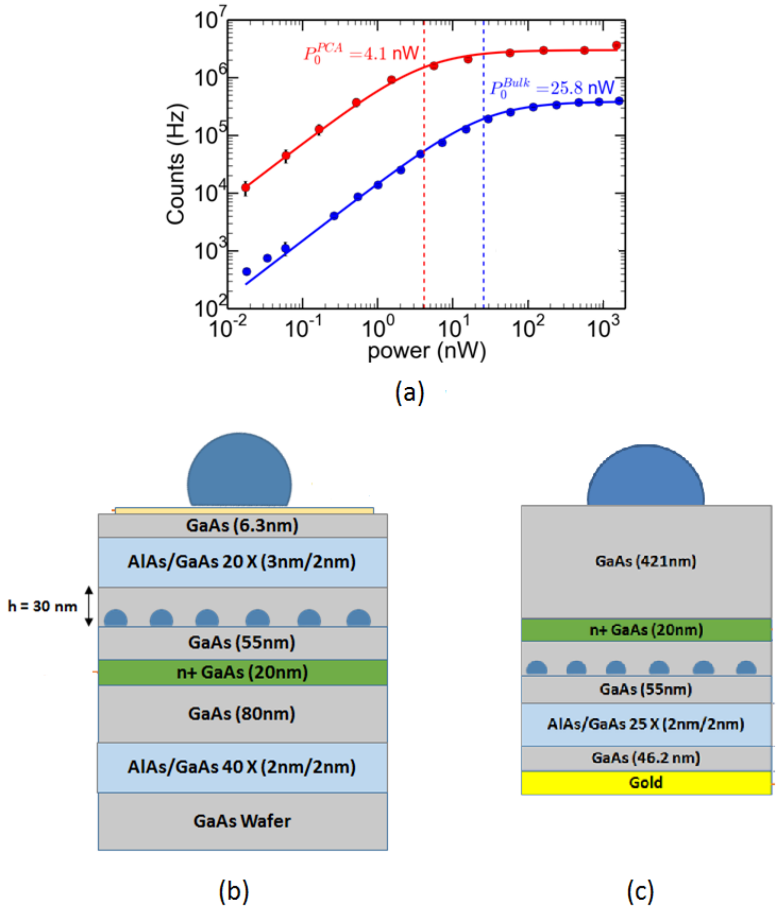

Figure 1.36: (a) Saturation curve for quantum dot in bulk GaAs sample with SIL (blue) and in planar microcavity sample (red) [picture courtesy: T. Santana], (b) schematic diagram of the bulk GaAs Sample with SIL and (c) schematic diagram of the planar microcavity sample.

1.7 Theory of Fourier Microscopy

The radiation pattern of a dipole has already been discussed in an isotropic medium and when placed next to an interface. When this radiation is collected through a microscope objective as shown in Figure 1.37, the objective focuses light emitted at angle θ w.r.t. the optics axis on to its back focal plane at a position ρ.

When a reference sphere is drawn around to convert angle of emission into position coordinate at the back focal plane of the objective, a sine relationship is obtained i.e. ρ = f sinθ. The situation is shown in Figure 1.38. Also, the intensity distribution at the back focal plane has an angular dependence. Along increasing angle θ, the pencil of light becomes thinner as shown and the cross-section area after the reference sphere is related to

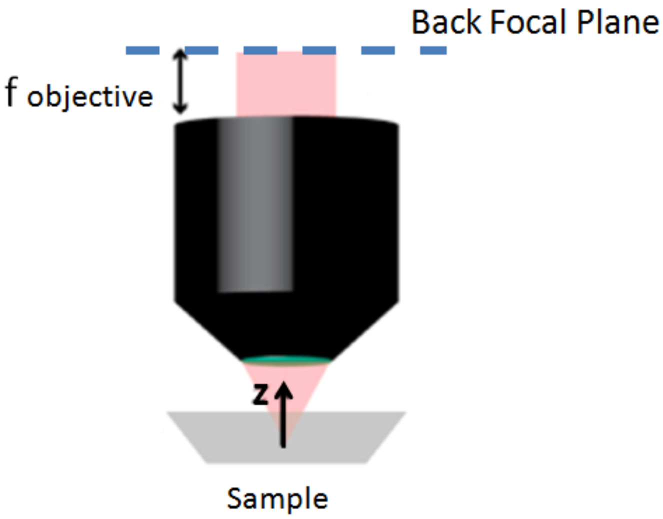

Figure 1.37: In back focal plane imaging, the light emitted by a dipole emitter is imaged at the back focal plane of the microscope objective. For most compound objective lenses with high NA, the back focal plane is inside the lens itself. It is shown explicitly outside the objective for clarity [105].

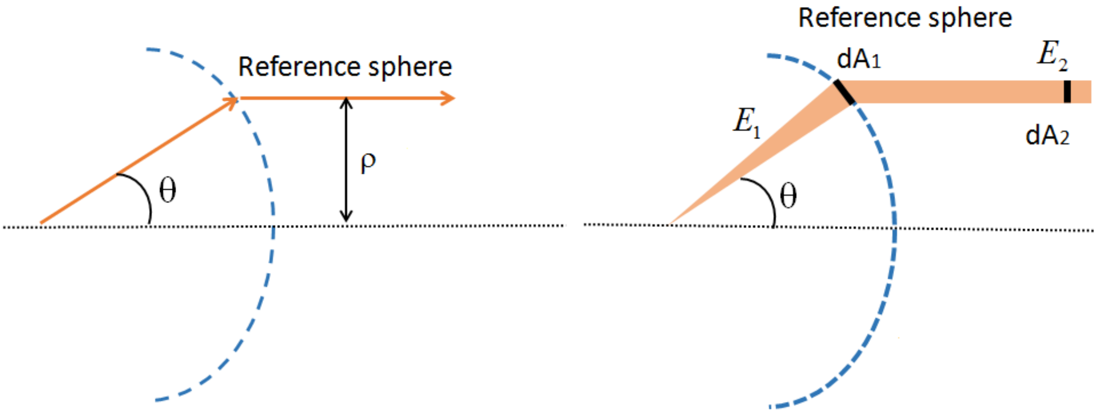

Figure 1.38: The reference sphere in microscope objective's object space converts angle of emission into position coordinate at the back focal plane given by $\rho = f sin\theta$ [67]. Light travelling at larger angles w.r.t. the optic axis result in a narrower pencil of light after the microscope objective. In order to conserve energy along each angular pathway, most objective lenses thus have a 1/cos(θ) apodization.

the cross-section area before by $dA_2 = dA_1 cos\theta$. Thus to conserve energy along each path, an apodization factor of $\frac{1}{cos\theta}$ is introduced [67] [94].

$$I_{BFP} \propto \frac{1}{cos\theta} |E_{emit}|^2 \tag{1.60}$$

The details of the imaging configuration and all necessary parameters are shown in

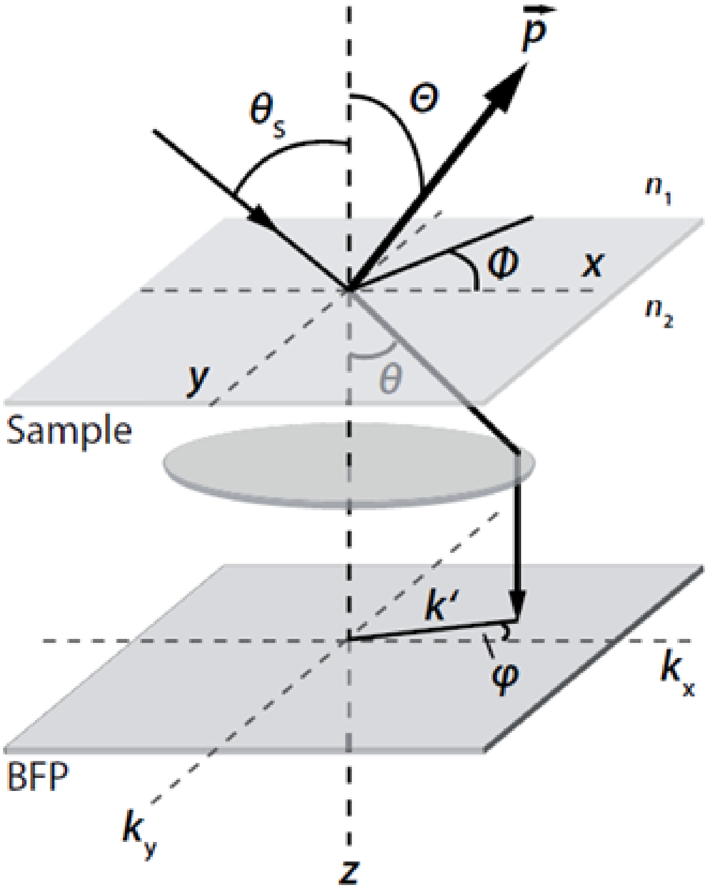

Figure 1.39: Schematic of Fourier imaging to obtain emission patterns from dipoles near a planar interface. The dipole moment is shown as $\vec{p}$ with an orientation of Θ and ϕ at the interface of media with refractive indices n_1 and n_2.

Figure 1.39. Here the dipole has an orientation of Θ and ϕ at the interface of media with refractive indices n_1 and n_2. The incidence angle θ_s is related to the emission angle θ by Snell's law. The parameter k' in the back focal plane image in Figure 1.39 is the same as parameter ρ used for the radial coordinate before. At the back focal plane, the emission angle θ is mapped to a function of k$_x$ and k$_y$. The relation between k' and θ is given by,

$$|k'| = 2\pi\frac{n_2}{\lambda}sin\theta = k_0 n_2 sin\theta \tag{1.61}$$

$$\begin{pmatrix} k'_x \\ k'_y \end{pmatrix} = \begin{pmatrix} cos\varphi \\ sin\varphi \end{pmatrix} |k'| \tag{1.62}$$

From Equation (1.60), it can be understood that the intensity distribution at the back focal plane of a microscope objective is given as the sum of contributions of both s- and p-polarized emissions.

$$I_{dipole}(\theta,\phi) \propto \frac{1}{cos\theta}\left(E_pE_p^* + E_sE_s^*\right) \tag{1.63}$$

According to reference [94], the parallel and perpendicular components of the electric field i.e. E_p and E_s are calculated as,

$$E_p = c_1(\theta)cos\Theta sin\theta + c_2(\theta)sin\Theta cos\theta cos(\varphi - \phi) \tag{1.64}$$

$$E_s = c_3(\theta)cos\Theta sin(\varphi - \phi) \tag{1.65}$$

The coefficients c_1, c_2 and c_3 are given by following expressions:

$$c_1(\theta) = (\frac{n_2}{n_1})^2\frac{cos\theta}{cos\theta_s}t_p(\theta_s)\Pi(\theta_s) \tag{1.66}$$

$$c_2(\theta) = \frac{n_2}{n_1}t_p(\theta_s)\Pi(\theta_s) \tag{1.67}$$

$$c_3(\theta) = -\frac{n_2}{n_1}\frac{cos\theta}{cos\theta_s}t_s(\theta_s)\Pi(\theta_s) \tag{1.68}$$

where the Fresnel transmission coefficients have been defined before in terms of incidence angle (θ_s) and angle in medium with refractive index n_2, and $\Pi(\theta_s)$ is given by,

$$\Pi(\theta) = e^{-ik_0n_1cos(\theta_s)\delta} \tag{1.69}$$

Based on above representation, back focal plane images can be simulated for several different orientations of the dipole as shown in Figure 1.40. The dipoles are placed on quartz-air (n_{quartz} = 1.45) interface for the calculations. A microscope objective with NA=1 collects light from the dipole and focuses it at the back focal plane. For a vertical dipole (Figure 1.40(a)), a rotationally symmetric intensity distribution is obtained with a bright ring corresponding to an angle slightly larger than the critical angle θ_{crit}. Another key feature of vertical dipole is that it does not emit in the central region of the microscope objective. The back focal plane patterns for the in-plane dipoles (1.40(b) and (c)exhibit symmetry with the symmetry axis oriented parallel to the dipole axis. In the case of in-plane dipoles, most of the radiation can be seen in the two lobes in the ring between the critical angle and the maximum angle collected by the objective.

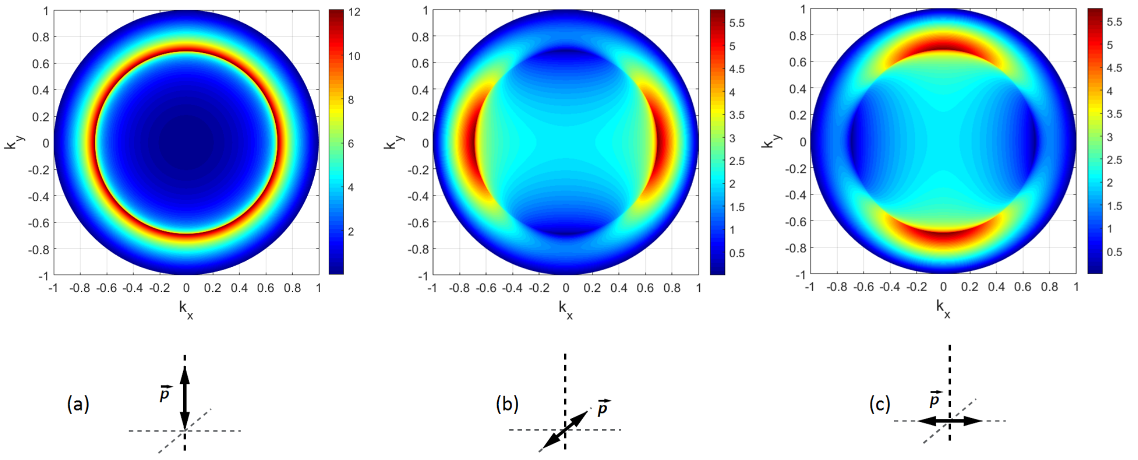

Figure 1.40: Calculated back focal plane patterns for dipoles on a glass/air interface with different orientations given below the patterns. In (a) $\phi = 0^o$ and $\Theta = 0^o$, in (b) $\phi = 0^o$ and $\Theta = 90^o$ and in (c) $\phi = 90^o$ and $\Theta = 90^o$

By imaging of the intensity distribution of the microcavity sample at the back focal plane of the objective lens, radiation travelling at angles higher than the NA of the objective can be identified/rejected as a possible cause for the observation of fewer than expected photons from the sample.

1.8 Theory of Defocused Imaging

The study of three-dimensional orientation of emission dipoles in molecules has progressed from ensemble studies to single molecules, which allows the study of properties normally obscured by ensemble averages. The studies have involved polarization optics whereby the two orthogonal polarizations are collected in different arms of a microscope. But this only allows the determination of in-plane component of the emission dipole. R.M. Dickson and colleagues demonstrated that by making use of spherical aberration in an optical imaging system, it is possible to infer complete three-dimensional orientation of the dipoles. In this approach, angle (w.r.t. the optics axis) dependent aberrations must be well-known in order to fit the images from arbitrarily oriented emitters. The light emitted at a larger angle w.r.t. the optic axis is out-of-phase to the light at shallow angle, and thus they get focused at different image planes [106]. In a separate approach, the emitter is moved towards/away from the microscope objective and the distribution of intensity in the obtained real plane image can be used to infer the complete three-dimensional orientation. This is called as defocused imaging and constitutes the results in the thesis [107].

The emission from a dipole undergoes significant changes near an interface as discussed above. J. Enderlein and colleagues make use of the integral representation of the radiation of a free electric dipole instead of the Hertz vector approach. The oscillation frequency of the dipole is taken as ω and dipole moment, electric field and magnetic field exhibit a time dependence of the form $e^{-i\omega t}$. For an electric dipole with dipole moment 'p' in a medium with refractive index of n_0 and at a distance of z above the interface, the emission configuration is shown in Figure 1.41. In the plane wave representation, the electric field of the dipole can be expressed by Equation 1.70.

$$E_D = \frac{ik_0^2}{2\pi\epsilon}\int \frac{d^2q}{k_z}\left[e_{0p}(e_{0p}.p) + e_s(e_s.p)\right] \times e^{iq.(\rho-\rho_0)+ik_z|z-z_0|} \tag{1.70}$$

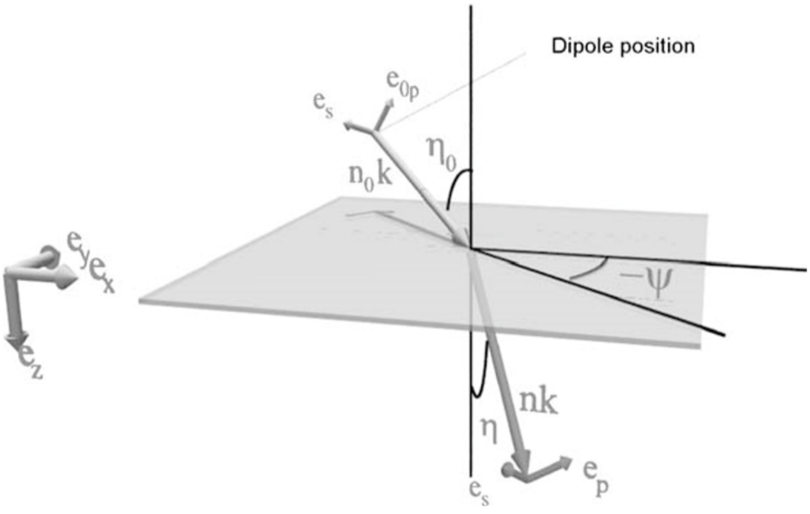

Figure 1.41: Geometry of dipole emitter at the interface of two media

In the above equation, (ρ_0, z_0) represents the coordinates of the dipole emitter and (ρ, z) represents the point at which the field is calculated. The wavevector is divided into an in-plane part 'q' and a z-component part given by k_z such that $k^2 = n_0^2k_0^2 = q^2 + k_z^2$. The unit vectors e_{0p}, e_s represent the direction of the electric field for the p-polarized and s-polarized emission. The fresnel coefficients are calculated for the interface and the reflected electric field E_R and transmitted electric field E_T can be obtained.

$$E_R = \frac{ik_0^2}{2\pi\epsilon}\int \frac{d^2q}{k_z}\left[e_{0p}R_p(e_{0p}.p) + e_sR_s(e_s.p)\right] \times e^{iq.(\rho-\rho_0)+ik_z(z+z_0)} \tag{1.71}$$

$$E_T = \frac{ik_0^2}{2\pi\epsilon}\int\frac{d^2q}{k_z}\big[e_pT_p(e_{0p}.p) + e_sT_s(e_s.p)\big] \times e^{iq.(\rho-\rho_0)+ik_zz_0+ik_{2z}|z|} \tag{1.72}$$

In the expression for the transmitted electric field E$_T$, the wavevector in the transmitted medium (lower medium in Figure 1.41) is given by $k_{2z} = \sqrt{n^2k_0^2 - |q|^2}$. The reflection and transmission coefficients at the interface of two media with refractive indices n$_0$ and n for an angle of incidence η_0 w.r.t. the optic axis are given by R_p and T_p, respectively. The expressions for the unit vectors e_{0p}, e_s and e_p are obtained as shown below.

$$\begin{aligned} e_{0p} &= (cos\psi cos\eta_0, sin\psi cos\eta_0, -sin\eta_0) \\ e_s &= (cos\psi cos\eta, sin\psi cos\eta, -sin\eta) \\ e_p &= (-sin\psi, cos\psi, 0) \end{aligned} \tag{1.73}$$

The angle of incidence and refracted angle in the lower medium are related by Snell's law i.e. $n_0sin\eta_0 = nsin\eta$. There are two orientations of the dipole that need to be considered for discussion: an orientation perpendicular/vertical to the interface and in-plane orientation. The angular distribution of radiation, E(η,ψ) in this scenario into a solid angle sinηdηdψ is shown in Equation 1.74, where β is the angle between the emission dipole axis and the optical axis.

$$E(\eta,\psi) = e_p\Bigg[cos\beta E_p^{\perp}(\eta) + sin\beta E_p^{||}(\eta)cos\psi\Bigg] + e_s sin\beta E_s^{||}(\eta)sin\psi \tag{1.74}$$

Due to self-interaction of the emission dipole with its reflected electromagnetic field at the interface, the angular distribution of radiation gets modified. The expression for the parallel and perpendicular components of the electric field in this situation are given by the following equations.

$$E_p^{\perp}(\eta) = sin\eta\Bigg[exp(-inzcos\eta) + R_p(\eta)exp(inzcos\eta)\Bigg] \tag{1.75}$$

$$E_{p,s}^{||}(\eta) = cos\eta\Bigg[exp(-inzcos\eta) \mp R_{p,s}(\eta)exp(inzcos\eta)\Bigg] \tag{1.76}$$

For the vertical dipole field, $E_p^{\perp}(\eta)$, the emission is polarized along e$_p$ in all directions and depends on the polar angle η. For the in-plane/parallel dipole orientation, the angular

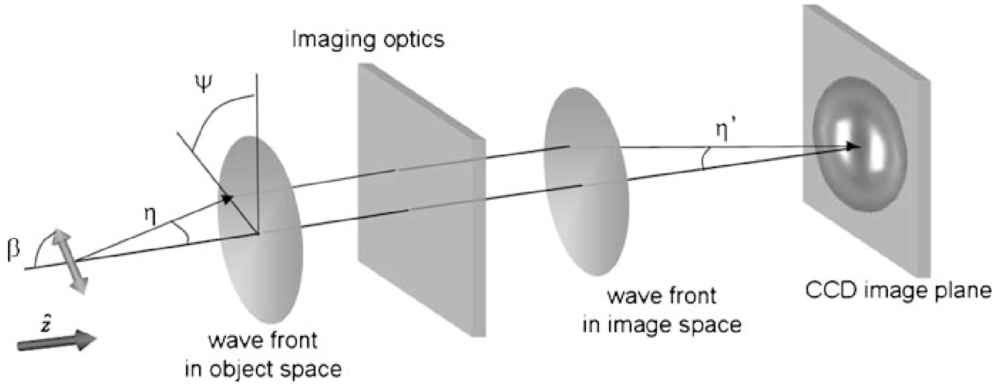

Figure 1.42: Widefield imaging of dipole emission onto a CCD camera [73]

distribution depends on the azimuthal angle ψ between the dipole orientation and direction of emission, and polar angle η. The widefield imaging configuration for imaging of dipole emission is shown in Figure 1.42. In order to express the energy density incident on the CCD camera, the electric and magnetic field amplitudes are calculated. The electric and magnetic field amplitudes in the image space are developed as a superposition of plane waves [72]. In reference [73], the electric and magnetic field on a CCD are given by the following equations.

$$E_j = \int_0^{\eta'_{max}} d\eta' sin\eta' \sqrt{\frac{n'cos\eta'}{ncos\eta}} e_j \times e^{ik\delta z cos\eta} \tag{1.77}$$

$$B_j = \int_0^{\eta'_{max}} d\eta' sin\eta' \sqrt{\frac{n'cos\eta'}{ncos\eta}} b_j \times e^{ik\delta z cos\eta} \tag{1.78}$$

where e_j corresponds to e_x and e_y, and b_j corresponds to b_x and b_y given by following expressions:

$$e_x = \frac{isin\beta}{2}\big[cos\eta'(J_0 - J_2cos2\psi)E_p^{||} + (J_0 + J_2cos2\psi)E_s^{||}\big] + in'cos\beta J_1 E_p^{\perp} cos\psi \tag{1.79}$$

$$e_y = \frac{isin\beta}{2}\big[-cos\eta' J_2 sin2\psi E_p^{||} + J_2 sin2\psi E_s^{||}\big] + in'cos\beta J_1 E_p^{\perp} sin\psi \tag{1.80}$$

$$b_x = \frac{in'sin\beta}{2}\big[J_2 sin2\psi E_p^{||} - cos\eta' J_2 sin2\psi E_s^{||}\big] - in'cos\beta J_1 E_p^{\perp} sin\psi \tag{1.81}$$

$$b_y = \frac{in'sin\beta}{2}\big[(J_0 - J_2cos2\psi)E_p^{||} + cos\eta'(J_0 + J_2cos2\psi)E_s^{||}\big] + in'cos\beta J_1 E_p^{\perp} cos\psi \tag{1.82}$$

In the above equations, n' is the refractive index of the imaging medium above the microscope objective, which is air. The Bessel functions of the first kind are represented by terms J_0, J_1 and J_2 with functional arguments of $k'\rho' sin\eta'$. The angle η and η' are connected by Abbe's sine law i.e. nsin$\eta = Mn'sin\eta'$. The expression under the square root is for conservation of energy when light travels from one medium to another. The defocusing distance δz is accounted as a phase term in theory. The z-component of the Poynting vector gives the intensity at the CCD.

$$S = \frac{c}{8\pi} e_z \dot{(} E \times B*) \tag{1.83}$$

If the above integrals with Bessel functions are denoted by F_0, F_1, F_2 in the expression for electric field and by G_0, G_1 and G_2 in the expression for magnetic field, then the expression for the fields can be written as,

$$E_x = [F_0(\rho, \delta f) \cos\beta - F_2(\rho, \delta f) \cos(2\phi - \beta)] \sin\alpha + F_1(\rho, \delta f) \cos\phi \cos\alpha \tag{1.84}$$

$$B_y = [G_0(\rho, \delta f) \cos\beta - G_2(\rho, \delta f) \cos(2\phi - \beta)] \sin\alpha + G_1(\rho, \delta f) \cos\phi \cos\alpha \tag{1.85}$$

where α is the angle between dipole and the optical axis; β is the angle between x-y projection of the dipole and x-axis; $\rho = \sqrt{x^2 + y^2}; \phi = \arctan(y/x)$ and z defines the position where the fields are calculated. The F_j and G_j contain the complete imaging properties of the optics including the defocusing as well as the modification of angular distribution of radiation when the dipole is at an interface.

The emission from quantum dot is assumed to arise from a circularly degenerate dipole (see Figure 1.43). ϕ, ω and Ω are angles between the dipole frame of reference and the lab frame of reference. For the self-assembled quantum dots and for localized excitons in WSe$_2$, κ=0 is assumed in the equation below for calculations.

$$P = \kappa I_z + (1 - \kappa)[\frac{1 + \eta}{2} I_y + \frac{1 - \eta}{2} I_x] \tag{1.86}$$

Defocused image is obtained for each orientation of the dipole i.e. a position dependent poynting vector is obtained for I_x, I_y and I_z. Depending upon the orientation of the dipole, equation 1.86 expresses the image of the dipole emission observed on the CCD. For different orientations of the dipole, different images can be obtained by controlling the

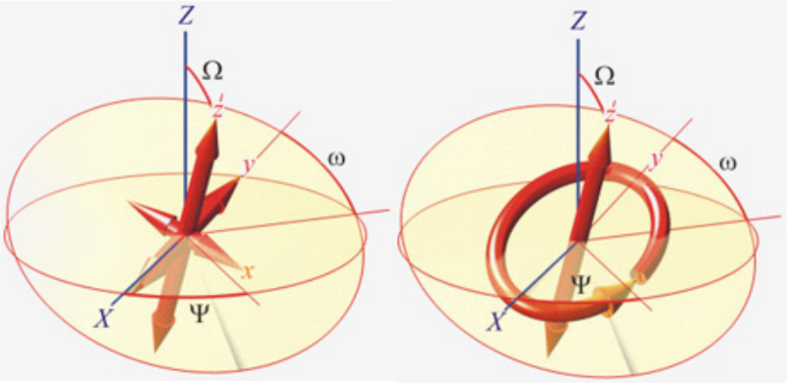

Figure 1.43: (a) A circularly degenerate in-plane dipole together with a perpendicular z-dipole and (b) three orthogonal dipole orientations for the theory of defocused imaging of emission dipole from QD [107].

parameters η and κ. The obtained expression is developed into a series over the angular coordinate ϕ,

$$P(\rho, \phi, \psi, \Omega, \omega, \kappa, \eta, \delta f) = C_0 + \sum_{m=1}^{4} (C_m \cos m\phi + S_m \sin m\phi) \tag{1.87}$$

where the coefficients C_j and S_j are expressed by the following equations:

$$\begin{aligned} C_0 = {} & (3-\kappa)F_0G_0^* + (1+\kappa)F_1G_1^* + (3-\kappa)F_2G_2^* - F_0 * G_0^* \cos 2\Psi[2(1-3\kappa)\sin^2\Omega + \\ & \eta(1-\kappa)X(3+\cos 2\Omega)\cos 2\omega] + (F_0G_0^* - F_1G_1^* + F_2G_2^*)X[(1-3\kappa)\cos 2\Omega + \\ & 2\eta(1-\kappa)\cos 2\omega \sin^2\Omega] + 4\eta(1-\kappa)F_0G_0^* \cos\Omega \sin 2\Psi \sin 2\omega \end{aligned} \tag{1.88}$$

$$\begin{aligned} C_1 = {} & -2[(2F_0 - F_2)G_1^* + F_1(2G_0^* - G_2)] \sin\Omega(\cos\Psi cos\Omega[1 - 3\kappa - \eta(1-\kappa) \\ & \cos 2\omega] + \kappa \sin\Psi \sin 2\omega) \end{aligned} \tag{1.89}$$

$$\begin{aligned} C_2 = {} & -(3-\kappa)F_2G_0^* + (1+\kappa)F_1G_1^* - (3-\kappa)F_0G_2^* + (F_2G_0^* + F_0G_2^*)\cos 2\Psi \\ & [2(1-3\kappa)\sin^2\Omega + \eta(1-\kappa)(3+\cos 2\Omega)\cos 2\omega] - (F_2G_0^* + F_1G_1^* + \\ & F_0G_2^*)X[(1-3\kappa)\cos 2\Omega + 2\eta(1-\kappa)\cos 2\omega \sin^2\Omega] - \\ & 4\eta(1-\kappa)(F_2G_0^* + +F_0G_2^*)\cos\Omega \sin 2\Psi \sin 2\omega \end{aligned} \tag{1.90}$$

$$\begin{aligned}C_3 = {} & 2(F_2G_1^* + F_1G_2^*)\sin\Omega[\cos\Psi\cos\Omega(1-3\kappa-\eta(1-\kappa)\cos 2\omega)+ \\ & \eta(1-\kappa)\sin\Psi\sin 2\omega]\end{aligned} \tag{1.91}$$

$$\begin{aligned}C_4 = {} & -F_2G_2^*(\cos 2\Psi[\eta(1-\kappa)(3+\cos 2\Omega)\cos 2\omega + 2(1-3\kappa)\sin^2\Omega]- \\ & 4\eta(1-\kappa)\cos\Omega\sin 2\Psi\sin 2\omega)\end{aligned} \tag{1.92}$$

$$\begin{aligned}S_1 = S_3 = {} & 2(F_2G_1^* + F_1G_2^*)\sin\Omega(\sin\Psi\cos\Omega[1-3\kappa-\eta(1-\kappa)\cos 2\omega]- \\ & \eta(1-\kappa)\cos\Psi\sin 2\omega)\end{aligned} \tag{1.93}$$

$$\begin{aligned}S_2 = {} & (F_2G_0^* + F_0G_2^*)(\sin 2\Psi[\eta(1-\kappa)(3+\cos 2\Omega)\cos 2\omega + 2(1-3\kappa)\sin^2\Omega]+ \\ & 4\eta(1-\kappa)\cos\Omega\cos 2\Psi\sin 2\omega)\end{aligned} \tag{1.94}$$

$$\begin{aligned}S_4 = {} & -F_2G_2^*(\sin 2\Psi[\eta(1-\kappa)(3+\cos 2\Omega)\cos 2\omega + 2(1-3\kappa)\sin^2\Omega]+ \\ & 4\eta(1-\kappa)\cos\Omega\cos 2\Psi\sin 2\omega)\end{aligned} \tag{1.95}$$

Based on the above model, defocused imaging patterns can be calculated for dipole emitters in any sample. In reference [107], the patterns obtained from CdSe nanocrystals when the sample is defocused towards the objective lens. The experimentally acquired images (left panel) are shown together with calculated patterns (right panel) in Figure 1.44.

The light from quantum emitters is collected and collimated by the microscope objective and then focused (using a lens with NA=0.15) into a single mode optical fibre. By making use of the theory of widefield imaging, the intensity distribution of the light that couples into the fibre can be calculated and an overlap can be obtained between the real plane pattern and the gaussian profile of the fibre to calculate coupling efficiency.

1.9 Summary

The goal of this thesis has been to study the emission from self-assembled InAs quantum dots in two kinds of cavities viz. photonic nanowires and planar membrane cavities. While

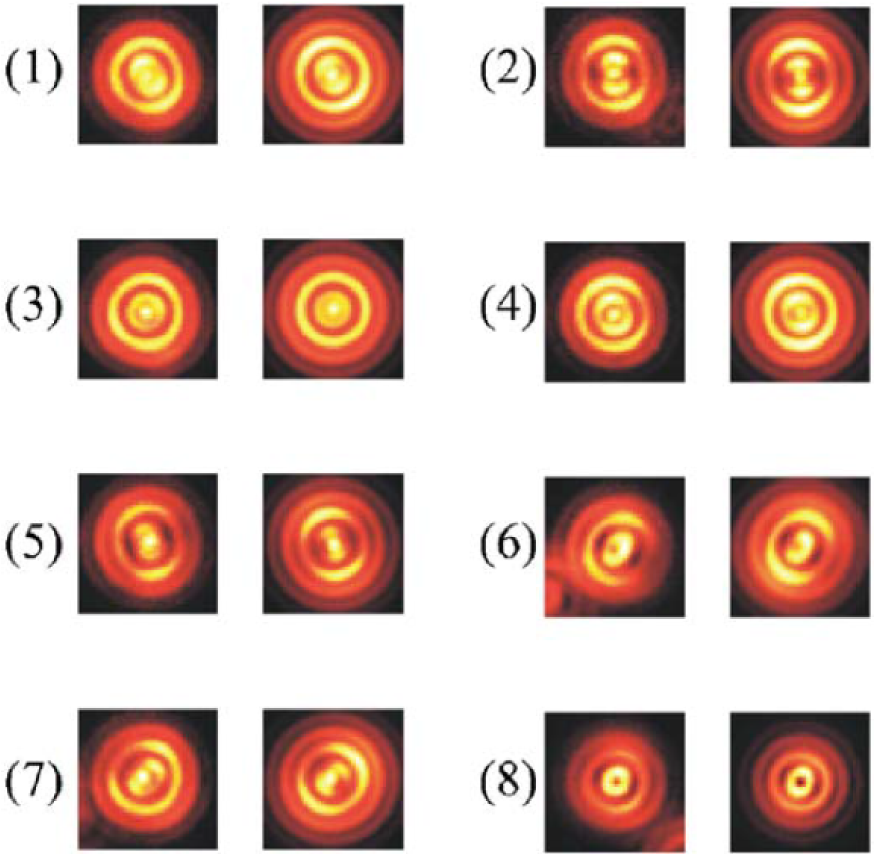

Figure 1.44: Calculated defocused images for emission from CdSe nanocrystals: (1) $\Omega = 87^o, \omega = 0^o, \Psi = 30^o, \kappa = 0.62, \eta = 0.81, \delta f = 1.2\mu$m; (2) $\Omega = 90^o, \omega = 4^o, \Psi = -173^o, \kappa = 1, \eta = 0.82, \delta f = 1.2\mu$m; (3) $\Omega = 2^o, \omega = 0^o, \Psi = -140^o, \kappa = 0.04, \eta = 0, \delta f = 1.21\mu$m; (4) $\Omega = 1^o, \omega = 48^o, \Psi = 155^o, \kappa = 0.24, \eta = 0, \delta f = 1.21\mu$m; (5) $\Omega = 87^o, \omega = 173^o, \Psi = -160^o, \kappa = 1, \eta = 0.80, \delta f = 1.25\mu$m; (6) $\Omega = 84^o, \omega = 69^o, \Psi = 149^o, \kappa = 0.44, \eta = 0.70, \delta f = 1.22\mu$m; (7) $\Omega = 82^o, \omega = 12^o, \Psi = -47^o, \kappa = 1, \eta = 0.72, \delta f = 1.22\mu$m; (8) $\Omega = 90^o, \omega = 60^o, \Psi = -113^o, \kappa = 0.16, \eta = 0, \delta f = 0.95\mu$m; (9) $\Omega = 87^o, \omega = 15^o, \Psi = -32^o, \kappa = 1, \eta = 0.74, \delta f = 1.1\mu$m; (10) $\Omega = 84^o, \omega = 3^o, \Psi = -122^o, \kappa = 1, \eta = 0.72, \delta f = 1.18\mu$m [107].

the global intention is to enhance the collection efficiency of photons from quantum emitters, angle resolved microscopy (k-space imaging) and defocused imaging have also been undertaken to unravel the possible mechanisms for loss of half the photons (i.e. 50%) from these emitters in the planar membrane device discussed in Chapter 2. In Chapter 3, single quantum dots in nanowires are studied via photoluminescence spectroscopy to determine the efficiency of photon emission, to demonstrate large strain tuning of the emission wavelength by integration on a piezoelectric substrate. Chapter 4 entails the angle resolved study of single quantum dots in bare GaAs and planar dielectric cavities to study the angular distribution of radiation in collection half-space. Numerical simulations have been carried out to study the match between theory and experiment as well. The motivation for this Chapter is to account for the correspondence between designed angular distribution of radiation and experimentally obtained patterns. Defocused imaging is a technique to determine orientation of dipoles buried in substrate and is carried out on InAs quantum dot samples in Chapter 5. From the obtained real plane images, efficiency of photon collection can be calculated. The effect of the relatives angles between the dipole frame and the lab frame on the collection efficiency are also investigated theoretically. In Chapter 6, two-dimensional excitons and localized excitons in WSe_2 are experimentally investigated for their back focal plane radiation pattern and real plane defocused images. Since little is known about localized emitters in WSe_2, the obtained images and match with theory can shed light on the nature of dipole emission in monolayer of transition metal dichalcogenides.

Chapter 2

Samples and Experimental Setup

This chapter describes the samples and experimental setups used in this thesis. Different microscope heads were assembled for quantum dot experiments and for excitons in WSe_2. Quantum dot samples were fabricated in Sheffield (UK) and Santa Barbara (USA). Processing of electrical contacts on the planar microcavity sample was done by Y. Ma at Heriot-Watt University. Monolayers of WSe_2 were exfoliated and transferred to SiO_2/Si and PMMA/Au substrate by A. Branny. Nanowires were etched by P. Kremer.

2.1 Quantum Dot Samples

All the quantum dot samples used in this thesis have a layer of self-assembled InAs quantum dots embedded in a GaAs wafer. These quantum dots are typically 3 nm - 7 nm in height and 15 nm - 20 nm in lateral direction. Quantum dots in bulk GaAs wafer (Sample 060726B) was grown by Brian Gerardot at the University of California Santa Barbara in USA. The planar dielectric cavity sample VN2455 was grown by Edmund Clarke at the University of Sheffield in UK. The quantum dots are inside a charge-tunable device, which has a heavily doped layer as an ohmic contact and a metal Schottky contact [109] [110] [111]. This allows the deterministic control over number of charge carriers in the quantum dots. When the electric field is applied across the quantum dot, the excitonic emission shifts in wavelength due to quantum confined stark effect. There is a superlattice of AlAs/GaAs between the quantum dot layer and the Schottky contact in order to prevent the carriers from leaking out of the heterostructure. Due to the small size of quantum dots, single electron/hole charging is easily observable from charge tunable samples at 4K. Spectroscopy and microscopy techniques used in this research rely on experiments conducted on single quantum dots.

2.1.1. Quantum Dots in Bulk GaAs Wafer

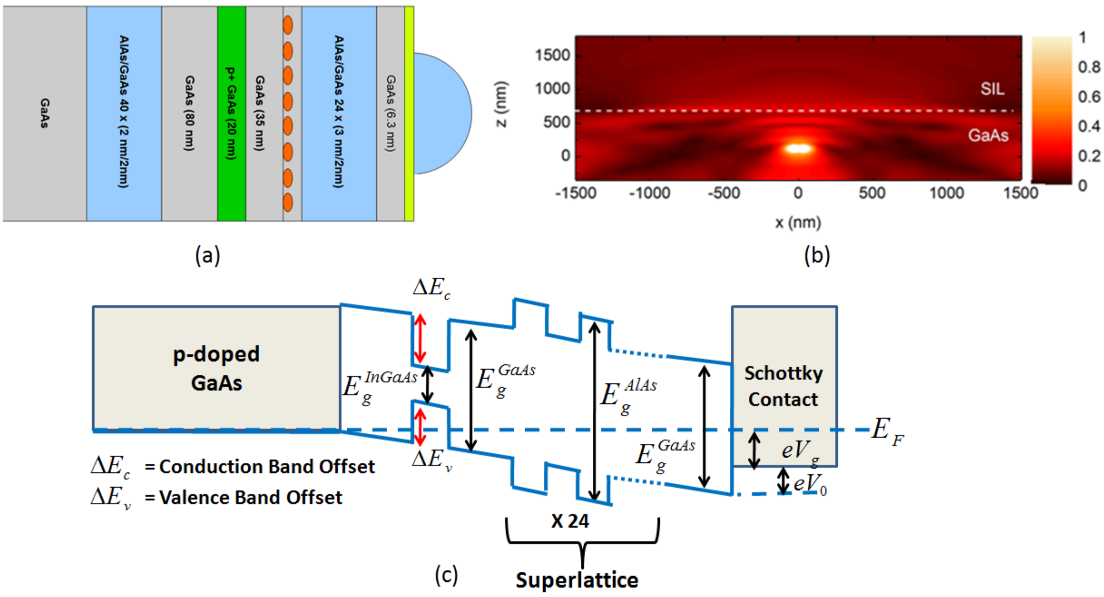

Figure 2.1: (a) Schematic diagram of the quantum dots in GaAs sample shows quantum dots in bulk GaAs are at a distance h = 136.5 nm from the solid immersion lens (SIL)-GaAs interface, (b) FDTD simulation shows that despite addition of SIL, most of the emission is confined within the sample [picture courtesy: Y. Ma], (c) electrons and holes are confined in the heterostructure region shown in the diagram. AlAs/GaAs superlattice acts as a blocking layer. Gate voltage is applied between the metal Schottky contact and the p-doped GaAs layer.

Quantum dots in p-doped bulk GaAs sample have electrical gates on them for controlling the number of electrons in the quantum dots. In bulk GaAs sample, the Nickle-Chrome Schottky-gate is deposited using an electron beam evaporator. The thickness of Ni-Cr gate is ∼3nm on the top surface of the sample. A hemispherical glass solid immersion lens (h-SIL) [112] is placed firmly on the sample. Using a lock-in amplifier, an oscillating voltage of frequency 130 Hz and peak-to-peak amplitude of 10 mV is applied between the top and back contacts. The current and phase are measured: the current 90^o out of phase with the voltage is determined by the capacitance of the device.

A schematic diagram of the quantum dots in bulk GaAs sample shows quantum dots are buried in the GaAs substrate at a distance of h = 136.5 nm from the interface. This distance corresponds to $h = m\lambda/2n_{GaAs}$ for m=1, λ=950nm and n$_{GaAs}$ = 3.48 i.e. the distance satisfies the condition of constructive interference. The addition of SIL allows the increase

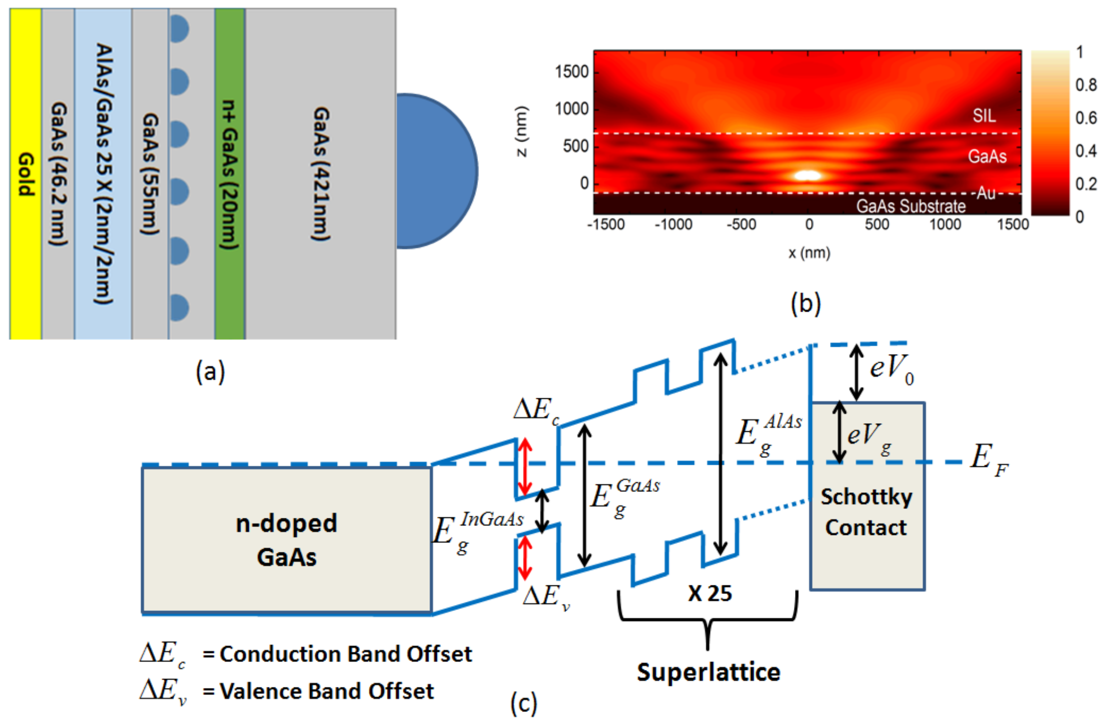

Figure 2.2: (a) Quantum dots in planar μ-cavity sample is at a distance of 471 nm from the top SIL-GaAs interface. A solid immersion lens (SIL) is added to improve the collection efficiency of photons, (b) FDTD simulation of the device with gold mirror shows a photon collection efficiency of 27% from the sample. The cavity is a 5^{th} order cavity and the standing waves in the sample can be seen in the GaAs layer in the FDTD simulation (Figure from Y. Ma). (c) Heterostructure diagram shows the Fermi level as a function of gate voltage applied between n+ GaAs Ohmic contact and the metal Schottky contact. Excitons are confined in the heterostructure region.

in effective numerical aperture of the microscope objective ($NA_{eff} = n_{SIL}NA_{objective}$, where n$_{SIL}$=2) and increases the photon collection by a factor of 4 [113]. As shown in Figure 2.1, despite the addition of SIL, FDTD simulation shows that a large fraction of the light from the quantum dot is confined in the substrate. As discussed in Chapter 1, photon collection efficiency of 1.75% is expected for bulk GaAs sample with SIL.

2.1.2. Planar Microcavity for Quantum Dots

Planar microcavity embedded with quantum dots (sample vn2455) was designed and fabricated by Dr Y. Ma at Heriot-Watt University [115] [116]. The quantum dots were grown in the GaAs wafer by Dr. E. Clarke at Sheffield University (UK) for planar dielectic sample VN2455. The thickness is much lesser than the p-doped bulk GaAs sample and is chosen to satisfy the condition of constructive interference in the upward direction. This increases the out-coupling efficiency of sample from the ∼1.75% expected from bulk p-doped GaAs sample with SIL to ∼27% for a 5th order microcavity (see the section on planar microcavity in Chapter 1). The gold mirror also acts as a Schottky contact in this sample. The AlAs/GaAs superlattice acts as the electron blocking layer and prevents carriers from travelling to the gold schottky contact.

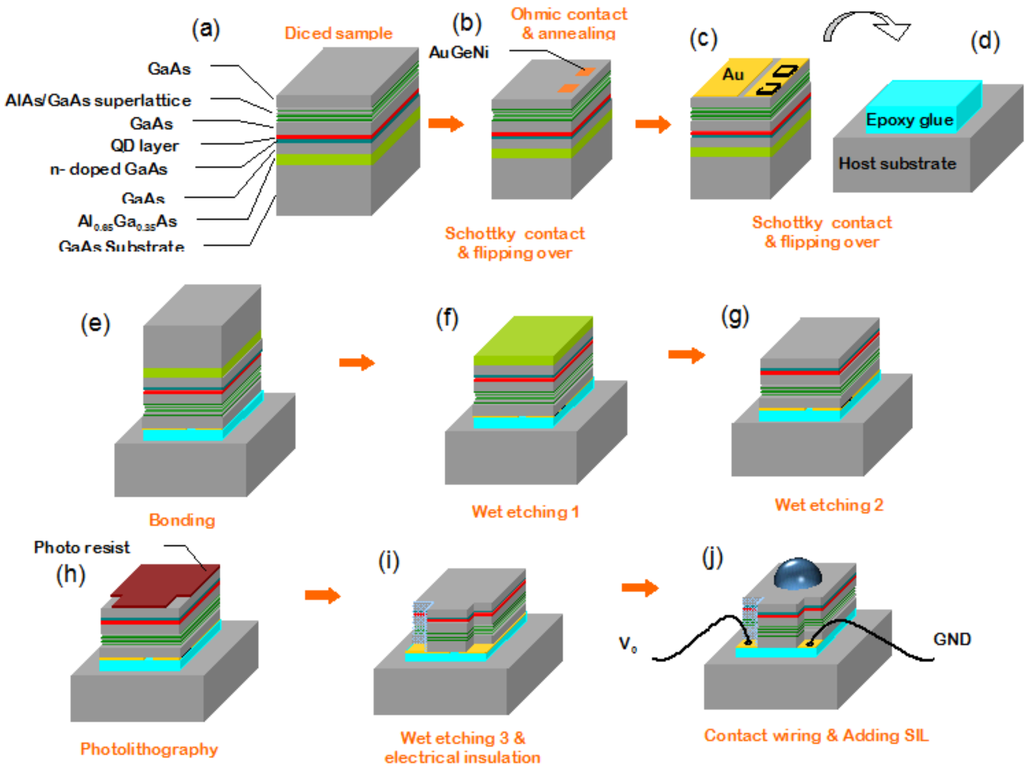

Figure 2.3: Fabrication steps from bulk sample to planar cavity sample: (a) 100 nm of AuGeNi is deposited and the sample is annealed at 400°C to create an Ohmic contact with the n-doped layer; (b) 150 nm Au layer is deposited as Schottky contact and rear mirror,(c) the sample is flipped and transferred to a host substrate using an epoxy glue and compression, (d) selective etching of the bonded sample is carried out to remove GaAs substrate and AlGaAs sacrificial layer of the QD sample in sequence; (e) access areas for both contacts are selectively teched, (f) silver paint is used to make wire contacts to the sample (Figure from Y. Ma).

The schematic diagram of the sample shows a layer of quantum dots at a distance h = 471 nm from the top interface (see Figure 2.2(a)). The device is a 5^{th} order cavity due to the chosen cavity width. In Chapter 1, the distances 'd' and 'h' were chosen to correspond to the brightest resonance for emission in cavity. There were two mirror configurations simulated for the geometry. Alternate layers of AlAs and GaAs with a thickness of λ/4n each provide a good mirror (distributed Bragg reflector) however it was observed that at higher angles the light was leaking out from the bottom side. On the contrary, gold mirror shows $> 95\%$ reflection for all wavelengths at all angles of incidence as shown in the FDTD simulation. Gold also acts as the schottky contact and eliminates the need of placing a top semi-transparent electrode like NiCr in the case of bare GaAs sample, which compromised the transmission of photons from bulk GaAs sample.

Based on these design criteria and the ones specified in Chapter 1 [114] [115], the step-by-step fabrication method has been outlined in the following Figure 2.3. The fabrication process consists of depositing and annealing AuGeNi in order to make the ohmic contacts with the n-doped layer, depositing a gold layer which acts as the back-mirror and Schottky contact, flipping it on to a host surface containing epoxy glue and wet etching the GaAs substrate and the $Al_{0.65}Ga_{0.35}As$ layer. Then the Au layer is made accessible by photolithography and wet etching. Current and phase measurements are carried out using a lock-in-amplifier on the samples. A functional charge tunable planar dielectric sample has a current around $\sim$60nA and a phase around 85^o.

2.1.3. Nanowire Embedded with Quantum Dots

Nanowire samples were etched by P.E Kremer at the nanofabrication facility at Heriot-Watt University. The design aspects of the nanowire were chosen from reference [117] [118]. The top-down fabrication procedure started with a wafer of GaAs with a layer of InAs quantum dots in it. A 100 nm thick layer of gold was deposited on the wafer by thermal evaporation. The substrate is then flipped with gold facing downwards and bonded to a host wafer of GaAs by applying a pressure of 8MPa at a temperature of 300^oC from above. Thereafter, the AlGaAs layer is removed by wet chemical etching with HF. Next, the e-beam lithography step is used to deposit 100 nm of MMA and 100 nm of PMMA polymer. A mask of 90 nm thick Nickel is deposited and PMMA is removed. On dry etching, tall and narrow nanopillars are obtained. The schematic of the whole fabrication process is shown in Figure 2.4 [119].

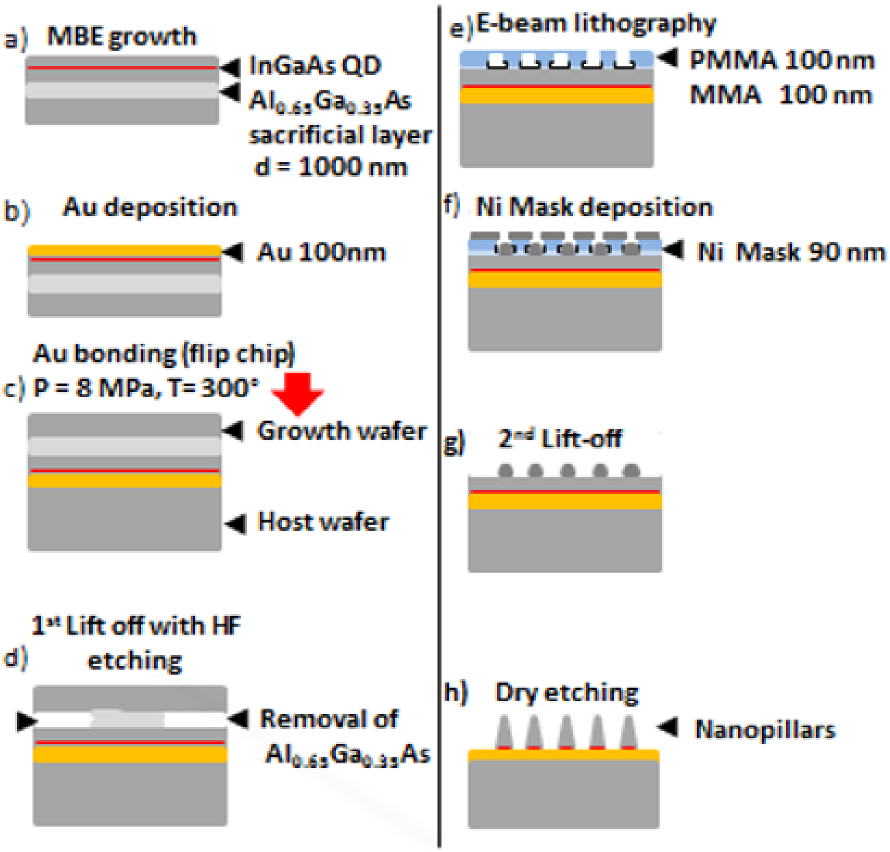

Figure 2.4: Fabrication steps of the nanowire: (a) A sample consisting of self-assembled InGaAs quantum dots with a 110nm-thick capping layer and embedded in a 2μm GaAs layer on an $Al_{0.65}Ga_{0.35}As$ sacrificial-etch layer is grown by MBE. (b) A 100 nm thick Au back mirror is deposited. (c) Following a flip-chip process, the Au layer is attached to the Au-coated PMN-PT crystal using thermo-compression bonding (T = 300^{o}C and P = 2 MPa). (d) Hydrochloric acid at T =0^{o}C is used to selectively etch the $Al_{0.65}Ga_{0.35}As$ layer. (e) Electron beam lithography is used to define circular apertures of the desired radius. (f) 90 nm of Ni is deposited followed by (g) lift-off and (f) dry etching of nanowires (Figure from P. Kremer).

2.2 Two-Dimensional Semiconductor Samples

Following the footsteps of research on graphene, TMD monolayers are mechanically exfoliated using a scotch tape. Mechanical exfoliation, however, produces inhomogeneous flakes i.e. of different sizes and thicknesses at random positions on the substrate. The monolayer in the flake is identified via optical contrast [120] in reflection or transmission mode. The contrast from a monolayer is much lower than that from bilayer.

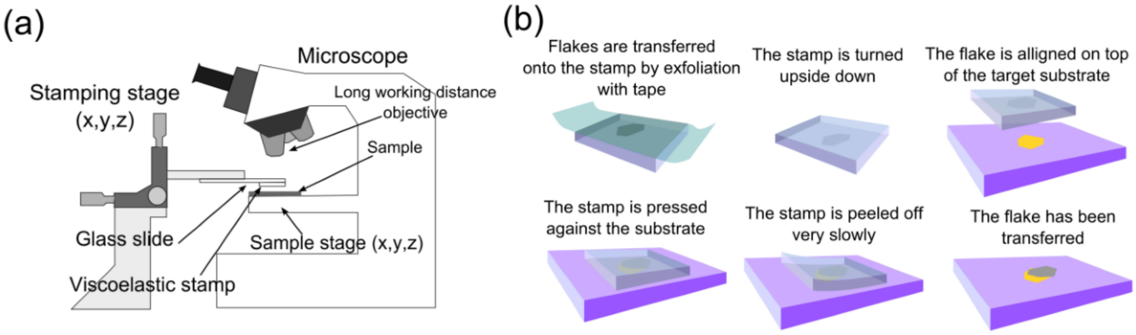

Figure 2.5: Mechanical exfoliation of WSe_2 monolayer from bulk crystal and transfer to substrate of choice by use of a PDMS stamp (taken from reference [120]).

Adoption of a dry transfer method can allow deterministic positioning on the substrate. The stamp used for this technique is a layer of commercially available viscoelastic film (Gelfilm from Gelpak) which is adhered to a glass slide in order to handle it easily. The 2D-TMD crystals to be transferred are deposited onto the viscoelastic layer by mechanical exfoliation of the bulk crystal with Nitto tape as shown in Figure 2.5. The substrate is stuck with double-sided tape on a fixed surface, and the stamp is then attached to the three axis manipulator with the flake facing towards the new substrate. The flakes are then transferred by applying a little pressure on the stamp and subsequent slow peel-off. This is a mature technique of transferring flakes to any substrate in a deterministic way. The full outline of the transfer process is shown in Figure 2.5 and can be seen in much greater detail in reference [120].

2.3 Confocal Microscopy

The intensity pattern at the focus of a lens is called the point-spread function which defines the resolution of an optical microscope. Light distribution at the focus of a lens arises from

Fraunhofer diffraction from the aperture of the lens. The full description of diffraction of wavelets from circular aperture is in section 8.5 of the book by Born and Wolf [125]. For the purpose of the thesis, it is sufficient to express the intensity at the focal point along the optic axis and transverse to it. Along the focal plane, the expression is shown as below and is called the airy disc pattern.

$$I(\rho, z=0) = \left(\frac{2J_1(\rho)}{\rho}\right)^2 I_0 \tag{2.1}$$

where ρ is the reduced radial coordinate such that $\rho = \frac{2\pi}{\lambda} r\mathrm{NA}$. The z-coordinate is similarly transformed by $\zeta == \frac{2\pi}{n\lambda} zNA^2$. The intensity along the axis is thus expressed by,

$$I(\rho=0, \zeta) = \left(\frac{sin\zeta/4}{\zeta/4}\right)^2 I_0 \tag{2.2}$$

Two adjacent points are said to be just resolved when the centers of the airy disc patterns are separated by a distance equal to the radius of the central disc in the Airy pattern. This is the Rayleigh Criterion for optical resolution. Following the Rayleigh Criterion, a dip is observed between two resolvable Airy functions. In contrast, the Sparrow Criterion requires no dip at the centre of the two Airy patterns. A constant level of intensity of maintained between the two Airy functions. This gives the value of r = 0.47λ/NA$_{objective}$ and is closer to the Abbe limit of resolution i.e. $0.5\lambda/NA_{objective}$.

While the resolution does not change, confocal optical microscopy allows imaging of samples with high contrast. The imaging configuration collects light from a focal volume determined by the numerical aperture of the microscope objective. By having a pin-hole in the image space in the form of a single mode optical fibre, a large sample can be imaged by scanning the sample in the focus of the microscope objective. When a pinhole is placed at the focus (focal point of object of interest) in the image plane, signal from the out of focus object is drastically reduced. This is the essence of confocal microscopy that selection of light from one point is made while light from all other points is rejected. This reduction in background leads to high contrast (signal to noise) in confocal microscopy.

Based on above benefits, a confocal microscope was assembled from mechanical and optical components acquired from Thorlabs as shown in Figure 2.6. Single mode optical fibres HP780 from Thorlabs acted as the pinhole for illumination and collection. The numerical aperture of lens 3 was 0.68 for quantum dot samples and 0.82 for emitters in WSe$_2$. The NA of lens 1 and lens 2 are 0.15 to match with the NA of the single mode fibre. Or-

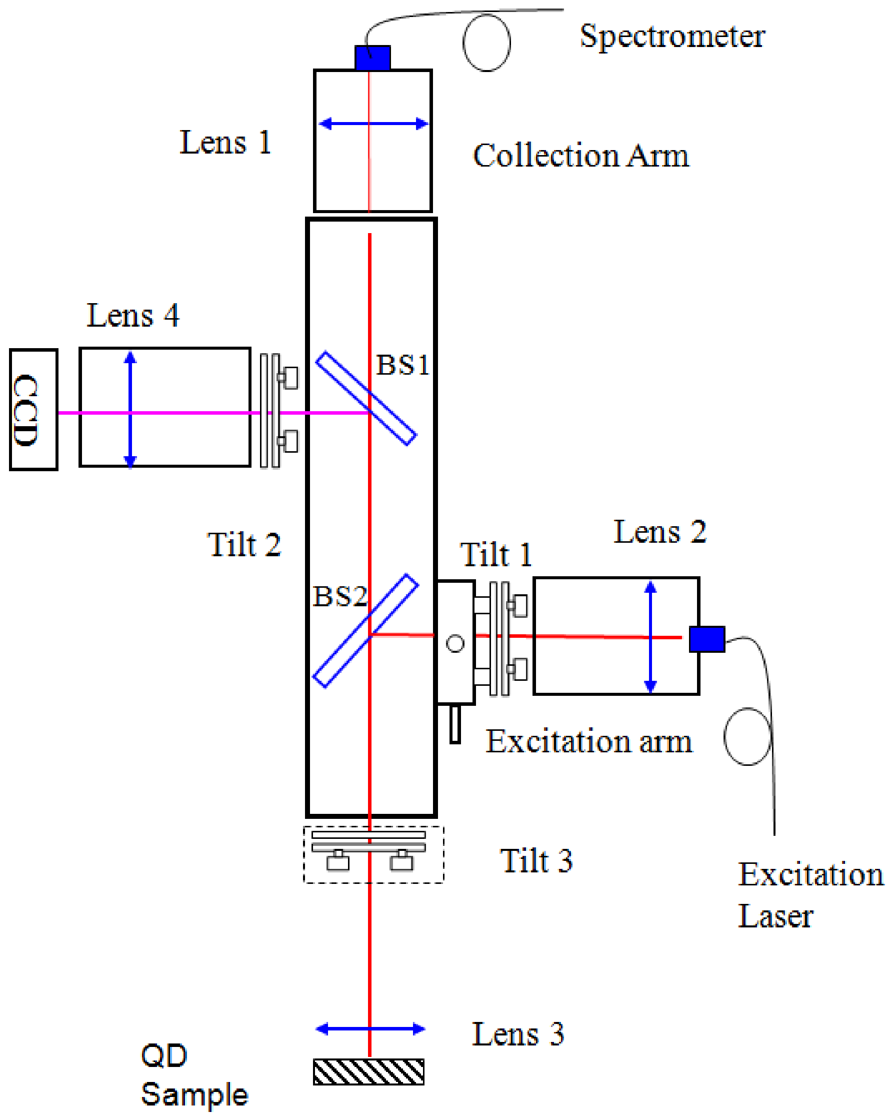

Figure 2.6: Schematic diagram of the confocal microscope. Lens1,2: C280TME-B (NA=0.15) from Thorlabs, Lens3: C330TME-B (NA=0.68) from Thorlabs, Lens4: achromat doublet AC254-75B-ML from Thorlabs, BS 1,2: Glass Beamspliter uncoated WG-11050 from Thorlabs

dinary NBK7 glass-plates were used as beam splitters to direct side-illumination on to the sample. The part of the microscope under tilt 3 stage is a separate unit which is mounted inside the cryostat. Thus tilt stage 3 allows to reduce any beam tilts between the top of the microscope and bottom of it. The excitation arm and collection arms are separately centered and collimated on an optical table using a CCD camera. In order to fix the position of the beam splitters BS2, collimated light from excitation arm is sent down the microscope and centered by maximising the light transmission via two narrow irises. There are two beams that travel downwards in the microscope due to reflection from the front and back surfaces of the beamsplitter BS2, thus care has to be taken to allow the beam reflected from the first surface to be centered down the microscope. Once the beamsplitter BS2 is aligned at 45^o to the excitation arm, the top surface of beamsplitter BS1 is centered by sending light down the collection arm. The two beamsplitters compensate for the beam walk-off that would be experienced by light travelling downwards from the collection arm. A CCD camera with Sony chip ICX829AL together with an achromatic lens AC254-100-B-ML is used to make sure that the illumination spots from the collection and excitation arms overlap, and are symmetric in and out of focus.

Thus, using the shown confocal microscope one can carry out the spectroscopy of single quantum dots in GaAs and localized excitons in WSe_2. The cryostat friendly confocal microscope was found to be very stable and could stay on the same quantum dot for more than two weeks at once. In order to measure the diffraction-limited response of the microscope, a checkerboard with transparent and opaque Aluminium squares with each square 10μm in size is placed at the focus of the confocal microscope. The checkerboard is mounted on a x-y scanner on top of x-, y-, z-nanopositioners. A silicon photodetector is integrated under the scanner to measure the transmitted power. When the transparent half is in focus, the transmission is high and the transmission drops when the detector is under the opaque Aluminium square. By taking the derivative of the transmission and calculating the full-width at half maximum of the peaks as shown in Figure 2.7, resolution of the microscope is determined. A resolution of $\sim$750 nm was obtained by Dr. Paul Dalgarno using an illumination wavelength of 950 nm for unity magnification of the microscope. The theoretical diffraction limit for NA = 0.65 and 950 nm wavelength is 780 nm.

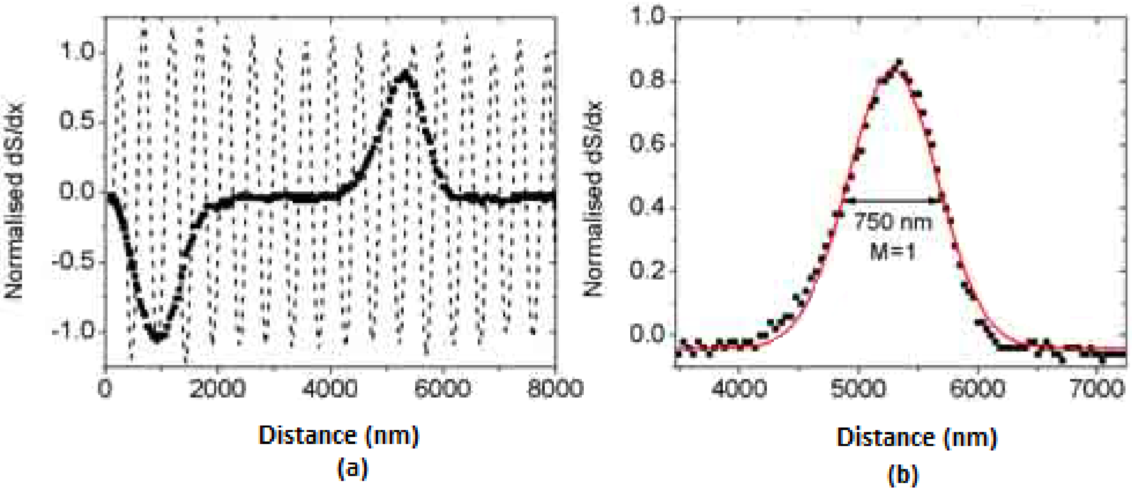

Figure 2.7: The data points correspond to the profile of the focused Gaussian spot. During the movement of the scanner, two interfaces from the 10 μm period grating are traversed. The reflection of the peaks correspond to traveling from Aluminium layer to glass and glass to the Aluminium respectively. b) Zoomed-in image of the second peak from (a) shown with a fitted Gaussian profile. The FWHM of the Gaussian is 750 nm, which can be compared directly to the theoretical diffraction limit of 780 nm. M corresponds to the magnification of the system, which in the absence of any solid immersion lens is 1 [123].

2.4 Cryostat

As the experiments to be performed are extremely sensitive to thermal effects such as inhomogeneous broadening of the quantum dot emission due to phonon interactions, the sample must be cooled to cryogenic temperatures. The effect of a single electron charging of the quantum dot, quantum confined stark shift in emission energy and the capability to isolate single quantum emitters can only be achieved when the sample is cooled at liquid Helium temperatures in a cryostat.

A closed-cycle pulse-tube cryostat (attocube attoDRY1000) was used [121] to cool down the samples for experiment. This cycles helium using a compressor to keep the contents of the cryostat at or below liquid helium temperatures (in practice, a sample temperature of $\sim$ 3.6K is usual). The outer tube of the cryostat is flushed with Helium gas while the microscope tube is lowered into it to prevent any moisture condensing on the walls of the outer tube, and the tube is then sealed and the sample allowed to cool down to operating temperatures. The temperature inside the cryostat and of the outer tube are measured by two calibrated cernox sensors. The temperature inside the sample tube is measured by the sensor underneath the sample. The temperature controller is from Lakeshore Model 335 and measures the temperature by using two sensor leads.

The cryostat is placed on wooden platform designed to neutralize the effect of vibrations. In experiment, this allows the ability to carry out measurement on a single quantum dot for extended periods of time. The microscope stick carrying the sample is attached to the sample tube only at the top which helps in isolation from vibrations coming from the cold plate. The sample is mounted on top of x-, y-, z- nanopositioners from Attocube Systems. The whole sample-nanopositioner assembly sits on top of a cage plate which is securely attached to the microscope stick via cage roads. The microscope objective (C330-TME-B from Thorlabs, 0.68NA or attoDRY 50X, 0.82NA is used) is mounted on a cage plate in close proximity to the sample. Care has to be taken while placing the objective close to the sample as during the cooling process the entire microscope assembly contracts. The microscope head (shown in Figure 2.6) rests on top of the cage plate of the microscope stick and is attached firmly via threaded screws. The microscope assembly is placed inside a sample tube, which is pumped to a high vacuum ($< 5 \times 10^{-5}$ mbar) using an Oerlikon dry vacuum pump. A small volume of helium 2 is introduced into the tube as an exchange gas (to a pressure of $\sim$ 100 mbar for the bare sample). The microscope stick has an anti-reflection coating window at at the top in line with the microscope head. For experiments with nanowire embedded quantum dots, a transparent window from Thorlabs was used as it requires white light imaging to identify the position on the sample. For planar samples, a near infra-red coated window was used. Once the sample tube is vacuumed and exchange gas is put in, the sample tube is mounted inside the cryostat while maintaining an overpressure of helium as the transfer gas because no amount of air/moisture should get inside the cryostat. Typically, a pressure of 2 bar is maintained for helium for planting the tube in or for taking it out of the cryostat for warming up after an experiment. The x-,y-,z-nanopositioners and the sample are electrically grounded during the process of cooling down and warming up.

The closed-cycle cryostat also incorporates a 9-Tesla superconducting magnet which can be used to apply a magnetic field to the samples parallel to the growth axis, and so for this reason all of the components of the microscope and sample assembly are non-magnetic. A Cryomagnetics 4G Superconducting Magnet Power Supply is used for controlling the magnet.

2.5 Nanopositioners and Scanners

For the movement of the sample w.r.t. the focus of the objective lens, the sample is mounted on precision motion x-,y-,z-nanopositioner. The positioners were acquired from Attocube systems. The x- and y-positioners were ANPx101/ANPx102 mounted along mutually orthogonal directions. The z-motor was ANPz101/ANPz102 which allowed to bring the emitters in focus w.r.t. the microscope objective lens. The positioners are connected to the microscope stick via pin connector cables, where the pin sockets are linked with connections built on the top of the microscope stick.

For use at 4K and high magnetic fields, the material of the positioners is chosen to be titanium. The travel range of each ANPx101 stage is 5 mm and the minimum step size is of the order of 10s of nm. The safe voltage range that can be applied to these positioners are between 0-70V at 4K. The frequency for continuous motion has to be below 1000Hz. A working positioner has a capacitance of $\sim$980nF at room temperature and around 140nF when cold below 4K. Two dimensional movement can also be achieved by using x-y-scanners ANSxy100 from Attocube systems. The resolution of movement is at least an order of magnitude (subnanometer) better than with nanopositioners. Scanners are useful in generating a space map of emitters in WSe_2 as the monolayer flakes are often smaller in size compared to the range of motion of these scanners (typically 10μm $\times 10\mu$m).

2.5.1. Excitation Laser

For non-resonant photoluminescence spectroscopy, a laser diode at 830nm was used for quantum dots. For alignment at a wavelength of 950nm, an external cavity diode laser from Toptica model number DLPro940 was used. This is a tunable laser with wavelength tunability from 910 nm to 980 nm. The wavelength can be tuned manually for long wavelength changes and via a voltage tuning of a piezoelectric element in the laser cavity for fine changes. A laser from Sacher which has a motor-controlled external cavity is used too (model number Sacher Lasertechnik Motorized Lion Littman/Metcalf ECDL TEC-500-0960-030-M) which has a tunability between 920nm - 980 nm.

The light from the lasers are coupled into single mode optical fibres via collimation and coupling lenses. There is a quarter wave plate and a half wave plate on rotation mount to control the polarization of light getting coupled into the microscope head. A High Finesse wavemeter with incorporated PID controller is connected to the Sacher and Toptica lasers to control and lock their wavelength with an accuracy of 0.001nm.

2.5.2. Photoluminescence Spectroscopy

For photoluminescence spectroscopy, the excitation laser at 830nm is sent down from the excitation arm for quantum dots in GaAs. A green laser at 532nm is used for excitation of excitons in tungsten diselenide monolayers. The microscope setup has been already shown in Figure 2.6.

The light emitted from quantum emitters is collected at the top of the microscope using a single mode fibre and is made incident on a grating spectrometer from Acton SpectraPro-500i to analyse its spectral properties. The spectrometer has a liquid nitrogen cooled silicon CCD and a turret with three gratings: 300 lines/mm, 1200 lines/mm and 1800 lines/mm. The 1800 lines/mm grating provides the highest resolution of $\sim 35\mu$eV. Light from quantum dots is incident through the entrance slit and is guided on to the CCD via reflections from the chosen grating and two highly reflective mirrors.

The light from the single mode fibre at the entrance of the spectrometer is collimated using a C280TME-B aspheric lens and then an achromatic doublet with a focal length of 75 cm was used to focus on the CCD. In order to get rid of any excitation laser scattering, a long pass filter at 900 nm was used for quantum dot measurements and a notch filter at 532 nm together with a long-pass filter at 600nm was used for experiments with monolayers of WSe_2. All spectra were obtained through the 1800 lines/mm grating on to the CCD for maximum resolution possible. The detector array for silicon CCD is 1340×100 with each pixel being 20μm $\times$ 20μm.

Under non-resonant excitation, the bandstructure of In(Ga)As quantum dot in GaAs is shown in Figure 2.8. The host material GaAs is shown in red, the wetting layer is shown in blue. The bandgap of the wetting layer is higher than that of quantum dots. When excited non-resonantly, carriers are generated in the GaAs layer and relax to the lowest energetic state called s-shell. Exciton recombination only occurs between s-shell particles or p-shell particles due to selection rules. While a large spectral separation between the excitation and emission wavelength makes non-resonant excitation easier to filter out, the time jitter in s-shell emission reduces the indistinguishability of photons [126].

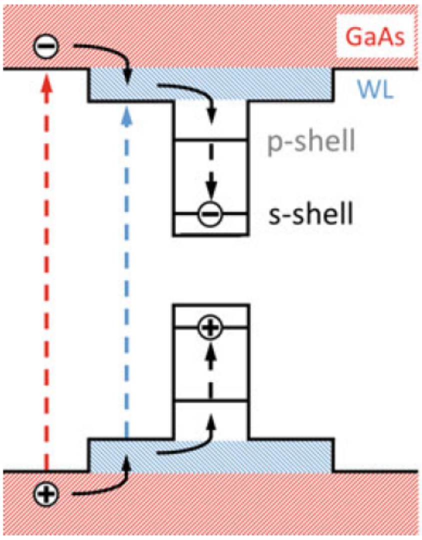

Figure 2.8: Sketch of the bandstructure of In(Ga)As QD hosted in GaAs under non-resonant excitation (taken from reference [126])

2.6 Optical Bandpass Filter

The bandpass filters used for spectral filtering of InAs quantum dot emission is acquired from Andover. These typically have a narrowpass wavelength range of around 1 nm. For one of the bandpass filters at 955 nm (model no. ANDV9415), the transmission at the peak wavelength was measured to be >80% with a measured filter bandwidth of around 1 nm. When the filter is rotated in the out-of-plane direction, the peak wavelength of transmission shifts to lower wavelength and the transmission efficiencies shown in Figure 2.9 are obtained.

2.7 k-Space Imaging

Confocal microscopy allows the investigation of objects with sizes that would not be possible with naked eye. There are super-resolution imaging techniques [127] [128] [129] and tip-enhanced techniques [130] [131] [132] that push the limit of detection even further. The role of the microscope objective in all these techniques is paramount. The microscope objective not only couples light from the nanoscale objects but also allows the study of angular distribution of radiated light. In Chapter 1, the role of angular distribution of radiation for extraction of maximum photons out of the sample was highlighted. By observing the Fourier plane of the microscope objective with a CCD camera, a technique called back

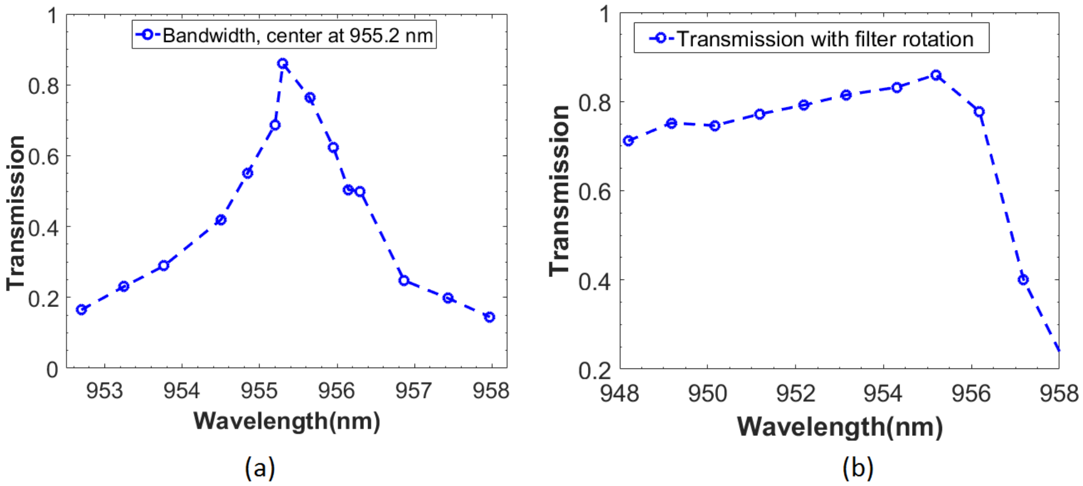

Figure 2.9: (a) Peak transmission of the ANDV9415 bandpass filter at 955 nm, (b) Rotation of the filter shifts the peak wavelength and the peak transmission is acquired at all wavelengths

focal plane imaging [133] or k-space imaging, the information about the angular radiation pathways can be extracted. Back focal plane imaging can also be used to obtain information about orientation of dipoles in new materials [134], and can be used to study material structure (layer thickness) as material surrounding an emitting dipole modifies the angular distribution pattern [135].

Since the planar microcavity is designed for higher photon extraction by tailoring the angular radiation profile, thus by imaging the emission from single quantum dots at the back focal plane one could study about the device structure and could also investigate the match between experimentally obtained patterns and theoretically designs. For realization of this goal, a novel cryostat friendly Fourier microscope was assembled. In addition, by slight modification of the optics for real plane imaging, the same Fourier microscope was also used to study the dipole radiation patterns of novel emitters in WSe_2.

A Fourier microscope involves four basic components: microscope objective, tube lens, Bertrand lens and a CCD camera. The back focal plane of a compound microscope objective lens is inside the lens and thus the back focal plane image has to be relayed to another plane where the image can be captured. The back focal plane can be imaged by several combination of optical elements as described in reference [136]. In Figure 2.10, the configuration to re-image the back focal plane of the microscope objective to the detector plane is shown. Lens 1 acts as the tube lens and lens 2 as the Bertrand lens. Together these two lenses act as the optical system to image the objective's Fourier plane. In literature, a Bertrand lens is a lens that performs a Fourier transform. This imaging configuration is relatively easier when there is a need to switch between k-space imaging and real plane imaging, as it only requires the addition of a Bertrand lens and translation of the CCD plane to the focus of the added lens.

In reference [136], Kurvits *et al.* highlight that plan-apochromatic lenses with high NA and low magnification make the best microscope objectives for Fourier plane imaging. In addition, it has been pointed out that a large focal length of the Bertrand lens gets rid of pixelation in the obtained image. For the purpose of the current research, the imaging configuration and choice of relay lenses were also dictated by the presence of cryostat. Single aspheric lens with 0.68 NA (C330TME-B from Thorlabs) was tested to survive multiple cycles of cryostat cooling and warming up and was tested for use in Fourier imaging. The lens exhibited aplanatic behaviour and was used for imaging of quantum dot samples. This lens was also chosen keeping in mind that there is a SIL ($\mathrm{NA}_{eff} = n_{SIL}\mathrm{NA} = 1.36$ where, $\mathrm{n}_{SIL}=2$) on the sample which limits the working distance from the sample. For WSe_2 samples, a 0.82NA, 50X plan-apochromat cryogenic lens provided by Partec was used.

The Fourier plane imaging setup here only shows the collection path. The excitation path has not been shown to avoid the loss of context. The physical height of the cryostat and of the microscope head dictated the focal length of the lenses used to relay the back focal plane of the microscope objective. The lenses are standard 40cm focal length achromat doublets from Thorlabs where the back focal plane is relayed outside the cryostat to a plane where a detector can be placed. The ratio of focal lengths of the two lenses determines the magnification of the back focal plane image and thus the CCD chip size and the clear aperture of the microscope objective determine the ratio of focal lengths of the two lenses shown. For quantum dot experiments, lens 1 and lens 2 are 40 cm focal length achromat doublets AC254-400B-ML from Thorlabs. For WSe_2, lens 1 is AC254-400B-ML while lens 2 is AC254-250B-ML. This is the because the partec microscope objective used for the experiment has a clear aperture of 6 mm which is larger than the chip size of the CCD and thus the back focal plane pattern needed to be demagnified in order to capture it. The long pass filter gets rid of the excitation laser. Narrowpass filters from Andover corporation for InAs quantum dots are used to resolve single quantum emitters for imaging. Semrock filters were used for spectral isolation of the emitters in monolayer of WSe_2.

The complete microscope also obtains the spectral data. As shown in Figure 2.11,

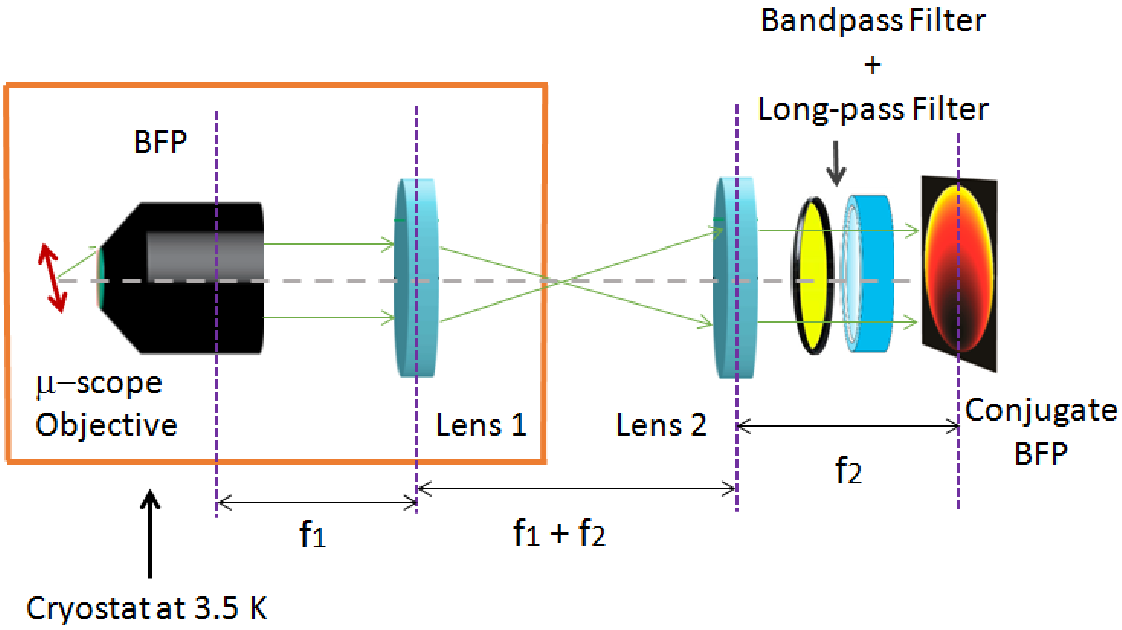

Figure 2.10: The Fourier plane imaging setup here only shows the collection path. The excitation path has not been shown to avoid the loss of context. The relay lenses are standard achromat doublets from Thorlabs where the focal length of the lenses have been chosen to relay the back focal plane outside the cryostat where a detector can be placed. The ratio of focal lengths of the two lenses determines the magnification of the back focal plane image and thus the CCD chip size and the clear aperture of the microscope objective determine the ratio of focal lengths of the two lenses shown.

the home-built modular Fourier microscope can allow photoluminescence spectroscopy, Fourier plane imaging and real plane imaging (by addition of another lens on the top of bandpass filter BPF 935). First, by use of bandpass filter a bright quantum emitter is isolated spectrally. The magnification of the microscope is small ($\sim$5) in photoluminescence mode and thus it is difficult to determine if there is only one or more emitters with the same spectrum within the filtered range of wavelengths. However, in the imaging mode, to avoid pixelated images, a large magnification is used for the microscope. This large magnification in imaging allows the visualization of number of emitters if there are more than one with the same emission spectrum. Thus, once the photoluminescence spectrum is obtained, an achromatic doublet lens is mounted on top of BPF935 and the CCD on the clamp is translated vertically to be at the focus of this new achromat lens. In this real plane imaging mode with the bandpass filter being positioned as it was for spectral data, image is obtained on the CCD to observe the number of emitters that contribute to the signal. Once it is made

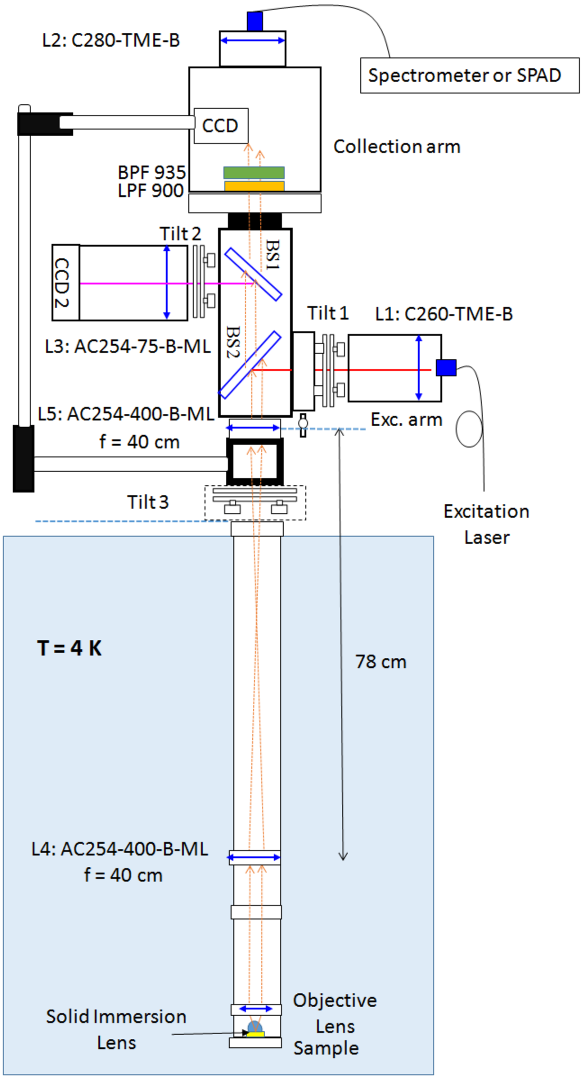

Figure 2.11: The home-built modular Fourier microscope can acquire photoluminescence spectra, image the back focal plane of the microscope objective and by addition of a lens acquire real plane images of single emitters. All components of the microscope have been labeled for completeness. LPF900 is the longpass filter at 900nm and BPF935 is the band-pass filter from Andover to isolate single quantum dot at 935nm.

sure that there is a single emitter in widefield real plane image, then the achromat lens is removed and the CCD is translated to the back focal plane of lens L5 to obtain the Fourier plane image.

In order to image the fourier plane for radiation from delocalized and localized excitons in monolayer of WSe_2, a different microscope is assembled as shown in Figure 2.12. An excitation laser at a wavelength of 532 nm is reflected from a dichroic beam-splitter (long pass at 550 nm) and is focused on the sample. The reflectivity of the dichroic beam-splitter is near unity at 532 nm. A beam-splitter block is mounted underneath the microscope head to place a transparent glass-slide at an angle. For alignment of the microscope to the sample, white light source is mounted at one of the ports of the beam-splitter block and is reflected towards the sample by using the glass-slide. The beam-splitter block is also used to mount the CCD for back focal plane imaging as can be seen in the Figure 2.12. While a symmetric relay of two achromatic doublets with identical focal lengths of 40 cm was used for the quantum dot microscope, here the achromatic doublet in the cryostat was a 40 cm focal length, B-coated lens and the lens outside the cryostat has a focal length of 25cm. The microscope objective has a NA of 0.82 with a clear aperture of 6 mm. In order to align the microscope at room temperature, laser light at 780 nm is used which corresponds to the typical wavelength of emission from the samples. Light at 780 nm is coupled into the optical fibre at the top of the microscope in the collection arm and the sample is brought to focus by observing the spot size on CCD2 in the alignment camera arm. The different tilt stages in the microscope assembly are used to compensate for mechanic tilts during the assembly process. White light imaging ensures the position on the flake. At this moment, the focus of the microscope is kept at one corner of the flake and photoluminescence signal is continuously acquired while scanning the sample in raster motion. This assists in identification of key positions of emitters on the monolayer sample. After acquisition of isolated photoluminescence from emitters in sample, CCD is brought in the path in the collection arm at a distance of 25 cm from the achromat doublet lens i.e. at the back focal plane. The full microcope configuration is shown here and the assembly allows easy switching between photoluminescence and imaging modalities.

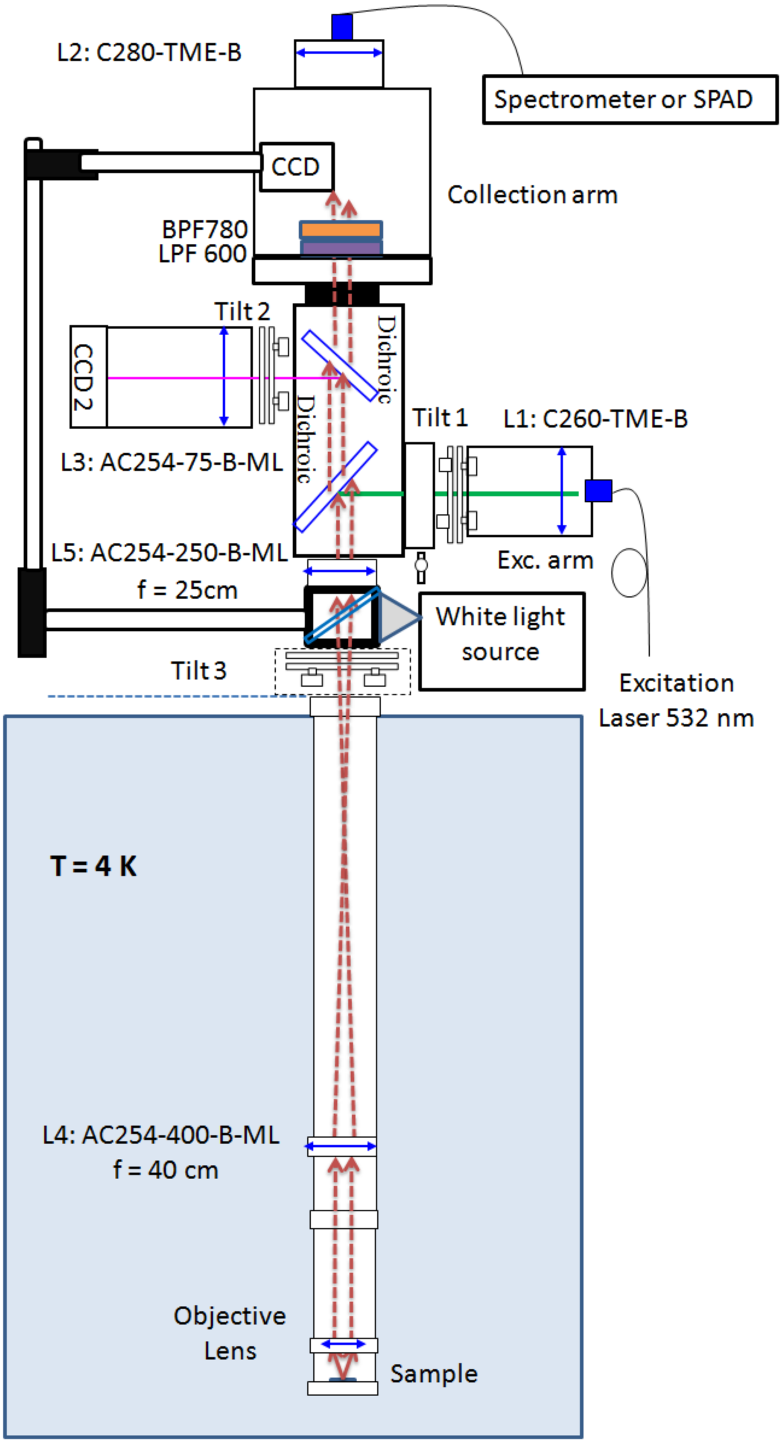

Figure 2.12: Modular microscope assembly for imaging of radiation from emitters in monolayer of WSe_2

2.8 Wide-field Microscopy of Photoluminescence Emission

In optical microscopy a magnified image of the illuminated object is obtained on a two-dimensional detector, while in photoluminescence microscopy the image of the emissive object is obtained and the illumination is filtered away. This implies that light of a lower wavelength (higher energy) is used to excite the object, which upon absorption, re-emits photons at a longer wavelength or lower energy. It is the emission from the photoluminescent object that is used for imaging unlike the excitation light in optical scattering microscopy. Fluorescent/photoluminescence microscopy has proven to be a vital tool in studying the physical and chemical properties of single quantum emitters. Unlike Fourier microscopy which happens at the back focal plane, widefield imaging happens at the real image plane as shown in Figure 2.13. As it was also discussed in the previous section, real plane widefield imaging is also essential to verify that the emission is being obtained from a single emitter before proceeding to Fourier plane imaging.

Of particular interest in widefield microscopy of photoluminescence emission is the orientation of the absorption and emission dipole in quantum emitters. Properties such as radiative lifetime, emission intensity often depend upon the orientation of emission dipole as has been demonstrated earlier through transfer-matrix models as well. Also, the measurement of orientation of the dipole can allow the study of its surrounding [137]. One of the approaches to determine the dipole orientation involves the measurement of emission along two orthogonally polarized detection channels [138]. The orientation of dipoles can also be obtained by modulation of the excitation polarization. In another approach, one can ascertain the orientation of dipoles by directly imaging the fluorescence. By intentional deterioration of the image via aberration [139] [140] or defined image defocusing [137] [141] [142], the emitter's emission dipole orientation can be obtained. Defocused imaging is much simpler to implement compared to excitation polarization modulation or using steering mirrors [143], and can allow the determination of three-dimensional orientation of the emitter.

For carrying out defocused imaging of orientation of emission dipole, the emission and imaging pathway are shown in Figure 2.13(c). Light from the dipole emitter is collected by the microscope objective, collimated and focused by the tube lens in the farfield. When the emitter is moved away or towards the microscope objective, the intensity distribution

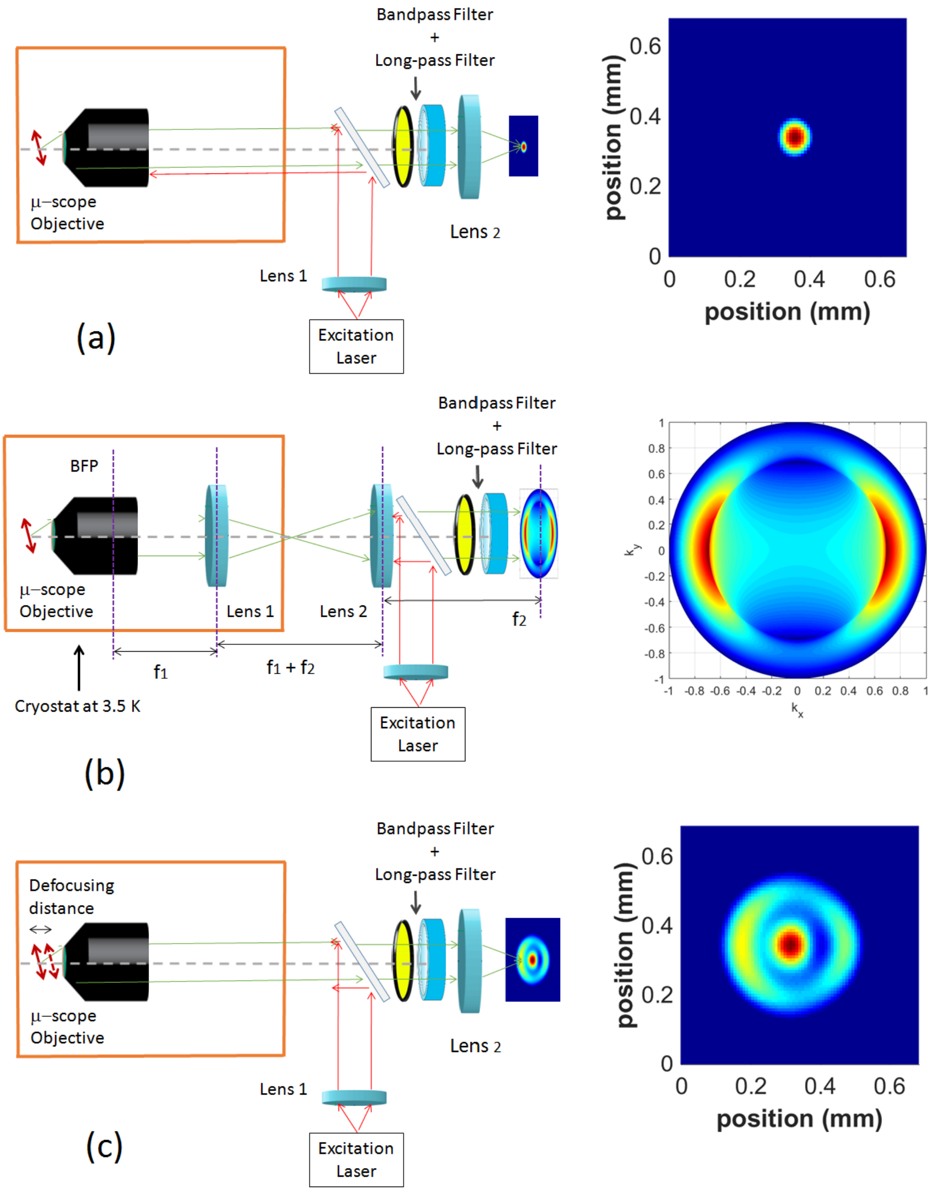

Figure 2.13: (a) Schematic diagram of the widefield real-plane imaging setup is shown together with the simulated image of a fluorescent emitter. (b) Schematic of back focal plane imaging setup is shown to image the angular distribution of dipole radiation pattern on CCD together with a simulated back focal plane imaging pattern. (c) Defocused imaging is an extension of widefield real-plane imaging where the emitter is moved towards or away from the focus of the microscope objective to obtain the three-dimensional orientation of the emission dipole on CCD. A simulated defocused image has been shown at the bottom right.

of the blurred image at the focus of the tube lens exhibits the orientation of the emission dipole. In order to isolate a single quantum emitter for imaging which improves the contrast in the images, the bandpass filter from Andover corporation is mounted on a turret mount. The turret mount rotates the filter in the out-of-plane direction which helps in filtering out emission based on its wavelength. When the density of emitters in the wavelength range of the filter is high, two filters are mounted and the bandwidth of the filter is sharpened further which gets rid of any other emitters which might have had similar spectral properties.

The theoretical foundations of this imaging modality lie in angular distribution of radiation of a dipole emitter, which was discussed mathematically in Chapter 1. Once the angular distribution of radiation is obtained, the expression for focusing it via a lens is generated. It is assumed that there are no aberrations in the optical system shown in Figure 2.13(c). The theory is borrowed from Richard and Wolf's seminal work [144] on imaging properties of aplanatic optical systems. The electric and magnetic fields in image space are calculated using the theory described in references [137] [145] and the energy density worked out from it. Based on J. Enderlein's research group's Matlab model for defocused imaging, dipole orientation images obtained in experiments can be accurately simulated [146].

Chapter 3

Spectroscopy of a Nanowire Single Photon Source

Nanowire single photon sources have provided the ability to generate two-dimensional arrays of high efficiency quantum dot based single photon sources with typically a few quantum dots in each wire. In this Chapter, low temperature photoluminescence spectroscopy of quantum dots embedded in nanowires has been carried out to study the emission characteristics of the emitters. The Chapter is written based on reference [149]. Nanowires were fabricated by P.E. Kremer. Exciton lifetime measurements were carried out together with Dr. A.C. Dada. Estimation/calibration of total efficiency of the nanowire was performed by Dr A.C.Dada. Strain-tuning of the quantum dot was carried out by P.E. Kremer.

3.1 Quantum dots in Nanowire

The schematic of the fabrication process is shown in Chapter 2 under the quantum dot samples section. The GaAs wafer with InAs quantum dots consists of a 1000nm thick $Al_{0.65}Ga_{0.35}As$ sacrificial-etch layer followed by a 2μm thick GaAs layer. As discussed in Chapter 1 under design rules for nanowire based photon sources, a gold mirror at the bottom of the nanowire reflects the downward travelling radiation into the collection half-space. In order to realize this in experiment, 100nm of gold is deposited by electron beam evaporation. Based on the chosen RF power, reactive ion etch gas pressure, during the dry etch process different shapes can be achieved for the GaAs nanowires as shown in Figure 3.1. Results described here are carried out on broadband nanowire antenna shown in 3.1(l).

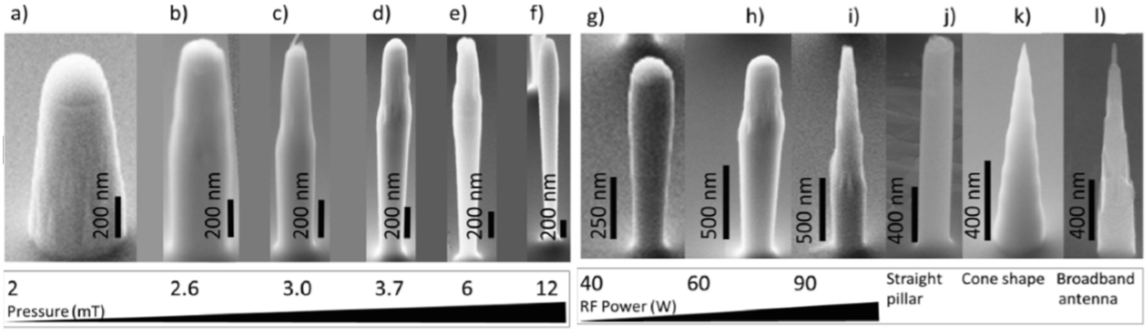

Figure 3.1: SEM images showing the influence of dry etch parameters on the GaAs nanowire shape, i.e., RF power, and RIE (reactive ion etch) gas chamber pressure [picture courtesy: P.E. Kremer].

3.2 Photoluminescence Spectroscopy

Micro-photoluminescence spectroscopy of the broadband nanowire antenna shown as (l) in Figure 3.1 is carried out using a cryostat-compatible confocal microscope. The sample chip is glued onto an aluminium holder which is mounted on top of x-,y-,z-nanopositioner from attocube systems. The confocal microscope is aligned on the sample by illuminating with a laser which is resonant with quantum dot emission from collection and excitation arms, and by obtaining a symmetric pattern in and out of focus with complete overlap between excitation and collection spots. The alignment is carried out for a wavelength of 950nm although the excitation laser wavelength is 830nm. This implies a larger than diffraction limit spot size for the excitation laser but the pitch of the nanowire array allows focus on only one nanowire at a time. After the sample tube is vacuumed to a pressure of 1×10^{-4}mBar or better, 25 mBar of helium is introduced in the sample tube. This added helium helps the sample to cool down once the sample tube is mounted in the cryostat. In order to mount the sample in the cryostat, an overpressure of helium is used as the transfer gas in order to prevent any condensation of air or moisture inside the cryostat.

The nanowire sample is designed to have different regions with varying geometrical profiles. The SEM micrograph of one such region is shown in Figure 3.2 which has 16 different nanowire samples, of which the measured sample has been shown enlarged on the right. In the measured region, the diameter of the nanowires is 232±4nm, distance from the gold layer is constant at 110nm, height of the pillar is 2μm,and opening angle of the taper is 9.8 ± 1.3^{o}. Each region on the chip is marked with a name which is etched deep in

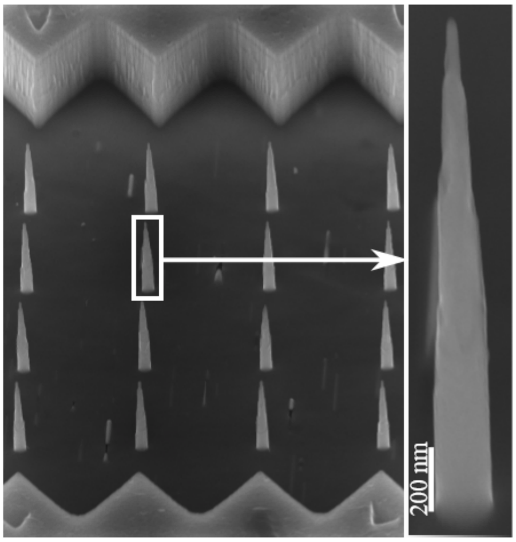

Figure 3.2: SEM image of an array of nominally identical tapered GaAs nanowires with diameter =232±4nm, separation from the gold layer = 110nm, height = 2μm,and opening angle α =9.8±1.3^o [picture courtesy: P.E. Kremer].

the GaAs. The alignment to a lump of gold was done at room temperature under an optical microscope. With this alignment marker as the starting point, the sample was translated to the region of interest on the sample.

Since the excitation laser is at 830 nm for photoluminescence spectroscopy of the nanowire sample and quantum dot emission is between 910 nm - 980 nm, a longpass filter at 900nm is used to get rid of the excitation laser light from the signal from the quantum dot. The spectrum is obtained on a liquid N_2 cooled CCD through an 1800 lines/mm diffraction grating. A standard photo-detector on the confocal microscope allows the calibration of incident excitation power on the sample. On an average every nanowire has three to five different quantum dots in the wafer. Due to inhomogeneity in the size and composition of self-assembled InAs quantum dots, the emissions are observed at different wavelengths.

3.3 Peak Assignment

Photoluminescence spectrum as shown in Figure 3.3 is observed in the experiment from the nanowire antenna shown before. In this spectrum, the neutral exciton (X^0) and single negative charged exciton X^{1-} are the prominent peaks at low excitation power. When the power from the excitation laser is increased, bi-exciton XX emission is also observed. The neutral exciton is identified via the fine structure splitting which is observable with the resolution of 1800 lines/mm diffraction grating [150]. The negative trion X^{1-} is identifiable by brighter photoluminescence and typically separated by $\sim$ 3.5nm from the neutral exciton in InAs quantum dots [151] [152].

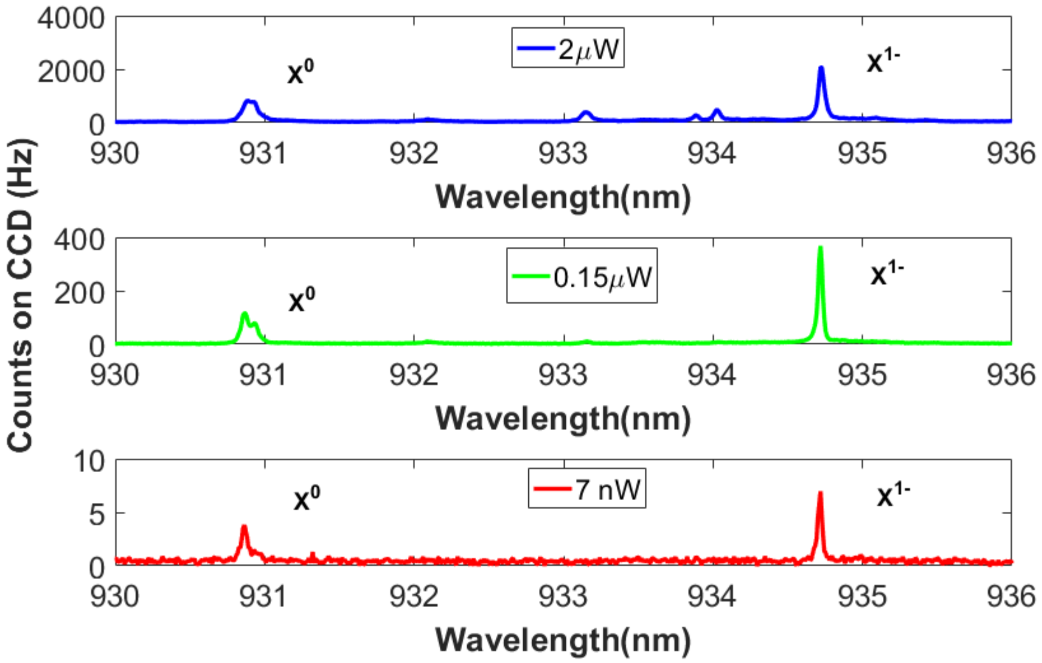

Figure 3.3: Photoluminescence spectra of the quantum dot emission at the wavelength of 934.5 nm at different excitation powers of the non-resonant 830 nm diode laser at a sample temperature of 4K

As shown in Figure 3.4, the intensity of the X^0 and X^{1-} peaks increase linearly with the power of the excitation laser and then saturate. At low power, X^0 and X^{1-} dominate the spectrum. At higher powers, two other peaks becomes prominent as well. The biexciton peak can be identified by the spectral separation from the X^0. The spectral separation between XX and X^0 is typically around 3.5 nm for InAs quantum dots in GaAs. While neutral exciton and single charged negative exciton show a linear rate of increase with increasing excitation power, the bi-exciton peak increases with a larger than unity slope when plotted on a logarithmic scale [152].

3.4 Stark Shift

When quantum dots in nanowire are illuminated by the non-resonant excitation laser, accumulation of charges occurs around the surface of the nanowire. The charges create a lateral

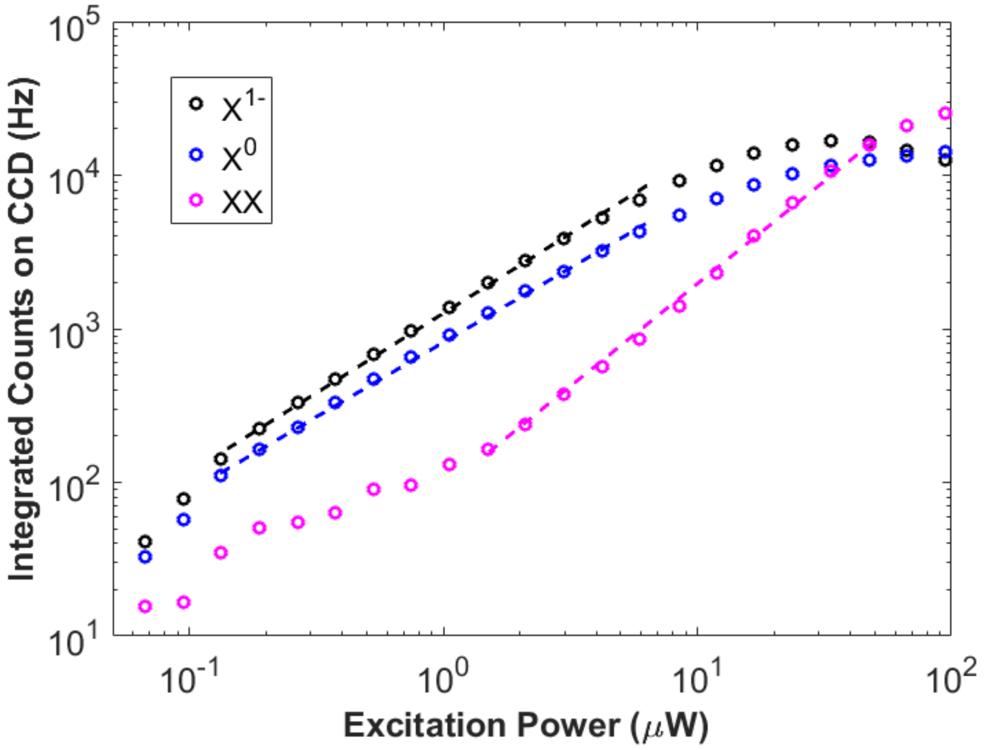

Figure 3.4: Power law behaviour observed for XX and for X^0, X^{1-} emissions in photoluminescence from quantum dots in nanowire. The shown data is from the dot emission at a wavelength of 934nm.

electric field at the position of the quantum dot. By varying the excitation intensity, the strength of the electric field and the fluctuation in electric field can be obtained from the linewidth broadening and shift in emission energy. When an electric field is applied, it can pull the electron and hole apart and the extent to which it happens is measured by a quantity called polarizability. A high value of polarizability imparts tunability to the emission energy of the exciton configuration [153] [154].

$$\Delta E = -pF + \beta F^2 \tag{3.1}$$

where F is the electric field, p the permanent dipole moment, and β is the polarizability. Permanent dipole moment is given by, p = er, where e is the electronic charge, and r is the electron-hole wave function separation. In InAs self-assembled quantum dots, the apex of the dot is Indium rich. The hole is thus at the top and the electron is delocalized over the whole dot at the bottom [153] [155]. The quadratic electric field term is negligible when vertical electric field is applied. Along the lateral direction, the permanent dipole moment is

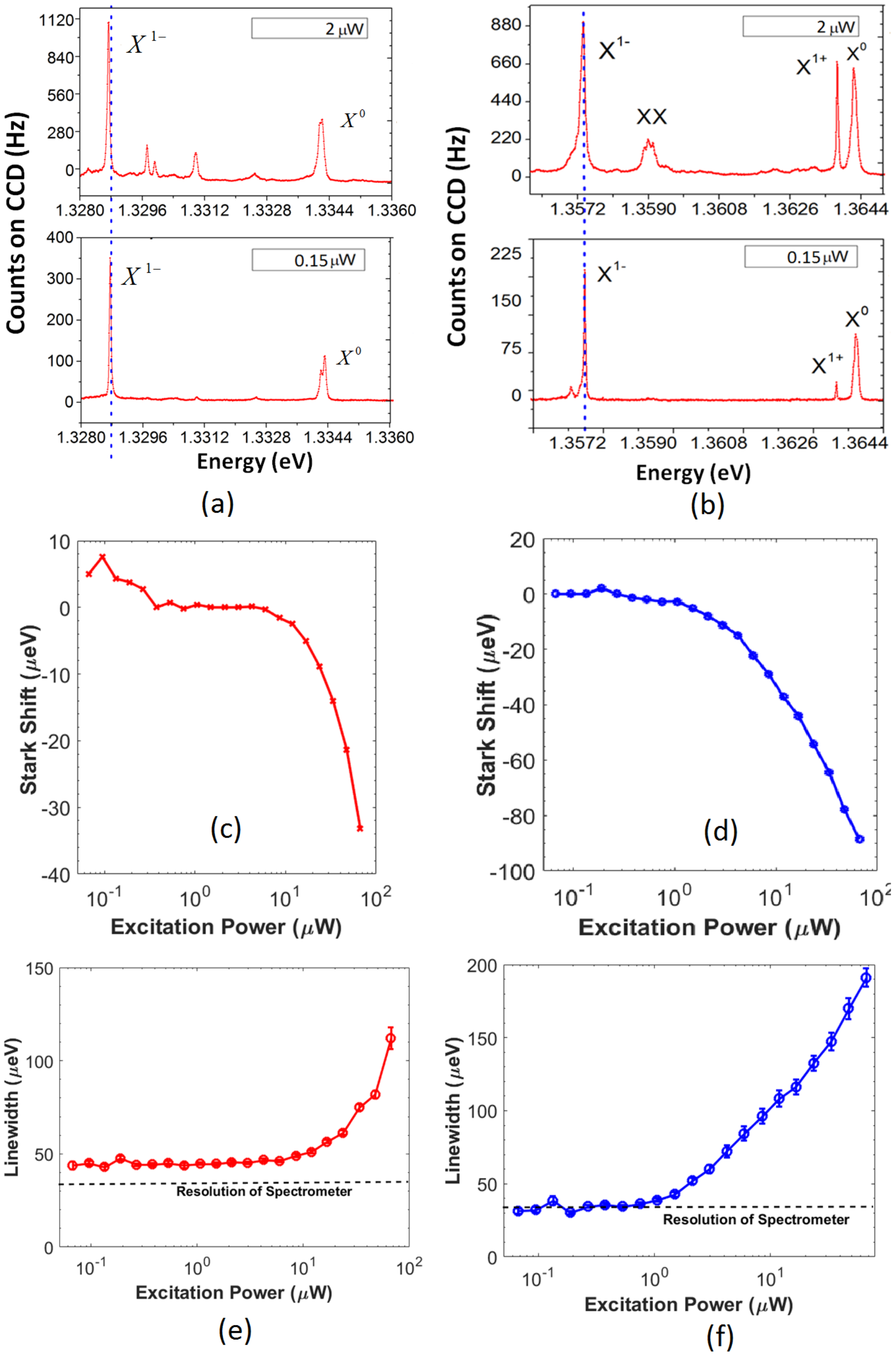

Figure 3.5: Photoluminescence spectrum of (a) quantum dot at 1.3288eV and (b) quantum dot at 1.3572eV. (c) Stark shift for X^{1-} exciton emission at 1.3288 eV, (d) for quantum dot at energy of 1.3572eV. (e) The fluctuation in electric field causes linewidth broadening for the negative trion at 1.3288eV and (f) at 1.3572eV.

absent and the stark-shift due to lateral field is dominated by the quadratic term. The value of polarizability for self-assembled InAs quantum dots is assumed to be $\beta = -4\mu\text{eV}/(\text{kV/cm})$ for lateral electric fields as presented in references [156] [157].

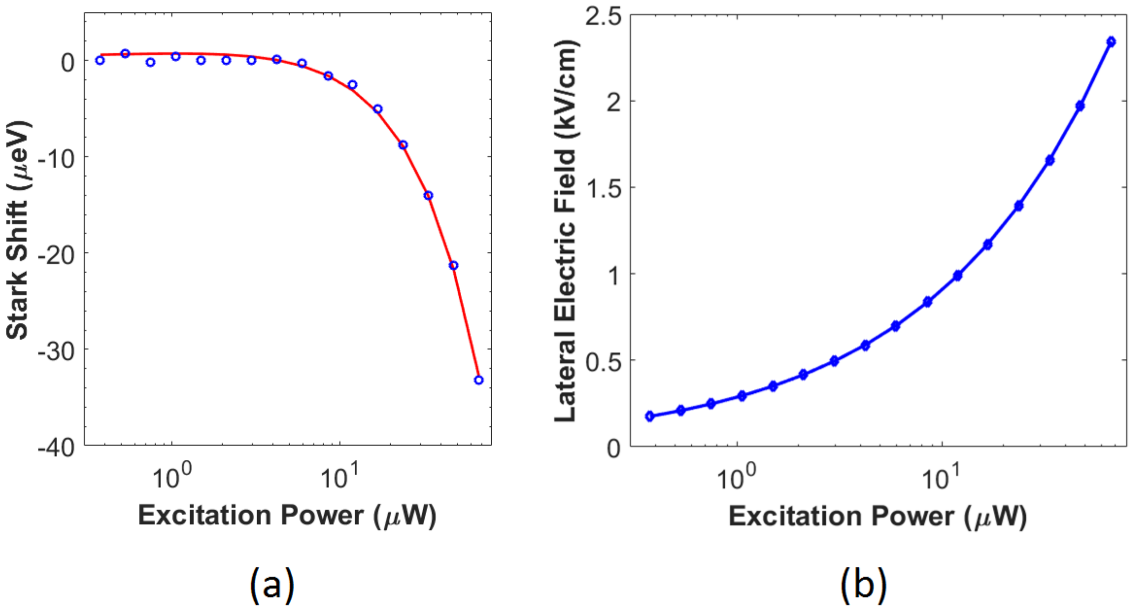

Figure 3.6: (a) Quadratic fit to the stark-shift in emission energy for the 934.5nm quantum dot exciton shows excellent match. The length of the dipole is determined to be 0.34Å. (b) The induced lateral electric field due to presence of charges trapped at the nanowire surface from non-resonant illumination shows a square root dependence to excitation power.

In Figure 3.5, the effect of increasing excitation power is shown on radiative linewidth and emission energy. While at low excitation powers, the linewidth of the X^{1-} exciton flatlines at the limit of resolution of the spectrometer, the increase in linewidth at higher excitation powers is due to electric field fluctuations at the position of the quantum dot due to trapped charges at the nanowire [158]. The effect on emission energy can be seen in Equation (3.1). The lateral electric field is directly proportional to the square root of excitation power and a least square fit to the stark-shift for the dot at 934.5nm yields an excellent fit as shown in Figure 3.6. The length of the dipole is obtained to be 0.34Å. This value of the dipole length is shorter than the reported values in reference [153].

3.5 Photon-Correlation Spectroscopy

In order to ensure that the X^{1-} emission is antibunched i.e. originating from a single quantum dot, photon-correlation measurements are carried out using the Hanbury-Brown-Twiss (HBT) interferometer. Light from a quantum emitter is split in two arms and the output of the arms go to two silicon single photon avalanche detectors from Excellitas.

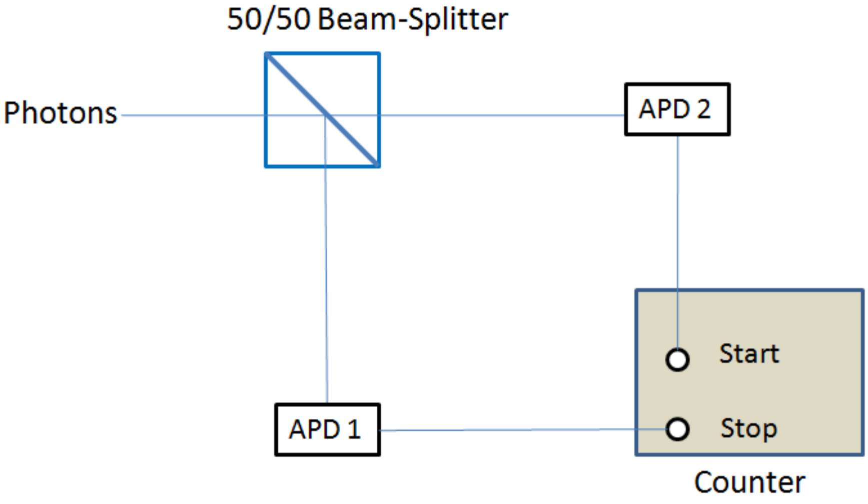

Figure 3.7: Schematic diagram of Hanbury-Brown-Twiss interferometer used for anti-bunching measurement

Single photon avalanche detectors at the two end of the interferometer are used to count the photons. The output voltage from the two avalanche photon detectors are connected to the start and stop channels of a picoharp time correlator as shown in Figure 3.7. By recording the correlation between the arrival times of photons on the two detectors, second order photon correlation is studied. For light from a single quantum dot , this shows a value of 0.3 for the second order correlation coefficient at zero delay ($g^{(2)}(0)$), as shown in Figure 3.9(left). Here X^{1-} exciton emission under continuous wave excitation illuminates the two arms of the HBT interferometer. This strong antibunching behaviour in the photon emission is a signature of single photon emission [159] [160]. This implies that as soon as a photon is emitted, the quantum dot falls back to the ground state and cannot emit immediately. Thus, a dip can be seen in $g^{(2)}(\tau)$ at zero delay.

For a single photon source, the experimental second order correlation at zero time delay has to be less than 0.5. The actual dip at zero delay goes almost to zero when the joint temporal response (jitter) of the two photodetectors is deconvolved from the data. In Figure 3.10 (a), the measured values of $g^{(2)}(\tau)$ are convolved with the joint time jitter of the two APDs. The function $g^{(2)}(\tau) = 1 - ae^{-t/\tau_m}$ is convolved twice with the instrument response of the detector to account for joint detector response. The resultant distribution is fit to the experimental data and the parameters a and τ are obtained using a least square fit. Using the parameters a and τ, deconvolved $g^{(2)}(\tau)$ is obtained. The obtained values of $g^{(2)}(0)$ i.e. $g^{(2)}(\tau)$ at $\tau = 0$ are plotted in Figure 3.10 (b). The value of $g^{(2)}(0)$ increases with

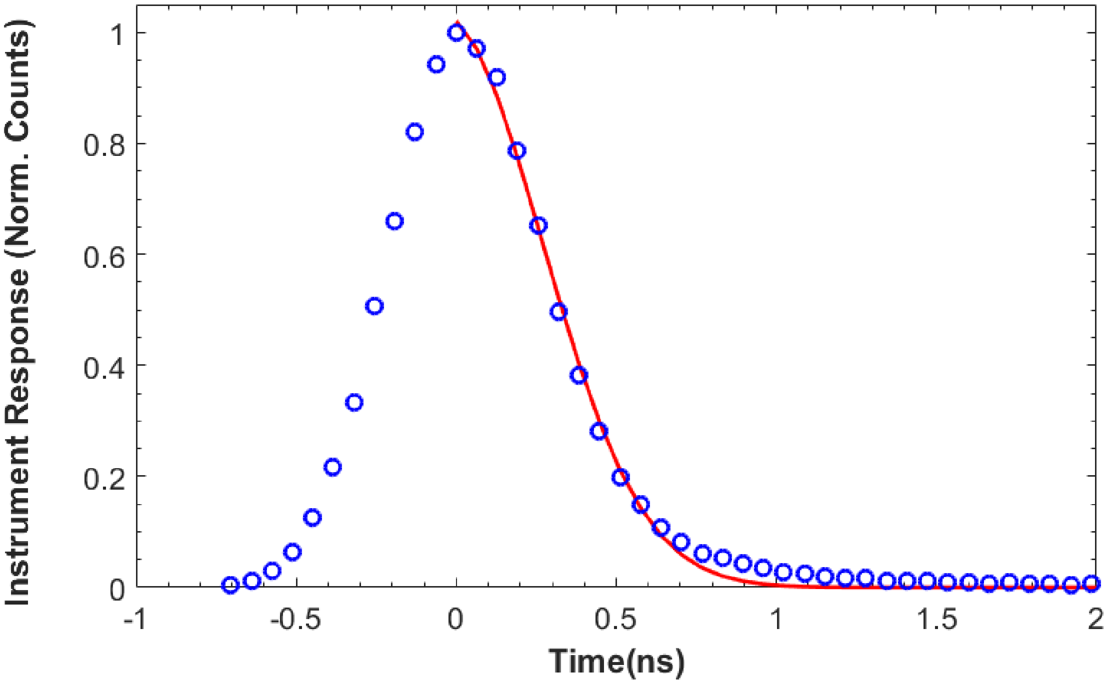

Figure 3.8: Temporal response of the APD is determined for deconvolution

increasing power. The parameter $\tau_m$is related to the radiative lifetime of the excitonic state by the relation: $1/\tau_m = 1/\tau_{X^{1-}} + 1/\tau_{pump}$. Here the term τ_{pump} is a parameter which is determined by the power of the excitation source.

Cross-correlation measurements were also performed using the HBT setup with APDs (avalanche photon detectors) and picoharp time correlator. The start channel of the picoharp is connected to APD receiving X^{1-} and the stop channel is connected to the other APD with X^0 emission directed to it. The second order correlation function is given by $g^{(2)_{cross}}(\tau) =<: I_{X^{1-}}(t) I_{X^0}(t+\tau) :> /[< I_{X^{1-}}(t) >< I_{X^0}(t) >]$, where $I_{X^{1-}}(t)$ and $I_{X^0}(t)$ are the intensities of X^{1-} and X^0 respectively. As can be seen in 3.9, there is a nice antibunching dip around the zero delay i.e. $g^{(2)}(0) = 0.25$. Since the emission of a X^{1-} photon puts the quantum dot back in the ground state, a simultaneous emission of X^0 photon is not observed. This confirms that the X^{1-} and X^0 emissions are from the same quantum dot. In contrast, when the HBT interferometer is illuminated by light from two or more emitters, the depth of the g$^2(0)$ dip decreases [161].

3.6 Lifetime Measurements and Efficiency

For calculations of the efficiency of photon emission, the quantum dot at 934.5 nm (shown in Figure 3.3) is used. In the path of the photons from the quantum dot emitted by the

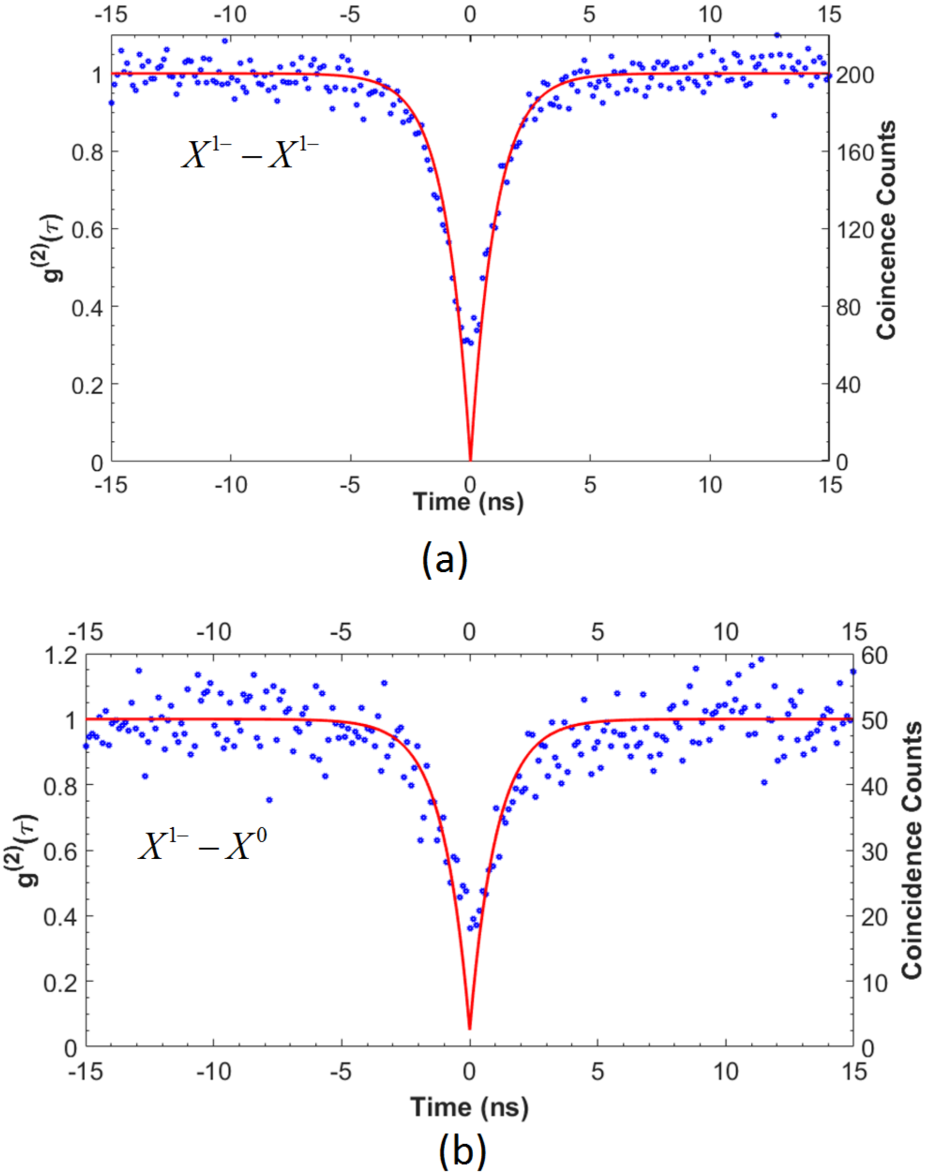

Figure 3.9: (a) Strong antibunching can be observed in second order correlation measurement on X^{1-} emission on the left. Light from the X^{1-} exciton is collected in a single mode optical fibre and then split in two arms of a Hanbury-Brown-Twiss interferometer. (b) Cross-correlation measurement is carried out between X^0 and X^{1-} excitons to show that both emissions arose from the same quantum dot. For this the two arms of the HBT interferometer are aligned to X^0 and X^{1-} emissions separately.

nanowire into the fundamental mode, there is microscope optics which consists of the objective lens, glass window (NBK7-B), two beam splitters combined (BS), a long pass filter (LP900), with their respective transmission efficiencies $T_{obj} = 93.47\%$, $T_{NBK7} = 94.4\%$, $T_{BS} = 63.87\%$, $T_{LP900} = 85.19\%$. This is followed by coupling into the collection fibre at the top of the head. The transmission efficiency due to alignment and collection at

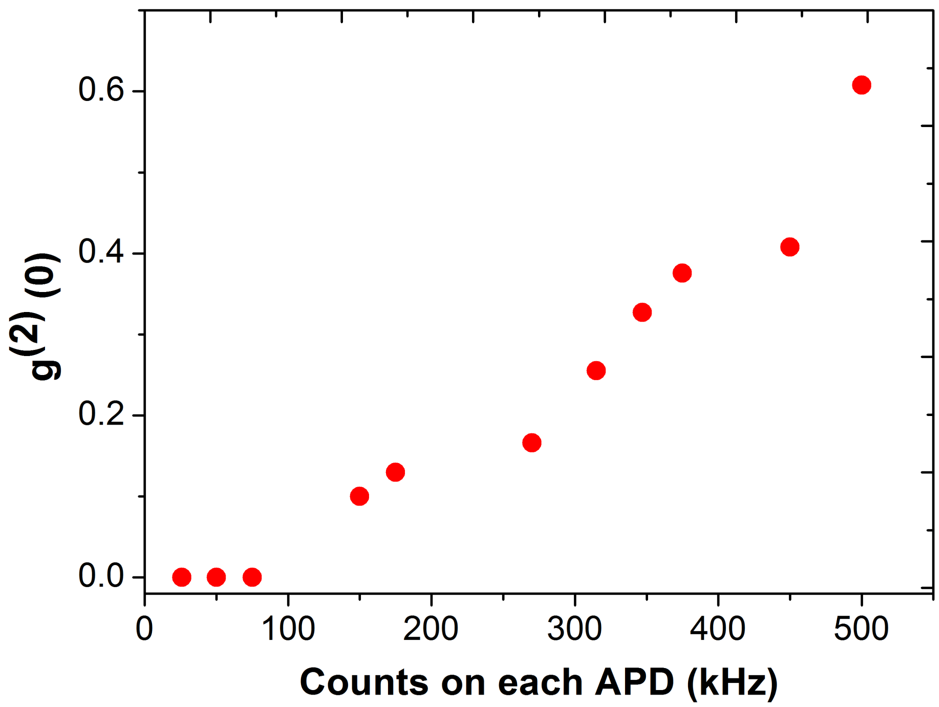

Figure 3.10: Antibunching necessitates a $g^2(0) < 0.5$; $g^2(0)$ increases at higher excitation powers which can be because of the increase in background due to contributions from neighbouring dots. The value of $g^2(0)$ are obtained for the X^{1-} emission at 4K from a HBT interferometer. The deconvolved position of the dip at zero time delay at different excitation powers of the 830nm laser are taken for the Figure.

the top of the microscope head was $T_{align} = 6.43\%$. This collection fiber was at one end of a 99/1 fibre beam splitter with the collection arm transmission of $T_{99/1}$= 98.87%. The Hanbury-Brown-Twiss (HBT) interferometer has an efficiency of $T_{HBT} = 56.56\%$, and the quantum efficiency for each of the APDs is QE_{APD} =26%. The combined transmission efficiency of the microscope is thus $T_{microscope} = T_{obj}$ X T_{NBK7} X T_{BS} X T_{LP900} X T_{align} X $T_{99/1}$ =3.05%.

This combined transmission efficiency is measured both individually and collectively. Using the known APD quantum efficiency, the counts on the APD and the corresponding photoluminescence spectra of both laser light and quantum dot emission, the total efficiency of the coupling into the spectrometer and detection on CCD using the 1800 lines/mm grating is found as $T_{spec} = 0.42\%$. This was verified by measurements at high and low powers.

To complete the calculation of η which is defined as the ratio of power that couples into

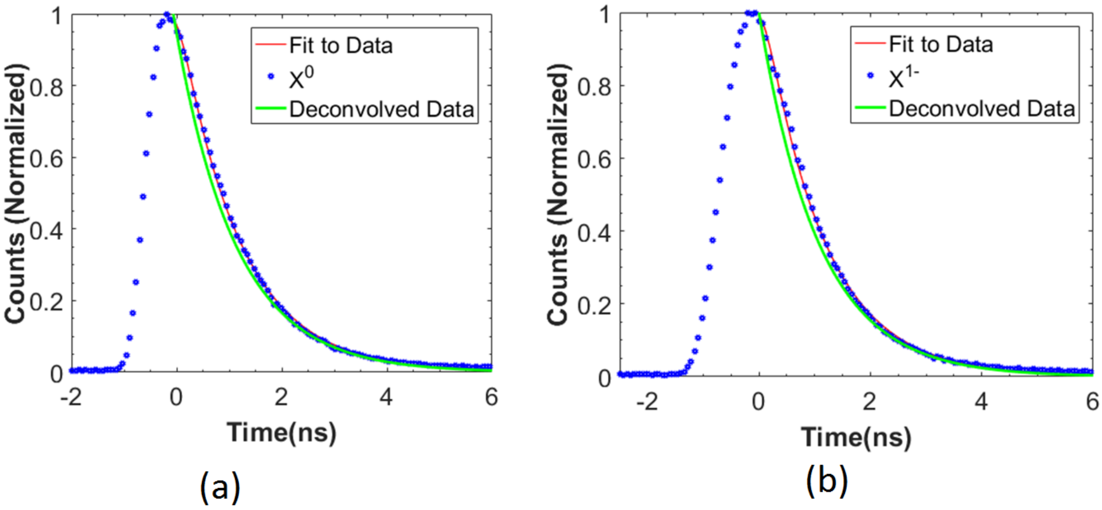

Figure 3.11: By using the correlator and using a pulsed laser as the trigger and X^{1-} emission into an APD connected to the other channel of the correlator, lifetimes can be determined for (a)X^0 and (b)X^1 excitons in GaAs nanowires. The inverse of emission lifetime shows the photon emission rate.

the lens with NA=0.82 to the total emission power from a dipole in GaAs, the experimentally measured lifetimes (see Figure 3.11) are used to determine the photon emission rate into all the available modes. Using the sync from a pulsed laser to the correlator, a radiative lifetime of 1.15 ns was obtained for X^{1-} emission. For X^0 transition, τ_{X^0} = 1.01 ns was obtained. The experimentally obtained lifetimes are around 20% larger than the ones reported for InAs quantum dots in reference [162].

The lifetimes corresponds to ~0.9 GHz and ~1.0 GHz and an average emission rate of 0.96 GHz respectively (assuming equal probabilities of the quantum dot being in either X^0 and X^1). Using this, the estimated value for η = 3.13 X 10^8 /0.96×10^9 =31.5%. When all the lines are included in the integration, η=57%. This data is for the brightest emitter in all the nanowires that were measured. A histogram of efficiencies for several measured GaAs nanowires embedded with InAs quantum dots is shown in figure 3.12.

3.7 Strain Tuning

Strain tuning of the quantum dot was carried out by P.E. Kremer to demonstrate tunability of exciton emission energy in GaAs nanowires. As shown in Figure 3.13(a), the nanowire is integrated on top of PMN-PT crystal for strain tuning. Finite-element modelling in

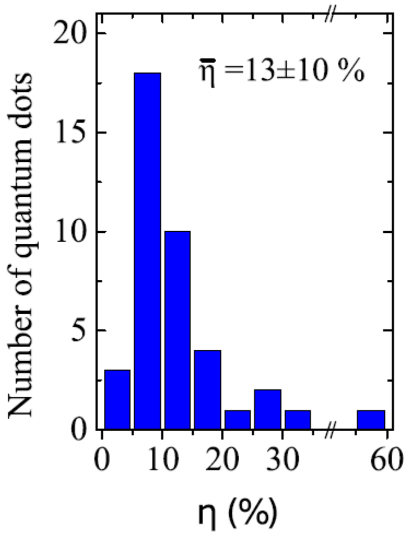

Figure 3.12: A histogram of extraction efficiency η for quantum dots in 16 nanowires shown in the SEM image before.

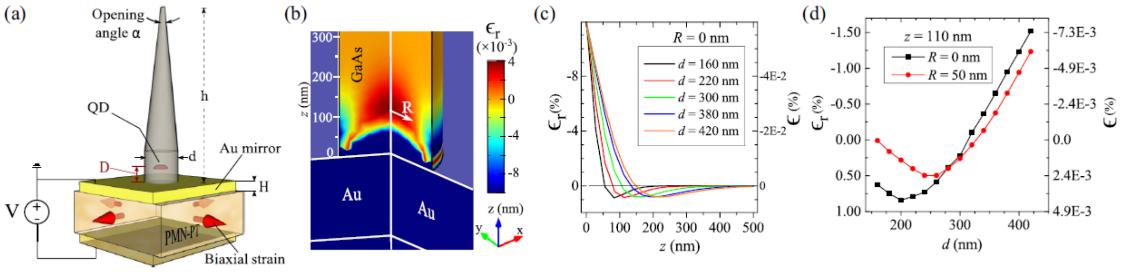

Figure 3.13: (a) Sketch showing the geometry of the device where D is the distance between the quantum dot and the Au mirror, d is the diameter of the pillar at the quantum dot position, h is the height of the pillar, and α is the opening angle of the pillar taper. The lead magnesium niobate lead titanate (PMN-PT) crystal has electrical gold contacts (with thickness H) on both sides for voltage tuning.(b) Simulation of strain relaxation in the nanowire using the finite-element method (FEM). The plot shows the profile of relative strain $\epsilon_r = \epsilon(\text{x,y,z})/|\epsilon_0|$ where the strain is ϵ(x,y,z) and the strain in the PMN-PT crystal is ϵ_0. The color legend is scaled to highlight the strain-field relaxation within the nanowire. (c) Plot of the strain ϵ and relative strain ϵ_r as a function of the distance along the z axis from the Au/GaAs interface (z = 0 nm at a radially centered position R = 0 nm). (d) Plot of ϵ and ϵ_r at z = 110 and R = 0,50 nm. The nanowire diameter d = 220 nm in (b), and ϵ_0 = 0.1% in (b)(d) [149].

COMSOL was carried out to study strain relaxation in these high aspect ratio nanowires. Strain-relaxation is obtained to be linear w.r.t. the applied strain. Although a silica layer between the GaAs nanowire and gold was suggested for reduction in coupling to surface plasmons [163] [164], it was observed in simulations that its absence increased strain transfer to the nanowire by 20%. Optimal strain-transfer was also the criteria for not choosing the optimal coupling distance of 80 nm of the quantum dot from the bottom mirror, as the relative strain increased from 0.04% to 0.8% for d=110nm.

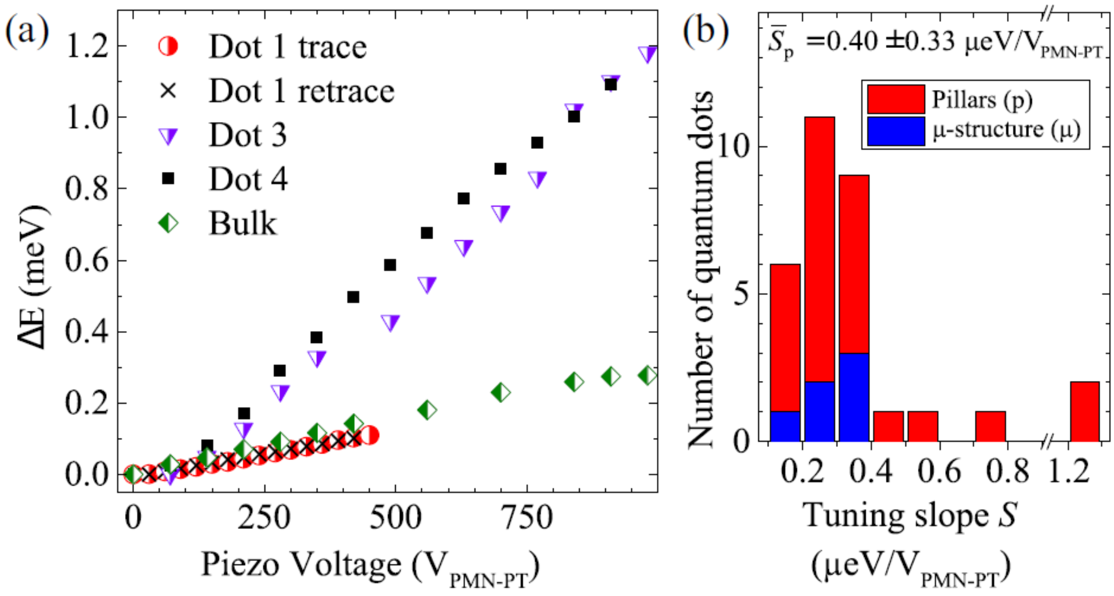

Figure 3.14: Strain tuning the energies of different single QD excitons. Each QD in each pillar exhibits a different strain tuning slope (S = ΔE/ΔV_{PMN-PT}) as shown in the histogram in (b). Also shown in the histogram are tuning slopes S_μ for QDs in the microstructure-structure membrane (S_μ = 0.29±0.06μeV/V_{PMN-PT}) [149].

When voltage is applied to the PMN-PT crystal, the quantum dot excitons respond with variable tuning slopes. A maximum tuning of 1.2meV was obtained for InAs quantum dots in GaAs nanowires as shown in Figure 3.14. The variation in tuning can be explained by relative radial positions of the quantum dots w.r.t. the centre of the wire axis and the variation in morphology of the quantum dots [149]. Strain-tuning can be enhanced by reducing the separation d between the quantum dot and the gold mirror, however this can lead to spectral fluctuations [165]. In Figure 3.14, dots not in nanowires were also characterized by application of strain. Despite the large aspect ratio of the GaAs nanowires, the tuning of emission energy by application of strain showed a larger slope than that of dots not in wires. A slope of S_μ = 0.29±0.06μeV/V_{PMN-PT} was determined for dots in the microstructure membrane (outside the nanowire area) compared to a tuning slope of S_μ = $0.40\pm0.33\mu$eV/V_{PMN-PT} for dots in nanowire. A large tuning of 1.2 meV for dots in GaAs nanowires is a sign of broadband nature of the nanowire.

3.8 Summary

Tunable excitonic emission from quantum dots in GaAs nanowires is shown. The tuning of emission energy of InAs quantum dots by 1.2meV can be used for generation of entangled photon pairs by reducing fine structure splitting of neutral exciton to zero. Tuning of emission can allow interference of two photons on a beam-splitter. The broadband nature of the emission from nanowires is demonstrated by large tuning of energy with strain without compromising the photon collection efficiency. Further, dots in GaAs nanowires show a larger strain-tuning slope than the dots in the membrane. An average photon collection efficiency of $13 \pm 10\%$ is observed for dots in GaAs nanowires. From Stark-shift data, the length of the dipole has been determined to be 0.34Åwhich is on the shorter side of the reported dipole lengths for InAs quantum dots. The linewidth broadening and Stark-shift occur due to charges trapped at the surface of the nanowire and due to fluctuation of these charges, respectively. Passivation of GaAs nanowires with $(NH_4)_2S$ can potentially eliminate this effect.

Chapter 4

Fourier Microscopy of Single Quantum Dots in Planar Devices

This Chapter entails the optical characterization of self-assembled InAs quantum dots embedded in a GaAs wafer with electrical contacts and in planar dielectric cavity with a rear gold mirror, which emit in 920 nm - 980 nm wavelength window of the spectrum. Charge tunability of single quantum dot allows the dot to specifically emit in one excitonic state. Fourier microscopy of this emission is carried out at different wavelengths to study the dipole emission pattern when emitters are embedded in the planar cavity. Using a transfer-matrix model in Matlab, a match with the theory of dipole emission in planar interfaces is obtained for single quantum dots in planar dielectric cavity. The goal of the experiment was to successfully carry out Fourier microscopy of single quantum dots in planar membrane devices to explain the fewer than expected photon counts observed at saturation from quantum dots in planar devices.

4.1 Planar Samples

As discussed in Chapter 1 and 2, for InAs quantum dots in a GaAs substrate, the photon collection efficiency is limited by the critical angle of 16.7^o at GaAs-air interface and large angular divergence of the emitted radiation in the farfield. Even with high numerical aperture (NA = 1) microscope objectives, the collection efficiency is limited to under 1% [166]. An efficient and broadband approach to extraction of photons from a quantum dot is necessary to realize quantum technology protocols where multilevel dot transitions are involved, such as entangled photon-pair generation [167] [168] and spin initialization, manipulation and read out [169]. The ease of incorporation of electrical control of the excitonic state of the quantum dot on planar microcavity devices make them stand out amid other approaches.

4.1.1. InAs Quantum Dots in Bulk GaAs

A schematic diagram of the quantum dots in the bulk GaAs sample shows quantum dots are buried in the GaAs substrate at a distance of h = 136.5 nm from the SIL-GaAs interface. This distance is chosen to satisfy the constructive interference relationship for an emission wavelength of 950 nm i.e. $\lambda/2n_{GaAs}$ as has been discussed in Chapter 1. The addition of solid immersion lens (SIL) allows the increase in effective numerical aperture of the microscope objective ($\mathrm{NA}_{eff} = \mathrm{NA}\times \mathrm{n}_{SIL}$ where n_{SIL}=2) and increases the photon collection by a factor of 4 [172].

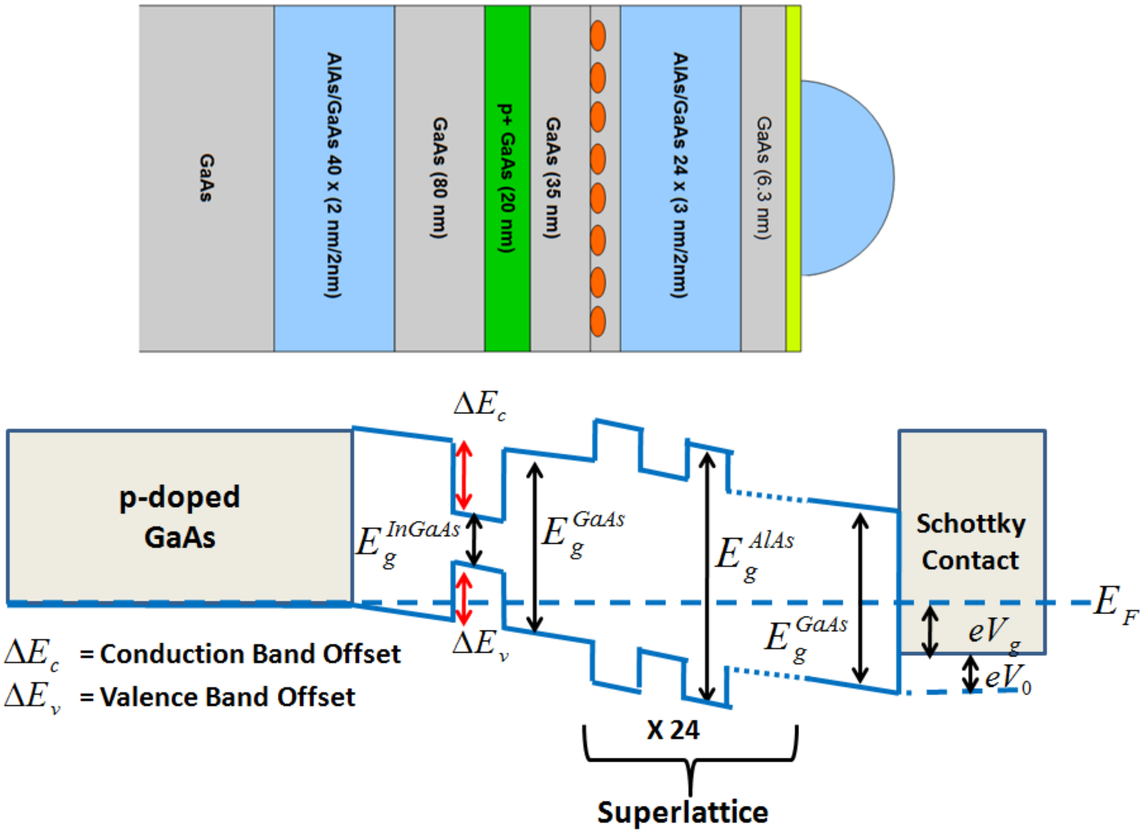

Figure 4.1: Schematic diagram of bulk p-doped GaAs sample and the corresponding heterostructure diagram to show field-effect device

The heterostructure diagram for the p-doped bulk GaAs sample is shown underneath. Holes tunnel into the quantum dot heterostructure region on application of gate voltage (V_g). This allows a high fidelity control of the hole population in the quantum dot. The sample is grown by molecular beam epitaxy and consists of In(Ga)As quantum dots tunnel coupled to a grounded back contact through a 25 nm thick GaAs barrier. In order to bring the dot emission into the 920nm-980nm wavelength range, the dots are capped with 10nm thick GaAs layer. The AlAs/GaAs superlattice acts as a blocking barrier. At the top, under the solid immersion lens (SIL), is a $\sim$3nm thick semi-transparent NiCr gate electrode. The carriers are confined within a heterostructure due to energy band offsets between In(Ga)As and surrounding GaAs layers. The quantum dots are between a heavily doped layer which acts as an Ohmic contact and a metal Schottky contact (see Figure 4.1). When a vertical electric field is applied on the sample, the exciton emission energy shifts due to quantum confined stark effect. A superlattice of AlAs/GaAs between the quantum dot layer and the Schottky contact prevents the carriers from leaking out of the heterostructure region [170].

4.1.2. InAs Quantum Dots in Planar Membrane

For the planar cavity optimized for photon collection, the quantum dot is placed at an antinode of the cavity. The cavity acts as a Fabry-Perot resonator and by virtue of interferences alters the angular distribution of radiation from the emitter, which manifests itself in light being confined in a narrow cone of angles outside the cavity. Due to the presence of a cavity, the design also has to ensure light coupling out as radiation mode rather than being confined in the sample as a guided mode. The approach has been discussed in detail in Chapter 1.

4.2 Model for Dipole Radiation Pattern

In order to generate angular distribution of radiation from dipole emitters buried in GaAs layer in a multilayer sample, the emitter is modelled as a source of plane waves with the magnitude of wave-vector k determined by wavelength of emission. For a self-assembled InAs quantum dot, the two in-plane orientations are symmetric in a planar sample described above however the refractive indices of the layers are different due to polarization of the photons that these two orientations emit.

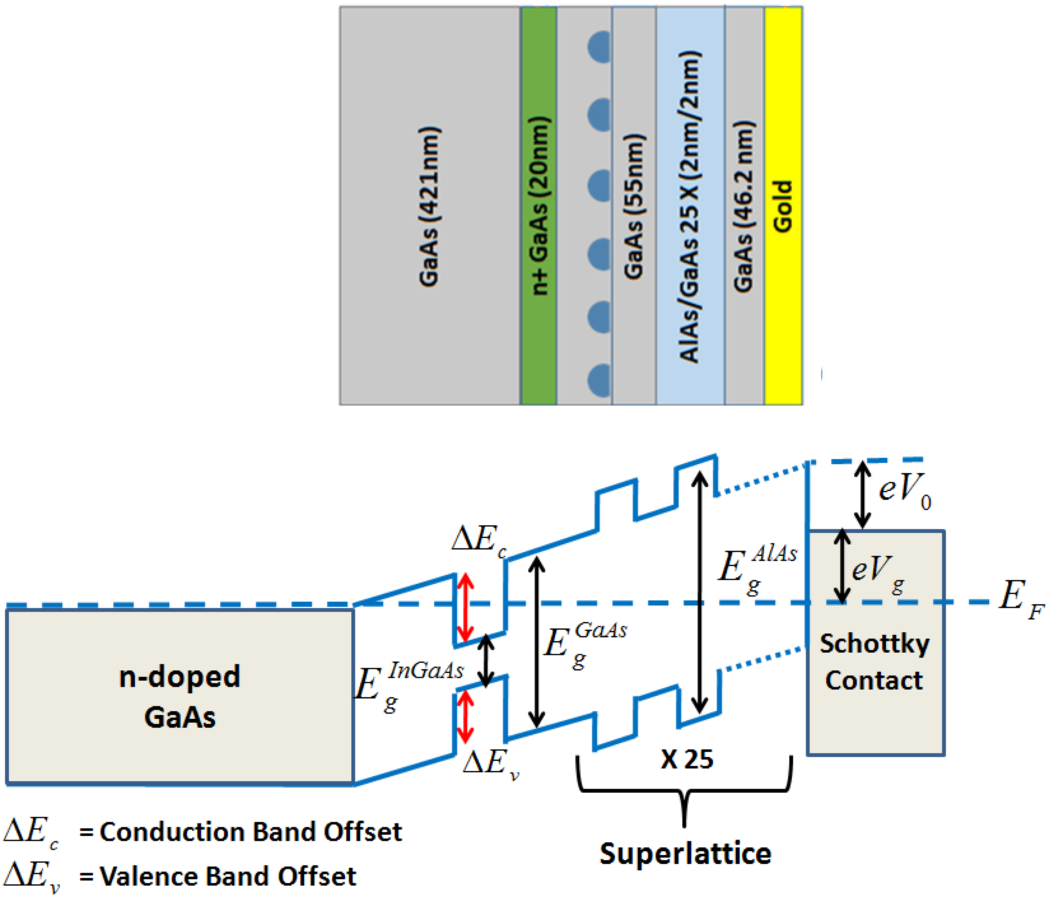

Figure 4.2: Schematic diagram of the planar microcavity shows the superlattice layer, gold contact, n+ GaAs layer as back contact. Energy diagram of the sample is shown. Excitons are confined in the heterostructure due to energy band offset between GaAs and In(Ga)As.

4.2.1. Model for Bulk GaAs Sample

In Figure 4.3(a), the angular radiation pattern from the two in-plane orientations of dipole in p-doped bulk GaAs sample can be observed. The radiation pattern outside the GaAs has a uniform distribution for emission at 935nm. The angular distribution of radiation has been calculated with the transfer-matrix model explained in Chapter 1. The layer stack used for transfer-matrix simulation for angular distribution of radiation is shown underneath. The stack represented by n_0 lists the layers on top of the embedding layer from top to bottom. The corresponding thicknesses of these layers are listed in d_0 where the outermost layer is either air or SIL and has no thickness listed in d_0. The embedding layer has a refractive index of n_1 and a thickness of d_1. The vertical separation of the dot layer from the top of the embedding layer gives the value of z. The layer stack underneath the embedding layer has the refractive indices and thicknesses listed in n_2 and d_2, also from top to bottom with the

Layer	**Ref. Index**	**Thickness (nm)**	**Repeats**
SIL	2	-	1
GaAs	3.56	6.3	1
AlAs/GaAs superlattice	n_{GaAs}= 3.56, n_{AlAs}=2.95	2 , 3	24
GaAs	3.56	10	1
InAs QD	-	-	1
GaAs	3.56	25	1
p+ GaAs	3.56	20	1
GaAs	3.56	80	1
AlAs/GaAs superlattice	n_{GaAs}= 3.56, n_{AlAs}=2.95	2 , 2	40
GaAs	3.56	-	-

Table 4.1: Layer stack for bulk GaAs sample with SIL

Layer Representation	**Ref. Index**	**Thickness (nm)**
n_0	$[n_{SIL}, n_{GaAs}, n_{AlGaAs}]$	d_0 = [6.3, 120]
n_1	n_{GaAs}	d_1 = 135
n_2	$[n_{AlGaAs}, n_{GaAs}]$	d_2 = [160]

bottom-most layer again having no thickness mentioned which implies a very thick layer so that reflection from the bottom of this layer will not alter the radiation profile.

In order to account for the apodization of the lens, the obtained angular distribution of radiation is multiplied by 1/cos(θ), where θ is the angle of emission w.r.t. the normal to the sample.

The thickness of the NiCr gate electrode is $\sim$3 nm and every nm of the electrode absorbs nearly 20% of the radiation emitted by the sample. Thus a photon extraction efficiency of $0.87 \times 4 \times 0.5$ % = 1.75% is expected from the device.

4.2.2. Model for Microcavity Sample

The fabrication schematic for planar microcavity with quantum dots was shown in Chapter 2. For the planar cavity sample with the gold mirror, the appropriate thickness of the embedding GaAs layer is d = 642 nm and the distance of the quantum dot layer ('h' in Figure 4.3(b)) from the air-GaAs interface is 471 nm. Gold layer in addition to acting as a mirror is used as the Schottky contact while a heavily n-doped GaAs layer above the quantum dot

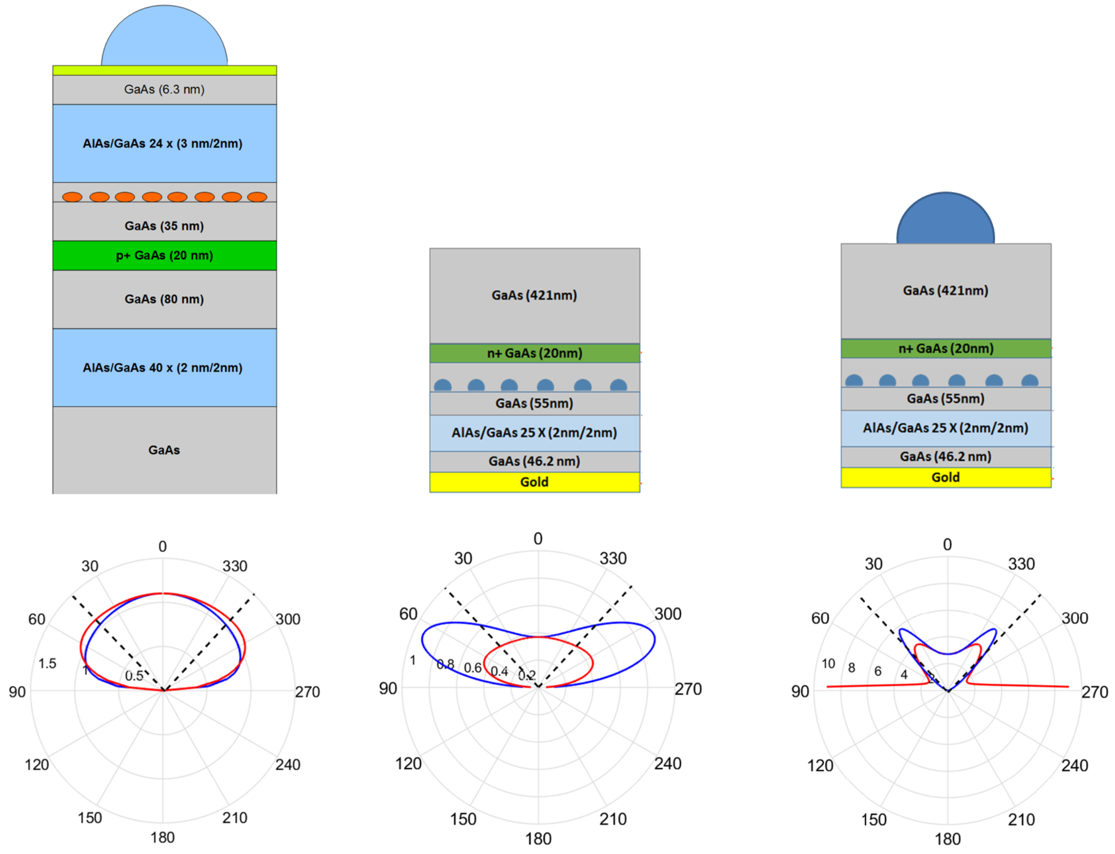

(a) (b) (c)

Figure 4.3: (a) Schematic diagram of the bulk GaAs sample with quantum dots at h = 136.5 nm from the SIL-GaAs interface and the simulated back focal plane pattern. The numbers in radii represent the value $|E|^2$ for p- and s-polarized emission from an in-plane dipole. (b) Schematic diagram of the planar microcavity VN2455 with gold mirror at the bottom. The simulated back focal plane pattern exhibits a lower intensity at the centre of the collection lens for s-polarization while the intensity i s maximized at the centre of the lens for p-polarization. (c) For the planar microcavity VN2455 with SIL, an extraction efficiency of 27% is estimated for collection using a 0.68 NA lens. Radiation escapes the cavity in a narrower cone of angles and the corresponding intensity distribution is estimated to be significantly brighter.

Layer	**Ref. Index**	**Thickness (nm)**	**Repeats**
SIL(air)	2(1)	-	1
GaAs	3.56	496	1
AlAs/GaAs superlattice	n_{GaAs}= 3.56, n_{AlAs}=2.95	each 2	25
GaAs	3.56	46	1
Gold	0.19+ 5.84i	200	1

Table 4.2: Layer stack for planar microcavity sample VN2455 with SIL (without SIL)

Layer Representation	**Ref. Index**	**Thickness (nm)**
n_0	[1 or n_{SIL}=2]	[ ]
n_1	n_{GaAs}	d_1 = 496
n_2	[$n_{AlAs/GaAs superlattice}$, n_{GaAs}, n_{Gold}]	d_2 = [100, 46]

acts as the Ohmic contact. There are two device configurations possible in this scenario. The sample schematic for VN2455 shown in Figure 4.3(b) and (c), where in the latter case the addition of SIL where $n_{SIL} = 2$ allows higher extraction in a narrower cone of angles. An extraction efficiency of 27% has been predicted for the planar microcavity with SIL compared to $< 2\%$ for the bulk sample with SIL [174].

In the above table, n_0 represents the refractive index and thickness of the layer stack above the embedding layer, n_1 and d_1 the refractive index and thickness of the embedding layer, n_2 the refractive indices and thickness of the layers underneath the dipole embedding layer. The response of the dipole in the layer stack is calculated by using the transfer-matrix. Similar to the case for the bulk sample, the angular distribution of radiation has been multiplied by 1/cos(θ) to account for the apodization of the lens.

4.3 Back Focal Plane Imaging

In Chapter 1, it was discussed that radiation from a dipole emitter in a homogeneous surrounding is radially symmetric w.r.t. the axis parallel to the dipole moment and the higher intensity is observed in a direction perpendicular to the axis of the dipole. When the dipole emitter is placed close to an interface at the focus of a microscope objective, the emitted radiation can couple into the objective lens in the collection half-space, or be lost in the forbidden zone in the lower half-space for incidence angle larger than the critical angle or get coupled as a guided mode [176]. The dipole emission which enters the microscope objective at an angle θ w.r.t. the optic axis, gets focused to the back focal plane of the microscope objective at a position ρ such that $\rho = \mathrm{f} \times \sin\theta$. The imaging of the distribution of emission intensity at this plane is called back focal plane imaging or Fourier microscopy [177].

The planar device embedded with self-assembled InAs quantum dots is glued on top of an aluminium plate, which is mounted on top of the x-, y- and z-nanopositioner-stack in a closed-cycle cryostat at a temperature of 4K. A continuous wave laser at the wavelength of 830 nm excites the sample in a confocal microscope setup. Photoluminescence from quantum dots is collected in a single mode optical fibre and the spectrum is obtained on a liquid nitrogen cooled silicon CCD via an 1800 lines/mm grating.

In order to image the angular distribution of radiation from the quantum dots, a modular Fourier microscope is used as shown in Chapter 2. The two achromatic doublet lenses (AC254-400B-ML) relay the radiation pattern that is obtained at the back focal plane of the microscope objective to the back focal plane of the second achromatic doublet lens where a silicon CCD (Sony chip: ICX829AL) is placed. For the photoluminescence spectroscopy, the CCD is swiveled out of the beam path and the emission is focused into a single mode optical fibre using a single aspheric lens with a NA of 0.15 which matches that of the single mode fibre. A narrow bandpass filter with a bandwidth of 0.8 nm from Andover is used for spectral filtering of the emission from a single quantum dot. The CCD is swiveled back into the beam path and placed at the back focal plane of the second achromat doublet. The intensity distribution at this plane is acquired for the experiment.

4.3.1. BFP Imaging of Bulk GaAs Sample

The presence of gates on the bulk GaAs sample allows the tuning of the excitonic state of the quantum dot. Using an in-house LabView program, a charge tuning map of the sample is generated as shown in Figure 4.4. As can be seen here, the emission at $\sim$ 933.4 nm corresponds to X^0 emission. An additional hole puts the quantum dot in the X^{1+} state as can be clearly observed in the photoluminescence-gate voltage map. The X^0 and X^{1+} transitions are $\sim$0.5 nm apart in the photoluminescence spectrum. The spectral separation between these two excitonic emissions are determined by the Coulomb and exchange interactions between charges inside the quantum [178].

The photoluminescence spectrum shown in Figure 4.4(a) is obtained at the bias volt-

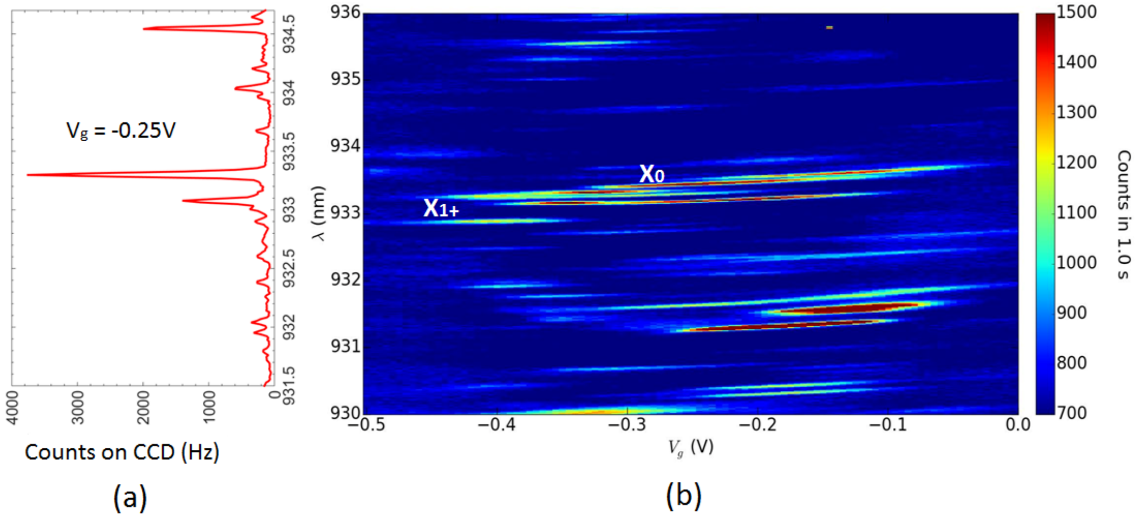

Figure 4.4: (a) The self-assembled InAs quantum dots in the sample at 4K are excited using a diode laser at 830 nm in a confocal geometry. Photoluminescence from X^0 exciton at a gate voltage of -0.25V is observed at 935 nm. The other lines in the spectrum correspond to emission from different quantum dots excited by the 830 nm laser. (b) Photoluminescence gate-voltage map of excitons in bulk GaAs: the gate voltage applied on the sample is tuned from -0.5V to 0V to observe the X^{1+} and X^0 exciton emissions from the sample.

age corresponding to the center of the plateau for each transition i.e. -0.25V for the X^0 transition. The quantum dots are excited using a diode laser at 830 nm to obtain photoluminescence from quantum dot excitons in bulk GaAs. Due to high density of quantum dots in the sample, a narrow bandpass filter is used to filter the emission from the quantum dot exciton at 934 nm. A 900 nm longpass filter is used to get rid of any excitation laser scattering being incident on the CCD. However, one can obtain more than one emitter with similar emission spectrum in the image. In order to avoid contribution from any neighbouring dots with similar spectrum, a real plane image is obtained to check the number of emitters. The progression to Fourier plane/k-space imaging is made after ensuring that there is only one emitter that has been spectrally filtered.

The angular distribution of radiation obtained at the back focal plane of the 0.68 NA microscope objective (effective NA = 1.36 due to SIL, n_{SIL}=2) is shown in Figure 4.5. The radiation pattern obtained on a CCD is converted from pixel number to angles. The CCD camera used for the imaging experiment is ICX829AL Sony Exview interline CCD. Each individual pixel is 8.2 μm x 8.4 μm. The characterization of the microscopic objective (aspheric lens in this case) at the back focal plane showed an aplanatic lens response as

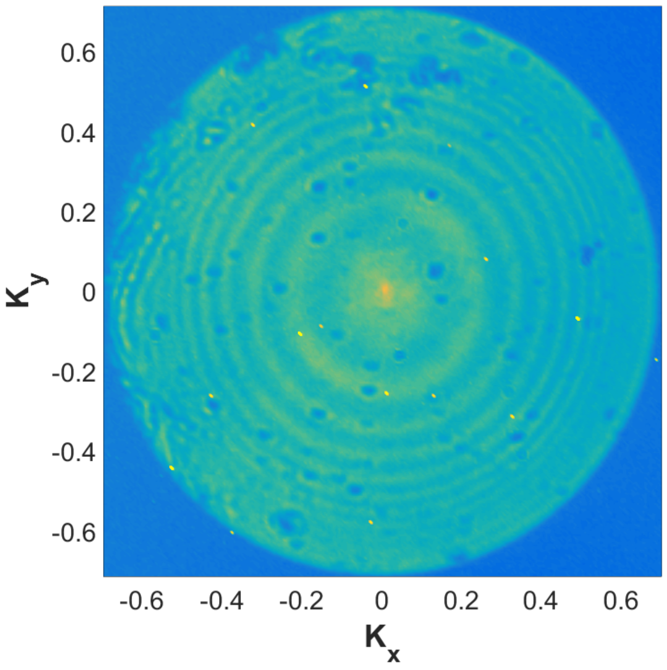

Figure 4.5: Photoluminescence from the the X^0 exciton from self-assembled InAs quantum dot in GaAs at 4K is obtained using an excitation laser at 830 nm. The gate voltage is kept at the centre of the exciton plateau i.e. -0.25V. Fourier plane image of the radiation from the X^0 exciton emission is obtained by placing a CCD at the back focal plane of the microscope objective. The effective numerical aperture of the microscope objective is 1.36 while the largest angle corresponds to 42.7^o. The axes in the figure represent the spatial frequencie K_x and K_y. Their values are given by $\sin(\theta)$, where θ is the angle of emission w.r.t. the optic axis. The rings in the Fourier plane image arise due to the response of the optical system.

was discussed in Chapter 2. An aplanatic microscope objective has a sinusoidal relationship between the position coordinate and the angle of emission at the back focal plane as explained by the Equations below, where a is the radius of the clear aperture of the lens and ρ_c corresponds to the centre of the image which implies along the optics axis of the objective lens.

Position coordinate on the image is converted to θ i.e. the angle of emission w.r.t. the optic axis of the lens using $\rho = \mathrm{f} \sin\theta$. The emission has a broad angular distribution profile with higher intensity at $\theta = 0^o$. The rings in the image arise due to the response of the optical system. In order to minimize the effect of diffraction (referred to as response of the optical system) observed in Fourier plane images, the imaging CCD is linearly translated to a position where the diffraction rings are the least pronounced in Fourier plane image. A higher NA microscope objective can also assist in elimination of diffraction rings in images.

4.3.2. BFP Imaging of Quantum Dots in Planar Microcavity

The planar cavity structure shown in Figure 4.2 tailors the angular distribution of radiation that is emanated from the emitters embedded in the sample. Back focal plane imaging of the radiation is a good way to study the match between the device design and the experimental realization of the device. The motivation to carry out back focal plane imaging was to ascertain the cause of fewer than expected photons from planar quantum dot microcavity samples. This can be explained by light being emitted at a higher angle than the NA of the microscope objective and thus not being captured by the microscope. Diffraction rings in Fourier/back focal plane images can also suggest light being clipped at the hard aperture of the microscope objective.

First, the photoluminescence map of the emitter is generated by running a bias voltage scan in order to determine the X^0 and X^{1-} exciton emission plateaus at a temperature of 4K under non-resonant excitation using a 830nm diode laser. The emitters are chosen based on their wavelength and are between 910 nm - 916nm, 930 nm - 936 nm and 950 nm - 956 nm. The choice of these wavelengths is limited by the choice of optical bandpass filters to filter out the emission for imaging of the radiation from the emitters. Each of the filters have a bandwidth of $\sim$0.8 nm and are tunable upto 5 nm in wavelength though at the cost of transmission efficiency. Transmission at the central wavelength for tuning of ANDV9415 filter between 950nm - 955nm has been shown in Chapter 2.

Emitter at 915.5 nm

The emission at 915.5 nm corresponds to negatively charged trion X^{1-} emission for the quantum dot as can be seen in Figure 4.6. The centre of the neutral exciton i.e. X^0 transition plateau corresponds to a wavelength of $\sim$ 912 nm for the studied quantum dot. Angular distribution of radiation from the X^{1-} exciton exhibits that most of the radiation is emanated at higher angles than the angles captured within the NA of the microscope objective, as can be seen in Figure 4.7. The significant feature in the radiation pattern is the presence of higher intensity rings oriented along two mutually perpendicular orientations. Since the X^{1-} exciton emission is circularly polarized, due to polarization dependent optical transmission across the optical system, it is suspected that one orientation is more pronounced than the other.

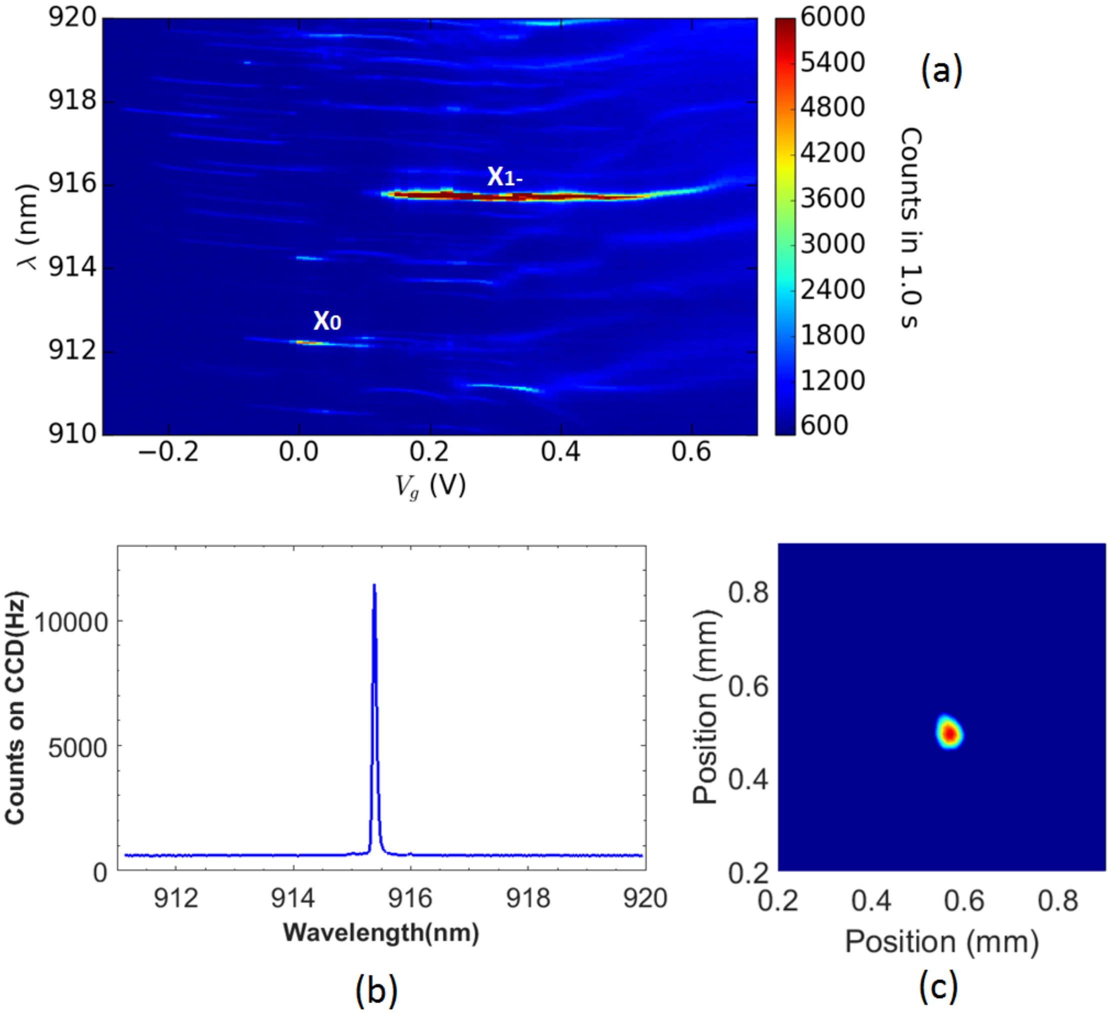

Figure 4.6: The self-assembled InAs quantum dots in planar dielectric membrane are at a temperature of 4K and photoluminescence is excited using a non-resonant laser at 830nm in a confocal setup. (a) Photoluminescence map for emission from a single quantum dot in the planar dielectric cavity sample in the 910 nm - 916 nm window: The gate voltage is varied from -0.3V to 0.7V in steps 0.01V for each step. (b) A single emitter at 915.5 nm is shown to be in its X^{1-} state here at a gate voltage of 0.22V. (c) Real plane imaging is carried out to verify single quantum dot as the photoluminescence spectrum can arise from multiple emitters in close vicinity.

$$I_{dipole}(\theta,\phi) = I_0 \frac{1}{cos\theta}\left(E_p E_p^* + E_s E_s^*\right) + I_{bg} \tag{4.1}$$

In order to understand the obtained radiation pattern theoretically, emission from an in-plane orientation of a dipole emitter is propagated across the device structure as shown in Equation (4.1). A flat background is taken for all angles to account for noise in the image.

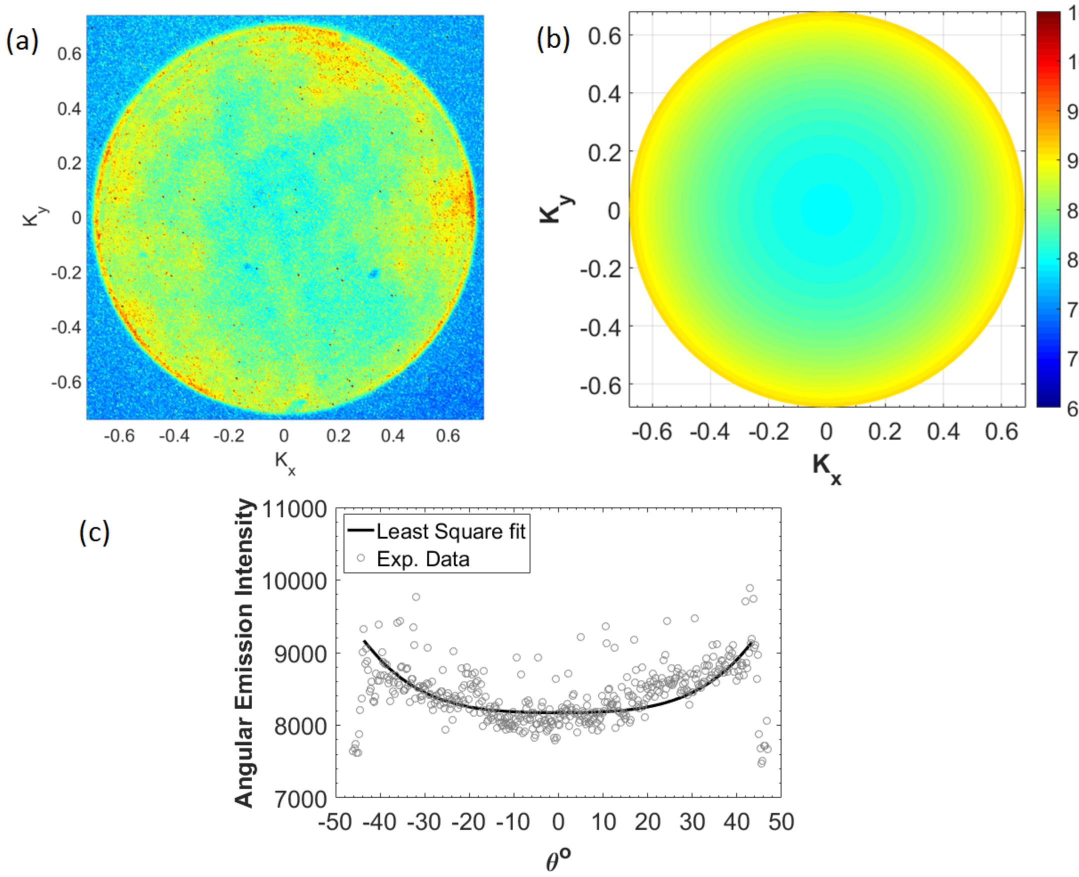

Figure 4.7: (a) Photoluminescence from X^{1-} exciton emission from single InAs quantum dot at 915.5 nm in the planar dielectric cavity at 4K under non-resonant excitation using a 830nm diode laser is imaged at the back focal plane of the microscope objective. The angular emission density reveals that most of the emitted radiation is at the edge of the collection cone of the microscope objective lens. The numerical aperture of the microscope objective is 0.68 with the maximum angle of collection being 42.7^o w.r.t. the optic axis. (b) Transfer-matrix model shows accurate match with the experimental data for emission at 915.5 nm. The model assumes azimuthally isotropic emission from a s-polarized dipole in the sample. The colour-scale is chosen to be the same as the experimental data. (c) A cross-section of the back focal plane experimental data K_y=0 is shown together with the theoretical least square fit.

The value of I_{bg} is chosen by matching the cross-section of the experimental Fourier plane image to the simulated one for a s-polarized in-plane dipole. A transfer-matrix model takes into account the reflection, transmission and refraction at the interfaces between different layers and accurately predicts the radiation pattern that is observed for the planar dielectric cavity VN2455. The details of the transfer-matrix have been presented before. For the X^0

neutral exciton, the radiation intensity for both s- and p-polarized dipoles are taken into account in the following way:

$$I_{X^0}(\theta,\phi) = \left[(I_0\frac{1}{cos\theta}E_pE_p^* + I_{bg})cos^2\phi + (I_0\frac{1}{cos\theta}E_sE_s^* + I_{bg})sin^2\phi\right] \tag{4.2}$$

$$I_{X^{1-},p(s)}(\theta,\phi) = I_0\frac{1}{cos\theta}E_{p(s)}E_{p(s)}^* + I_{bg} \tag{4.3}$$

In order to take the circular polarization of the emission into account for X^{1-}, the angular emission profile is assumed isotropic for all azimuthal angles at the back focal plane. As shown in Equation (4.3), there is no dependence on azimuthal angle ϕ for the intensity. This yields a symmetric image for the negative trion, while for the neutral exciton an axis of symmetry coincident with the orientation of the dipole is observed. For the trion at 915.5 nm, I_0 = 8790 ± 460 and I_{bg} = 5258 ± 149, respectively. The values of I_0, I_{bg} and the polarization of the photon are the only tuning parameters to match the experimental data. The fit is obtained using a least-square fitting model in Matlab. The R^2 statistics measures the accuracy of the fit in explaining the variation of the experimental data i.e. R^2 is the square of the correlation between the response values and the predicted response values and is obtained to be 0.9451. It implies that the fit explains 94.51% of the total variation in the data about the average [179].

Emitter at 934 nm

The emission at 934 nm corresponds to negatively charged trion X^{1-} emission for the quantum dot as can be seen in Figure 4.8. The centre of the neutral exciton i.e. X^0 transition plateau corresponds to a wavelength of $\sim$ 930 nm for the studied quantum dot. X^{1-} emission is spectrally $\sim$4 nm separated from the X^0 emission due to Coulomb interaction on addition of an extra electron in the quantum dot.

A near-Gaussian emission pattern is observed for 933 nm emission from the sample (see Figure 4.9(a)). With a near-Gaussian, directive angular radiation, microscope objectives with modest NA ($\leq$ 0.7) can be used to collect photons efficiently from the sample.

Again an in-plane dipole with the polarization of the photon being 'p' or 's' is undertaken to model the experimentally obtained data. From the cross-section fit for the back focal plane image for the emitter at 934 nm, I_0 = 37313 ± 2090 and I_{bg} = 0. The theoretical model deviates from the experimental data for the emitter at 934 nm which can arise due

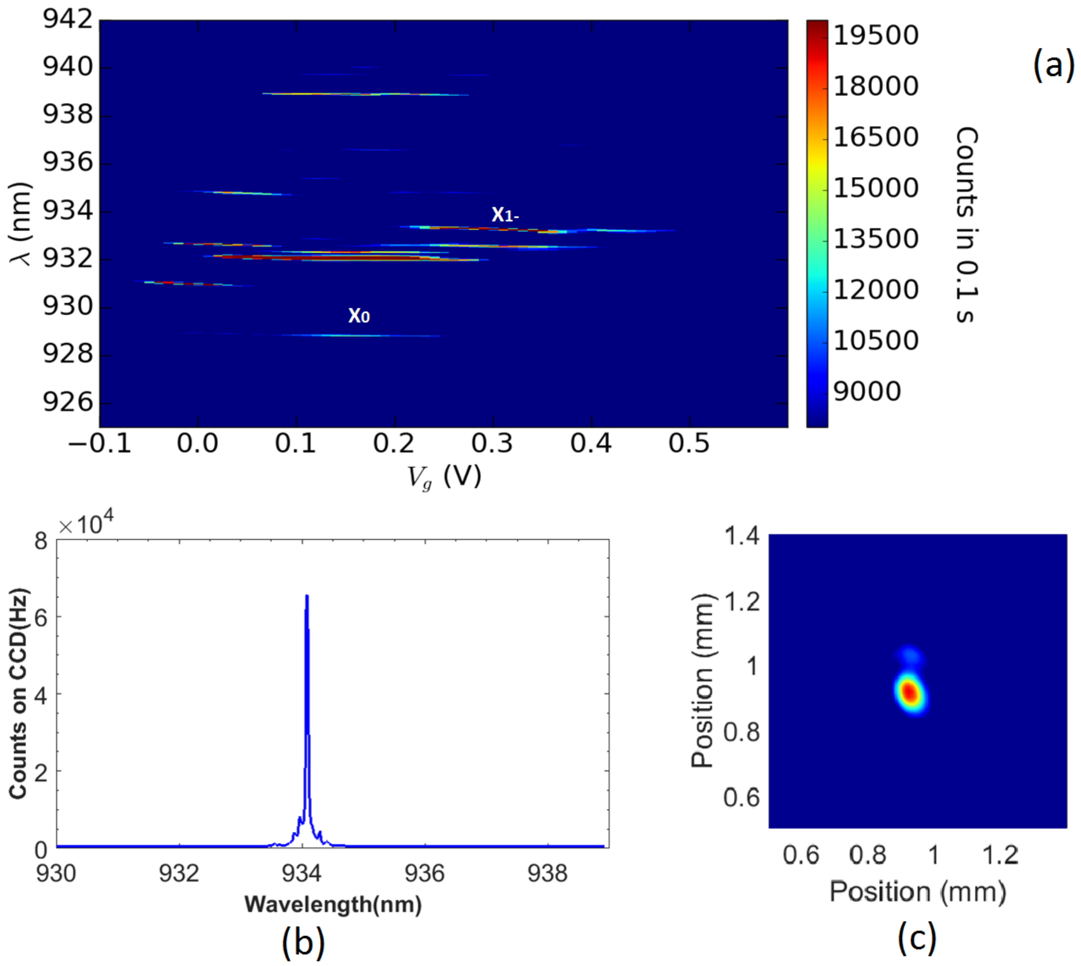

Figure 4.8: (a) Photoluminescence map for emission from a single InAs quantum dot at 4K in the planar dielectric cavity sample in the 930 nm - 935 nm window is generated by exciting the sample using a non-resonant laser at 830nm. The gate voltage on the sample is varied from -0.1V to 0.5V. (b) Photoluminescence from X^{1-} exciton at 934 nm in the planar dielectric membrane is isolated for Fourier microscopy by using a bandpass optical filter. The bias voltage is kept at 0.3V to stay at the center of the plateau for the trion emission. (c) Real plane image of the emitter is taken to verify the number of quantum dots contributing to the emission at 934nm.

to the angular intensity response of the objective itself. The contribution to the emission from neighbouring quantum dots at the same wavelength can result in the deviation from the theoretical model presented for the emitter at 934 nm. The parameter R^2 = 0.9784 is obtained for the emission at 934 nm.

The angular intensity response of the device changes from light being confined at edges to near Gaussian distribution as a function of wavelength of emission. This behaviour is theoretically expected from the device as a change in wavelength leads to different phase

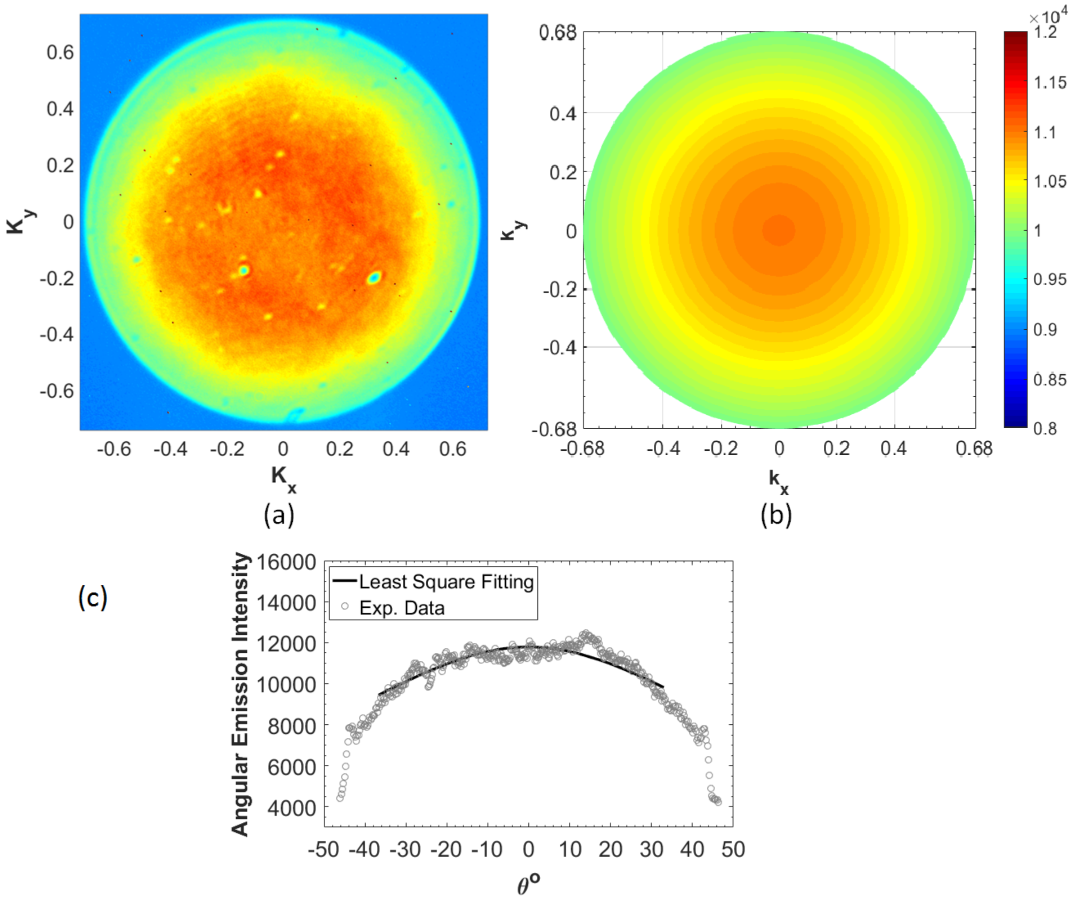

Figure 4.9: (a) Fourier plane image obtained for emission at 934 nm from the negatively charged trion for the InAs quantum dot exhibits near-Gaussian profile. Photoluminescence is excited using a 830nm non-resonant laser and filtered out using an optical bandpass optical filter. (b) Theoretical prediction of angular distribution of radiation from X^{1-} exciton emission from quantum dot at 934 nm in the planar dielectric cavity assumes an in-plane dipole radiation. The emission is assumed to be azimuthally isotropic as the trion emission is circularly polarized. (c) A cross-section of the back focal plane experimental data K_y=0 is shown. The corresponding cross-section at K_y=0 is shown for simulated pattern.

term ($e^{ikn_l d_l}$, where n_l is the refractive index of the layer and d_l is the thickness) on propagation through the device. As was discussed in Chapter 1, the cavity itself shows discrete angular resonances for wavelengths i.e. for different wavelengths, the angular radiation profile is expected to be different. The modified interference relations require the angular distribution to change with wavelength. The in-plane orientation of the dipole also has a significant influence on the radiation profile as can be observed between the two emitters shown here. While the emitter at the wavelength of 915.5 nm was simulated using a s-polarized in-plane dipole emission, p-polarized emission was used to simulate the pattern for emitter at 934nm.

4.4 Polarization Sensitive Fourier Plane Imaging

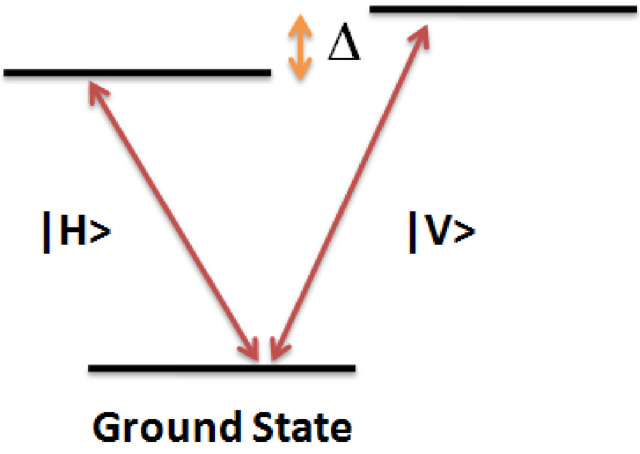

Figure 4.10: (a) Neutral exciton emission exhibits fine structure splitting which gives rise to linearly polarized $|H>$ and $|V>$ photons.

Polarization-resolved k-space imaging can be used to ascertain the orientation of the emission dipole. This approach is useful for studying neutral exciton emission. The neutral exciton X^0 has two linearly polarized emissions (shown in Figure 4.10) due to the structural asymmetry of a self-assembled InAs quantum dot. Based on which of the two linearly polarized transitions is sampled, two mutually orthogonal orientations can be observed in experiment.

Photoluminescence is excited in the quantum dot using a non-resonant laser at 830 nm at a sample temperature of 4K. The gate voltage is tuned from -0.2V to 0.6V in steps of 0.01V. The photoluminescence thus obtained is shown as a photoluminescence-gate voltage map for the planar dielectric membrane sample in Figure 4.11. The angles on the linear polarizer for the two transition are identified by rotating the polarizer in front of the collection lens in photoluminescence spectroscopy mode. Polarization-resolved imaging is performed by placing the linear polarizer in the photoluminescence path together with the bandpass filter before the CCD at the back focal plane.

As can be observed in Figure 4.12, the axis of symmetry in the image corresponds to the axis of the dipole i.e. the dipole orientation. In absence of the linear polarizer,

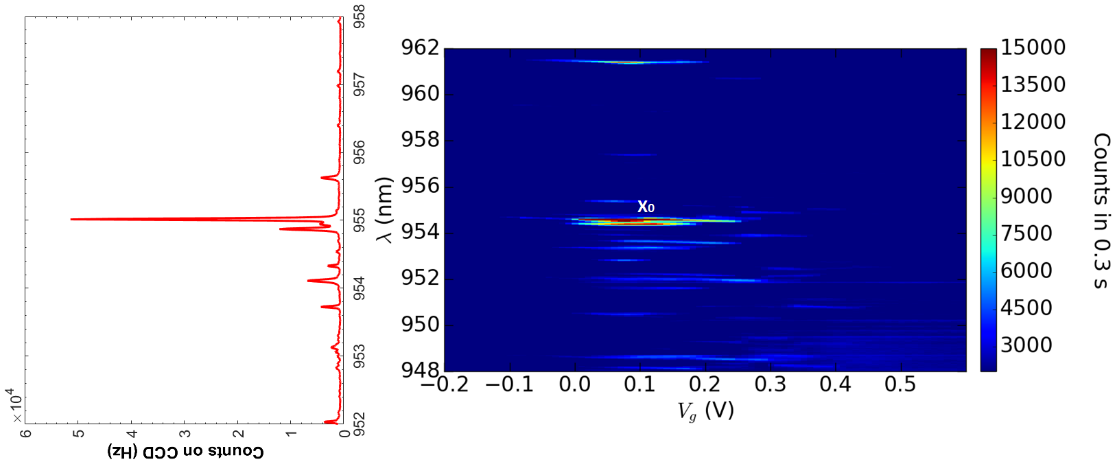

(a)

(b)

Figure 4.11: (a) Neutral exciton emission is observed at a bias of 0.1V in the planar dielectric membrane. Self-assembled InAs quantum dots at 4K are excited using a non-resonant laser at 830nm. Due to the fine structure splitting in neutral exciton emission, the two peaks are resolved using a linear polarizer in the collection path. (b) Photoluminescence map for emission from quantum dots in the planar dielectric cavity sample in the 950 nm - 960 nm window is shown here. The gate voltage is varied from -0.2V to 0.6V in steps of 0.01V. Each bright point on the image corresponds to a photoluminescence signal such as the one shown on the left.

the radiation pattern was observed to be circularly symmetric as in that case it can again be explained by circularly degenerate dipole emission. The cross-sections are shown for $K_x = 0$ and $K_y = 0$ for the two dipole orientations. As can be observed from the cross-sections, the cross-sectional cut along $K_y = 0$ of one image matched with the cross-section along $K_x = 0$ of the orthogonal polarization/orientation. The photoluminescence emission exhibits Gaussian radiation pattern in back focal plane imaging i.e. brighter emission for smaller angles w.r.t. the optic axis. The change in intensity due to sampling of orthogonal polarization of the photon is expected to happen because of the polarization-dependent response of the microscope.

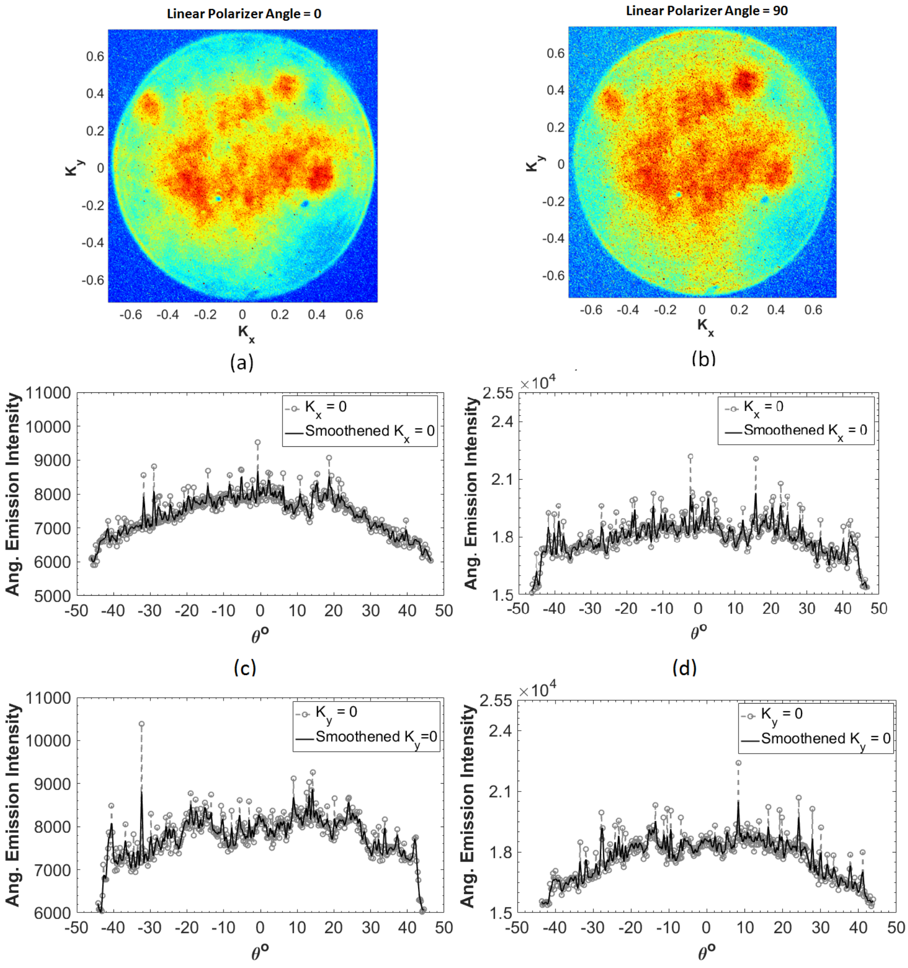

(a) (b)

(c) (d)

(e) (f)

Figure 4.12: (a),(b) Photoluminescence from the two linearly polarized emissions of the X^0 exciton in the planar dielectric cavity sample is imaged at the Fourier plane of the microscope objective. The self-assembled InAs quantum dot at 955nm is excited using a non-resonant laser at 830nm at a temperature of 4K. The bias voltage is chosen to be at the centre of the neutral exciton emission plateau at 0.1V. The Fourier plane image shows brighter emission for smaller angles and the rotation angle of the linear polarizer samples out two mutually orthogonal azimuth orientations for the two transitions. (c),(d) Cross-sections of the back focal plane images for the two transitions are shown along $K_x = 0$. (e),(f) Cross-sections of the back focal plane images are shown along $K_y = 0$.

4.5 Summary

In summary, back focal plane imaging of single quantum dots in planar dielectric membrane is carried out at multiple wavelengths. An in-plane dipole orientation is simulated to match the experimental data for emitters at 915 nm and 934nm in the planar microcavity sample. By placing a linear polarizer before the imaging CCD at the Fourier plane, polarization-resolved Fourier plane imaging can be carried out to ascertain the orientation of the dipoles in a neutral exciton. A close match (R^2 = 0.9451) between theory and experimental back focal plane image was observed for emitter 915.5 nm in sample VN2455 without SIL. A constant background, I_{bg}=5258 ± 149, was added to the simulated pattern to accurately simulate the experimental image and a value of 8790 ± 460 was obtained for the coefficient I_0 by least square fitting, in the case of the emitter at 915.5 nm. For the emitter at 934 nm, the coefficient I_0 = 37313 ± 2090 was obtained from the least square fit. Also, the in-plane orientation used for the two emitters were orthogonal to each other. Although the device sustains bright quantum dots over a large wavelength range, the angular response was designed for an emission wavelength of 950 nm. The relative ease of electrical charging and high photon counts (shown in Chapter 1) confirm these devices to be a promising solid-state source of single photons essential for realization of quantum technologies.

However, the fewer photon counts at saturation than theoretically expected efficiency of 27% from membrane samples (refer to Chapter 1) can be further investigated by using microscope objectives with different NAs. A high numerical aperture should allow maximum collection of photons and would help eliminate some possible reasons for the loss of photons. A relatively easily upgrade is a single aspheric lens with NA = 0.77 with the same working distance as the one with NA = 0.68. Further, if the fabrication process allows it, a polymer/dielectric layer/epoxy with a low refractive index can be spin coated at the bottom of the sample and then thermally deposited Gold on top of GaAs can be flip-bonded onto the epoxy layer. The use of a low-index spacer between the Gold mirror and GaAs can potentially avoid photons being lost at the semiconductor-metal interface [180] [181].

Chapter 5

Defocused Imaging of InAs Quantum Dots

The Stranski-Krastanov growth mode elongates the quantum dots along the crystal axis of the GaAs substrate. This structural asymmetry of the self-assembled quantum dot lifts the degeneracy and linearly polarized photons are observed in X^0 exciton emission. In negatively charged trion, X^{1-}, the emission is circularly polarized. Since, the emission intensity from a dipole emitter is dependent on the orientation of the emission dipole as has been observed from the angular distribution of radiation, the knowledge of the orientation can assist in design of samples for higher photon collection efficiency. The complete three-dimensional orientation of the emission dipole in quantum dot excitons can be obtained by defocused imaging of the dipole radiation. Defocused imaging experiment on quantum dots is an extension of the Fourier microscopy approach used to ascertain the possible causes of fewer than expected photon counts from quantum dots in planar microcavity sample.

5.1 Defocused Imaging

The intensity distribution from a point source at infinity when focused using a high numerical aperture (NA) lens can be expressed using vector optical diffraction theory [182] [183]. Under the assumption of aplanatic imaging i.e. following Abbe's sine law, a reference sphere can be drawn around the focus of the lens.

A ray emanated by the dipole emitter at angle θ_1 from optic axis in the object space refracts at the reference sphere 1 in object space. Light is focused in the image space where reference sphere 2 acts as the focusing objective. The Abbe's sine law relates the angle

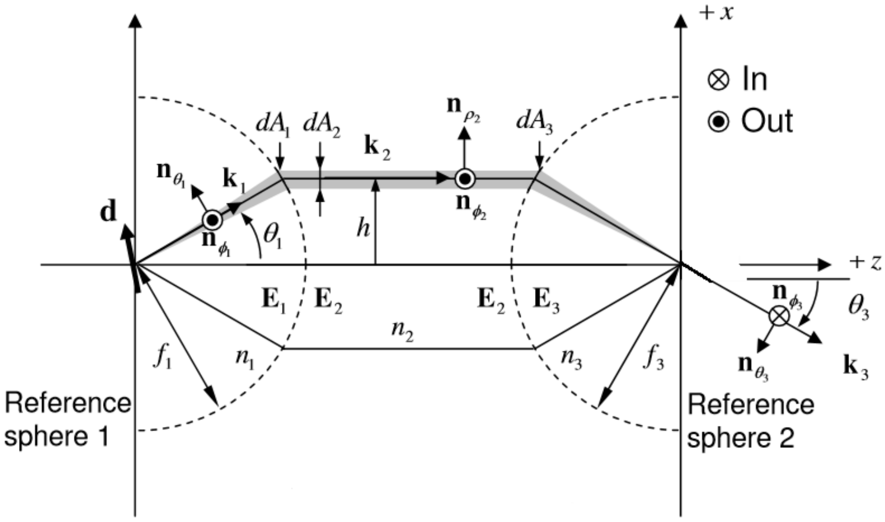

Figure 5.1: The optical system configuration used to image an arbitrarily oriented dipole orientation ’d’ [184].

of light w.r.t. the optic axis in the object space to the angle in the image space given by $Mn_1 \sin\theta_1 = n_3 \sin\theta_3$, where n_1 and n_3 are refractive indices in the object and image spaces, respectively, and M is the magnification determined by the ratio of numerical aperture in the object space and that in the image space. The setup shown in Figure 5.1 relates the azimuthal angles in the object space and image space as $\phi_1 = \phi_3 - \pi$ [184]. Further the law of conservation of energy requires the inverse cosine apodization for angles w.r.t. the optic axis as was discussed for angular representation of electromagnetic fields in the theory section in Chapter 1 [182] [185] [186].

The theory makes use of angular spectrum representation of electromagnetic fields and can express the electric and magnetic fields at any point P in image space by use of three integrals I_0, I_1 and I_2. The coordinates of P in spherical coordinate system is given r_p, θ_p, ϕ_p. Taken from reference [182], the integrals are defined as following:

$$I_0 = I_0(kr_p, \theta_p, \alpha) = \int_0^\alpha cos^{\frac{1}{2}} sin\theta(1 + cos\theta) J_0(kr_p sin\theta sin\theta_p) e^{ikr_P cos\theta cos\theta_P} d\theta \tag{5.1}$$

$$I_1 = I_1(kr_p, \theta_p, \alpha) = \int_0^\alpha cos^{\frac{1}{2}} sin^2\theta J_1(kr_p sin\theta sin\theta_p) e^{ikr_P cos\theta cos\theta_P} d\theta \tag{5.2}$$

$$I_2 = I_2(kr_p, \theta_p, \alpha) = \int_0^\alpha cos^{\frac{1}{2}} sin\theta(1 - cos\theta) J_2(kr_p sin\theta sin\theta_p) e^{ikr_P cos\theta cos\theta_P} d\theta \tag{5.3}$$

The expression for electric and magnetic fields along the x-, y- and z-axes of Cartesian frame make use of the above integrals.

$$e_x(p) = -iA(I_0 + I_2 cos2\phi_p) \tag{5.4}$$

$$e_y(P) = -iAI_2 sin2\phi_p \tag{5.5}$$

$$e_z(P) = -2AI_1 cos\phi_p \tag{5.6}$$

$$h_x(P) = -iAI_2 sin2\phi_p \tag{5.7}$$

$$h_y(P) = -iA(I_0 - I_2 cos2\phi_p) \tag{5.8}$$

$$h_z(P) = -2AI_1 sin\phi_p \tag{5.9}$$

The above equations can analytically represent the field at any point in image space based on the coordinates. Based on this approach, the field distribution at the real plane image of a dipole emitter can be thus determined. The dipole emitter can be simulated as a source of plane waves. In order to determine the full three dimensional orientation of the dipole emitter itself, one has to systematically introduce an aberration into the optical system or move the emitter away from the focus of the objective lens to use a technique called defocused imaging.

5.2 Model for Defocused Imaging

Defocused imaging has been used to ascertain the three-dimensional orientation of single molecules [185] [187] and colloidal quantum dots [188] [189]. Information extracted from dipole orientation measurements can facilitate the study of dependence of emitter's emission intensity on orientation [185]. When a dipole emitter is buried inside a multilayer sample, the defocused images can be used to study the structure of the sample as well [188].

The radiation pattern emitted by an exciton in a single InAs quantum dot in farfield is described as the emission pattern of an oscillating electric dipole. By use of spectral filtering using a bandpass optical filter, and charge tuning of the photoluminescence emission from the quantum dot excitons, single emitters can be super-resolved within the irradiated focal volume. In theory, in order to completely describe the emission pattern from a quantum emitter, a weighted-superposition of three mutually orthogonal dipoles is taken [188]. Self-assembled InAs quantum dots, however, have a structural asymmetry which only allows the existence of in-plane dipole orientations. In order to account for this in numerical simulations, the weight of the vertical dipole is taken as null i.e. $\kappa = 0$. Mathematically,

$$P = \kappa I_z + (1-\kappa)(\frac{1-\eta}{2} I_x + \frac{1+\eta}{2} I_y) \tag{5.10}$$

Based on a Matlab model for defocused imaging made available online by the research group of J. Enderlein [190], images of emission from a dipole emitter can be generated for arbitrarily oriented emitters in multilayer quantum dot samples. The Matlab model makes use of the transfer-matrix model presented in Chapter 1 to determine the angular distribution of radiation from an electric dipole embedded in a medium. With the knowledge of relative weights of x-, y- and z-dipole in emission, angular distribution of radiation is obtained. Further the knowledge of magnification and NA of the optical system, the relative orientation of the dipole frame w.r.t. the lab frame (see Theory of Defocused Imaging in Chapter 1) and the pixel size of the imaging detector can allow accurate simulation of defocused images. The model allows two different configurations to be used for the in-plane dipoles: (a) separate I$_x$ and I$_y$ dipoles with any intensity ratio and (b) I$_{xy}$ dipole with circularly degenerate dipole emission. Mathematically, such I$_{xy}$ dipole emission generates the same pattern as for separate I$_x$ and I$_y$ dipoles with equal emission strengths.

5.2.1. In-plane Dipole in Bulk GaAs

For an in-plane y-dipole embedded in GaAs at a distance of 136.5 nm from GaAs-air interface, when defocused towards an aplanatic microscope objective with a numerical aperture of 1, the images on a CCD can be generated for defined defocusing distance towards the microscope objective as shown in Figure 5.2. Typically, the sample has to be defocused towards the objective lens by distance of $\sim 1.3\mu$m in order to observe the orientation of the dipole. The dipole frame is assumed to be aligned with the lab frame in Figure 5.2.

The output space is air. The layer stack above the dipole emitter embedding layer is represented by variable n$_0$ which is only air in this case. The embedding medium is

Layer	Ref. Index	Thickness (nm)	Repeats
air	1	-	1
GaAs	3.56	273	1
GaAs	3.56	-	1

Table 5.1: Layer stack for y-dipole in bulk GaAs

Layer Representation	Ref. Index	Thickness (nm)
n_0	[1]	[ ]
n_1	n_{GaAs}	d_1 = 273nm
n_2	[n_{GaAs}]	[ ]

represented by n_1. Since the quantum dot is buried at the centre of a 273 nm thick GaAs layer, the embedding medium is GaAs with a thickness of 273 nm. In the model, the variable z represents the distance of the dipole emitter from the embedding layer - top stack interface. The layer stack underneath the dipole embedding layer is represented by n_2, which is again GaAs in this case. For the media at the two extreme ends of the sample, no thickness is taken in simulation.

In the Matlab model, the value κ i.e the weight of the emission intensity of the z-dipole is kept as zero due to in-plane nature of dipole emission from InAs quantum dots (κ is represented as ratio in the model). The weight of the x-dipole is also kept as zero for simulation of images from y-dipole i.e. η=1 (η is represented as κ in the Matlab model). The value of h is kept at 136.5 nm (in Matlab, this variable is called z which is the distance of the dipole emitter from the top interface of the embedding layer). A magnification of 520 and NA of collection objective is kept at 1 for all images. The values of Ω, ω and ϕ are kept as zero for the simulated images shown in Figure 5.2.

In practical experimental situations, there are several sources of mechanical/optical misalignment which can induce an angle between the dipole frame and the lab frame. In Figure 5.3, the effect of these relative angles on defocused images of y-dipole is shown. The angle ω is the relative azimuthal angle between the dipole and lab frames, and Ω is the relative polar angle. So, Ω introduces out-of-plane tilt while ω introduces azimuthal rotation of the defocused images.

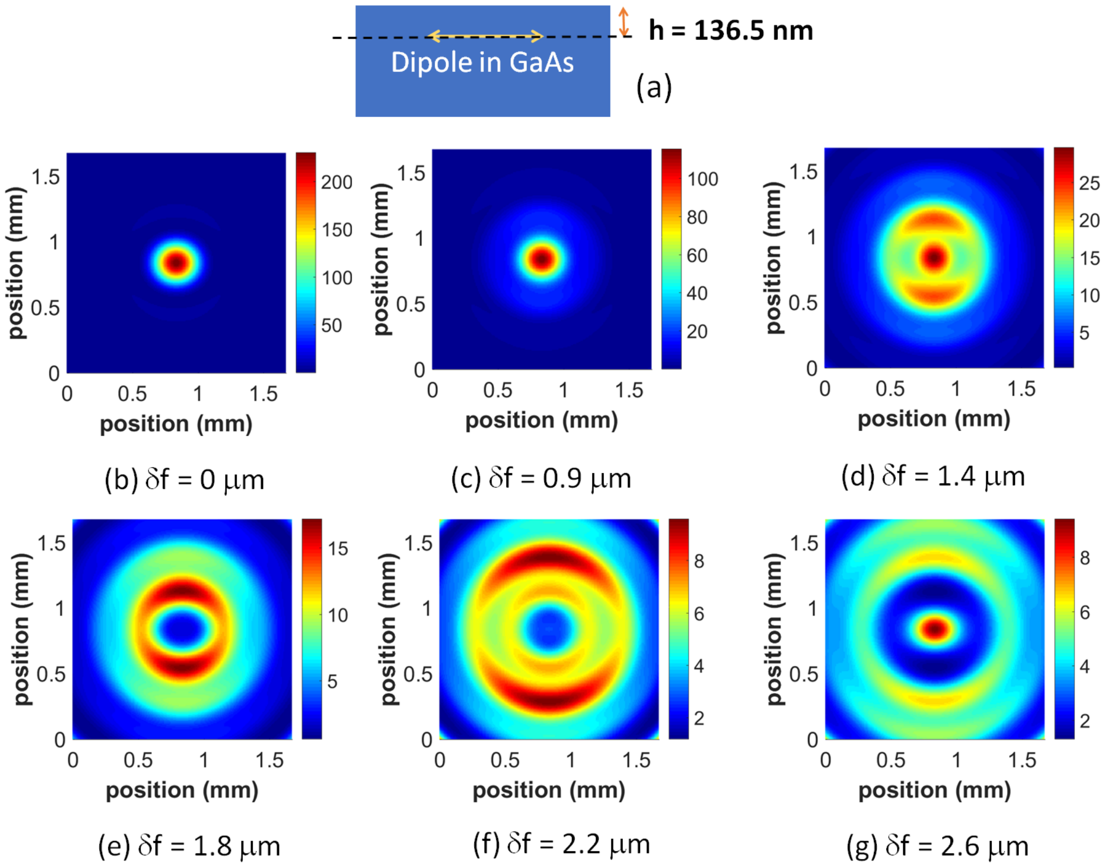

(b) δf = 0 μm (c) δf = 0.9 μm (d) δf = 1.4 μm

(e) δf = 1.8 μm (f) δf = 2.2 μm (g) δf = 2.6 μm

Figure 5.2: Simulation of an in-plane y-dipole in bulk GaAs when defocused towards the microscope objective by (b) 0μm, (c) 0.9μm, (d) 1.4μm, (e) 1.8μm, (f) 2.2μm and (g) 2.6μm.

5.2.2. In-plane Dipoles in Planar Microcavity Sample

In order to obtain essential information about the orientation of dipoles from the defocused images of InAs quantum dots in the planar microcavity sample VN2455, the Matlab model is adapted to simulate images of dipole emitters in multilayer cavities. Similar to the approach used in Chapter 4, first the angular distribution of radiation is obtained for the in-plane x-dipole and y-dipole, and the out-of-plane z-dipole using the layer stack given below. In the Matlab model for sample VN2455, κ=0 and η=-1 for x-dipole, z = 471 nm i.e. the distance of dipole emitter from air-GaAs interface, magnification = 160, NA = 0.68 for all images. The value of Ω is varied at three defocusing distances in the simulated images shown in Figure 5.4 at a wavelength of 915.5 nm in the planar microcavity sample.

The output space is again air in this case. The layer stack above the emitter layer is represented by variable n_0 which is only air in this case. The embedding medium is GaAs with a thickness of 496 nm with z = 471 nm being the distance of the dipole emitter from

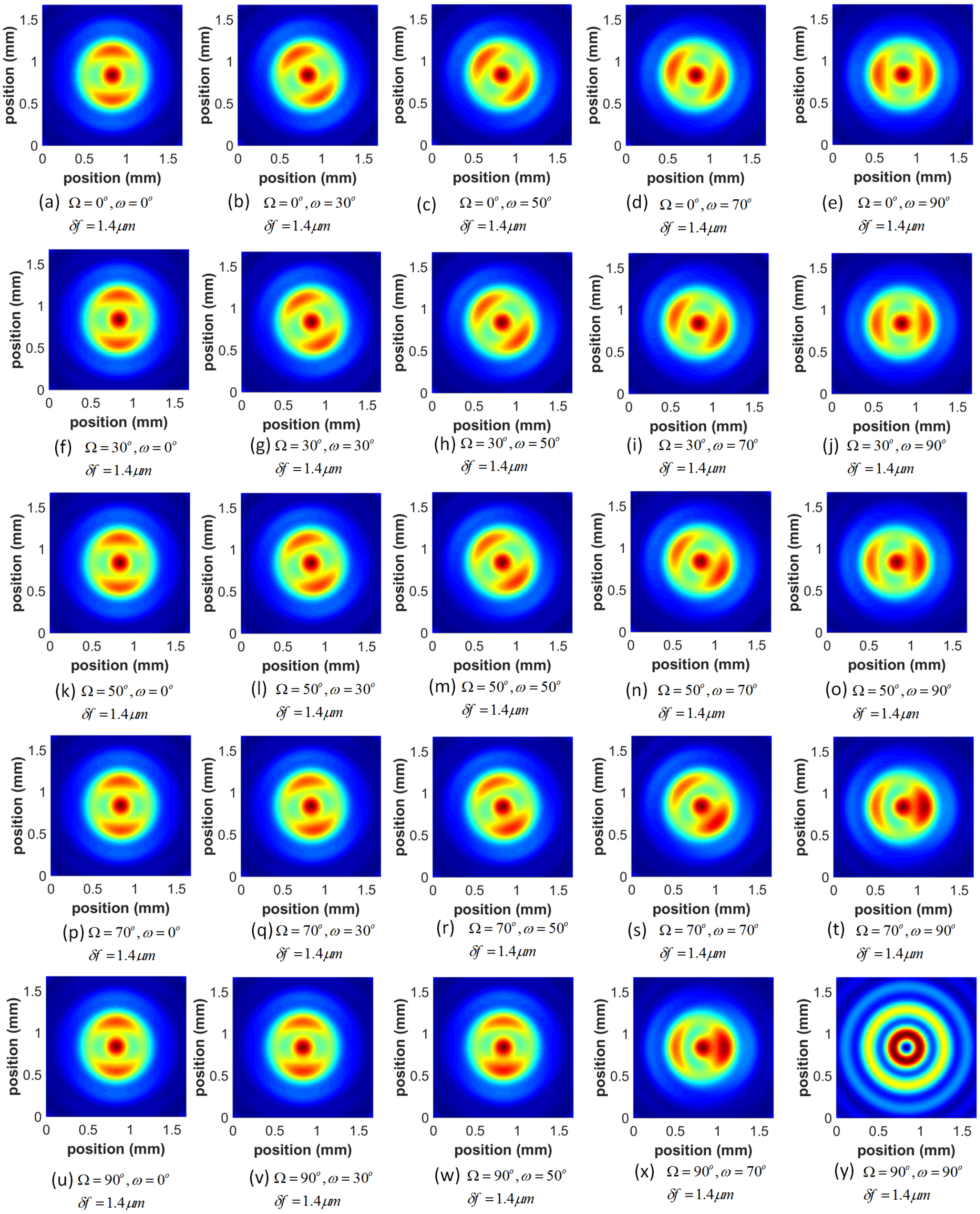

(a) $\Omega=0^\circ,\omega=0^\circ$ $\delta f=1.4\mu m$
(b) $\Omega=0^\circ,\omega=30^\circ$ $\delta f=1.4\mu m$
(c) $\Omega=0^\circ,\omega=50^\circ$ $\delta f=1.4\mu m$
(d) $\Omega=0^\circ,\omega=70^\circ$ $\delta f=1.4\mu m$
(e) $\Omega=0^\circ,\omega=90^\circ$ $\delta f=1.4\mu m$
(f) $\Omega=30^\circ,\omega=0^\circ$ $\delta f=1.4\mu m$
(g) $\Omega=30^\circ,\omega=30^\circ$ $\delta f=1.4\mu m$
(h) $\Omega=30^\circ,\omega=50^\circ$ $\delta f=1.4\mu m$
(i) $\Omega=30^\circ,\omega=70^\circ$ $\delta f=1.4\mu m$
(j) $\Omega=30^\circ,\omega=90^\circ$ $\delta f=1.4\mu m$
(k) $\Omega=50^\circ,\omega=0^\circ$ $\delta f=1.4\mu m$
(l) $\Omega=50^\circ,\omega=30^\circ$ $\delta f=1.4\mu m$
(m) $\Omega=50^\circ,\omega=50^\circ$ $\delta f=1.4\mu m$
(n) $\Omega=50^\circ,\omega=70^\circ$ $\delta f=1.4\mu m$
(o) $\Omega=50^\circ,\omega=90^\circ$ $\delta f=1.4\mu m$
(p) $\Omega=70^\circ,\omega=0^\circ$ $\delta f=1.4\mu m$
(q) $\Omega=70^\circ,\omega=30^\circ$ $\delta f=1.4\mu m$
(r) $\Omega=70^\circ,\omega=50^\circ$ $\delta f=1.4\mu m$
(s) $\Omega=70^\circ,\omega=70^\circ$ $\delta f=1.4\mu m$
(t) $\Omega=70^\circ,\omega=90^\circ$ $\delta f=1.4\mu m$
(u) $\Omega=90^\circ,\omega=0^\circ$ $\delta f=1.4\mu m$
(v) $\Omega=90^\circ,\omega=30^\circ$ $\delta f=1.4\mu m$
(w) $\Omega=90^\circ,\omega=50^\circ$ $\delta f=1.4\mu m$
(x) $\Omega=90^\circ,\omega=70^\circ$ $\delta f=1.4\mu m$
(y) $\Omega=90^\circ,\omega=90^\circ$ $\delta f=1.4\mu m$

Figure 5.3: Simulation of defocused images of in-plane y-dipole in the bulk GaAs sample when defocused by a distance of 1.4μm towards the microscope objective as a function of the angles between the axes in dipole frame and lab frame. Here Ω is the angle between the z-axes of dipole frame and lab frame, and ω is the relative azimuthal angle. The magnification of the system is kept at 520 for the simulated images.

the embedding layer - top stack interface. There is a superlattice of AlAs/GaAs, followed by a layer of GaAs and gold mirror in the stack underneath the emitter layer, represented by n_2.

Layer	**Ref. Index**	**Thickness (nm)**	**Repeats**
air	1	-	1
GaAs	3.56	496	1
AlAs/GaAs superlattice	n_{GaAs}= 3.56, n_{AlAs}=2.95	each 2	25
GaAs	3.56	46	1
Gold	0.19+ 5.84i	-	1

Table 5.2: Layer stack for planar microcavity sample VN2455 without SIL

Layer Representation	**Ref. Index**	**Thickness (nm)**
n_0	[1]	[ ]
n_1	n_{GaAs}	d_1 = 496
n_2	[n_{AlGaAs}, n_{GaAs}, n_{Gold}]	d_2 = [100, 46]

5.3 Imaging of InAs Quantum Dots in Planar Microcavity

Planar cavity sample VN2455 described in Chapter 1 and 2 is used as the quantum dot sample for defocused imaging experiment. The sample is mounted on top of x-, y-, z- nanopositioners inside a cryostat at 4K. For sample with solid immersion lens (SIL), the effective numerical aperture (NA) is 1.36. In absence of SIL, where n_{SIL} = 2, the NA of the optical system is 0.68. An astro-photography CCD camera Lodestar X2 with a Sony chip ICX829AL was used for imaging. The choice of camera was made taking into account the fragility of the microscope head on top of the cryostat, enhanced detection in the 920 nm - 980 nm wavelength window and size of the chip compared to the clear aperture of the microscope objective used in experiments. The pixel size on the CCD chip is 8.2μm × 8.4μm and it has 752 × 580 pixels which is sufficient photosensitive area to obtain images for defocused imaging experiment. Non-resonant excitation of the quantum dots is carried out using a continuous wave laser at 830 nm in a confocal microscope setup at a sample temperature of 4K. Photoluminescence imaging pathway includes narrow bandpass filter, longpass filter and a focusing lens before the CCD as shown in the setup in Chapter 2.

In order to study single quantum dots, a photoluminescence gate voltage map of the quantum dot emission is generated at a sample temperature of 4K to identify the exciton emission. In order to spectrally filter out a single transition, the narrow bandpass filter is mounted on top of a turret mount from Thorlabs and is rotated in the out-of-plane direc-

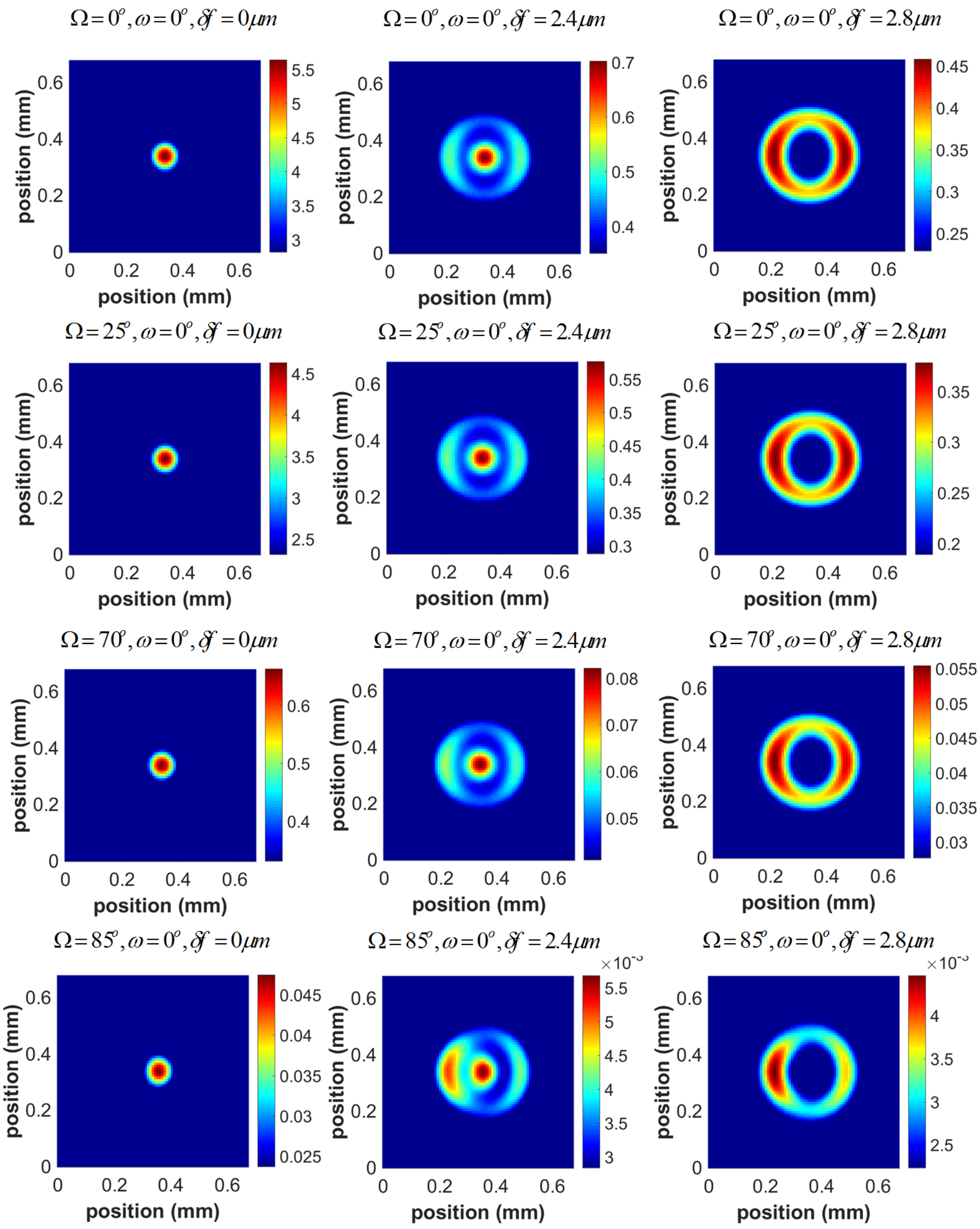

Figure 5.4: Simulation of defocused images of in-plane x-dipole in the planar microcavity sample VN2455 (no SIL) when defocused towards the microscope objective as a function of the angles between the axes in dipole frame and lab frame. Here Ω is the angle between the z-axes of dipole frame and lab frame, and ω is the relative azimuthal angle. The magnification of the system is 160, NA = 0.68, pixel size is 8.4μm × 8.4μm for the simulated images.

tion. The filter has a bandwidth of ~0.8 nm. Despite the high density of quantum dots in the sample, by virtue of confocal microscopy, charge tuning and spectral filtering, single quantum dots can be observed in photoluminescence spectroscopy.

For imaging, a lens with a large focal length (>15 cm to avoid pixelated images) is mounted in the emission pathway and a CCD is placed at the focus of it. In order to obtain the three-dimensional orientation of the dipole, the emitter is defocused towards the microscope objective and the real plane images are acquired on the CCD. The microscope objective has a NA of 0.68 with the maximum collection angle being θ_{max}= 42.8^o. Images of the sample were acquired for less than a second on the CCD when the emitters are in focus, and with higher integration times as the defocusing distance increases. The magnification is calculated to be ∼160 for the optical assembly when the emitter is at focus.

5.3.1. Emitter at 915.5 nm

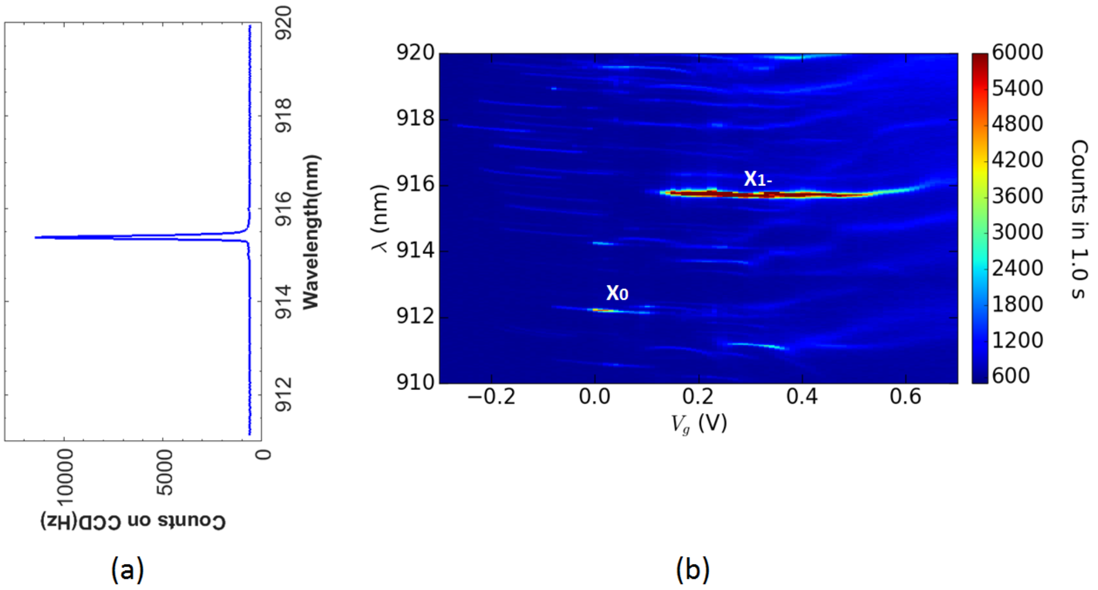

Figure 5.5: (a) Photoluminescence spectrum obtained from a single quantum dot at 4K excited using non-resonant laser at 830nm at V$_g$ = 0.22 V. (b) Photoluminescence-gate voltage map is generated to identify the excitons in the quantum dot. For X^{1-} exciton at 915.5 nm in sample VN2455, the center of the emission plateau is at 0.3V. The center of the neutral exciton emission is observed at 0V.

For defocused imaging of the X^{1-} exciton from sample VN2455 as shown in the photoluminescence gate voltage map in Figure 5.5(b), the photoluminescence emission (shown in Figure 5.5(a) is filtered using a narrowband filter from Andover Corporation. The addition of optical filter walks the beam and thus after the filter is added re-optimization of the confocal microscope w.r.t the sample is often necessary. Once the photoluminescence is filtered, a lens with a focal length of 25cm is added in the optical path. A CCD is placed at the image plane of the lens to capture real plane images from the quantum emitter.

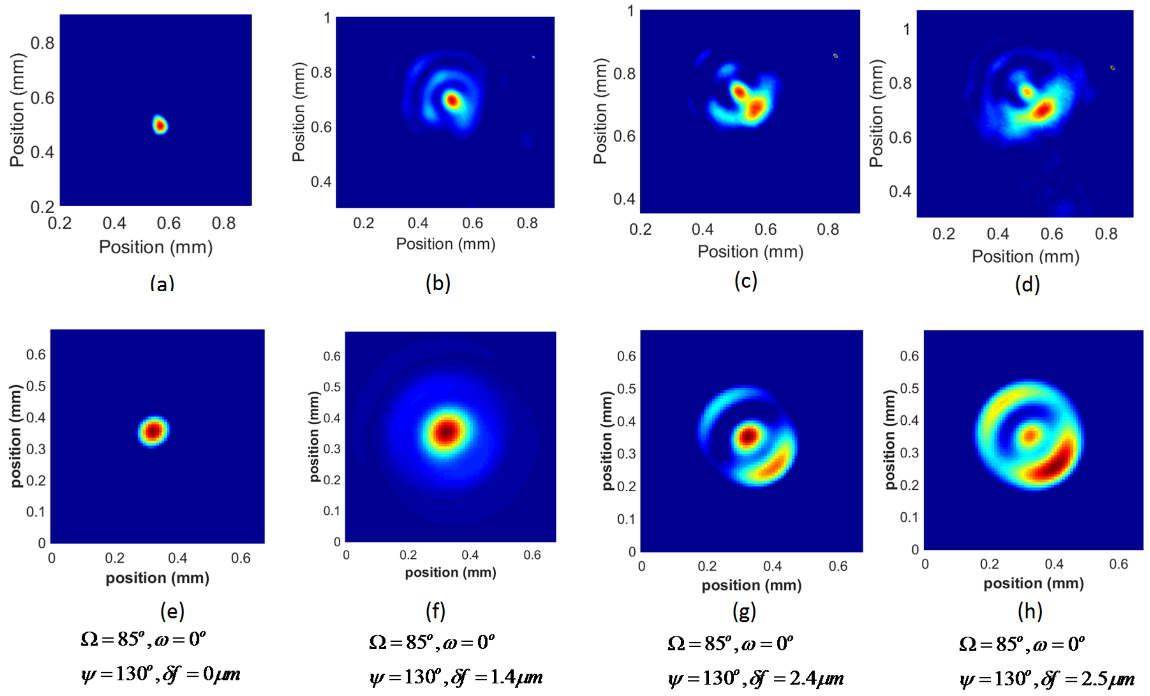

Figure 5.6: Defocused Imaging of X^{1-} exciton emission at 915.5 nm in sample VN2455 at 4K under non-resonant excitation at 830 nm; defocusing distance increases from (a) to (d). Images are simulated in matlab for an angle ψ=130^o and $\Omega = 85^o$ for dipole emitter in sample VN2455 for defocusing distances of (e) 0μm, (f) 1.4 μm, (g) 2.4 μm, (h) 2.5 μm

In Figure 5.6, progressive defocusing of the emitter is carried out towards the lens shown from (a) to (d). As the emitter at 915.5 nm is translated towards the microscope objective, the blurred image at the real plane can be used to infer the orientation of the emission dipole in the quantum dot. Defocusing distance and the orientation of the dipole emitter are obtained from match between the experimental data and simulated patterns. The model only takes into account the contribution from x-dipole in X^{1-} emission to simulate the experimental result.

5.3.2. *Emitter at 934 nm*

For the quantum dot at 934 nm in planar cavity VN2455, the charge tuning of the device yields that the exciton emission at 934 nm is a trion as shown in Figure 5.7. Emission plateaus in photoluminescence-gate voltage map are significantly longer for trions due to increased coulomb interaction and energy needed to occupy p-shell (s-shell gets occupied by two electrons in negative trion X^{1-}) for addition of another electron to the quantum dot.

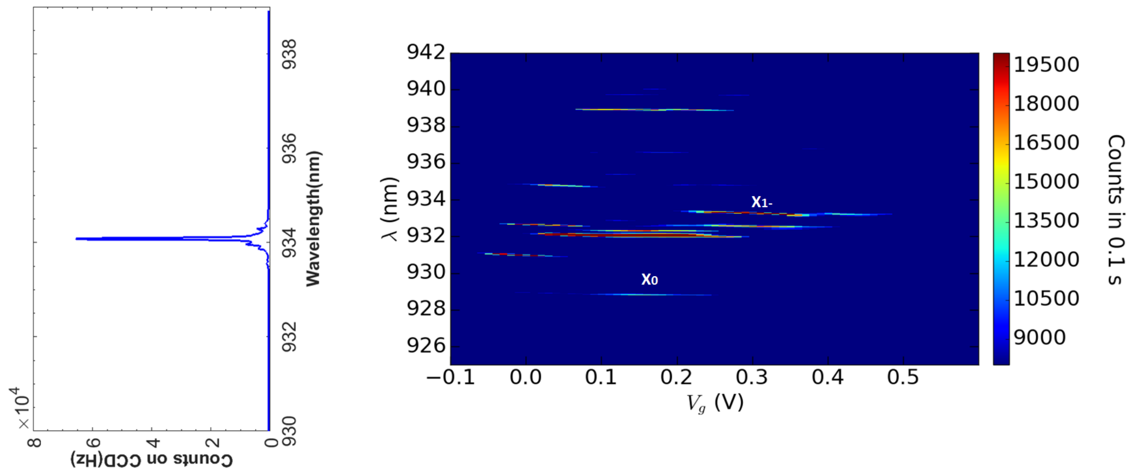

(a) (b)

Figure 5.7: (a) Photoluminescence spectrum of the X^{1-} emission from the quantum dot at 4K in planar dielectric sample VN2455. (b) Photoluminescence-gate voltage map for the quantum dot at 4K (under non-resonant excitation at 830 nm) at a wavelength of 934 nm: X^{1-} exciton is at 934 nm and the corresponding X^0 is at ∼930 nm.

The radiation from the X^{1-} exciton is filtered using a narrow-bandpass filter and using the same experimental strategy as for emitter at 915.5nm, the emitter is defocused towards the lens to obtain real plane images as shown in Figure 5.8. From (a) to (c), the defocusing distance correspond to 0μm, $\sim 1\mu$m and $\sim 2.4\mu$m as obtained by fits to experimental data. The Matlab model used for the simulation of defocused images only assumes contribution from the x-dipole and the relative angles $\Omega = 87^o$ and $\psi = 130^o$ between the dipole frame and the lab frame yielded the closest fits.

The elongated nature of the real plane image at zero defocusing can arise because of the dipole being oriented along the crystal axis of the GaAs substrate. This can also arise because of astigmatism in real plane imaging systems which basically can be defined as the deviation from a circular spot at focus. While the fitting of the experimental data yields similarity between theory and experiment, the deviation between theory and experiment can arise because of presence of neighbouring quantum dots or an absence of scattering surface.

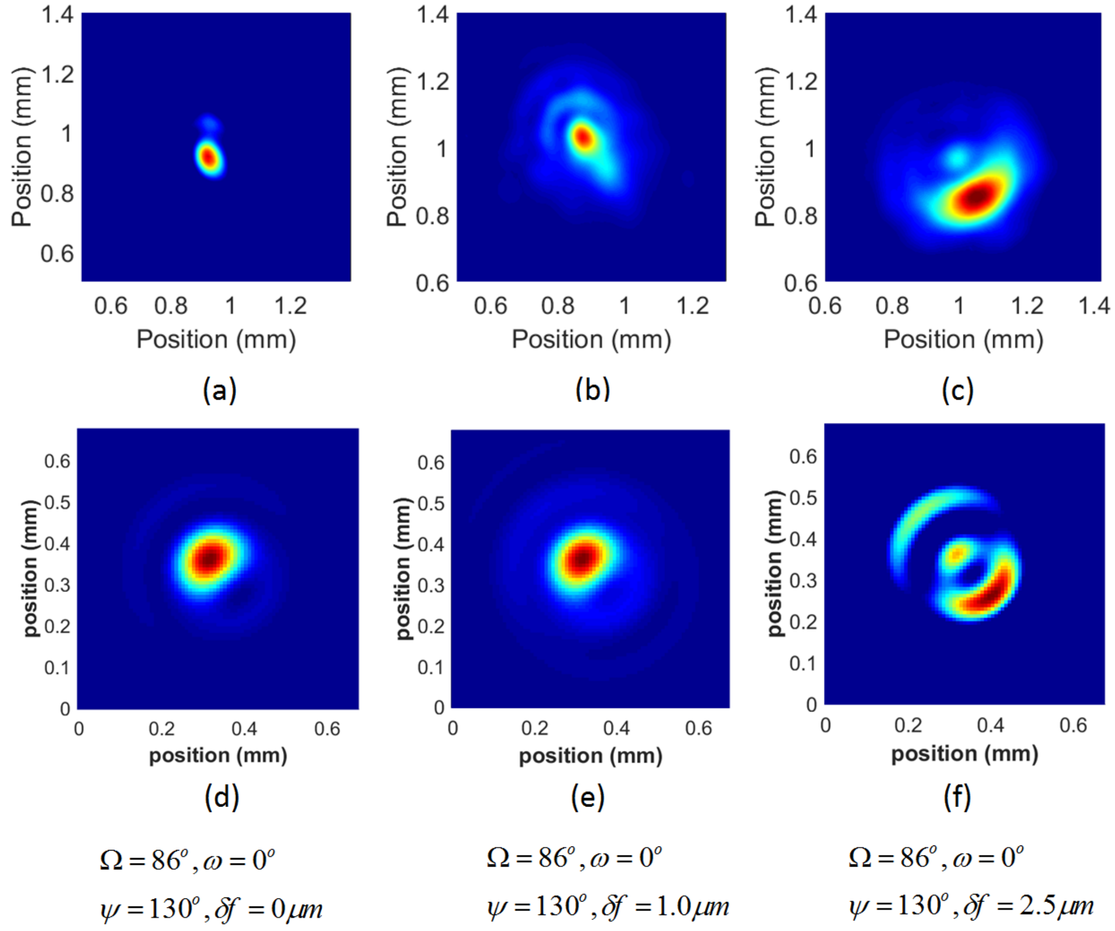

$\Omega = 86^o, \omega = 0^o$
$\psi = 130^o, \delta f = 0 \mu m$

$\Omega = 86^o, \omega = 0^o$
$\psi = 130^o, \delta f = 1.0 \mu m$

$\Omega = 86^o, \omega = 0^o$
$\psi = 130^o, \delta f = 2.5 \mu m$

Figure 5.8: Photoluminescence imaging of X^{1-} exciton at 934 nm is carried out by defocused imaging. Photoluminescence is generated from the quantum dots at 4K using a laser at 830 nm. The defocusing distance increases from (a) to (c).

5.4 Collection Efficiency from Imaging

While the defocused imaging experiment with excitons in planar cavity VN2455 provides valuable information about the emission from self-assembled InAs quantum dots and the role of optics in the imaging and photon collection process, one can also study the intensity of light that gets coupled into the microscope objective with NA of 0.68 as a function of the relative polar angle Ω between the dipole frame and lab frame. This approach, however, does not calculate the coupling into a single mode optical fibre but gives insights into mechanisms which can contribute to photon collection problems from quantum emitters.

For the simulated result shown in Figure 5.4, when gradually the relative angle Ω between the z-axes of the dipole frame and that of the lab frame increases, the intensity of collected light reduces. This can be vividly observed from the colorbar in the plot. Thus,

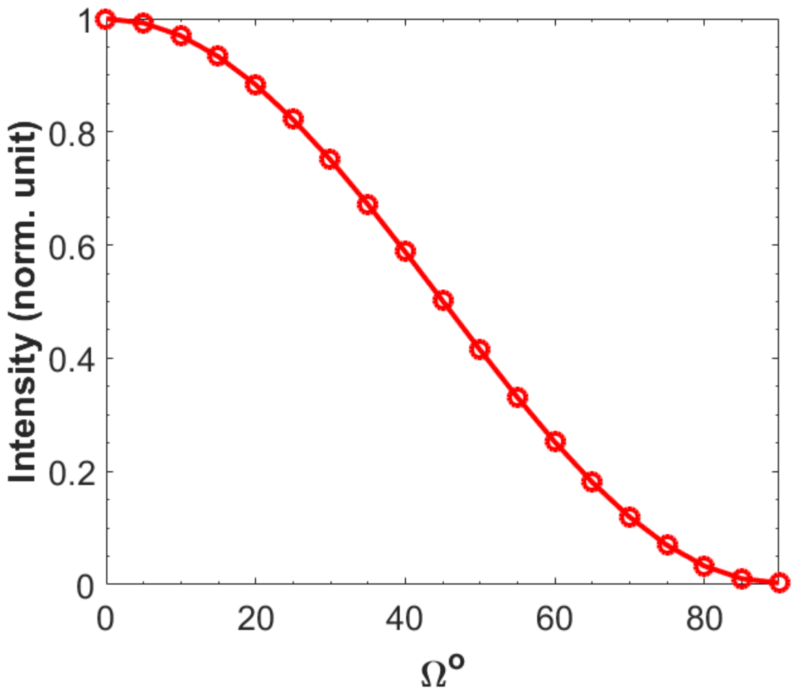

Figure 5.9: Relative collected photon intensity on CCD as a function of the angle Ω between the z-axes of the dipole frame and lab frame

if the intensity pattern incident on the CCD for zero defocusing distance is summed up as a function of this relative angle between the z-axes, the dependence of collected intensity can be determined. In Figure 5.9, this result is presented for gradual 5^o increments from 0^o to 90^o. According to this simplistic model, an angle of 75° can reduce the collected photon intensity by a factor of 10.

5.5 Summary

In summary, the in-plane dipole emission from self-assembled InAs quantum dots in GaAs when collected through a microscope objective is verified via fitting with the defocused imaging model. An angle of $\Omega = 85^o$ has been used in simulation to obtain a similar defocused imaging pattern at the CCD in simulation for emission at 915.5 nm. The large angle between the z-axes of the dipole and lab frames can cause photon collection issues shown via integrated intensity incident on the CCD as a function of angle Ω. While this information is suggestive of causes of photon loss in collection from quantum emitters, a detailed study of several quantum dots in the planar microcavity sample VN2455 can shed more light on the suggestion.

Chapter 6

Excitons in 2-Dimensional Semiconductors

Localized excitons in monolayers of two-dimensional semiconductors such as WSe_2 have emerged as a promising source of single photons. Since little is known about these emitters, photoluminescence spectroscopy, back focal plane imaging and defocused imaging of emitters are undertaken to study the properties of the localized excitons in WSe_2. It is also shown in theory that by placing the monolayer on top of a PMMA layer with a gold reflector, farfield radiation profile of the emission can be engineered. Monolayer samples were exfoliated and transferred to SiO_2/Si by A. Branny.

6.1 Two-Dimensional Semiconductor Sample

A mechanically exfoliated monolayer of WSe_2 [195] is perched over 285 nm of SiO_2 on top of silicon wafer. The sample is mounted over a x-y scanner on top of x-, y- and z-nanopositioners in a closed-cycle cryostat at 4K. The microscope head is assembled for photoluminescence spectroscopy and fourier microscopy as described in Chapter 2. Once the sample is aligned with the microscope at room temperature, the microscope stick is placed in the sample tube and pumped out to a vacuum better than 1×10^{-4}mBar before being mounted in the cryostat.

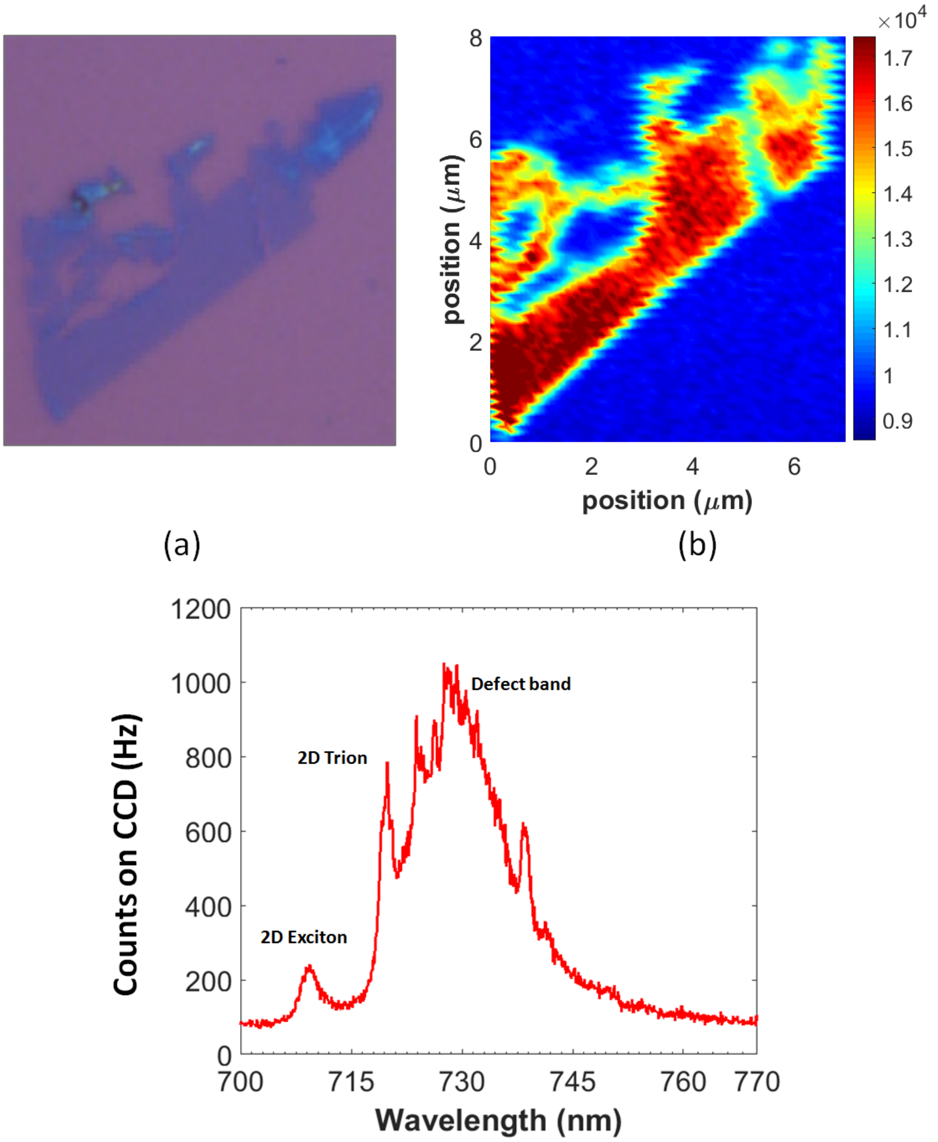

(a) (b)

(c)

Figure 6.1: (a) The image of the monolayer WSe_2 flake is obtained using a white light microscope. b) Two-dimensional photoluminescence map of the monolayer of WSe_2 is obtained at 4K under a 532 nm laser excitation. The map has been spectrally filtered to show emission between 705 nm - 720 nm.(c) The unfiltered photoluminescence spectrum at high excitation power shows three distinct features. Monolayer 2D-exciton at 710 nm, 2D-trion emission at 720 nm and a broad defect band which spans 730 nm - 745 nm is observed.

6.2 Photoluminescence Spectroscopy

For alignment on the monolayer, first the sample is defocused towards the microscope objective (NA=0.82) so that a sharp image is obtained on the CCD in the alignment camera arm under white light illumination. When the monolayer is identified by its contrast, a resonant laser at 780nm sent down from the collection arm is brought to focus on the sample. The power of the resonant laser is kept low to prevent the monolayer from getting damaged. Then the spot from the excitation green laser at 532 nm is overlapped on the sample. The resonant laser is switched off then and the collection arm optical fibre is sent to the CCD. A python program syncs the movement of the x-y-scanner and the acquisition of photoluminescence spectra on the spectrometer. The scan range of the scanner is $10\mu m \times 10\mu m$ which is large enough to map out entire monolayer samples.

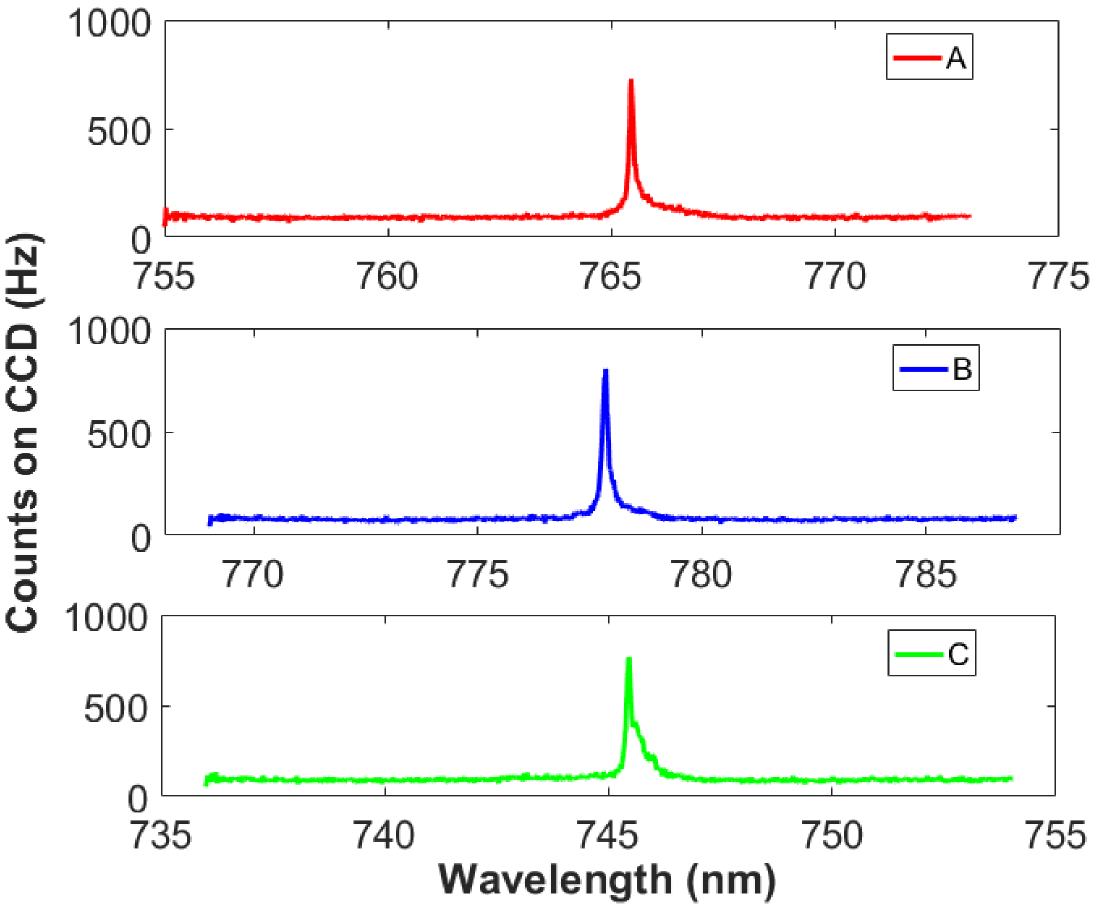

Figure 6.2: Photoluminescence from localized excitons in monolayer WSe_2 sample at a wavelength of 765 nm (emitter-A), 778 nm (emitter-B) and at 745 nm (emitter-C) under non-resonant excitation at 532 nm at a sample temperature of 4K.

A map of the monolayer WSe_2 flake is generated by scanning the sample in a confocal photoluminescence mode as shown in Figure 6.1. By spectral filtering of the confocal photoluminescence map, position of the monolayer and localized excitons are identified. The quantum-well based normal exciton emission is observed at 710 nm with a linewidth of $\sim$ 10 meV. The corresponding negatively-charged trion is observed at 720 nm. A defect emission-band is also observed between 730 nm - 750 nm as shown in Figure 6.1(c). Quantum well excitons in monolayer of WSe_2 typically have a lifetime of ∼4 ps.

In addition to the monolayer quantum well photoluminescence, local strain gradient [196] [197], defects [198] and structural discontinuities in the monolayer give rise to quantum dot like emission spectra from monolayers of semiconductors. In Figure 6.2, the photoluminescence emission from localized excitons in the monolayer WSe_2 sample are shown. The emitters are labeled as A, B and C. Emitter 'A' shows emission at 765 nm with significant phonon tail observed in photoluminescence. Photoluminescence from emitter 'B' was observed at 778 nm and showed near complete linear polarization when a linear polarizer was rotated in the collection arm as shown in Figure 6.3. Almost all localized excitons in WSe_2 on silica/silicon showed a high degree of linear polarization in photoluminescence. In Figure 6.3, the photoluminescence signal for a localized exciton emission at a wavelength of 778 nm almost vanishes for an angle of 0^o on the linear polarizer while reaches its maximum when the linear polarizer is rotated by 90^o. Emitter 'C' is a single emitter at 745.5 nm.

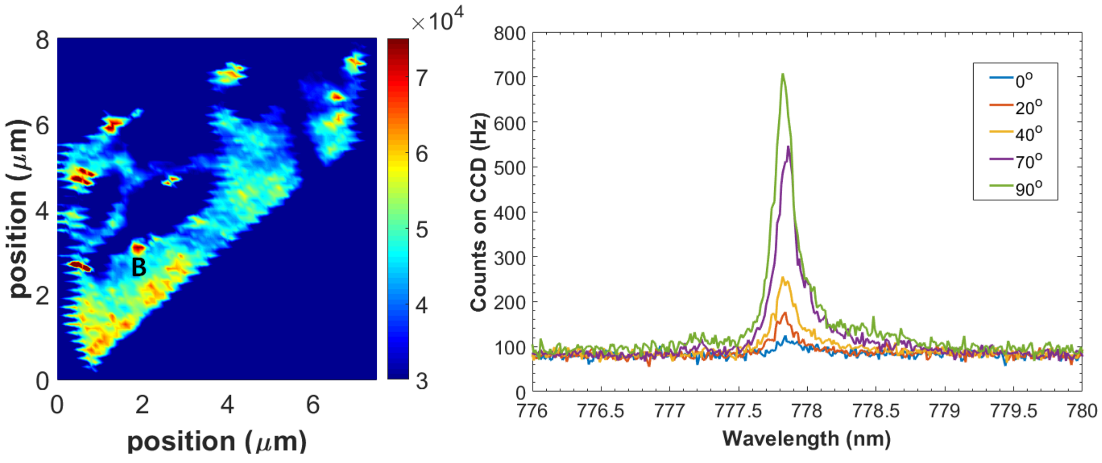

(a) (b)

Figure 6.3: (a) Localized exciton emission at 778 nm on the monolayer of WSe_2 ,(b) A strong linear polarization is observed in photoluminescence when detected through a linear polarizer

Layer	Ref. Index	Thickness (nm)
air	1	-
air	1	0
SiO_2	n_{SiO_2}= 1.4539	285
Si	3.7181	-

Table 6.1: Layer stack for monolayer of WSe_2 sample on SiO_2/Si

Layer Representation	Ref. Index	Thickness (nm)
n_0	[1]	[ ]
n_1	1	0
n_2	[n_{SiO_2}, n_{Si}]	[d_{SiO_2} = 285]

6.3 Back Focal Plane Imaging of Radiation

In order to study the angular distribution of radiation from the monolayer emission, the back focal plane of the compound microscope objective (NA = 0.82) is relayed by using two achromatic doublets from Thorlabs (AC254-400B-ML and AC254-250B-ML) on to a conjugate back focal plane where the CCD is placed. The lenses were chosen to demagnify the back focal plane pattern as the clear aperture of the microscope objective was larger than the size of the CCD chip.

For the simulation of the back focal plane imaging pattern, the localized exciton emission is modelled as a point source of plane waves on top of 285 nm of silica, which is on top of a thick silicon wafer. The layer stack is shown here. The output space is air. The layer stack above the dipole emitter is represented by variable n_0 which is only air in this case. The embedding medium is represented by n_1. Since the monolayer of WSe_2 sits on top of silica, the embedding medium is air with zero thickness. In the model, the variable z represents the distance of the dipole emitter from the embedding layer - top stack interface. The layer stack underneath the dipole embedding layer is represented by n_2.

6.3.1. Monolayer Exciton Emission

Monolayer photoluminescence arises out of an in-plane dipole as the observed angular distribution of radiation from spectrally filtered 2D exciton emission closely resembles the simulation result. For simulation, the refractive index of silica is taken as n_{silica} = 1.4539

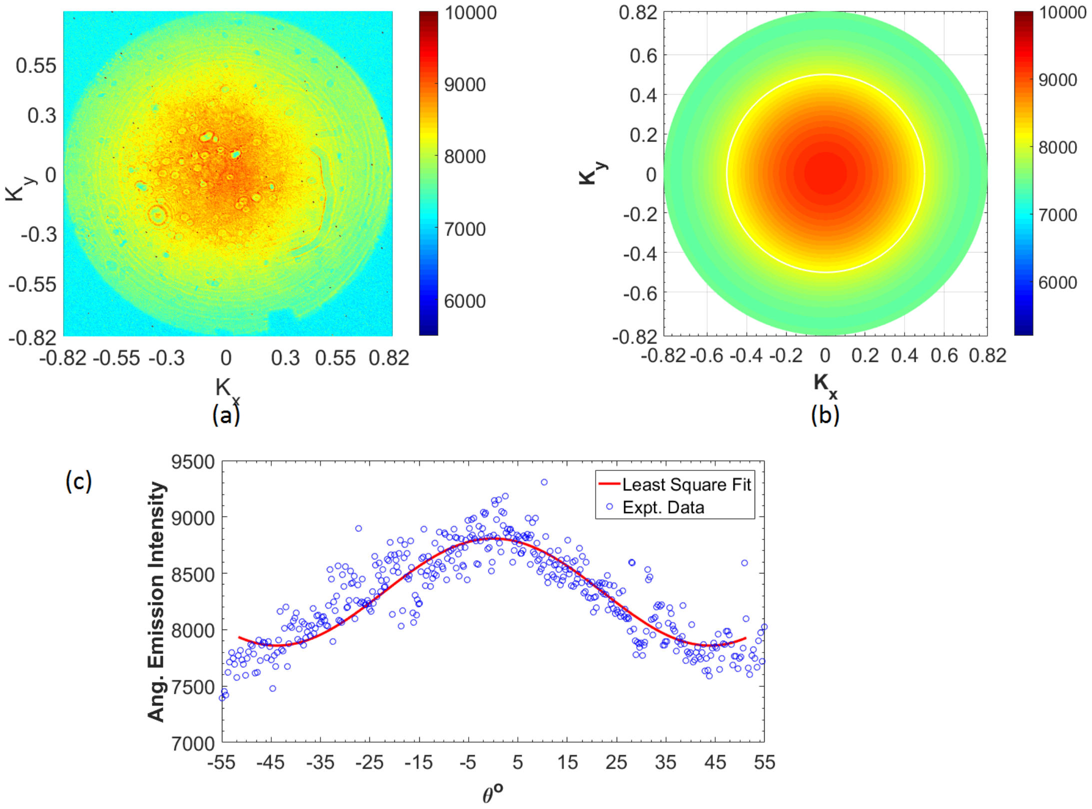

Figure 6.4: (a) Back focal plane imaging of monolayer exciton emission at 4K shows a gaussian radiation pattern for monolayer of WSe_2 on silica/silicon. Non-resonant excitation at 532 nm was used to excite the sample and the emission was filtered to only allow the 2D-exciton emission to be imaged. (b) Angular distribution of radiation is modelled for WSe_2 monolayer emission on 285 nm silica/silicon using a transfer-matrix program in Matlab. (c) Cross-section of angular distribution of radiation is shown here to match with the theoretical cross-section.

and for silicon, $n_{Si} = 3.7181$. Dipole radiation is modelled as a point source of plane waves on top of 285 nm of silica with silicon wafer under it. The radiation pattern is obtained in air and the axes are labeled in terms of the spatial frequencies k_x and k_y ($\sin\theta$ where θ is the angle w.r.t. the optic axis). As can be seen from the data and the model, for a monolayer of WSe_2 on silica/silicon, the radiation is confined within a NA = 0.5, marked as the region inside the white circle in Figure 6.4. The general expression in theory to match experimental cross-section is shown underneath:

$$I(\theta,\phi) = \left[(I_0\frac{1}{cos\theta}E_pE_p^* + I_{bg})cos^2\phi + (I_0\frac{1}{cos\theta}E_sE_s^* + I_{bg})sin^2\phi\right] \qquad (6.1)$$

For monolayer exciton emission back focal plane simulation, circularly symmetric p-polarized dipole emission is taken. Thus, the expression reduces to,

$$I(\theta, \phi) = I_0 \frac{1}{cos\theta} E_p E_p^* + I_{bg} \tag{6.2}$$

where I_0 = 4490 ± 150 and I_{bg} = 6920 ± 40. The parameters are extracted using a least square fit in Matlab. A significant match between the theory of dipole radiation and back focal plane imaging experiment confirms the validity of the approach to study monolayer samples designed for different farfield radiation patterns [199] [200]. The parameter R^2 = 0.9483 which implies that the fit explains 94.83% of the total variation in the data about the average.

6.3.2. Localized Exciton Emission

In addition to the signal from the 2D exciton from the monolayer, of particular interest are the localized excitons with quantum dot like emission spectrum. As shown in Figure 6.2, the linewidth of the emission at 745 nm (emitter 'D') is $\sim 100\mu$eV. The emission shows near-complete linear polarization as was observed by rotation of a linear polarizer in front of the collection fibre. Emission spectrum also shows a distinct phonon-sideband. For back focal plane imaging of single localized excitons in WSe_2, a narrowpass optical filter from Semrock Corporation (LL01-780-12.5) is used. Depending on the density of emitters in the filtered spectral window, two bandpass filters were often used to narrow the filter bandwidth down further. The addition of bandpass filters causes the beam to walk but it does not influence the pattern observed on the CCD in Fourier plane imaging.

As shown in Figure 6.5, the back focal plane image for the localized exciton emission at 745 nm exhibit a gaussian pattern which can be explained to arise out of in-plane p-dipole on top of 285 nm of silica layer flanked by a thick silicon wafer. Thus, both monolayer exciton and localized exciton emission in a monolayer of WSe_2 can be described by in-plane luminescent dipoles. For the theoretical model, following equation with the mentioned parameter set is used:

$$I(\theta, \phi) = I_0 \frac{1}{cos\theta} E_p E_p^* + I_{bg} \tag{6.3}$$

where I_0 = 17660 ± 580 and I_{bg} = 18320 ± 150. The least square fit yields R^2 parameter of 0.9614 which means that the fit explains the 96.14% of the variance of the data about the average.

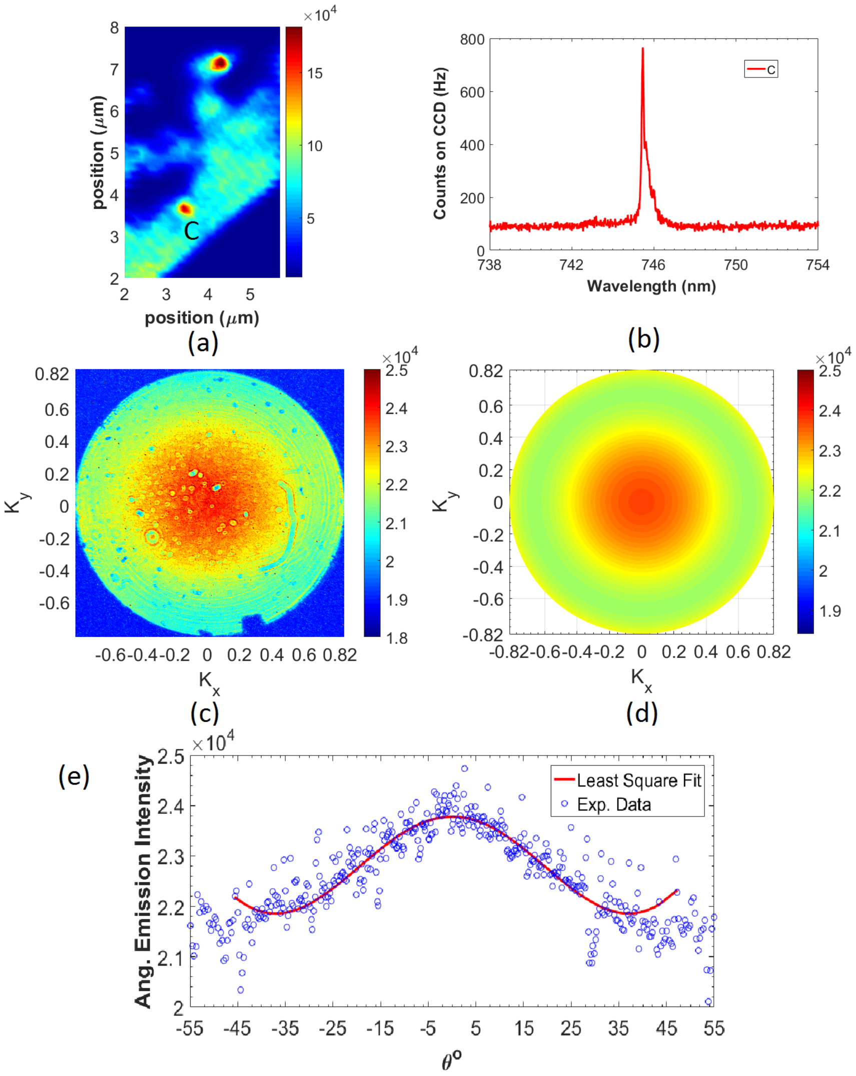

Figure 6.5: (a) Localized exciton emission (emitter-C) at a wavelength of 745 nm on the monolayer WSe_2 sample under non-resonant excitation at a wavelength of 532 nm at a sample temperature of 4K, (b) wavelength filtered photoluminescence emission spectrum at 745 nm; (c) back focal plane imaging of filtered radiation is carried out to study the angular distribution of radiation. A Gaussian pattern is obtained on the CCD from the emitter on SiO_2/Si. (d) Transfer-matrix simulation is carried out to generate the back focal pattern for dipole emission at the air-silica interface. The emission response suggests emission due to in-plane p-dipole. (e) The experimental cross-section and the theoretical least square fit are shown.

Information about distribution of radiation in k-space and the orientation of luminescent dipoles are important to design the optical system and the sample for optimal collection and extraction of photons emitted by localized excitons in the monolayer WSe_2 sample in

Layer Representation	Ref. Index	Thickness (nm)
n_0	[1]	[ ]
n_1	1	0
n_2	[n_{SiO_2}, n_{Si}]	[d_{SiO_2} = 285]

addition to confirming that radiation from localized excitons in monolayer of WSe_2 arises from in-plane dipole.

6.4 Defocused Imaging

Microscope objective lens collects light from the quantum emitter and collimates it towards collection optics in the microscope. Collimated light from single localized excitons in monolayers of WSe_2 are focused using an achromatic doublet lens on to a CCD to obtain real plane images of the emitter itself. The point-spread function of the focused emission can be used to identify the position of the emitters with a better resolution than the diffraction limit by spectrally filtering only one emission. When the emitters are defocused w.r.t. the microscope objective, the blurred intensity profile obtained at the CCD can be used to infer the orientation of the emission dipole in the emitter [200].

6.4.1. Model for Defocused Imaging

In theory, the emission from a quantum emitter can be modelled as the superposition of three orthogonal x-,y- and z-dipoles or a z-dipole and a circularly degenerate xy-dipole [201] [202]. Using the approach of simulation similar to that used for InAs quantum dots in Chapter 5, the following layer stack is used for simulation of defocused images.

The variable 'ratio' determines the weight of the z-dipole in emission. For simulation of defocused images shown in this Chapter, the value of ratio has been kept at 0. The variable κ determines the ratio of the x- and y- dipole in emission. For κ = 0, the situation is similar to a circularly degenerate dipole i.e. $I_x = I_y$. A value of -1 for κ implies contribution from only x-dipole. The relative angles between the dipole frame and lab frame are represented by variables Ω (between z-axes), ω (between y-axes) and ψ (between x-axes).

For the parameters shown above and varying defocusing distance and the angle Ω, the simulated defocused imaging patterns for the monolayer sample at an emission wavelength of 765 nm are shown in Figure 6.6.

Parameter	**Value**
λ	0.765
ratio	0
κ	-1
Ω	5^o
ω	0^o
ψ	10^o

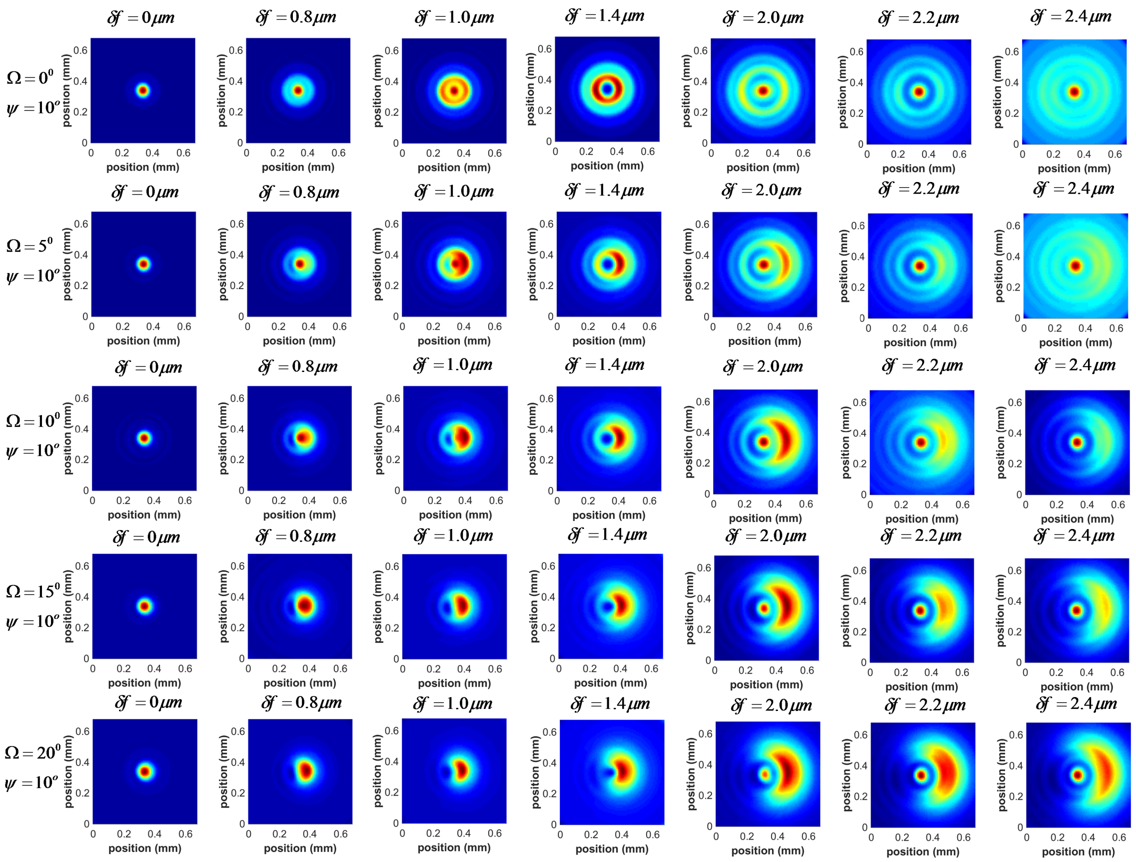

Figure 6.6: Simulated defocused imaging patterns for the localized exciton emission at a wavelength of 765 nm for $\psi = 10^o$, and Ω varied from 0^o to 20^o in steps of 5^o for defocusing distances of 0 μm, 0.8 μm, 1.0 μm, 1.4 μm, 2.0 μm, 2.2 μm and 2.4 μm.

By comparing experimentally obtained defocused images with a library of simulated images for different values of the parameters in the parameter space, the complete three-dimensional orientation of the dipole can be obtained.

6.4.2. Localized Exciton at 765 nm

The localized exciton emission at the wavelength of 765 nm is shown on the photoluminescence-space map in Figure 6.7(a) and is marked as 'A'. The filtered spectrum shows a single emitter at a sample temperature of 4K under non-resonant excitation at wavelength of 532 nm. The localized exciton emission in monolayers of WSe_2 has been shown to arise around local strain pockets which can influence the orientation of the emission dipole. Tensile strain in semiconductor quantum dots is known to create light hole excitons, which implies an out-of-plane component of dipole emission [206]. Similar behaviour can happen in the monolayer WSe_2 system due to strain. By defocused imaging of localized excitons, and by obtaining corresponding match with the theoretical model, one can ascertain if the out-of-plane component is contributing to the radiation.

The orientation of the localized exciton at the wavelength of 765 nm can be inferred by defocused imaging of photoluminescence from the emitter. The modular microscope setup has been shown in Chapter 2 to carry out the experiment. The defocusing distance w.r.t. the microscope objective are 0 μm, 0.97 μm, 1.2 μm and 2.2 μm respectively in Figure 6.7(c),(g),(k),(o), respectively. The defocusing distance is obtained from the least square fits to the cross-sections of the experimental data. The emitter is moved away from the microscope objective for imaging. The theoretical pattern shows that the z-axis of the dipole frame is oriented at an angle of $\sim$10.4^o w.r.t. the z-axis of the lab frame and the relative azimuthal angle Ψ = 15^o. The magnification of the optical system is obtained to be 140 and is used to generate the patterns.

A very close match between the simulated defocused images using an in-plane x-dipole and the experimentally acquired images confirms that the emission is not arising from the out-of-plane dipoles for these emitters. Further, in order to generate a bright source of single photons, the knowledge of the orientation of the emission dipole is vital in designing samples. The information about the relative angles between the dipole frame and lab frame is useful in the design of the optical system for maximum collection of photons emitted from localized excitons in monolayers of WSe_2.

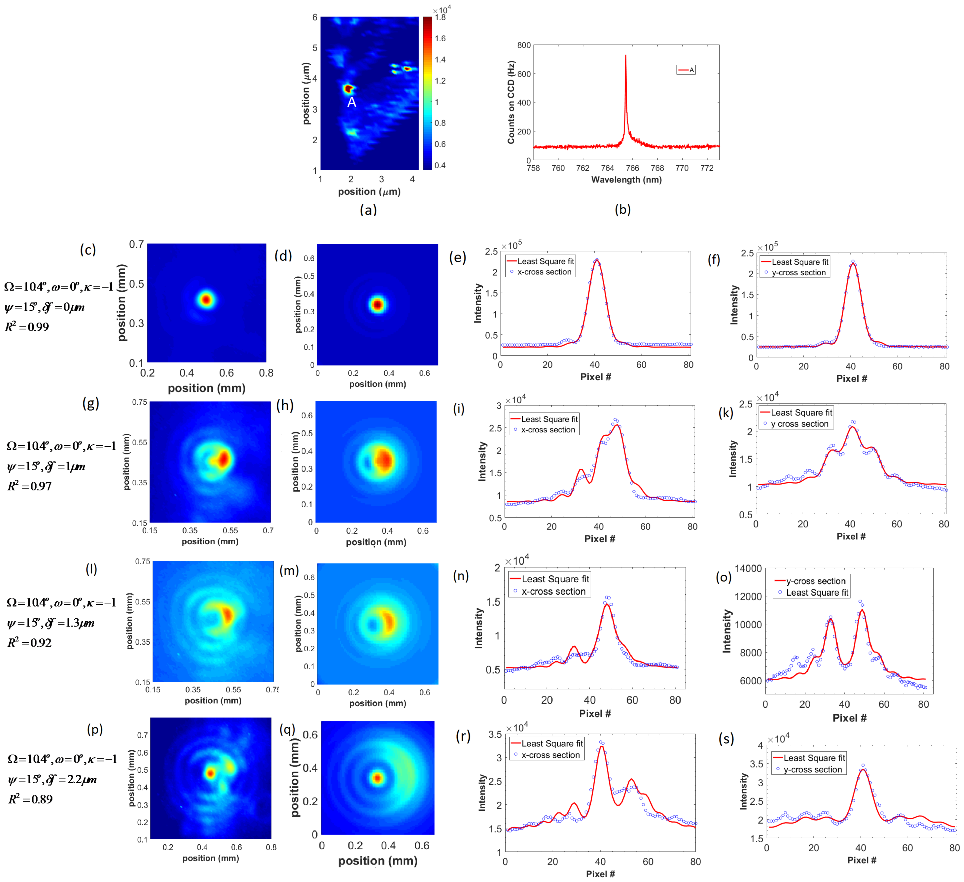

Figure 6.7: (a) Localized exciton emission at the wavelength of 765 nm at T = 4K, generated using a 532 nm laser, is shown on the photoluminescence space map. (b) The spectrum for the exciton emission at the wavelength of 765 nm is shown. (c) Experimental image for zero defocusing distance. (d) Simulated image for Ω=10.4^o, ω=0^o, Ψ = 15^o. The values are obtained by least square fitting of the x- and y-cross sections shown in (e) and (f). (g) Experimentally acquired image for defocusing distance of 0.97 μm and (h) simulated pattern using fit parameters obtained from least square fitting of cross-sections shown in (i) and (j).(k),(l) Experimental pattern and simulated pattern for a defocusing distance of 1.2 μm. The cross-sections of simulated and experimental patterns are shown in (m) and (n). A relative angle of 10.4^o (Ω) between the z-axes of the dipole frame and the lab frame, and an azimuth angle ψ = 15^o has been obtained from the fits. (o)-(r) Defocusing distance of 2.2 μm. All the fits yielded a goodness of fit factor, R^2 > 0.875.

6.4.3. Localized Exciton at 745 nm

In Figure 6.8, the localized exciton at 745 nm shown on the photoluminescence map as emitter 'c' is filtered for defocused imaging. The emitter is moved away from the microscope objective to observe the orientation of the emission dipole in the emitter. By match

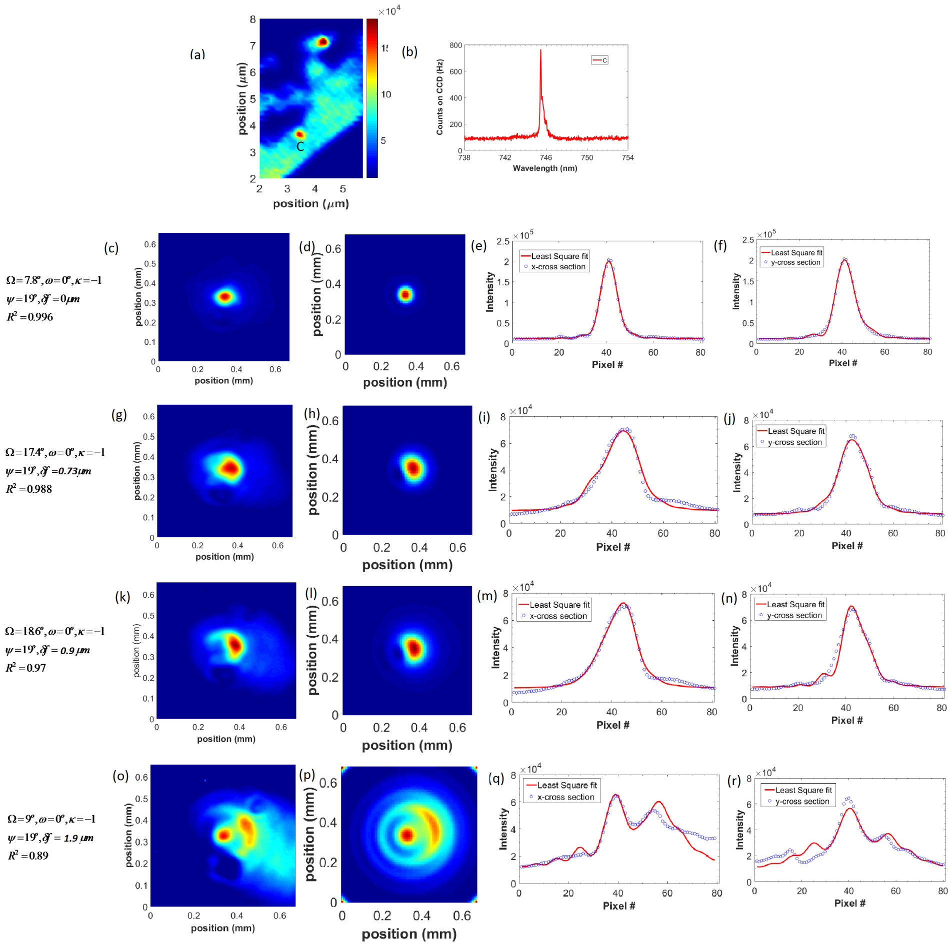

Figure 6.8: Defocused imaging of localized exciton emission observed at 745 nm is carried out to obtain the orientation of the emission dipole. (a) The photoluminescence is generated using a 532 nm laser exciting the monolayer flake in a confocal geometry. By scanning the sample at the focus of the microscope, the space map is generated. (b) The spectrum of the localized exciton at 745 nm. (c) - (f) Defocused images obtained in experiment for the localized exciton at 745 nm for δf = 0μm are shown together with simulated pattern and cross-section. Defocused images and simulated images and cross-sections are shown for defocusing of (g)-(j) 0.73μm, (k)-(n) 0.9 μm, (o)-(r) 1.9 μm. The fit also yields the z-axis of the dipole frame between 7.8^0-18.6^o w.r.t. the z-axis of the lab frame. An azimuth angle ψ = 19^o is used to match the experimental data.

of experimental data with theoretical prediction, the defocusing distance and the relative angles between the dipole frame and lab frame of emitter 'C' are obtained. From (c) to (g), the defocusing w.r.t. the microscope objective are 0 μm, 0.73 μm, 0.9 μm and 1.9 μm respectively. As can be observed in Figure 6.8, the angle between the z-axes of the dipole frame and lab frame also changes with change in defocusing distance. This is possible due to mechanical motion induced tilts in the system. A magnification of 140 was was used to simulate the patterns. The emission pattern was rotated in the plane of the CCD by 19^o w.r.t. the sample.

The imaging of the localized exciton emissions provides valuable information for the design of the optical system for maximal collection, the nature of emission from the novel quantum emitters (in-plane dipole emission) in this relatively new material system and the design of samples to extract maximum photons from the emitters. The goodness of fit parameter exhibited a high value of $\sim 90\%$ with an in-plane x-dipole source. In-plane dipole emission was also used to explain the back focal plane images obtained for the emitter at the wavelength of 745 nm. While the two results point to conclusive in-plane dipole emission for this emitter, a more detailed study on several emitters is a logical stepping stone.

6.5 WSe_2 on PMMA-Gold

As discussed in the first Chapter, the angular distribution of radiation from a dipole emitter can be engineered by embedding it in a planar microcavity or placing it close to an interface. The idea behind engineering of farfield radiation is to make sure that the light emitted from the dipole emitter can be collected by an off-the-shelf microscope objective with modest numerical aperture (NA). In addition to the light being confined in a small cone of angles, this also requires engineering the layer thicknesses in the microcavity to make sure that most of the light is coupled out as a radiation mode rather than a guided mode [207]. By virtue of interferences, extraction of photons from an emitter embedded in a high-index material can be enhanced.

Since the monolayer of WSe_2 can directly be placed on top of a polymer or semiconducting material, a half cavity approach is taken here. The polymer of choice is PMMA and the monolayer flake of WSe_2 is transferred on top of PMMA. In order to collect the light travelling downwards as shown in Figure 6.9, a gold reflector is used at the bottom of PMMA layer. The thickness 'h' of the PMMA layer is chosen to optimize the coupling of photons from an emitter in the microscope objective. In addition to controlling the fraction of emitted light being coupled out as a guided mode, the thickness of the PMMA layer also controls the 'Purcell effect' on the properties of the emitter itself. The vicinity of a metal layer close to a dipole emitter modifies the local density of states at the emitter's position and can influence its lifetime [91]. When all the above mentioned factors are taken into

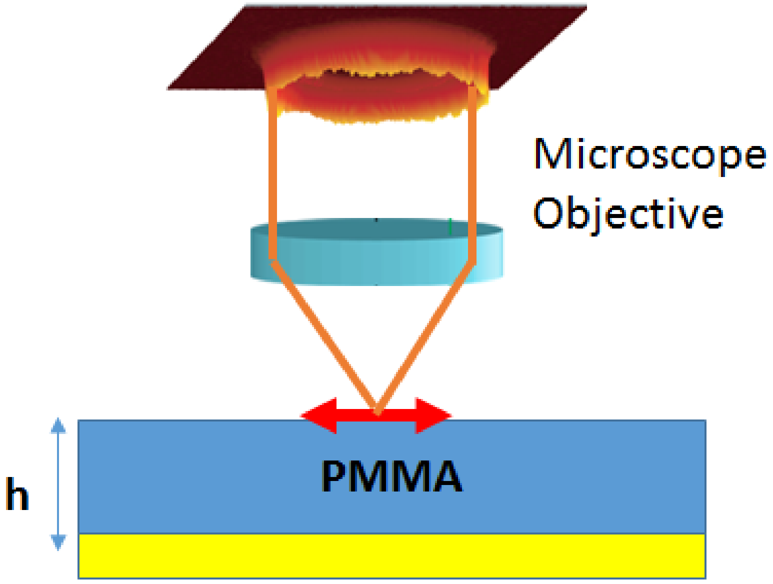

Figure 6.9: Schematic diagram of a dipole emitter on PMMA with gold reflector at the back to reflect radiation towards the collection half space

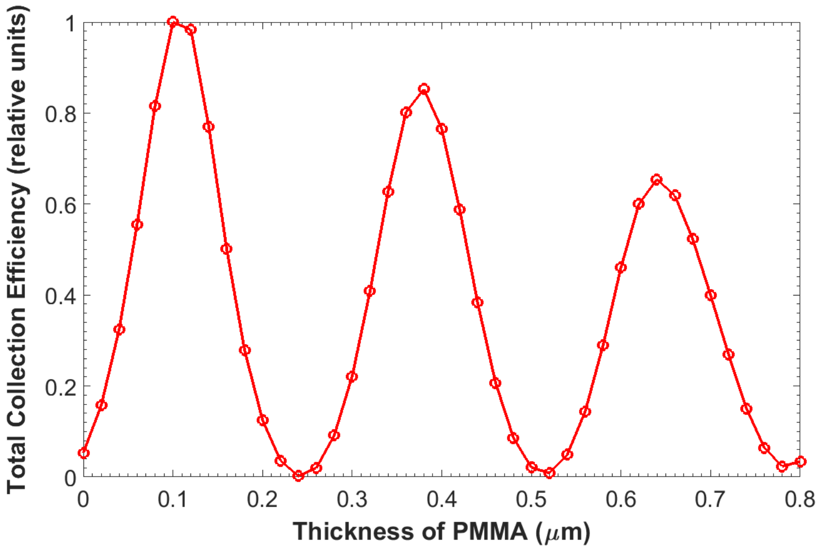

Figure 6.10: Relative collection efficiency into a single mode optical fibre with NA of 0.13 for varying thickness of PMMA for an in-plane dipole

account and studied in theory using a transfer-matrix approach, it is observed that the total collection efficiency of emission varies periodically as a function of the thickness of the PMMA layer as shown below (Figure 6.10).

For calculation of relative collection efficiency into a single mode optical fibre (NA=0.13), the model calculates real plane images for a magnification of 6.31 given by the ratio of NA

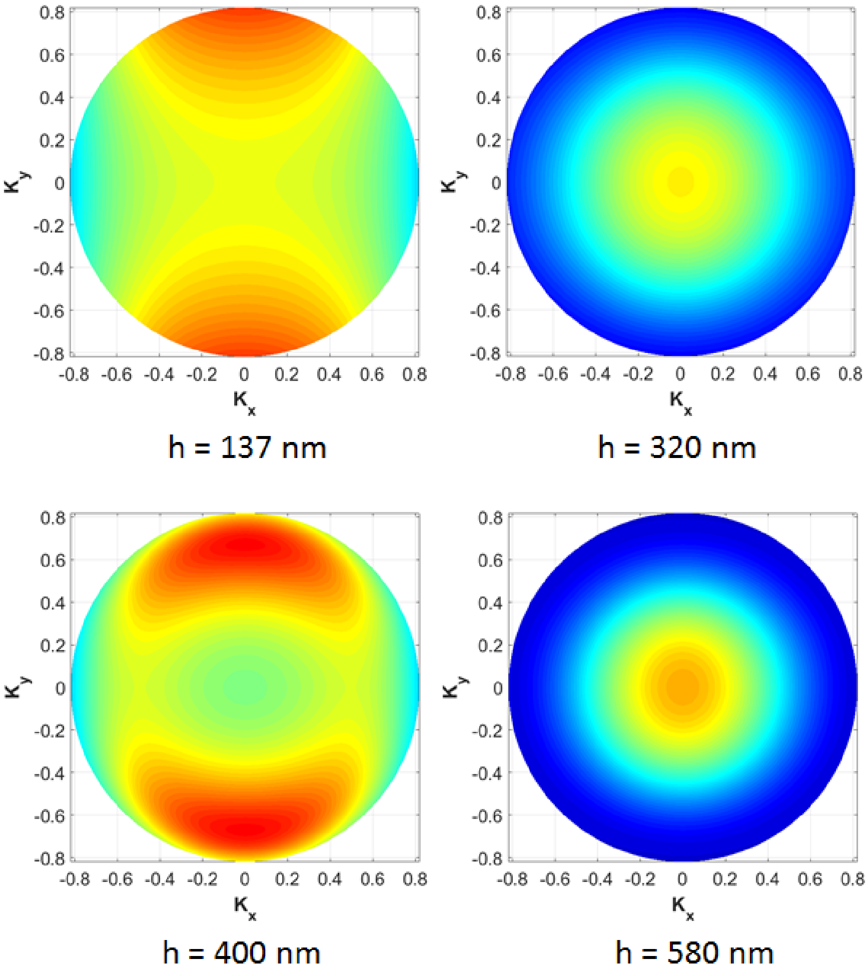

Figure 6.11: Farfield for varying thickness of PMMA for an in-plane dipole emitter on PMMA with gold reflector

of the microscope objective and that of the single mode optical fibre i.e. 0.82/0.13. The image plane is modelled to compose of pixels which are 20 nm × 20 nm in size. The proportion of the intensity of the simulated radiation pattern that falls into the physical area covered by the mode field diameter of an optical fibre is used to calculate the collection intensity. As can be observed in Figure 6.10, the collection intensity peaks for a thickness of 120 nm with a periodicity of $\sim$ 270 nm. The periodicity corresponds to the product of $n_{PMMA} \times$ 2h, which implies meeting the condition for constructive interference for emission travelling directly upwards and the one reflected from the gold layer.

The collection efficiency response as a function of PMMA thickness can also be studied by studying the pattern at the back focal plane of the microscope objective. From Figure 6.11, it can be observed that despite Gaussian patterns for thickness of 320 nm and 580 nm, the relative collection efficiency is higher for thickness of 137 nm and 400 nm. This can be explained by the coupling of light into guided modes and destructive interference between forward travelling and reflected radiation from gold.

6.6 Photon Collection Efficiency from Imaging

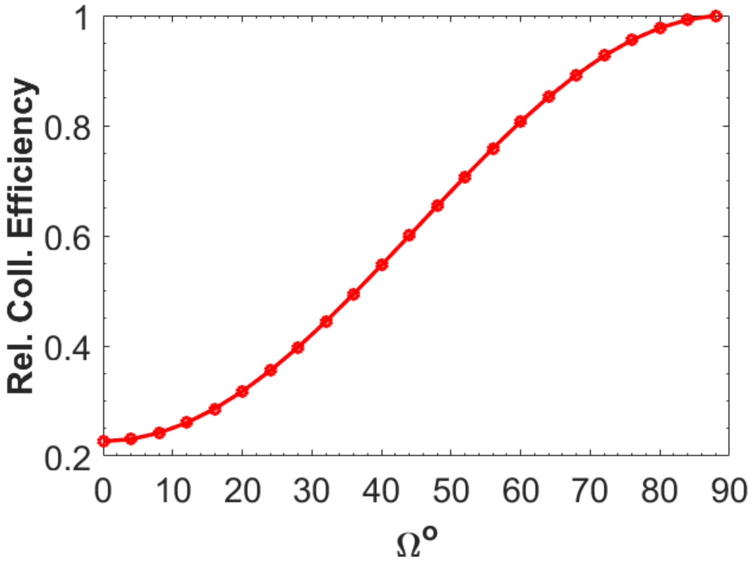

Figure 6.12: Relative collection efficiency of photon as a function of Ω i.e. the angle between the z-axes of the dipole frame and the lab frame

From defocused imaging, it was inferred that there can be a small angle (Ω) of 7^o-20^o between the z-axes of the dipole frame and the z-axes of the lab frame. From simulated defocused images, it was also observed that this relative orientation between the two frames of reference can affect the efficiency of photon collection into the optical system. In order to quantitatively obtain the relationship between efficiency and Ω, the intensity incident on the CCD in the real plane images can be summed up and plotted as a function of Ω for a x-dipole in monolayer WSe_2 on top of 285 nm of SiO_2 on silicon wafer. For an in-plane x-dipole emitter on SiO_2/Si, the intensity incident on the CCD shows an increase as Ω is increased. While this is predicted in theory, the sample can be mounted on an out-of-plane tilt stage and the relative collection efficiency be determined to test this in practice. In addition to the x-,y- and z-nano-positioners, this can potentially provide another mechanism photon collection.

6.7 Summary

Monolayer excitons and localized excitons in WSe_2 have been studied by photoluminescence spectroscopy, Fourier microscopy and defocused imaging of dipole orientation. By matching Fourier microscopy data for monolayer exciton and for localized exciton emission at a wavelength of 745 nm with theoretical modelling, the in-plane nature of dipole emission was confirmed. The fit to the data showed explained >96% variance of the data about the mean. Defocused imaging, further, allowed a match of experimental patterns with simulated patterns by using in-plane x-dipoles. The in-plane nature of emission from localized excitons can be further reaffirmed by studying several other localized emitters in this material system. The role of the angle between the z-axes of the dipole and the lab frame has been highlighted as well. Contrary to the case for self-assembled InAs quantum dots in GaAs, the excitons in monolayer WSe_2 on SiO_2/Si are expected to show an increment in photon collection when the relative angle between the z-axes of the dipole and lab is increased. The knowledge of in-plane nature of dipole emission and the relative orientational angles provide crucial information for the design of sample and experimental setup for maximal collection of photons from this material system.

Chapter 7

Summary of Results

Efficient generation of single photons can revolutionize the field of quantum communication and linear optical quantum computing. An approach is presented to realize this long-term vision using self-assembled InAs quantum dots and excitons in novel two-dimensional semiconductors such as WSe_2. Enhancement of collection efficiency of photons from quantum dots/localized excitons is the first necessity to march towards this goal. The thesis entails the non-resonant spectroscopy of single quantum emitters in high efficiency single photon sources based on self-assembled InAs quantum dots and localized excitons in WSe_2.

Single InAs quantum dots in GaAs-nanowire were studied using photoluminescence spectroscopy to characterize the behaviour of quantum dots in the device. Although the reproducibility of the device is a little cumbersome to achieve, high efficiency of photon collection was observed from the sample. Photoluminescence from quantum dots also exhibited broadening of the emission linewidth when a higher excitation power was used. This is explained to happen because of charges trapped at the surface of the nanowire producing a lateral electric field at the position of the quantum dot. While this electric field caused a shift in emission wavelength/energy, the fluctuations in electric field caused the linewidth to broaden. Time-correlated counting was carried out using a Hanbury-Brown-Twiss interferometer to establish the quantum nature of photon emission. Lifetime of the excitons was measured by triggering the correlator with sync from a pulsed laser at 830 nm. The photoluminescence from quantum dot at 4K was collected on an avalanche photon detector which was connected to the other port of the time correlator. Estimation of the efficiency of photon emission was made based on transmittance of the microscope, fibre and detector hardware and inverse of the lifetime of quantum dot excitons studied for this. Nanowire promises to be an efficient source of photon under non-resonant excitation.

For planar dielectric samples embedded with self-assembled InAs quantum dots, photoluminescence spectroscopy is used for characterization of the sample for the broadband nature of photon collection from the device. The planar dielectric sample tailors the angular distribution of radiation from a dipole emitter to extract more photons from an emitter by virtue of interferences. The key concept behind the devices is radiation from an electric dipole emitter whose angular radiation pattern is modified by choice of materials and design of sample. For the design of the optical system to collect photons from these devices, it is important to study the angular distribution of radiation that is emitted from an emitter embedded in the device because of the limitation on the numerical aperture of the microscope objective used to collect light. Thus Fourier microscopy is carried out on InAs quantum dot samples to study the angular distribution of radiation. Planar dielectric samples show strong photoluminescence signal from 910 nm to 980 nm. The incorporation of electrical contacts on the planar sample allows one to study charge tuning of the sample. Voltage applied between the Schottky contact and n+ layer tunes the emission wavelength of the exciton. The small size of quantum dots makes coulomb energy terms significantly stronger and thus single electron charging is achieved in experiment at 4K. Fourier microscopy is carried out to obtain radiation patterns from emitters at three different wavelengths of 915.5 nm, 934 nm and 955 nm. A transfer-matrix model in Matlab is used to simulate the obtained patterns in experiment for quantum dots embedded in the sample. For emitters at 934 nm and 955 nm, near Gaussian patterns were observed at back focal plane. The emitter at 915.5 nm, however, exhibited a higher radiation intensity at the edge of the NA of the lens which can partly explain the lower photon counts obtained on CCD for this emitter. The least-square fit to the experimental cross-section obtained by Fourier microscopy yielded a goodness of fit paramater $R^2 = 0.945$ for the emitter at 915.5 nm and $R^2 = 0.97$ for the emitter at 934nm. The fit to the data thus explains $\sim$95% of the variance in the data about the mean, which implies that the layer structure used in the model is the same as the layer structure in the sample grown by molecular beam epitaxy. Further, by placing a linear polarizer in the imaging path, orientation of the emission dipoles in neutral excitons can also be obtained. Study of several quantum dots under the solid-immersion lens on micro-cavity sample VN2455 by back focal plane imaging can reveal a more detailed relationship between the design and experimentally obtained patterns.

The orientation of emission dipole in a sample can also affect the efficiency of photon emission and collection from the emitter. In order to extract the orientation of emission dipoles of InAs quantum dots in planar devices in a more direct way, the photoluminescence collected from the emitter at 4K under non-resonant excitation at 830 nm is focused on a CCD. When the emitter is moved towards the microscope objective which is used to collect the light, the pattern obtained on the CCD can be used to infer the complete three-dimensional orientation of the emission dipole. Defocusing distance, the in-plane orientation of the dipole, and the relative angles between the dipole frame and lab frame are extracted from the simulated patterns for defocused imaging to match the experimentally obtained patterns. The role of angles between the dipole frame and the lab frame also has an effect on the collection efficiency. An increment in the relative angle between the z-axes of the dipole frame and the lab frame can be observed to reduce the collection of photons in simulations.

Experiments were carried out to unravel the properties of the excitons in monolayer of WSe_2 by using photoluminescence spectroscopy, Fourier microscopy and defocused imaging for single emitters at a sample temperature of 4K. Two-dimensional semiconductors have shown great promise for realization of a solid-state single photon source. Monolayer excitons in WSe_2 have linewidths of the order of a few meV and a lifetime of few ps. Delocalized quantum well based monolayer exciton emission is observed at higher powers once the localized states are saturated. The monolayer exciton emission is observed at 710 nm, the associated trion emission is observed at 720 nm and a broadband defect emission is observed between 730 nm - 745 nm. At low excitation power from the source, localized exciton emission has been observed from the samples under study. These quantum-dot like emitters exhibit antibunching and show linewidth of $\sim 100\mu$eV. The lifetime of these localized excitons are a few ns and are observed at a higher wavelength than the monolayer excitons. To understand the nature of emission from these novel emitters, Fourier microscopy and defocused imaging have been used to obtain the angular distribution of radiation and orientation of emission dipoles, respectively. Defocused imaging has revealed a relative angle Ω between the dipole frame and the lab frame when the dipole emission from these emitters is collected using the optical microscope shown in Chapter 2. A theoretical approach has also been shown to design half-cavity devices to extract photons efficiently from localized excitons in monolayer samples.

In summary, a dipole radiation approach has been taken to extract maximum number of photons from the two quantum emitter systems. By non-resonant photoluminescence spectroscopy, Fourier microscopy and defocused imaging of exciton emissions in self-assembled InAs quantum dots and monolayer WSe_2, an insight into the role of angles between the dipole and the microscope system has been shown. Identification of in-plane dipole emission from localized excitons in WSe_2 by matching defocused images obtained in experiment and the simulated ones, and by matching Fourier plane imaging data is also crucial for design of samples for this material system. A study of several more localized excitons in WSe_2 can further reaffirm the nature of dipole emission suggested by the experiments in this thesis.

References

[1] P. Shor, In Foundations Comp. Sc., 35th Ann. Symp., IEEE (1994).

[2] L. K. Grover, Proc. twenty-eighth ann. ACM symp. Theory of computing (1996).

[3] D. Deutsch and R. Jozsa, Proc. Royal Soc. London Ser. **A439** (1992).

[4] J. I. Cirac and P. Zoller, Phys. Rev. Lett. **74**,20 (1995).

[5] D. Loss and D. P. DiVincenzo, Phys. Rev. A **57**,1 (1998).

[6] A. Politi, J. C. F. Matthews, J. L. O'Brien, Science **325**,5945 (2009).

[7] E. Lucero *et al.*, Nat. Phys. **8** (2012).

[8] L. M. K. Vandersypen *et al.*, Nature **414** (2001).

[9] B. E. Kane, Nature **393** (1998).

[10] C. H. Bennett, G. Brassard and A. K. Ekert, Sci. Am. **267**, 4 (1992).

[11] V. Giovannetti, S. Lloyd and L. Maccone, Phys. Rev. Lett. **96**,1.010401 (2006)

[12] P. Kok *et al.*, Rev. Mod. Phys. **79** (2007).

[13] E. Knill, R. Laflamme and G. J. Milburn, Nature **409** (2001).

[14] C. H. Bennett and G. Brassard, Int. Conf. Comp., Sys. and Sig. Proc. **175**, 150 (1984).

[15] E. Rieffel and W. Polak, ACM Comp. Surv. **32**, 3 (2000).

[16] W. K. Wooters and W. K. Zurek, Nature **299** (1982).

[17] W.-Y. Hwang, Phys. Rev. Lett. **91** (2003).

[18] V. Scarani *et al.*, Phys. Rev. Lett. **92** (2004).

[19] K. Inoue, E. Waks, and Y. Yamamoto, Phys. Rev. Lett. **89** (2002).

[20] D. Stucki *et al.*, App. Phys. Lett. **87** (2005).

[21] N. Sangouard and H. Zbinden, J. Mod. Opt. **59**, 17 (2012).

[22] C.H. Bennett *et al.*, Phys. Rev. Lett. **70**, 13 (1993).

[23] H. de Riedmatten *et al.*, Phys. Rev. Lett. **92**, 4 (2004).

[24] L. M. Duan *et al.*, Nature **414**, 6862 (2012).

[25] H. Fearn and R. Loudon, Opt. Comm. **64**, 6 (1987).

[26] C.K. Hong, Z.Y. Ou and L. Mandel, Phys. Rev. Lett. **59**, 18 (1987).

[27] T. Jennewein, M. Barbieri, and A. G. White, J. Mod. Opt. **58**, 3-4 (2011).

[28] M. Varnava, D.E. Browne and T. Rudolph, Phys. Rev. Lett. **100**, 6 (2008).

[29] A. Kiraz, PhD Thesis, Univ. California Santa Barbara (2002).

[30] D. Walls and G. Milburn, *Quantum Optics*, (Springer, 2008).

[31] M. O. Scully and M. S. Zubairy, *Quantum Optics*, (Cambridge University Press, 1997).

[32] H.J. Kimble, M. Dagenais and L. Mandel, Phys. Rev. Lett. **39**, 11 (1977).

[33] T. Basche *et al.*, Phys. Rev. Lett., **69**, 10 (1992).

[34] C. Kurtsiefer *et al.*, Phys. Rev. Lett., **85**, 2 (2000).

[35] P. Michler *et al.*, Nature **406**, 6799 (2000).

[36] P. Michler *et al.*, Science **290**, 5500 (2000).

[37] S. Buckley, K. Rivoire and J. Vuckovic, Rep. Prog. Phys. **75**, 12 (2012).

[38] M. Usman, Quantum Dot Based Photonic Devices, URL - http://nanohub.org/resources/16542/download/2012.03.09-Usman.pdf (2012).

[39] A. Tartakovskii, *Quantum Dots: Optics, Electron Transport and Future Applications*, (Cambridge University Press, 2012), chapter 1.

[40] M. Colocci *et al.*, App. Phys. Lett. **70**, 23 (1997).

[41] D. Bimberg, M. Grundmann and N.N. Ledenstov, *Quantum Dot Heterostructures*,(John Wiley and Sons, 1999), chapter 2-4.

[42] A.N. Vamivakas, *APS Tutorial: Quantum Optics of Quantum Dots*, University of Rochester (2013).

[43] A. Lorke *et al.*, arXiv: cond-mat/9609266 (1996).

[44] L. Wang, A. Rastelli and O. G. Schmidt, J. App. Phys. **100**, 6 (2006).

[45] A. Hartmann *et al.*, App. Phys. Lett. **71**, 10 (1997).

[46] G. Bester, S. Nair and A. Zunger, Phys. Rev. B **67**(R) (2003).

[47] R.N.E. Malein, PhD Thesis, Heriot-Watt University (2015).

[48] R.J. Warburton *et al.*, Nature (London) **405** (2000).

[49] P.A. Dalgarno, Chapter 6, PhD Thesis, Heriot-Watt University (2005).

[50] K. S. Novoselov, Rev. Mod. Phys. **83**, 3 (2011).

[51] Z. Jin *et al.*, ACS Nano **5**, 4112 (2011).

[52] W. Zhao *et al.*, ACS Nano **7**, 1 (2012).

[53] R. Coehoorn, C. Haas and R. A. D. Groot, Phys. Rev. B **35**, 12 (1987).

[54] W. Yao, D. Xiao, Q. Niu, Phys. Rev. B **77**, 23 (2008).

[55] X. Xu *et al.*, Nat. Phys. 10,(2014).

[56] K. F. Mak *et al.*, Phys. Rev. Lett. **105**, 13 (2010).

[57] T. Yan *et al.*, arXiv:1507.04599v1 (2015).

[58] A. Castellanos-Gomez *et al.*, 2D Materials **1**, 1 (2014).

[59] Y. You *et al.*, Nature Physics **11** (2015).

[60] A.K. Singh, PhD Thesis, The Univ. Texas at Austin (2016).

[61] J. Huang, T. B. Hoang and M. H. Mikkelsen, Scientific Reports **6**, 22414 (2016).

[62] S. Kumar, A. Kaczmarczyk and B.D. Gerardot, Nano Letters **15**, 11 (2015).

[63] A. Srivastava *et al.*, Nat. Nanotech. **10**, 6 (2015).

[64] M. Koperski *et al.*, Nat. Nanotech. **10**, 6 (2015).

[65] Y.-M. He *et al.*, Nat. Nanotech. **10** (2015).

[66] A. Branny *et al.*, Nat. Comm. (2017).

[67] L. Novotny and B. Hecht, *Principles of Nano-Optics*, (Cambridge University Press, 2012).

[68] J. Enderlein, Tutorial: Elec. of Fluor. (2003) (unpublished)

[69] L. Luan, P. R. Sievert and J. B. Ketterson, New J. Phys. **8**, 11 (2006).

[70] W. Lukosz, J. Opt. Soc. Am. **69** (1979).

[71] S.J. Orfanidis,*Electromagnetic Waves and Antennas*, (www.ece.rutgers.edu/ orfanidi/ewa, 2016), Chapter 5 and 6.

[72] B. Richards and E. Wolf, Proc. R Soc. Lond. A **253**, 1274 (1959).

[73] M. Bohmer and J. Enderlein, J. Opt. Soc. Am. B **20**, 3 (2003).

[74] W. L. Barnes *et al.*, Euro. Phys. J. D **18** (2002).

[75] P. Bharadwaj, B. Deutsch and L. Novotny, Adv. in Opt. and Phot. **1**, 3 (2009).

[76] C.F. Wang *et al.*, App. Phys. Lett. **85**, 3423 (2004).

[77] M. Toishi *et al.*, Opt. Exp. **17**, 17 (2009).

[78] K. H. Madsen *et al.*, Phys. Rev. B **90**, 15 (2014).

[79] O. Gazanno *et al.*, Nat. Comm. **4**, 1425 (2013).

[80] L. Sapienza *et al.*, Nat. Comm. **6** (2015).

[81] M. Davanco *et al.*, App. Phys. Lett. **99**, 4 (2011).

[82] S. Strauf *et al.*, Nat. Phot. **1** (2007).

[83] O. Benson *et al.*, Phys. Rev. Lett. **84**, 2513 (2000).

[84] A. Dousse *et al.*, Nature **466**, 217 (2010).

[85] A. Greilich *et al.*, Nat. Phot. **5** (2011).

[86] S. M. Mansfield and G. S. Kino, App. Phys. Lett. **57** (1990).

[87] K. A. Serrels *et al.*, J. Nanophot. **2**, 1 (2008).

[88] M. Born and E. Wolf, *Principles of Optics*, (Cambridge University Press, 2002), 7th Edition.

[89] E.M. Purcell, Phys. Rev. **69** (1946).

[90] R.B. Patel *et al.*, Nat. Phot. **4**, 9 (2010).

[91] K. Drexhage, J. Luminescence **1**, 2 (1970).

[92] H. Benisty, H. De Neve and C. Weisbuch, IEEE J. Quant. Elec. **34**, 9 (1998).

[93] W. Lukosz and R. E. Kunz, J. Opt. Soc. Am. **67**, 12 (1977).

[94] M.A. Lieb, J.M. Zavislan and L. Novotny, J. Opt. Soc. Am. B **21**, 6 (2004).

[95] J. Claudon *et al.*, ChemPhysChem **14**, 11 (2013).

[96] J. Claudon *et al.*, Nat. Phot. **4** (2010).

[97] N. Gregersen *et al.*, Opt. Exp. **18**, 20 (2010).

[98] M.E. Reimer *et al.*, Nat. Comm. **3**, 737 (2012).

[99] N. Gregersen *et al.*,Opt. Lett. **33**, 15 (2008).

[100] P.E. Kremer *et al.*, Phys. Rev. B (R) **90**, 20 (2014).

[101] X.-W. Chen, S. Götzinger and V. Sandoghdar, Opt. Lett. **36**, 18 (2011).

[102] K. G. Lee *et al.*, Nat. Phot. **5** (2011).

[103] Y. Ma, P.E. Kremer and B.D. Gerardot, J. App. Phys. **115**, 023106 (2014).

[104] Y. Ma, P.E. Kremer and B.D. Gerardot, 12th IEEE Int. Conf. Nano. (IEEE-NANO) (2012).

[105] A.S. Backer and W.E. Moerner, J. Phys. Chem. B **118** (2014).

[106] A.P. Bartko and R.M. Dickson, J. Phys. Chem. B **103**, 16 (1999).

[107] D. Patra *et al.*, App. Phys. Lett. **87** (2005).

[108] Group webpage, Prof. Dr. Ir. J. Enderlein, Univ. Gottingen.

[109] A. Högele *et al.*, Phys. Rev. Lett. **93**, 21 (2004).

[110] P.A. Dalgarno *et al.*, Phys. Rev. B **77**, 24 (2008).

[111] R.J. Warburton *et al.*, Nature (London) **405** (2000).

[112] S. M. Mansfield and G. S. Kino, App. Phys. Lett. **57** (1990).

[113] K. A. Serrels *et al.*, J. Nanophot. **2**, 1 (2008).

[114] H. Benisty, H. De Neve and C. Weisbuch, IEEE J. Quant. Elec. **34**, 9 (1998).

[115] Y. Ma, P.E. Kremer and B.D. Gerardot, J. App. Phys. **115** (2014).

[116] Y. Ma, P.E. Kremer and B.D. Gerardot, 12th IEEE Int. Conf. Nano. (IEEE-NANO) (2012).

[117] M.E. Reimer *et al.*, Nat. Comm. **3**, 737 (2012).

[118] N. Gregersen *et al.*, Opt. Lett. **33**, 15 (2008).

[119] P. E. Kremer *et al.*, Phys. Rev. B **90**, 20 (2014).

[120] A. Castellanos-Gomez *et al.*, 2D Materials **1**, 1 (2014).

[121] Attocube Systems AG User Manual (2013).

[122] R. H. Webb, Rep. Prog. Phys. **59** (1996).

[123] P. A. Dalgarno, PhD Thesis, Heriot-Watt University (2005).

[124] http://www.hi.helsinki.fi/amu

[125] M. Born and E. Wolf, *Principles of Optics*, (Cambridge University Press, 2002), 7th Edition.

[126] P. Michler, *Quantum Dots for Quantum Information Technologies*,(Springer, 2017)

[127] U. Kubitschek, *Fluorescence Microscopy - From Principles to Biological Applications*, (Wiley-Blackwell, 2013), 1st Edition.

[128] B. Huang, M. Bates, X. Zhuang, Ann. Rev. Biochem. **78** (2009).

[129] T. Müller, C. Schumann, A. Kraegeloh, ChemPhysChem **13** (2012).

[130] A. Hartschuh, Angew. Chem. Int. Ed. **47** (2008).

[131] A. Hartschuh *et al.*, Anal. Biochem. Chem. **394** (2009).

[132] M. Böhmer *et al.*, Angew. Chem. Int. Ed. **50** (2011).

[133] M. A. Lieb, J. M. Zavislan and L. Novotny, J. Opt. Soc. Am. B **21**, 6 (2004).

[134] J. A. Schuller *et al.*, Nat. Nanotech. **8** (2013).

[135] S. Otsuki, N. Murase, H. Kano (2013), Opt. Commun. **294** (2013).

[136] J.A. Kurvits, M. Jiang and R. Zia, J. Opt. Soc. Am. A **32**, 11 (2015).

[137] M. Böhmer and J. Enderlein, J. Opt. Soc. Am. B **20**, 3 (2003).

[138] T. Ha *et al.*, J. Phys. Chem. B **103**, 33 (1999).

[139] A. P. Bartko and R. M. Dickson, J. Phys. Chem. B **103**, 16 (1999).

[140] M.A. Lieb and A.J. Meixner, Opt. Exp. **8**, 7 (2001).

[141] J. Sepiol *et al.*, Chem. Phys. Lett. **273** (1997).

[142] D. Patra *et al.*, App. Phys. Lett. **87** (2005).

[143] F. Aguet *et al.*, Opt. Exp. **17**, 8 (2009).

[144] B. Richards and E. Wolf, Proc. Royal Soc. London. Series A, Maths. and Phys. Sc. **253**, 1274 (1959).

[145] L. Novotny and B. Hecht, *Principles of Nano-Optics*, (Cambridge University Press, 2009).

[146] Single Molecule Imaging, Prof. dr. ir. J. Enderlein's research group page, Univ. Gottingen.

[147] J. Enderlein, Opt. Lett. **25**, 9 (2000).

[148] A.S. Backer and W.E. Moerner, J. Phys. Chem. B **118** (2014).

[149] P. E. Kremer *et al.*, Phys. Rev. B **90**(R), 20 (2014).

[150] G. Bester, S. Nair and A. Zunger, Phys. Rev. B **67**(R) (2003).

[151] R.J. Warburton *et al.*, Nature **405** (2000).

[152] P.A. Dalgarno, PhD Thesis, Heriot-Watt University (2005).

[153] R.J. Warburton *et al.*, Phys. Rev. B **65**, 11 (2002).

[154] J. Houel *et al.*, Phys. Rev. Lett. **108**, 10 (2012).

[155] P. W. Fry *et al.*, Phys. Rev. Lett. **84**, 733 (2000).

[156] B. D. Gerardot *et al.*, App. Phys. Lett. **90** (2007).

[157] M. Vogel *et al.*, App. Phys. Lett. **91** (2007).

[158] S. A. Empedocles and M. G. Bawendi (1997), Science **19**, 278 (1997).

[159] A. Kiraz, PhD Thesis, Univ. California Santa Barbara (2002)

[160] A. Kiraz *et al.*, Phys. Rev. B **65**, 16 (2002).

[161] P. Michler, *Quantum dots for Quantum Information Technologies, Chapter 1*, (Springer, 2017).

[162] P.A. Dalgarno *et al.*, Phys. Rev. B **77**, 24 (2008).

[163] N. Gregersen *et al.*, Opt. Lett. **33**, 1693 (2008).

[164] J. Claudon *et al.*, ChemPhysChem **14**, 2393 (2013).

[165] C. Wang *et al.*, Appl. Phys. Lett. **85**, 3423 (2004).

[166] W.L. Barnes *et al.*, The Eur. Phys. J. D **18** (2002).

[167] O. Benson *et al.*, Phys. Rev. Lett. **84**, 2513 (2000).

[168] A. Dousse *et al.*, Nature **466**, 217 (2010)

[169] A. Greilich *et al.*, Nat. Phot. **5** (2011).

[170] R.J. Warburton *et al.*, Nature (London) **405** (2000).

[171] S. M. Mansfield and G. S. Kino, App. Phys. Lett. **57** (1990).

[172] K. A. Serrels *et al.*, J. Nanophot. **2**, 1 (2008).

[173] H. Benisty, R. Stanley and M. Mayer, J. Opt. Soc. Am. A **15**, 5 (1998).

[174] Y. Ma, P.E. Kremer and B.D. Gerardot, J. App. Phys. **115** (2014).

[175] Y. Ma, P.E. Kremer and B.D. Gerardot, 12th IEEE Int. Conf. Nanotech. (IEEE-NANO) (2012).

[176] M.A. Lieb, J.M. Zavislan and L. Novotny, J. Opt. Soc. Am. B **21**, 6 (2004).

[177] A.S. Backer and W.E. Moerner, J. Phys. Chem. B **118** (2014).

[178] R.J. Warburton *et al.*, Phys. Rev. Lett. **79**, 26 (1997).

[179] URL: https://in.mathworks.com/help/curvefit/evaluating-goodness-of-fit.html

[180] K. G. Lee *et al.*, Nat. Phot. **5** (2011).

[181] X.L. Chu *et al.*, Optica **1**, 4 (2014).

[182] B. Richards and E. Wolf, Proc. Royal Soc. London. Ser. A, Math. and Phys. Sciences **253**, 1274 (1959).

[183] J. Enderlein, Opt. Lett. **25**, 9 (2000).

[184] A. N. Vamivakas, A. K. Swan and M. S. Ünlü, Opt. Lett. **32**, 8 (2007).

[185] M. Bohmer and J. Enderlein, J. Opt. Soc. Am. B **20**, 3 (2003).

[186] M. A. Lieb, J. M. Zavislan and L. Novotny, J. Opt. Soc. Am. B **21**, 6 (2004).

[187] A.S. Backer and W.E. Moerner, J. Phys. Chem. B **118** (2014).

[188] D. Patra *et al.*, App. Phys. Lett. **87**, 10 (2005).

[189] M. Barth *et al.*, Phys. Rev. Lett. **96**, 24 (2006).

[190] Single Molecule Imaging webpage, Research Group of Prof. dr. ir. J. Enderlein, Univ. Gottingen.

[191] A. Högele *et al.*, Phys. Rev. Lett. **93**, 21 (2004).

[192] P.A. Dalgarno *et al.*, Phys. Rev. B **77**, 24 (2008).

[193] R.J. Warburton *et al.*, Nature (London) **405** (2000).

[194] D. Gammon *et al.*, Phys. Rev. Lett. **76**, 16 (1996).

[195] A. Castellanos-Gomez *et al.*, 2D Materials **1**, 1 (2014).

[196] S. Kumar, A. Kaczmarczyk and B.D. Gerardot, Nano Lett. **15**, 11 (2015).

[197] A. Branny *et al.*, Nat. Comm. (2017).

[198] M. Koperski *et al.*, Nat. Nanotech. **10**, 6 (2015).

[199] M.A. Lieb, J.M. Zavislan and L. Novotny, J. Opt. Soc. Am. B **21**, 6 (2004).

[200] A. S. Backer and W. E. Moerner, J. Phys. Chem. B **118** (2014).

[201] D. Patra *et al.*, App. Phys. Lett. **87**, 10 (2015).

[202] M. Bohmer and J. Enderlein, J. Opt. Soc. Am. B **20**, 3 (2003).

[203] B. Richards and E. Wolf, Proc. Royal Soc. London. Ser. A, Math. and Phys. Sc. **253**, 1274 (1959).

[204] J. Enderlein, Opt. Lett. **25**, 9 (2000).

[205] Single Molecule Imaging, Research webpage of Prof. dr. ir. J. Enderlein, Univ. Gottingen.

[206] Y.H. Huo *et al.*, Nat. Phys. (2013).

[207] H. Benisty, H. De Neve and C. Weisbuch, IEEE J. Quant. Elec. **34**, 9 (1998).

[208] K. Drexhage, J. Luminescence **1**, 2 (1970).